



Multispectral imaging of painting: potentialities and limitations of the technique in relation with the chemical and optical proprierties of the pictorial materials

Lucilla Pronti

► To cite this version:

Lucilla Pronti. Multispectral imaging of painting: potentialities and limitations of the technique in relation with the chemical and optical proprierties of the pictorial materials. Radiochemistry. Université d'Avignon; Università degli studi La Sapienza (Rome), 2016. English. NNT : 2016AVIG0262 . tel-01488628

HAL Id: tel-01488628

<https://theses.hal.science/tel-01488628>

Submitted on 13 Mar 2017

HAL is a multi-disciplinary open access archive for the deposit and dissemination of scientific research documents, whether they are published or not. The documents may come from teaching and research institutions in France or abroad, or from public or private research centers.

L'archive ouverte pluridisciplinaire **HAL**, est destinée au dépôt et à la diffusion de documents scientifiques de niveau recherche, publiés ou non, émanant des établissements d'enseignement et de recherche français ou étrangers, des laboratoires publics ou privés.



SAPIENZA
UNIVERSITÀ DI ROMA



Dottorato di ricerca:

**Scienze Applicate per la Protezione
dell'Ambiente e dei Beni Culturali**

Dipartimento di Scienze della Terra

Coordinatore Adriana MARAS

Chimica

UMR IMBE - CNRS 7263 / IRD 237

**Università d'Avignon e dei Paesi della
Vaucluse, Avignone, Francia**

Coordinatore Olivier DANGLES

Tutore Scientifico

Mario PIACENTINI

Cathy VIEILLESCHAZES

Revisori

Anna Candida FELICI

Matthieu MÉNAGER

Docenti Esaminatori

Rémy CHAPOULIE

Anna PELAGOTTI

Riassunto

Lo scopo di questo lavoro è quello di valutare le potenzialità e le limitazioni dell'imaging multispettrale per l'analisi dei dipinti, confrontando questa tecnica con quelle tradizionali come la fotografia di fluorescenza indotta dalla radiazione UV e la riflettografia infrarossa. L'applicazione dell'imaging multispettrale allo studio dei materiali pittorici è stata supportata da altre tecniche analitiche come la spettroscopia di riflettanza e fluorescenza, la spettroscopia di fluorescenza dei raggi X (XRF), la spettroscopia di assorbimento UV-visibile e la spettroscopia infrarossa a

MULTISPECTRAL IMAGING OF PAINTINGS

Potentialities and Limitations of the technique in
relation with the chemical and optical properties of
the pictorial materials

Lucilla PRONTI

XXVII Ciclo

trasformata di Fourier in riflettanza totale attenuata (FTIR-ATR). L'imaging multispettrale è stato testato come strumento diagnostico su materiali pittorici realizzati in laboratorio: strati pittorici costituiti da pigmenti (moderni e antichi), leganti (uovo e olio di lino) e vernici naturali. Per i composti organici sono stati valutati i cambiantichi chimici e ottici introdotti da processi di invecchiamento artificiale (fotochimico e termico).

Inoltre, è stata effettuata una campagna diagnostica su due dipinti conservati all'Accademia di San Luca (Roma) tramite fotografia di fluorescenza indotta da radiazione UV, radiografia, spettroscopia di riflettanza, spettroscopia di fluorescenza dei raggi X (XRF), imaging multispettrale di fluorescenza UV, di riflettanza e riflettografia infrarossa multispettrale.

Rispetto alle tecniche tradizionali di imaging, quella multispettrale permette l'individuazione di peculiari caratteristiche spettrali, che, in alcuni casi, consentono di identificare il pigmento e/o aree disomogenee della superficie pittorica. La possibilità di selezionare specifiche regioni infrarosse consente di visualizzare dettagli diversi dello strato preparatorio, consentendo un'analisi più accurata della tecnica di esecuzione.

Uno dei limiti dell'imaging multispettrale riguarda l'identificazione delle miscele complesse e/o stratificazioni dei materiali pittorici, così come per le spettroscopie di riflettanza e di fluorescenza. Inoltre, la possibilità di rilevare una determinata emissione e/o riflessione di luce è affidata al filtro ottico; la scelta dei filtri, quindi, rimane una questione piuttosto delicata.

TABLE OF CONTENTS

Introduction

PART I : MULTISPECTRAL IMAGING. GENERAL ASPECTS

1.	UV-VIS-NIR multispectral imaging	1
1.1.	Multispectral imaging and spectroscopy	2
1.2.	Multispectral reflectance imaging	4
1.2.1.	Spectral reflectance factor and Reflectance	4
1.2.2.	Fiber optics reflectance spectroscopy (FORS)	9
1.2.3.	FORS vs Multispectral reflectance imaging	10
1.3.	Multispectral fluorescence imaging	10
1.3.1.	UV-fluorescence phenomena	10
1.3.2.	Fluorescence spectra and auto-absorption correction	12
1.3.3.	UV photography vs UV multispectral imaging	14
1.4.	Multispectral Near Infrared imaging	17
1.4.1.	IR Reflectography. Fundamental principles	17
1.4.2.	IR Reflectography vs Multispectral Infrared imaging	17
2.	Multispectral acquisition system	19
2.1	Acquisition setup	20
2.2	Light sources	20
2.2.1.	UV lamps	20
2.2.2.	Visible and infrared lights	22
2.1.	CCD cameras	22
2.2.	Optical system and interferential filters	23
2.3.	Dark, Bias and Flat field	24
2.4.	Multispectral reflectance image processing	29

2.5.	Linear optoelectronic transfer function of the acquisition system	30
2.6.	Radiometric calibration	32
2.7.	Multispectral UV fluorescence image processing	34
2.8.	Reconstruction of the spectra from multispectral imaging	34

PART II: MULTISPECTRAL IMAGING APPLIED ON PICTORIAL MATERIALS

1.	Binders media	37
1.1.	Introduction	38
1.2.	Materials	40
1.3.	Accelerated ageing	40
1.4.	Methods	40
1.5.	Results and discussion	41
1.5.1.	Chicken egg	41
1.5.1.1.	Fluorescence excitation emission spectroscopy (EES)	41
1.5.1.2.	ATR-FTIR	49
1.5.2.	Linseed oil	52
1.5.2.1.	Fluorescence excitation emission spectroscopy (EES)	52
1.5.2.2.	ATR-FTIR	55
1.6.	Conclusions	58
2.	Pigments and pictorial layers	61
2.1.	UV-VIS-NIR spectroscopy and multispectral imaging for the pigments identification	61
2.1.1.	Introduction	61
2.1.2.	Materials	61
2.1.3.	Methods	63
2.1.4.	Results and discussion	63
2.1.4.1.	Reflectance spectra	63

2.1.4.2.	Reflectance spectra and the influence of the backgrounds	68
2.1.4.3.	Reflectance spectra and the influence of experimental setups	71
2.1.4.4.	Multispectral reflectance imaging	74
2.1.4.5.	Fluorescence spectra	89
2.1.4.6.	Multispectral UV-fluorescence imaging	96
2.1.4.7.	Multispectral Near Infrared imaging	98
2.1.5.	Conclusions	
2.2.	Study of the spectral behaviour of pigments mixed with oil and egg yolk in different percentages by means of UV-VIS spectroscopy and UV-VIS multispectral imaging	106
2.2.1.	Introduction	106
2.2.2.	Materials	106
2.2.3.	Methods	114
2.2.4.	Results and discussion	115
2.2.4.1.	Reflectance spectra	115
2.2.4.2.	Fluorescence spectra	124
2.2.4.3.	Correction of UV-fluorescence spectra	135
2.2.4.4.	Multispectral imaging	137
2.2.5.	Conclusions	141
2.3.	White pigment identification by means of reflectance and fluorescence spectroscopies and multispectral imaging	143
2.3.1.	Introduction	143
2.3.2.	Materials	145
2.3.3.	Methods	145
2.3.4.	Results and discussion	146
2.3.4.1.	Spectroscopic analysis	146
2.3.4.2.	Multispectral imaging	155

2.3.5.	Conclusions	159
3.	Spirit and oil varnishes	161
3.1	Introduction	162
3.2	Materials	165
3.3	Accelerated ageing	165
3.4	Methods	166
3.5	Results and discussion	167
3.5.1	ATR-FTIR	167
3.5.1.1	Photo-thermal effects	171
3.5.1.2	Thermal ageing	171
3.5.2	Spectrofluorimetry	175
3.5.2.1	Mastic	175
3.5.2.2	Dammar	181
3.5.2.3	Colophony	187
3.5.3	UV-VIS Absorption spectra and yellowing	193
3.5.4	Multispectral fluorescence imaging	202
3.6	Conclusions	207

PART III: MULTISPECTRAL IMAGING AS A DIAGNOSTIC TOOL FOR PAINTINGS

1.	Diagnostic study of two paintings of Lazoni's collection	209
1.1.	Introduction	209
1.2.	"Virgin and the Child and Saint Catherine of Alessandria" by Matteo di Giovanni's imitator	211
1.2.1.	Non-destructive stratigraphic investigation	211
1.2.2.	Pigments identification	222
1.3.	"Virgin and the Child" by Venetian school	230
1.3.1.	Non-destructive stratigraphic investigation	230

1.3.2.	Pigments identification	244
1.4.	Conclusions	252

General conclusions and perspectives

Bibliography

APPENDIX A: EXPERIMENTAL CONDITIONS AND SETUPS

APPENDIX B: FORS SPECTRA with different backgrounds

APPENDIX C: FLUORESCENCE SPECTRA with different backgrounds

APPENDIX D: XRF ANALYSIS

Introduction

The study of an art work consists on the analysis of several historical, technical and stylistic elements that allow to collocate the work in a precise time and, in some cases, to attribute the work to a specific artist or artists. During this complicate process, the scientific investigations help the art historians to understand the nature of the pictorial materials and the execution techniques. Moreover, the scientific investigations can guide the restorers to a proper conservation work, evaluating the state of degradation and monitoring the restoration iter.

In recent years, the development of non invasive techniques have permitted to perform scientific analysis in situ without any damage of the art work, however in the presence of a complex heterogeneity the study of a small sample is necessary.

Among the non-invasive analyses, the imaging techniques are preferred because they allow an overview of the entire art work and can direct the analysis point to point, that return more detailed results but related to small areas.

The aim of this work is to investigate the potentiality and the limitations of the multispectral imaging applied on paintings comparing the results obtained with traditional imaging techniques, such as ultraviolet-induced visible fluorescence photography and infrared reflectography. The assessment of the multispectral imaging was performed with the support of other techniques such as fluorescence and reflectance spectroscopy, X-ray fluorescence spectroscopy (XRF), UV-VIS absorption and Attenuated Total Reflectance Fourier Transform Infrared Spectroscopy (ATR-FTIR).

We tested the multispectral imaging as a diagnostic tool on pictorial materials realized in laboratory, including several ancient and modern pigments, egg and linseed oil as binders, natural varnishes and several mixtures among them. For the organic materials, we evaluated their optical and chemical modifications due to photochemical and thermal ageing.

Moreover, we conducted a diagnostic investigation on two paintings preserved in the Gallery “Accademia di San Luca” by means of ultraviolet-induced visible fluorescence photography,

infrared reflectography, reflectance spectroscopy, ED-XRF, radiography and UV-VIS-NIR multispectral imaging.

PART I:

MULTISPECTRAL IMAGING.
GENERAL ASPECTS

Chapter 1

UV-VIS-NIR MULTISPECTRAL IMAGING

In this section we illustrate the chemical and physical principles of UV-VIS-NIR multispectral imaging and its applications on paintings. Fiber optics reflectance spectroscopy (FORS) and multispectral reflectance imaging are discussed as diagnostic tools for pigments identification. Moreover we will focus on the comparison between the traditional imaging techniques, i.e. UV-fluorescence photography and IR reflectography, with multispectral imaging.

1.	UV-VIS-NIR multispectral imaging	1
1.1.	Multispectral imaging and spectroscopy	2
1.2.	Multispectral reflectance imaging	4
1.2.1.	Spectral reflectance factor and Reflectance	4
1.2.2.	Fiber optics reflectance spectroscopy (FORS)	9
1.2.3.	FORS vs Multispectral reflectance imaging	10
1.3.	Multispectral fluorescence imaging	10
1.3.1.	UV-fluorescence phenomena	10
1.3.2.	Fluorescence spectra and auto-absorption correction	12
1.3.3.	UV photography vs UV multispectral imaging	14
1.4.	Multispectral Near Infrared imaging	17
1.4.1.	IR Reflectography. Fundamental principles	17
1.4.2.	IR Reflectography vs Multispectral Infrared imaging	17

1.1 Multispectral imaging and spectroscopy

The characterization of the materials constituting a painting is an important step to understand the pictorial techniques used by the artists and to determinate the preservation status of the work. Modern analytic techniques provide information on the chemical composition of the materials, based on micro-samples (~1 mg) taken from the objects. However the samples can not be put back in place and the achieved results are valid only for that specific specimen and in general they cannot be extended to neighbouring areas. This limit occurs also with non-invasive techniques such as X-ray fluorescence (XRF), laser-induced breakdown spectroscopy (LIBS), Raman and FTIR spectroscopies, due to the fact that they are performed on very small areas. A diagnostic approach involving the whole area of the painting is useful to individuate heterogeneous features and, eventually, to direct local analysis; multispectral imaging can be employed for this purpose.

Multispectral imaging was developed 40 years ago and until the 1990s its use was mainly restricted to astrophysics, remote sensing and terrestrial military applications [Rencz et al. (1999)]. This technology has undergone a rapid development during the last 20 years and has been applied in many research fields, such as the remote sensing of Earth's atmosphere [Green et al. (1998)], the detection of contaminants on food [Polder et al. (2002)], the analysis of plants and fruits [Kim et al. (2001)], and the diagnostic of cancer tissue [Martin et al. (2006)].

Over the last decade, it has also gained importance in the field of conservation, due to the extensive application in the study of paintings with the Infrared Reflectography (IRR) [Bonifazzi et al. (2008)], UV fluorescence and Reflectance imaging [Pelagotti et al. (2006), Delaney et al. (2009)].

Multispectral Imaging has been developed by combining digital imaging and spectroscopy. In fact this technique permits to acquire a set of two-dimensional images at different wavelengths within a given spectral range. This means that spatial and spectral information is simultaneously recorded: the light intensity is registered as a function of both location (pixel of the image) and wavelength.

To be thorough, it is necessary to mention another technique based on the same principles: hyperspectral imaging. This differs from multispectral imaging for the number of spectral images produced: less than 12 for the multispectral imaging, and much more for the hyperspectral system. For this purpose, the hyperspectral system is constituted by tunable filters (liquid-crystal tunable filter, LCTF) [Attas M. et al. (2003)], or acousto-optical tunable filters (AOTF) [Liang. H et al. (2010)], or grating spectrometers [Delaney J. K. et al. (2010)].

The less expensive multispectral acquisition system consists in two light sources, placed so as to illuminate uniformly the surface of the painting, and a digital charge coupled device (CCD) camera equipped with different filters for capturing the images at different wavelengths.

Changing the source of illumination and the filters in front of the CCD camera, it is possible to obtain stratigraphic information of the painting: using visible filters (from 400 nm to 750 nm) and illuminating with UV sources, the fluorescence emission from the superficial layers (UV Multispectral Imaging) is collected. With the same acquisition set up but using visible light, the system acquires reflectance images of the pictorial layers, whereas using an IR source and IR filters (from 800 to 1000 nm for a silicon CCD camera) the CCD camera takes images of the underdrawing, depending on the chemical and physical properties of the pictorial layers.

Taking multispectral images, it is possible to reconstruct the fluorescence emission spectra and the spectral reflectance factor curves (from visible to IR ranges) at every sampled point of the painting and this is a really useful feature when dealing with heterogeneous surfaces.

Moreover it is possible to combine this information with those obtained in the usual RGB visible photographs and to propose digital or “virtual” restoration of a painting, taking into account its history, modifications and repaintings done in the past [Landi et al. (2011)].

Deepening the study of previous papers on multispectral imaging, we noticed some misunderstandings regarding the term “multispectral imaging”. The recent meaning is related to the use of a set of filters (generally more than three) or other devices that select wavelengths, so that the term is mainly referred to the acquisition system. This approach can be also named “image spectroscopy” or “spectral imaging”. The other meaning involves the entire set of diagnostic

images: UV fluorescence photography, infrared reflectography, grazing light photography, radiography, and, often, the RGB image. So the acquisition system remains the same for most of these techniques (for example a color camera) but the excitation source changes. This is a subtle difference but it is necessary to underline it since this work is focused on the modern meaning of the term, even if we acquired multispectral images using different sources [Blažek J. et al. (2013)]. The multispectral and hyperspectral images can be acquired at several wavelengths using a scanning system [Carcagni P. et al. (2007), Bonifazzi C. et al. (2008)]. The scanning device is based on contact-less and single-point measurement of the spectral reflectance: the detector is a spectrophotometer that is moved in front of the painting; by recording its position the images can be reconstructed.

1.2 Multispectral reflectance imaging

1.2.1 Spectral reflectance factor and Reflectance spectroscopy

The basic principle for the identification of pigments with multispectral reflectance imaging is the same as for reflectance spectroscopy. Structures in the reflectance spectra are strictly connected to the selective absorption of light from the materials. The electromagnetic radiation can be absorbed by a material when its energy equals the energy difference between two quantum states of the material. In the case of the UV-VIS radiation the two quantum states are electronic states (or orbitals), so that the radiation causes electronic transitions. Since the energies of the electronic states are different in each material, measuring the absorption (or reflectance) of the radiation as a function of its energy can be used for the identification of the chemical composition of the material [Wendlandt W.W. et al. (1966), Bacci M. (2000), Feller (2001)]. For example, in pigments constituted by semiconductors, such as cinnabar or cadmium yellow, band-band transitions occur. In semiconductors the energies of the valence electron states spread and group, forming two energy bands separated by an energy gap. The lowest energy band, called valence

band, is completely filled with the valence electrons; the highest energy one is the conduction band and it is empty. When the electromagnetic radiation hits a semiconductor, the electrons may absorb the photons and jump from the valence band to the conduction band. If the energy gap corresponds to visible wavelengths (400 - 750 nm \approx 3.1 - 1.65 eV), a specific colour appears. Cinnabar, HgS, which has a 2 eV band gap, absorbs the violet-blue and green portions of the visible spectrum, resulting red coloured. When the energy gap is less than the energy of the visible radiation, all the visible radiation is absorbed and the material results of black colour [<http://www.webexhibits.org/causesofcolor/10.html>].

A beam of electromagnetic radiation impinging upon an object may undergo to: reflection (specular or diffused), scattering and transmission. The latter is measured by means of UV-VIS-IR spectroscopy in transmittance mode, while the other effects are measured by means of reflectance spectroscopy.

A simple model describing the interaction of light with a layer of a diffusive medium (for example, a pictorial layer) is the Kubelka-Munk model [Kubelka P. et al. (1931), Kubelka P. (1948)]. The model assumes that 1) the light beam propagates and reflects perpendicular to the layer crossed; 2) the layer exhibits infinite lateral extension (the edge effects are neglected); 3) the light absorbing and scattering particles are uniformly distributed in the layer, 4) particle dimensions are much smaller than the thickness of the layer and the incident wavelengths, ; 5) the whole layer is homogeneously illuminated with a monochromatic diffuse light source [Vargas et al. (1997)]. So the Kubelka-Munk theory takes into account only the absorption and the scattering phenomena occurring within a layer [Oleari C. et al. (1998)]. The theory starts with two differential equations describing the variation of two opposite light fluxes of wavelength λ (nm), $dI(\lambda, z)$ and $dJ(\lambda, z)$, crossing an infinitesimal thickness dz at depth z from the layer front surface, with a light absorption coefficient, $K(\lambda)$, and a light scattering coefficient, $S(\lambda)$. $I(\lambda, z)$ is the downward flux while $J(\lambda, z)$ is the upward flux:

$$dI(\lambda, z) = -(K(\lambda) + S(\lambda)) I(\lambda, z) dz + S(\lambda) J(\lambda, z) dz$$

$$dJ(\lambda, z) = (K(\lambda) + S(\lambda)) J(\lambda, z) dz - S(\lambda)I(\lambda, z) dz$$

The variation $dI(\lambda, z)$ of the downward flux $I(\lambda, z)$ is caused by:

- a reduction due to the absorption: $-K(\lambda)I(\lambda, z)$
- a reduction due to the diffusion: $-S(\lambda)I(\lambda, z)$
- an increase due to the back diffusion of the upward flux: $+S(\lambda)J(\lambda, z)$

The same things affect the upward flux $J(\lambda, z)$.

The total photon flux, I_{tot} is the sum of the two light fluxes $I(\lambda, z)$ and $J(\lambda, z)$. Both fluxes $I(\lambda, z)$ and $J(\lambda, z)$ decrease non-linearly with increasing depth. We define the reflectance $r(z)$ of the infinitesimal layer dz at depth z as:

$$r(z) = J(\lambda, z)/I(\lambda, z)$$

Considering the derivative of the reflectance $r(z)$ with respect to z , we obtain:

$$\frac{1}{2S} \frac{dr}{dz} dr = -(r^2 - 2ar + 1) \quad \left(a = 1 + \frac{K}{S}\right)$$

Integrating this equation and using the boundary conditions:

- $r = R$ (factor of reflectance of the sample) for $z = 0$
- $r = R_f$ (factor of reflectance of the underlying layer) for $z = d$,

we obtain:

$$\ln \frac{(R-a-b)(R_f-a+b)}{(R_f-a-b)(R-a+b)} = 4bSz \quad b = \sqrt{a^2 - 1}$$

For a very thick layer ($d \rightarrow \infty$) R is independent from R_f , then we can put $R_f = 0$. If we define R for a very thick layer as R_∞ , we obtain:

$$R_{\infty} = a - b = 1 + \frac{K}{S} - \sqrt{\left(\frac{K}{S}\right)^2 + 2\frac{K}{S}}$$

In this case the reflectance is only a function of the coefficients of absorption and scattering.

By solving this equation for K/S for each wavelength, we obtain the Kubelka-Munk function, or remission function, $f(R_{\infty})$

$$f(R_{\infty}) \equiv \frac{K}{S} = \frac{(1 - R_{\infty})^2}{2R_{\infty}}$$

The reflectance of a finite layer and/or in the condition of $R_f \neq 0$, is given by

$$R = \frac{(1/R_{\infty})(R_f - R_{\infty}) - R_{\infty}(R_f - 1/R_{\infty}) \cdot \exp[2sd(1/R_{\infty} - R_{\infty})]}{(R_f - R_{\infty}) - (R_f - 1/R_{\infty}) \cdot \exp[2sd(1/R_{\infty} - R_{\infty})]}$$

The Kubelka-Munk theory takes into account only the light propagation inside a layer but it does not consider surface effects, such as the Fresnel reflection. The Saunderson correction [Saunderson J. L. (1941)] takes into account the discontinuity of the refraction index at the air-layer interface and it considers the geometry of illumination used with the integreted sphere.

The pigments, and consequently the painted surfaces, present a refractive index higher than that of air ($n_{\text{air}}=1$). If we consider the incident light perpendicular to the boundary surface between two substances (air and pictorial layer), the intensity of the reflected light is given by:

$$I = \left(\frac{n_1 - n_2}{n_1 + n_2}\right)^2 I_0$$

where I_0 is the intensity of the incident light and n_1 and n_2 are the refractive indexes of the two media. Taking into account the Kubelka-Munk theory, we describe the fraction of incident light transmitted into the layer as $(1 - r_e)$ where r_e is the portion of incident light reflected in air and, in the opposite side, the fraction of transmitted light to the air $(1 - r_i)$ where r_i is the portion of the reflected light into the layer.

Introducing the refractive index, n , we obtain the following equation:

$$(1 - r_e) = n^2 (1 - r_i)$$

The flux relative to the reflection phenomena decreases whenever it interacts with the interface, then the reflectance defined by Saunderson, R_1 , is given by:

$$\begin{aligned} R_1 &= r_e + (1 - r_e)(1 - r_i)R + (1 - r_e)(1 - r_i)r_iR^2 + (1 - r_e)(1 - r_i)r_i^2R^3 + \dots \\ &= r_e + (1 - r_e)(1 - r_i)R \cdot \sum_{j=0}^{\infty} (r_iR)^j \end{aligned}$$

which is a geometric series converging to:

$$R_1 = r_e + (1 - r_e)(1 - r_i) \frac{R}{1 - r_iR}$$

When $r_e = r_i = 0$, R_1 coincides with the Kubelka-Munk model one.

In practice it is difficult to assess this contribution because it is necessary to know the refraction index of the materials.

In 1962 Duncan D. R. showed that the total absorption coefficient (the scattering coefficient) of a system made by a mixture of pigments is the weighted sum of the absorption coefficients, $K_i(\lambda)$ (of the scattering coefficients $S_i(\lambda)$) of each pigment [Duncan D.R. (1962)]; the weight is given by the relative concentrations, c_i , of each pigment. The basic Kubelka-Munk equation then becomes:

$$\frac{K_{mix}(\lambda)}{S_{mix}(\lambda)} = \frac{\sum_i c_i K_i(\lambda)}{\sum_i c_i S_i(\lambda)}$$

This means that the reflectance spectrum measured on a painting depends on the number of pigments present in the sampled area and on their concentrations.

1.2.2 Fiber Optics Reflectance Spectroscopy (FORS)

The fiber optics reflectance spectroscopy is based on the measure of the spectral reflectance factor (SRF). This is defined as the ratio between the reflected radiant flux, $\Phi_{\Omega \text{ sample}}$, from a surface into a specific cone Ω of a sampling aperture, and the reflected radiant flux, $\Phi_{\Omega \text{ ideal diffuser}}$, of an ideal diffuser, illuminated with the same incident light:

$$R(\lambda) = \frac{\Phi_{\Omega \text{ sample}}}{\Phi_{\Omega \text{ ideal diffuser}}}$$

The term fiber optics reflectance spectroscopy refers to the use of two optical fibers: one for illuminating and one to collect the reflected/diffused light from the sample. However there are other devices that measure the spectral reflectance factor in the same way but without fibers; for example, the compact colorimeter that collects directly the reflected/diffused light from the sample into the spectrometer.

The scientific literature shows that this technique is a helpful tool for pigments identification, even if complex pigment mixing and stratifications may prevent a correct discrimination [Bisulca et al. (2008), Bacci M. et al. (2003)]. One of the methods to solve this problem is to build databases of reference spectrophotometric curves of well-known pigments and binders; some databases are already available on line [<http://fors.ifac.cnr.it>, Cosentino A. (2014)].

Another aspect to underline is that the SRF spectra are affected by both the reflected and the scattered light. Whereas the absorption of light is a relatively straightforward phenomenon to interpret, the scattering of light is more complex. For instance, it depends on the difference between the refractive indexes of the pigment and of the suspending medium, as well as on the particle size relative to the wavelength of the incident light.

1.2.3 FORS vs Multispectral reflectance imaging

We can consider that the multispectral reflectance imaging is an upgrade of the reflectance spectroscopy. Certainly the multispectral images are less performant than spectroscopy in terms of spectral resolution, but their advantages are the spatial resolution and the possibility of mapping a specific pigment on the painting surfaces[Zhao Y. et al. (2008), Cosentino A. (2015)].

1.3 Multispectral fluorescence imaging

1.3.1 UV fluorescence phenomena

The UV fluorescence emission is the consequence of the excitation induced by ultraviolet radiation of an electron in atoms or molecules; the excited electron, relaxing to the ground state, emits fluorescence photons. If the excitation wavelengths are in the UV region, the emitted photons are in the visible range, because the radiative emission occurs at longer wavelengths than the exciting radiation (Stoke rule). UV fluorescence emission has been exploited on paintings since the 1920's to identify the state of conservation and/or the chemical composition of the pictorial materials. The use of fluorescence based techniques is extremely useful for the study of organic materials; but good results can be obtained also on minerals [Feller R. J. (2001)].

The first studies focused on the fluorescence spectroscopy of art materials were carried out in 1982 by Rène de la Rie. He measured the fluorescence spectra of several pigments [De la Rie E. R. (1982a)], linseed oil films and natural resins both fresh and artificially aged[De la Rie E. R. (1982b)] and some oil painted surfaces [De la Rie E. R. (1982c)].

After these pioneering studies, several researches have dealt with the understanding of the chemical-physical properties of the molecules, analysing the pictorial materials realized ad hoc or measuring directly work of art by means laboratory or portable spectrofluorimetries [Lalli C. et al. (1990), Anglos D. et al. (1996), Miliani C. et al. (1998), Pelagotti A. et al. (2005), Thoury M. et al.

(2007), Nevin A. et al. (2008b), Aldrovandi A. et al. (2010), Romani A. et al. (2010), Sandu I. C. A. et al. (2011), Mannino M. R. et al. (2013)].

UVabsorption measurements and spectrofluorimetry are the main fluorescence spectroscopies used in laboratory. They show high performance but they need a small sample. Thus they are extremely useful for the study of reference samples that simulate the pictorial materials, but less useful for real paintings due to the necessity of a sampling. Many investigations are performed in solution, since for complex samples the dilution is necessary to identify single molecules.

The fluorescence phenomenon is a highly sensitive analytical tool, which can be used to measure concentrations of most fluorescent compounds as low as a few picograms per ml, for example the the most common set up for the chromatographic technique is based on the detection of fluorescence emissions

Other fluorescence spectroscopies can be performed in situ thanks to devices equipped with optical fibers such as Laser-Induced Fluorescence spectroscopy (LIF), consisting of a laser excitation source, optics (lenses or fibers) and a spectrometer. If the laser is replaced by UV LEDs, the technique is just called UV fluorescence spectroscopy.

In spite of the wide scientific production about the fluorescence spectroscopy applied to pictorial materials, it is very difficult to compare new results with those already published. The reasons are linked to:

- The fluorescence emission depends extremely on the presence of impurities, aging and the conservation state of the sample. The same materials, such as linseed oil, can be produced by using different treatments and processes, that can modify the final chemical composition and then the spectral features.
- The fluorescence spectra can be influenced by the geometry and the excitation wavelengths used, that affect the position of the maximum and the full width at half-maximum of the fluorescence peaks.
- Heterogeneous materials can produce fluorescence spectra difficult to interpret.

1.3.2 Fluorescence spectra and auto-absorption correction

The identification of a material by the fluorescence spectra is quite arduous on painted surfaces due to the presence of complex compounds mixed together (i.e. pigments and binders) and/or constituted by stratified layers (i.e. varnish coatings above painted surfaces).

In a heterogeneous layer such as a painted surface, some relevant phenomena occur that influence the recorded spectra leading to an apparent change of the intensity and the spectral distribution of the emission of a specific fluorophore or the appearance of new emission bands [Verri G. et al. (2008)]. This is due to the fact that the pigments scatter and absorb the radiation emitted by the surrounding fluorophores such as the binders. Auto-absorption process between fluorescent molecules can also occur.

In order to explain these phenomena, the contributions of the radiation coming from a painted layer when it is reached by an UV beam are:

- 1) The fluorescence emission of the binder without any further interactions;
- 2) The emitted photons coming from the binder interact with other fluorophores and cause scattering and auto-absorption phenomena;
- 3) The emitted photons can interact with the pigments, whose chemical and optical/physical properties produce other multiple scattering and auto-absorption processes.

Among these phenomena, the third one produces the most significant changes of the fluorescence spectra and the absorbing agents can be pigments or dyes.

A model for correcting the fluorescence spectra in the presence of scattering and absorbing particles, based on the Kubelka-Munk theory, see par. 1.2.1, was developed by Ramos M. E. and Lagorio M. G. for the correction of the fluorescence spectra of chlorophyll in plant leaves [Ramos et al. (2004)].

Supposing the hypothesis assumed for the Kubelka-Munk theory, we can write again the remission function as

$$f(R) = \frac{K}{S} = \frac{(1-R)^2}{2R}$$

Considering that the radiation emitted by a fluorophore produces two photon beams traveling in the direction of the incoming and reflected radiation, respectively, the primary re-emitted radiation beam at the front surface of the sample can be obtained:

$$F(\lambda) = \varphi f(\lambda) I_0 \alpha_0 [1 - R_{\lambda_0}] \gamma(\lambda, \lambda_0)$$

where λ and λ_0 represent the emission and the excitation wavelengths, respectively, φ is the fluorescence quantum yield, $f(\lambda)$ is the normalized spectral emission distribution, I_0 is the intensity of the incoming radiation, α_0 is the absorbance value of the fluorescence specie at λ_0 , and $\gamma(\lambda, \lambda_0)$ is the correction factor given by:

$$\gamma(\lambda, \lambda_0) = \left\{ \frac{1}{1 + \sqrt{\frac{f(R)}{f(R) + 2}}} \right\} \times \left\{ \frac{1}{1 + \sqrt{\frac{f(R) [f(R) + 2]}{f(R_{\lambda_0}) [f(R_{\lambda_0}) + 2]}}} \right\}$$

This equation is obtained under the further assumption that the scattering coefficient, S , is independent of the wavelength and that the re-absorbed radiation does not suffer from further re-emission. This is the case of a painted surface composed by an organic binder with a not-fluorescent pigment.

Under these assumptions, the “true” emission spectrum, $C(\lambda)$, normalized to its maximum value, can be obtained as :

$$C(\lambda) = \frac{F(\lambda)}{\gamma(\lambda, \lambda_0)}$$

where $F(\lambda)$ is the recorded fluorescence.

Thus, for correcting the experimental fluorescence spectrum of a sample, we can apply the above model taking into account that:

- $F(\lambda)$ is the fluorescence spectrum measured in a fixed interval of wavelengths;
- R is reflectance measured in the same fixed interval of wavelengths;
- $f(R)$ is calculated
- $R_{\lambda_0} = R(\lambda = \lambda_0)$ is measured;
- the $f(R_{\lambda_0})$ is calculated;
- $\gamma(\lambda, \lambda_0)$ is calculated;

This correction works well in the case of opaque and not fluorescent pigments but it does not work for dyes due to their own fluorescence and the possible presence of other fluorescent compounds [Verri et. al. (2008)].

1.3.3 UV photography vs UV multispectral imaging

Ever since the 1920s, paintings have been investigated under a UV light source to reveal the visible fluorescence emission of the various pictorial materials present on the outer layers of paintings. Traditionally this diagnostic method is used mainly to reveal the presence of old varnish layers or to individuate the lack of fluorescence that may indicate retouched or newly repainted areas and/or to identify fluorescent pigments [Aldrovandi A. et al. (2001), Cardinali et al. (2002)].

In Fig. 1 we show several fluorescence images taken on the painting “Virgin with the Child” of Francesco di Giorgio Martini. The UV-fluorescence photography taken with a compact camera (Coolpix) shows a blue-green fluorescence on the Virgin’s profile. In the images taken with the cooled CCD camera and the common RGB filters the fluorescence emission appears strong using the green filter and weak with the blue filter. However, it is arduous to recognize the colour of

fluorescence, because the RGB filters select a wide spectral interval, as shown in Fig. 2. In addition, the recorded fluorescence emission is affected by the spectral sensitivity of the camera, that generally simulate the human visual sensitivity, which is high for the green wavelengths. In fact, commonly employed imaging systems, such as photographic cameras, do not allow neither a correct colorimetric reproduction of the UV induced fluorescence nor its quantitative correct radiometric or photometric evaluation.

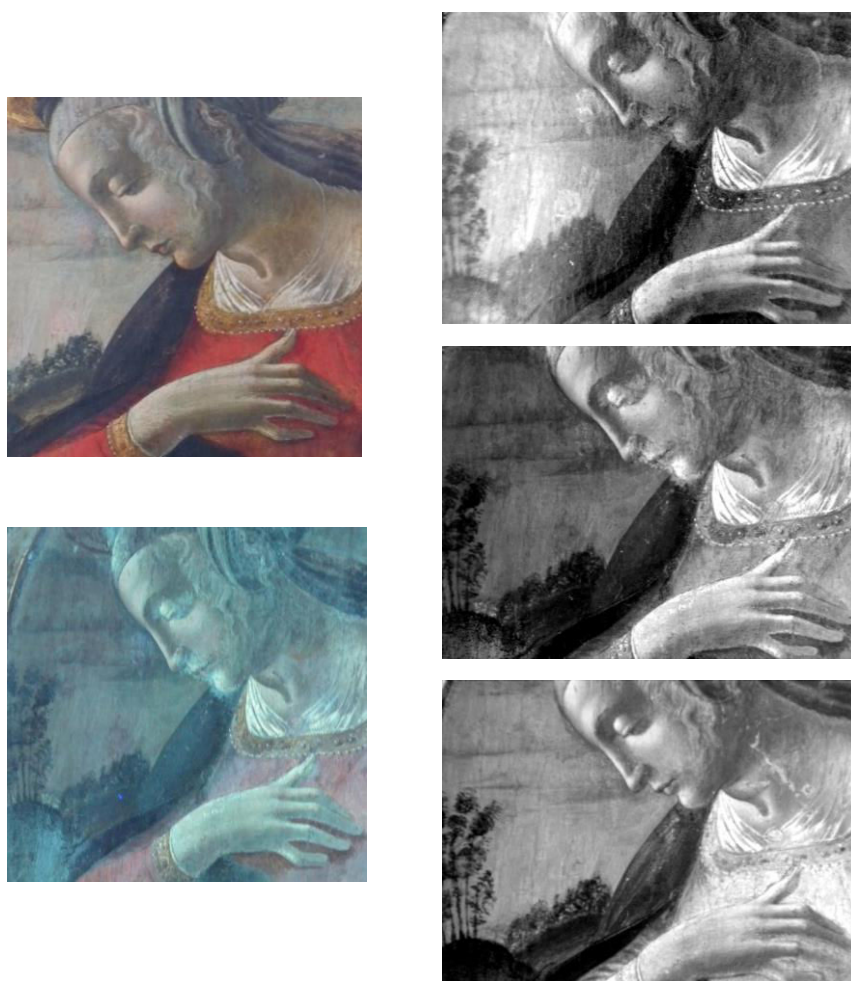


Fig. 1: Images of the painting “Virgin and the Child” of Francesco di Giorgio Martini. Colour and UV-fluorescence photography on the left side, top and bottom panel respectively. Fluorescence images taken with the blue filter (right, top), green filter (right, middle) and red filter (right, bottom).

However it is possible to measure the fluorescence emitted by a surface through the acquisition of fluorescence spectra either on selected small areas of the entire painting or on pictorial samples, as

described in the previous section, so this means a limited number of analysed areas and a careful selection of the spot to be investigate, trying to guess which areas of the painting are expected to carry relevant information. Imaging techniques avoid this difficulty since the entire surface is measured simultaneously.

In recent years some research groups [Pelagotti A. et al. (2006), Bonifazzi C. et al. (2008), Comelli D. et al. (2008)] have been working on developing multispectral acquisition systems for art imaging. The technique consists in irradiating the painting surface with two UV sources, placed so as to illuminate it uniformly, and in detecting the fluorescence radiation emitted by the painted surface within spectral narrow bands in the VIS and NIR ranges, in order to obtain information about the spectral fluorescence factor curves at every sampled point of the surface.

Another potentiality of the multispectral UV fluorescence imaging would be the possibility to obtain stratigraphic information due to the fact that the use of interference narrow band filters allows us to eliminate the fluorescence signal coming from a specific material; in this way the hidden fluorescence of other pictorial layers will show up. The knowledge of complex pictorial layers would be possible if the UV exciting radiation is able to reach the internal layers.

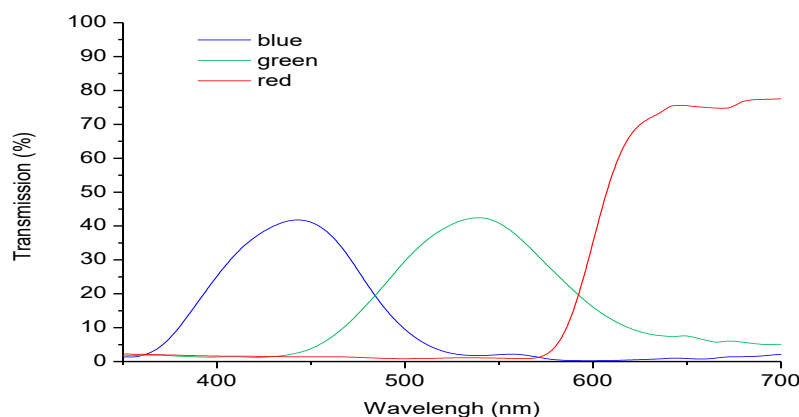


Fig. 2: Transmittance of the RGB filters

1.1 Multispectral Near Infrared Imaging

1.1.1 IR Reflectography. Fundamental principles

The infrared reflectography allows to detect the presence of preparatory drawings or “pentimenti” under the painted surface. Therefore, this technique provides similar and/or complementary information to the radiography. The infrared reflectography is performed by illuminating the painting with infrared radiation and collecting the radiation backscattered from it with a suitable detector. The possibility to visualize the underlying drawing is related to the fact that, in the infrared spectral range, many pigments are more or less transparent and to the high contrast occurring between the materials used for the drawing, like carbon black or black bone, and the preparation layer, consisting of chalk or white lead.

From the physical point of view, the fundamental principles of the IR reflectography are linked to the theory of the reflectance, described in the section 1.2.1.

An important parameter for IR reflectography is the contrast, C , defined as

$$C = \frac{R_b}{R_w}$$

where R_b is the reflectance of a black line and R_w is the reflectance of a white layer. The contrast may range between 0 and 1, the zero value meaning that the black line stands out from the background. The contrast depends on several factors, among which the reflectance and/or the transmittance of the pictorial layer.

1.1.2 IR Reflectography vs Multispectral Infrared Imaging

The IR reflectography can be performed using several types of cameras with different image sensors. Cameras for visible pictures use silicon-based sensors, which can detect photons up to

1100 nm (even if the signal to noise ratio is very low at these wavelengths), while the other ones are projected for applications in the IR ranges. The early systems using PbO-PbS vidicon cameras had sensitivities up to 2200 nm; more suitable systems use InGaAs or PtSi detectors with a broader sensitivity. Although the IR detectors are more performant, the silicon cameras are able to detect the underlying drawing with good results.

Normally IR reflectography is carried out using a high-pass filter (that removes the UV-VIS portions of the spectrum), acquiring the NIR image in a single large band; the acquired information is integrated over the broad spectral range instead of being obtained in a spectral narrow band.

Multispectral imaging allows to select a narrow-band specific IR portion in which the painted layer presents low absorbance, permitting a better visualization of the background layers.

Various NIR multispectral devices based on different detectors and on a filtering or dispersing system are used by a number of research groups [Mansfield J. K. et al. (2002), Balas C. et al. (2003), Bacci M. et al. (2005), Liang H. et al. (2005), Karagiannis G. et al. (2007), Delaney J. K. et al. (2009)]

Like the multispectral reflectance imaging, a scanning system for IR reflectography was designed by Daffara [Daffara C. et al. (2010)]. The instrument prototype is a no-contact optical scanner with a single-point measurement of the reflectance, capable of simultaneously collecting a set of 14 spatially registered images at different wavelengths in the NIR range of 800-2300 nm. The data can be analysed as a spectral cube, both as a stack of wavelength resolved images (multi-NIR reflectography) and as a series of point reflectance spectra, one for each sampled pixel on the surface (NIR spectrometry).

Moreover, it is important to underline here that, in the visible and NIR ranges, the absorbance of the pictorial materials is due to the electronic transitions, and in the SWIR (short wave infrared) to the molecular vibrations. Thus, it is possible to recognize the molecular composition of the pictorial materials by means of spectral imaging.

Chapter 2

THE MULTISPECTRAL ACQUISITION SYSTEM

In this section we describe the acquisition set up used for the multispectral imaging applications. We describe the components and the features of the equipment, such as the emission spectra of the radiation sources, the specifications of the CCD cameras, the optical lenses and the filters and the calibration procedures. In this section we describe, also, the image processing carried out on the Reflectance and UV fluorescence multispectral data.

2.	Multispectral acquisition system	19
2.1	Acquisition setup	20
2.2	Light sources	20
2.2.1.	UV lamps	20
2.2.2.	Visible and infrared lights	22
2.1.	CCD cameras	22
2.2.	Optical system and interferential filters	23
2.3.	Dark, Bias and Flat field	24
2.4.	Multispectral reflectance image processing	29
2.5.	Linear optoelectronic transfer function of the acquisition system	30
2.6.	Radiometric calibration	32
2.7.	Multispectral UV fluorescence image processing	34
2.8.	Reconstruction of the spectra from multispectral imaging	34

2.1 Acquisition set up

A good procedure for image acquisition is to place vertically the painting (that is the object to be studied) on an easel and to put the acquisition system in a parallel position. The distance between the painting and the acquisition system can be changed depending on the optical system used.

The illumination of the scene has to be uniform enough to avoid an inhomogeneous distribution of the radiation intensity on the painting; therefore we mounted the lamps for illuminating the painting surface at 45° . The radiation sources are chosen according to the imaging technique employed: UV lamps for the multispectral fluorescence imaging, visible-infrared lamps for multispectral reflectance imaging and multispectral infrared reflectography.

The filters with a diameter greater than one inch were placed in front of the optical system, whereas the filters of one inch were positioned in the internal wheel of the CCD camera.

2.2 Light sources

We measured the spectral emission of different kinds of lamps. For the acquisition of multispectral images we need a high power monochromatic source for UV fluorescence applications and a good spectral distribution emitted by the illuminant for visible and infrared applications.

2.2.1 UV lamps

In the cultural heritage field, the Wood lamps are the most UV-excitation sources employed [Aldrovandi A. et al (2010), Comelli D. et al. (2011)], probably since they are low cost UV sources and they emit at long UV wavelengths (365 nm); this property has the advantage of limiting the risk of damaging the painting, considering the closeness to the visible range. However the strong emission band centred at 365 nm has a long tail extending also in the visible well above 400 nm; in addition the emission presents several visible and infrared narrow bands, Fig. 3.

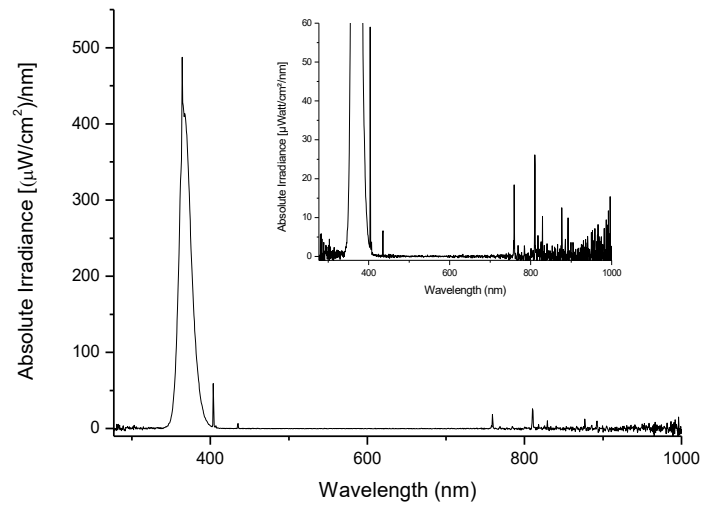


Fig. 3: Emission spectrum of the wood lamp

To avoid the contributions of these additional bands, we realized two UV lamps with three UV LEDs (Thorlabs' High Power LED M365D1) for each lamp. They have a dominant emission wavelength at 365 nm with a FWHM of 10 nm, Fig. 4; this means that no visible block filters are required. The LEDs are mounted on a metal core PCB. The emitted optical power is above 190 mW.

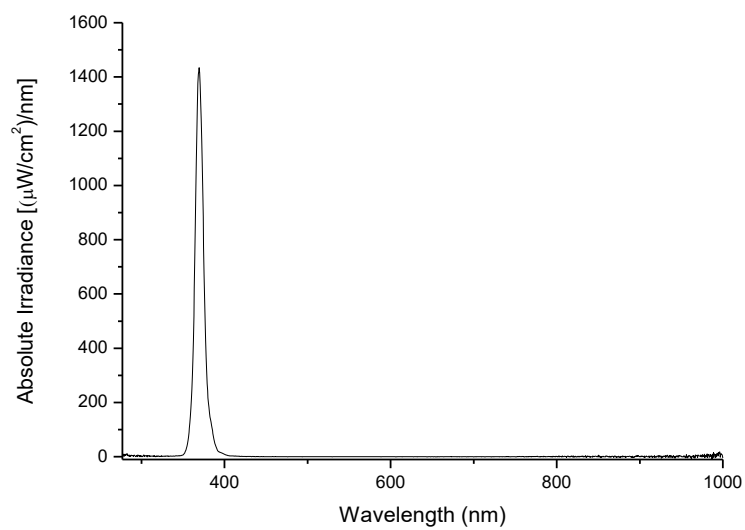


Fig. 4: Emission spectrum of the Thorlabs High Power LED M365D1

2.2.2 Visible and Infrared lamps

For the visible and infrared images we used tungsten halogen lamps that emit a continuous spectrum extending from near UV to IR. In order to avoid the IR emission, in some applications we used two white LED sources that emit a narrow band at 450 nm and a broad band centred at about 550 nm, Fig. 5.

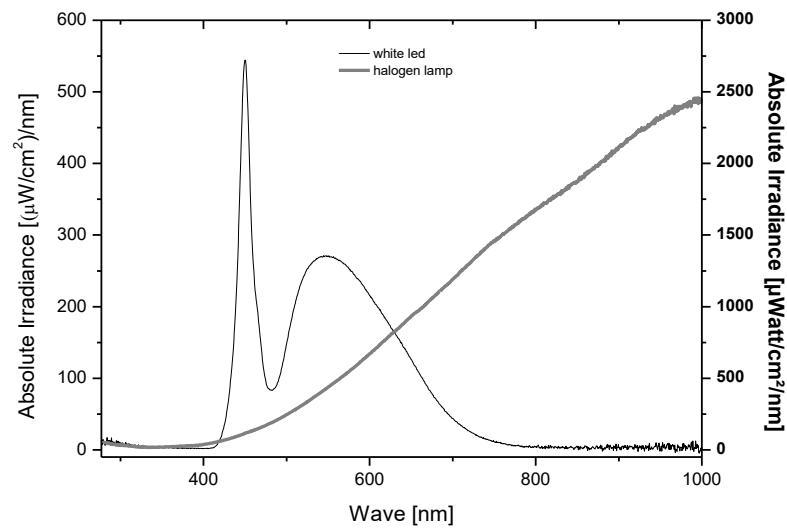


Fig. 5: Emission spectrum of the halogen lamp (grey line) and white led (black line)

2.3 CCD cameras

We used two cooled silicon monochromatic cameras: EuroPixel Hisis 23 E and QSI 583w. The first one employs a CCD sensor (KODAK KAF0402ME) with a matrix of 768x512 pixels (pixel size $9 \mu\text{m}^2$). The second one mounts a CCD full-frame sensor (KAF8300) with 3326x2504 pixels (image size of 17.96mm x 13.52mm, pixel size of $5.4 \mu\text{m}^2$). The camera is equipped with a filter wheel with 8 positions. The analog output signal from both sensors is converted into a digital 16 bits signal (65536 levels of gray).

2.4 Optical system and interferential filters

We used different optical lenses according to the painting size to be analysed and the environmental brightness. The EuroPixel Hisis 23 E camera is equipped with a Canon lens PH6x8 MACRO 8-48 mm focal length and $f/1.0$. The QSI 583w is equipped with three optical paths: Leica Summitar 50 mm $f/2$, Micro-Nikkor 55 mm $f/2.8$ and AF Nikkor 35 NM $F/2D$.

For our multispectral imaging apparatus, we preferred interferential narrow - band filters due to the wide selection of wavelengths. This means that we can select a single wavelength of the electromagnetic spectrum for revealing a specific spectral feature of the sample to be analysed.

However, due to the structure of the interference filters, a shift to shorter wavelengths occurs if the angle of incidence varies from normal. At angles greater than 20 degrees, the transmittance of the filters falls significantly and the wavelength of the maximum of the band pass shifts to short wavelengths, as shown in Fig. 6. We suppose that the radiation coming from the painting arrives approximately normal to the CCD camera placed at 1 m from the painting.

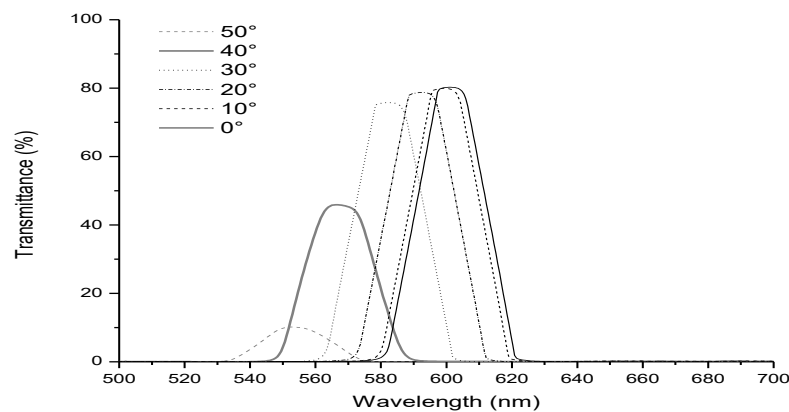


Fig. 6: Transmittance of a filter obtained changing the incident angle.

The blurring of the images is a serious problem of multispectral acquisitions. This effect is due to the different refractive indexes of the filters and to the chromatic aberrations, so that the focal length of the lenses changes with wavelength. Without particular algorithms we can obtain good images finding a optimizing the aperture, the exposure time and the lighting power of our lamps.

We tested different combinations and we found the blurring effect is highly influenced by the choice of the diaphragm aperture. In

Fig. 7 we report an example for the Leica optical system. The image obtained with $f/11$ are blurrier than the image with $f/16$, because the narrowing of the diaphragm produces a greater field depth. Although we do not reach an excellent focus with $f/16$ for all wavelengths, we have chosen this aperture rather than changing the focus for each filter, because the manual focus adjustment is a long, tedious, time - consuming procedure; the main problem is that it produces a small variation of the size of the images; which is a significant complication for the subsequent processing of the data.

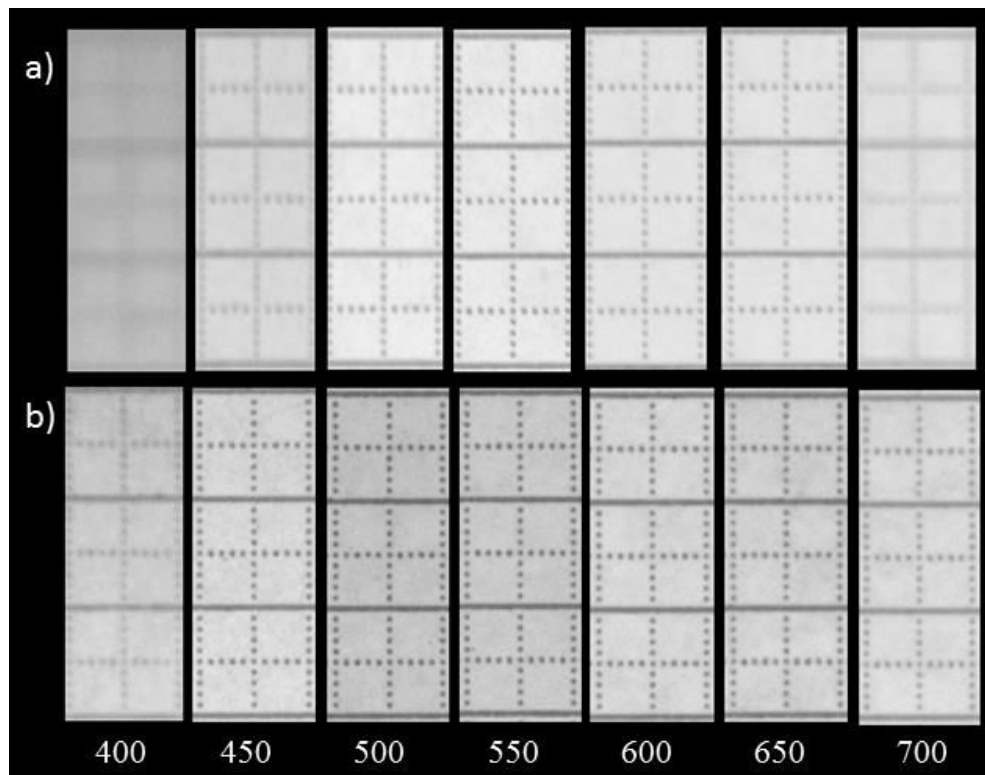


Fig. 7: Blurring effect using a $f/11$ aperture (a) and $f/16$ aperture (b) by introducing different filters.

1.5 Dark, Bias and Flat Fields

We discuss, in this paragraph, some of the important corrections to be made to the raw images in order to obtain calibrated images. They consist in the acquisition of the dark, bias and flat frames.

A dark frame (obtained averaging several dark frames) has to be subtracted from a raw image to correct the fixed-pattern noise such as that caused by dark current. The dark image is acquired with the shutter closed and with the same time of exposure of the raw images.

A bias frame is an image that contains noise due to the electronics that elaborate the sensor data, that is different from the noise coming from the charge accumulation (e.g. from dark current) within the sensor itself. It is acquired with the shutter closed and it is independent to the time of exposure. The bias frame is included in the dark frame.

The flat image is required for correcting the variations of the light intensity on the surface to be analysed (*light inhomogeneity*) and several effects due to the combination between the optical-system, the filters and the CCD system: pixel-to-pixel sensitivity variations across the array, the effect of dust or scratches on the CCD window, the vignetting induced by the filters and lens optics. In this work, flat images were acquired capturing the light diffused by a white opaque panel both for the visible and infrared images. For the fluorescence acquisition we used the same white panel, that emits an intense blue fluorescence. We used the flat image of the filter at 450 nm for calibrating the other multispectral images.

The choice of the most suitable white panel, the distribution of the illumination and the correction are a fundamental point for the reconstruction of spectra from multispectral images. We carried out several experiments to select the best white panel for the acquisition of the flat field and we focused also on the study of the light distribution. For this purpose, we acquired several images of a reflectance standard located in different positions of the painting surface, as shown in Fig. 8, in order to evaluate if the flat field used can correct the light inhomogeneity's.

We firstly choose a white PVC panel for the acquisition of the flat images, two examples are shown in Fig. 9, and we applied a calibration procedure to the raw images, that consist on the multiplication of the average value of the flat image to the ratio between the raw image and the flat image,

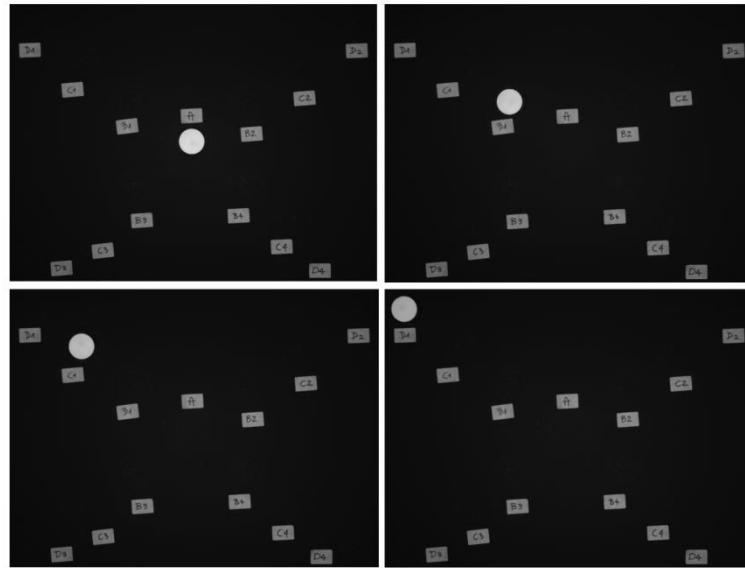


Fig. 8: Images of the reflectance standard at different position A1, B1, C1 and D1

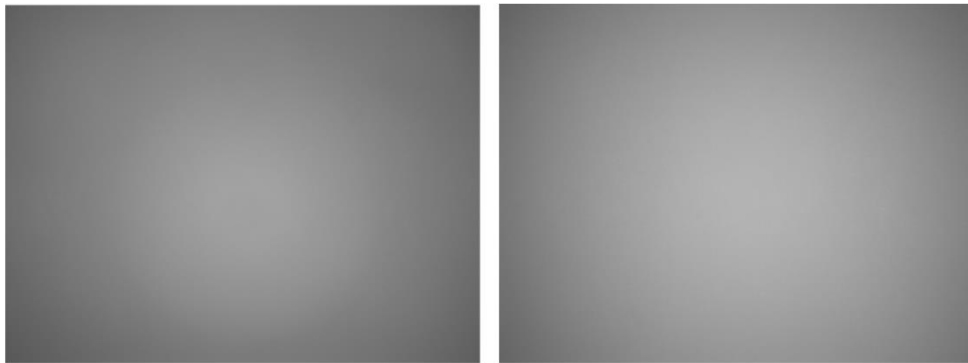


Fig. 9: Flat images at 450 nm (left panel) and 650 nm (right panel)

This correction is independent from the acquisition time; this means that the flat image can be acquired with the exposure time providing the best signal – to - noise ratio.

In Fig. 10, we show the average pixel values of the reflectance standard for several filters (450 nm, 470 nm, 500 nm, 550 nm, 600 nm, 700 nm), calculated in the central position A1 and in the top left corner of the shot, D1 (see Fig. 8). The images without flat correction, labelled “no flat”, show a high decrease of the intensity from the centre to the corner of the image, while the corrected ones display a weak increase of the intensity. This trend of the corrected image, taken at 450 nm, is better shown in Fig. 11, where the semi-dispersion errors, calculated on the selected pixels, are included.

The increase of the light intensity at the D1 position can be explained with the presence of some reflected light from the white panel although the panel surface is satinized.

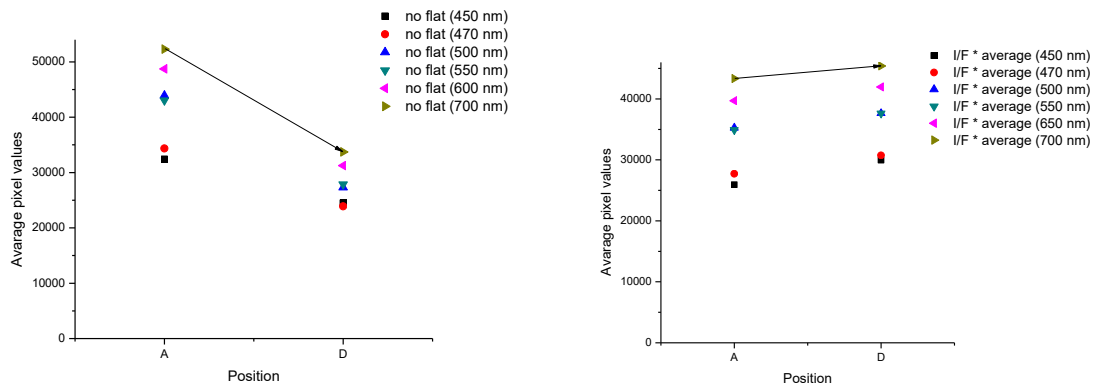


Fig. 10: Average pixels' values of the reflectance standard at centre position (A) and corner position (D) using various filters (450 nm, 470 nm, 500 nm, 550 nm, 600 nm and 700 nm). The graph in the left panel refers to the images without flat frame correction, the graph in right panel refers to the corrected images.

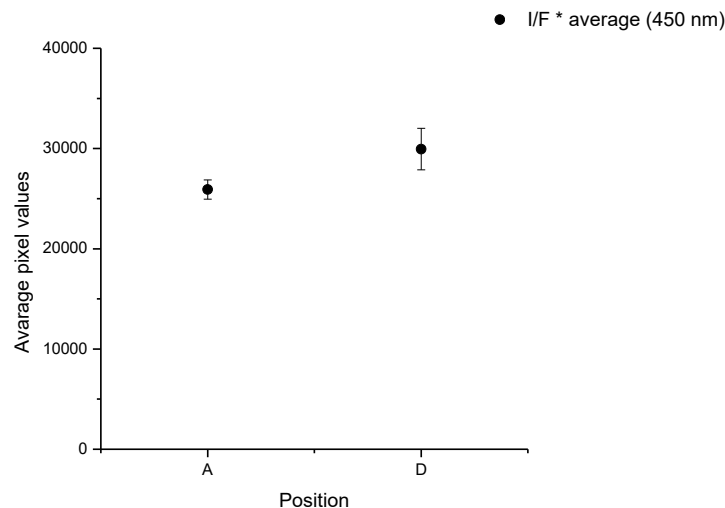


Fig. 11: Average pixels values of the reflectance standard of the calibrated images taken at 450 in different positions (A and D).

After these observations, we changed panel and we tested a white cardboard panel, repeating the same measurements as above. We reported the results obtained by using two filters centred at 450 nm and 650 nm, respectively, in Fig. 12. The average pixel values of the reflectance standard are quite constant by changing the position. This means that the cardboard panel works better than the PVC panel for the flat image.

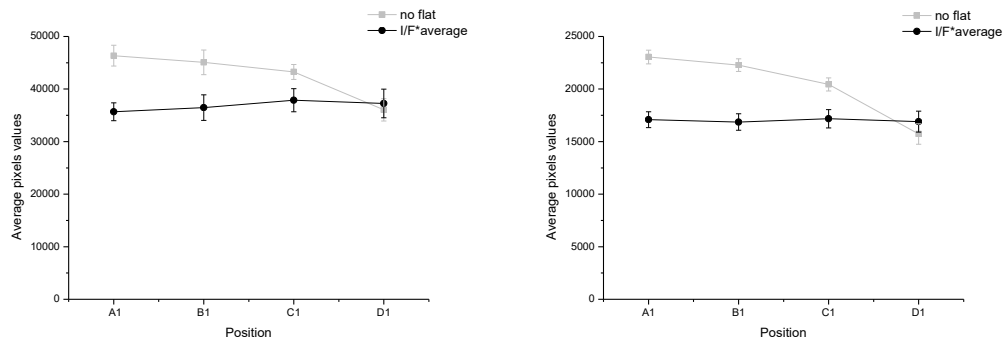


Fig. 12: Average pixel values of the reflectance standard at different positions (A1, B1, C1 and D1) using the filters at 450 nm (left panel) and 650 nm (right panel). The values referring to the image without flat frame correction are reported as grey symbols, those corrected with black symbols.

However this correction works if the illumination is as most uniform as possible. In the same experiment we changed the positions of the light sources. The flat image obtained with the 650 nm filter is shown in Fig. 13. The graph in Fig. 14 shows that the flat image does not correct the effect of light inhomogeneity's.

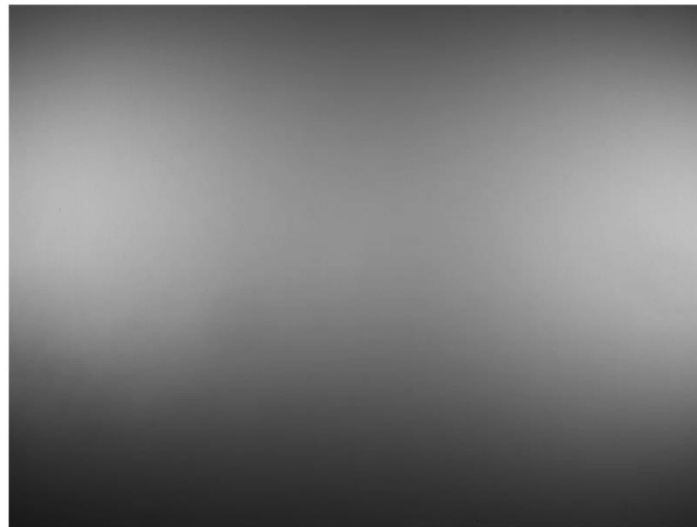


Fig. 13: Flat image measured at 650 nm

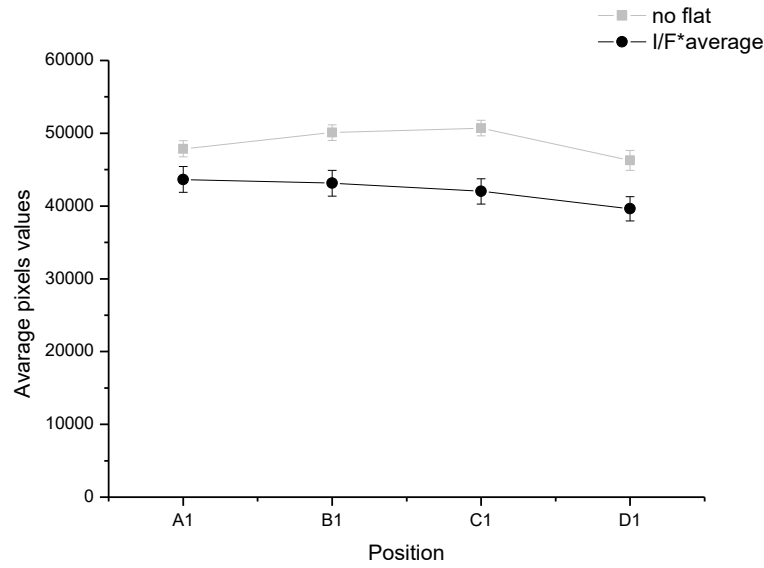


Fig. 14: Average pixels' values of the reflectance standard at different positions (A1, B1, C1 and D1) using the 650 nm filter. The values refer to the image without flat frame correction are reported as grey symbol, those corrected with black symbol.

We conclude that the choice of the flat panel and a good light uniformity are very important to obtain images properly calibrated.

Taken into account the dark field and the flat field, the calibration procedure for each image can be summarized as:

$$I_c = \frac{I_r - D_{I_r}}{F - D_F} * a_F$$

where I_c is the corrected image, I_r is the raw image, D_{I_r} is the dark image of the raw image, F is the flat image, D_F is the dark image of the flat image, and a_F is the average of the pixel values of the flat image.

2.6 Multispectral reflectance image processing

The acquisition of reflectance imaging needs the same reflectance standard as that used for the reflectance spectrometry, inserted into the scene to capture, as shown in Fig. 15.



Fig. 15: Reflectance image of a painting with the reflectance standard

As for the reflectance spectroscopy, in order to obtain the reflectance image, R , from the raw image, I_r , it is necessary to divide it by the average of the pixel values of the reflectance standard, a_{ref} :

$$R = \frac{I_r}{a_{ref}}$$

The values of the pixels of the reflectance image ranged from 0 to 1; 1 is the value of the reflectance standard. For this study, the images have been processed by means of Mat lab software equipped with the image process toolbox.

2.7 Linear optoelectronic transfer function of the acquisition system

The image data processing requires that the efficiency of the pixels of the CCD is linear with light intensity. This means that the pixel electric signal should be proportional to the number of

photons incident on the pixel. In other words, measuring the reflectivity of a target, plotting the average pixel values vs. the exposure time a straight line should be obtained.

We checked the linearity of the QSI camera by exposing a selected area of the pixels to the light emitted by a stabilized halogen lamp. The camera was equipped with the optical lens Micro Nikkor, f/32 and the 532 nm interferential filter; dark and bias field corrections were done. The exposure time was changed from the minimum value of 0.03 s to a maximum value such that the maximum average pixels values was about 61000 ADU; we know that above the linearity of the CCD is compromised. The plot shown in Fig. 16 confirms the linear relationship between the exposure time and the average pixel values.

Moreover, we checked also the linear behaviour for the long exposure times generally used for the multispectral UV fluorescence imaging, by using a filter at 420 nm, as shown in Fig. 17.

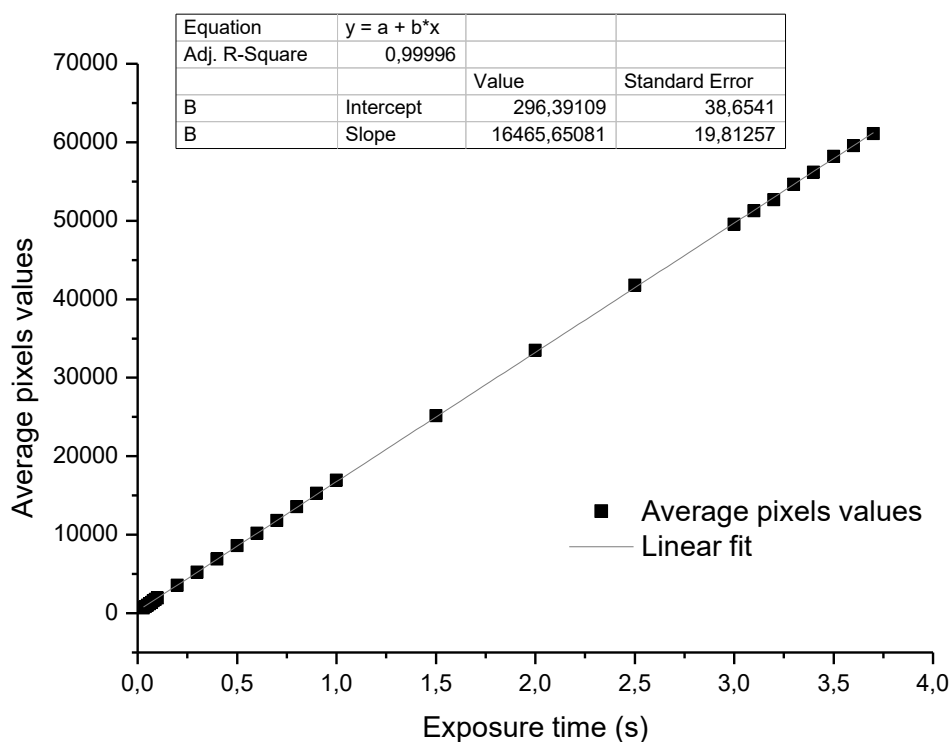


Fig. 16: Plot of the average pixel values of the CCD camera equipped with the Nikkor optical lens and the 532 nm filter vs. the exposure time.

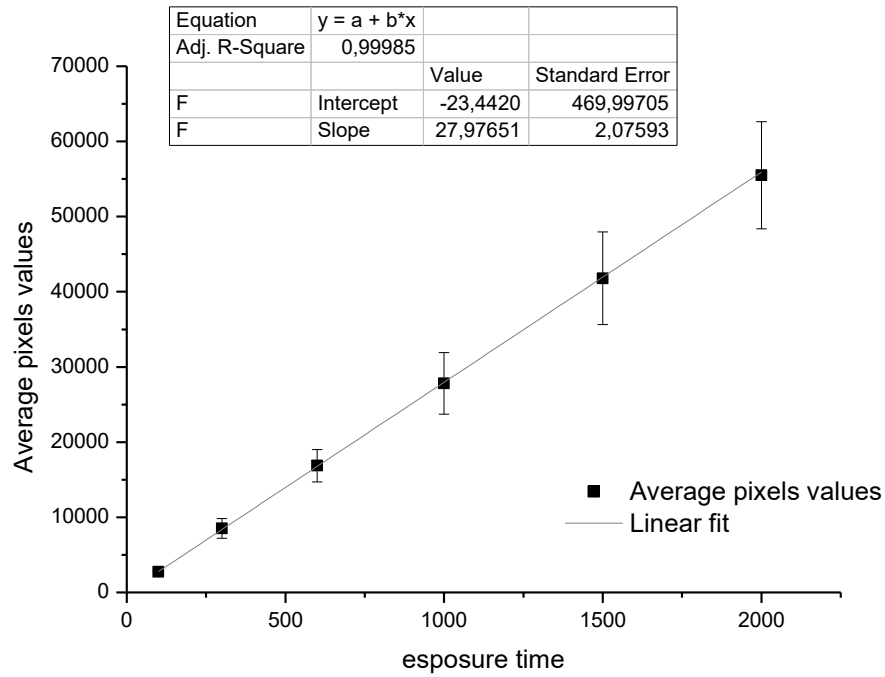


Fig. 17: Plot of the average pixels values of the CCD camera, equipped with the Nikkor optical lens and the 420 nm filter vs. long exposure time.

2.8 Radiometric calibration

After the correction by the dark and flat fields discussed above, the multispectral images obtained with the UV excitation do not represent the “true” fluorescence emissions of the painting for each spectral interval (defined by the type of filter employed) since the image is the result of different factors: the spectral fluorescence emission of the object, $I(\lambda)$, the spectral transmittance of the optical system, $o(\lambda)$, the spectral transmittance of the interferential filters, $\Phi_k(\lambda)$, the spectral sensitivity of the CCD camera, $\alpha(\lambda)$, and the acquisition time. Taking into account the linear optoelectronic transfer function of the acquisition system, discussed in the previous paragraph, the camera response c_k for an image pixel is

$$c_k = \int_{\lambda_{min}}^{\lambda_{max}} I(\lambda) o(\lambda) \Phi_k(\lambda) \alpha(\lambda) t d\lambda$$

Taking into account this relation, we deduced c_k with an undirected method:

A halogen lamp, equipped with a diffuser slide to avoid the shadows of the tungsten filament, was turned on in front of a calibrated spectrometer for measuring the irradiance of the lamp. Then, we placed the CCD camera, equipped with the filters, in front of the halogen lamp and we acquired the multispectral images.

Introducing the spectral sensitivity $\omega_k(\lambda)$ of the k-th channel as

$$\omega_k(\lambda) = o(\lambda)\Phi_k(\lambda)\alpha(\lambda)$$

the camera response c_k becomes

$$c_k = \int_{\lambda_{min}}^{\lambda_{max}} I(\lambda)\omega_k(\lambda) t d\lambda$$

For each filter, we estimated the factor $\omega_k(\lambda)$ dividing the average over the pixel's values of the diffuse light coming from the source, I_{CCD} , by the values achieved with the spectrometer, I_s , as follows:

$$\omega_k(\lambda) = I_{CCD}/I_s$$

In Fig. 18 we show the values of ω_k of our acquisition system for two optical lenses used in this work, the Leica and the Macro lens, respectively.

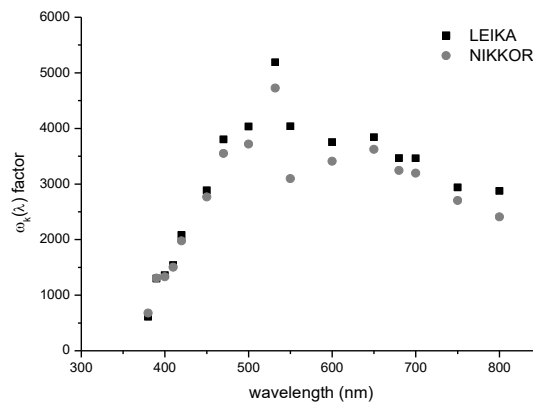


Fig. 18: Estimated spectral sensitivity ω_k for two of our optical lenses (Leica and Nikon)

It is possible to estimate ω_k also illuminating directly the acquisition system with a calibrated source as suggested by [Blažek J. et al. (2013)].

2.9 Multispectral UV fluorescence processing

The multispectral UV fluorescence images were captured at different exposure times for each filter in order to obtain a good signal – to – noise ratio of the image. After the dark, bias and flat corrections, the images were normalized to their exposure time and then divided by ω_k , calculated as described above. In this way, we can achieve multispectral UV fluorescence images corrected by the changing of the exposure time and the radiometric calibration.

2.10 Reconstruction of spectra from multispectral imaging

From the multispectral imaging it is possible to reconstruct, approximately, the reflectance and UV-fluorescence spectra. A good match was achieved between the reflectance or the fluorescence spectra and those reconstructed from the multispectral images, demonstrating that the calibration procedures, described in the previous sections, are effective to correct the images.

For this purpose we use Matlab software by selecting the area of interest for each multispectral image, as shown in Fig. 19. Then we calculate the average pixel values and their errors (maximum dispersion).

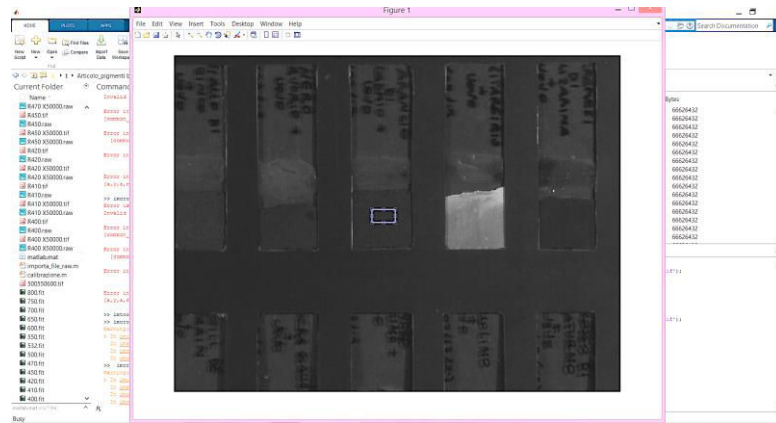


Fig. 19: Matlab window with the area selected for the spectra reconstruction

In Fig. 20, we show the comparison between the fluorescence spectra obtained with a spectrometer and the reconstructed spectra achieved from multispectral fluorescence images. The reconstructed curve is in agreement with the fluorescence spectra.

We tested also the accuracy of the reconstruction of the multispectral reflectance images with the reflectance spectra, an example is shown in Fig. 21. We found a similar trend but the multispectral reconstruction shows an increase of the pixels values, probably this effect is caused by the presence of scattering phenomena during the image acquisition that produces a higher baseline of the spectra.

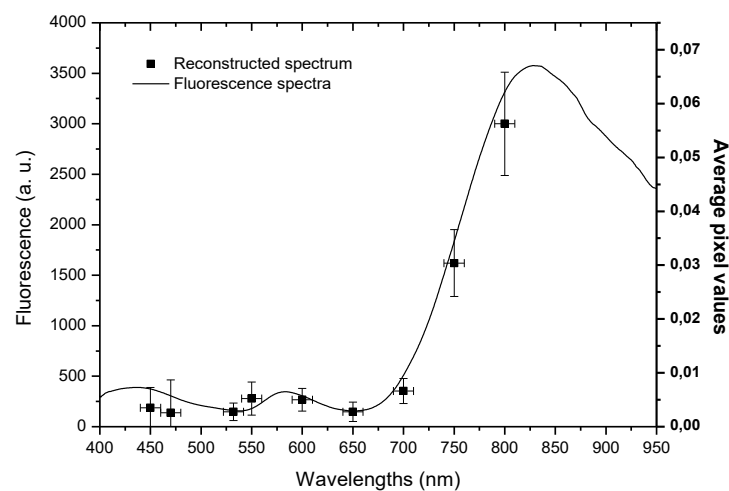


Fig. 20: Fluorescence spectrum of cadmium orange in yolk (full line) and reconstructed spectrum from the UV multispectral fluorescence images (squares).

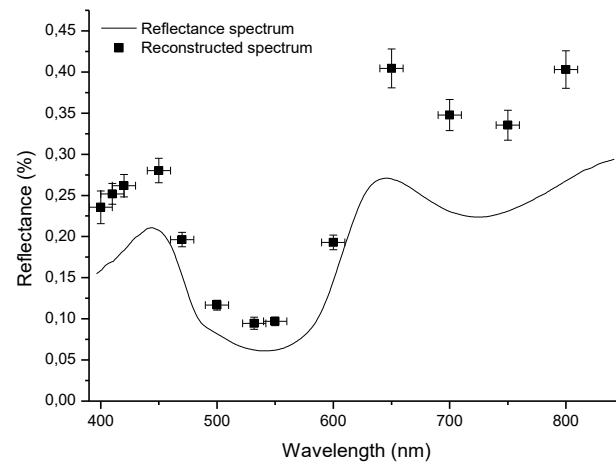


Fig. 21: Reflectance spectrum of cobalt violet in yolk (full line) compared with the reflectance values obtained with the multispectral reflectance images (squares).

PART II:

**MULTISPECTRAL IMAGING APPLIED ON
PICTORIAL MATERIALS**

Chapter 1

Binders media

In recent years, the interest in the identification of binders media is increasing, especially by means of non-destructive methods. Fluorescence spectroscopy and imaging can be useful for this purpose, since both are non-destructive and can be employed in situ. In this chapter we explore the potentiality of the fluorescence emission for the identification of the main binders used in easel paintings: egg yolk and linseed oil; we shall consider briefly also egg white.

Dried and accelerated aged samples were analysed in order to evaluate their optical and chemical modifications with ageing by means of fluorescence excitation emission spectroscopy (EES) and ATR-FTIR. Photodegradation and thermal ageing processes were applied to linseed oil and the results of the two methods are compared between each other.

1.	Binders media	37
1.1.	Introduction	38
1.2.	Materials	40
1.3.	Accelerated ageing	40
1.4.	Methods	40
1.5.	Results and discussion	41
1.5.1.	Chicken egg	41
1.5.1.1.	Fluorescence excitation emission spectroscopy (EES)	41
1.5.1.2.	ATR-FTIR	49
1.5.2.	Linseed oil	52
1.5.2.1.	Fluorescence excitation emission spectroscopy (EES)	52
1.5.2.2.	ATR-FTIR	55
1.6.	Conclusions	58

1.1 Introduction

The pictorial layer consists of one or more pigments and a binding medium. A wealth of organic compounds has been used as binders over the years: egg white, egg yolk, casein, animal glue, siccative oils. On the analytical point of view, each binder give the name to the technique used by the painter, as the use of egg yolk for *egg tempera* paintings, and oil for *oil paintings*.

Egg tempera technique consists in dispersing the pigments in egg yolk, or egg white or a mixture of both. It has been used in easel paintings since long ago: in fact it is already mentioned at the beginning of the 10th century [Theophilus P. (1979), Cennini C. (1971)]. It has been extensively used by the Italian artists in the 14th and 15th centuries.

From a chemical point of view, egg white contains a mixture of different proteins such as ovalbumin, conalbumin and lysozyme. Egg yolk contains similar proteins and also vitamins and fatty acid esters. The main degradation processes involve the interaction of glucose with other egg compounds. These processes are known as the glucose-protein reaction (Maillard) and the glucose-cephalin reaction. The Maillard reactions begin with the bonding of the glucosidic hydroxyl groups of sugars with the amine groups of the peptides and the proteins. This process is the first of a series of other reactions that induce UV fluorescence, colour alterations (browning) and insolubility. Instead, the reaction between a cephalin amino group and aldehydes leads to the discoloration of the egg [Stadelman W. J. et al. (1995)].

Linseed oil has been the main painting binder used in oil paintings since the sixteenth century [Mills J. et al. (1980)]. Its widespread employment can be ascribed to its drying faster than that of the other common oils, probably due to the high content of linolenic acid, that is the most unsaturated fatty acid [Juita *et al.* (2012)].

Drying oils are natural fatty oils, largely composed of mixtures of triglycerides. These are glycerol esters composed by one molecule of glycerol and three molecules of various linear fatty acids.

In general, the composition of drying oils are constituted by saturated acids with 12, 14, 16 or 18 carbon atoms, as lauric, myristic, palmitic and stearic acids and C18 polyunsaturated acids with 1,

2 or 3 double bonds, as oleic, linoleic and linolenic acids [Lazzari et al. (1999)]. The unsaturated bonds are responsible for the drying power of the oils, due to the possibility to react with the oxygen leading to the curing.

Autoxidation is the main degradation process of vegetable oils; it starts during the drying and can be accelerated by thermal and photodegradation procedures.

The drying involves lipid autoxidation, leading to the cross-linking polymerization, consisting in the intermolecular coupling of radicals originated by the decomposition of the unstable peroxide groups [Juita *et al.* (2012)]. Degradation also implies a peroxidation leading to the formation of radical hydroperoxides which undergo rapid degradation in smaller fatty acids and dicarboxylic acids [Passi et al. (1993), Nawar W. W.(1969)].

Generally, the analysis of organic compounds in paintings are performed with micro-destructive techniques, that need very small samples taken from the pictorial layer, such as Gas Chromatographic-mass spectrometry (GC-MS) and matrix assisted laser desorption ionisation (MALDI)-time of flight (TOF) mass spectroscopy. However, also non-invasive techniques, such as Fourier transform infrared (FTIR) spectroscopy, Raman spectroscopy and fluorescence spectroscopy, can be very useful for the identification of binders.

Taking into account that the ageing strongly influences the fluorescence phenomena of the organic compounds, fluorescence spectroscopy can be employed for the recognition of specific ageing patterns. However, the spectra cannot be interpreted easily due to the presence of many fluorophores in the samples. Moreover, the procedure for accelerated ageing only offer a simulation of the natural ageing, and cannot be fully representative of the natural degradation occurring in the binder.

In this work, we assess the effects of both the accelerated and the natural ageing of egg yolk, egg white and linseed oil by using attenuated total reflection (ATR)-Fourier transform infrared (FTIR) spectroscopy and fluorescence excitation emission spectroscopy (EES).

This work is a preliminary study for understanding the potential of multispectral fluorescence imaging to the recognition of these materials.

1.2 Materials

We separated the egg white from the egg yolk of a chicken egg. Egg yolk was extracted by piercing the yolk membrane, then it was aspirated with a pipette and spread on a microscope slide. Egg white was beaten to form a foam that was spread on a microscope slide. Linseed oil is available in four varieties: raw, boiled, stand and refined oil. For this study we focused on raw linseed oil without additives, selecting a ratified linseed oil purchased from Lefranc & Bourgeois. The oil samples were spread on microscope slides and stored at 35°C for one month in the darkness to reach a complete drying.

1.3 Accelerated ageing

The samples were photodegraded in a Suntest CPS+photoreactor (Atlas) equipped with a xenon lamp and a filter that prevents the transmission of wavelengths shorter than 290 nm. The lamp was fixed with an irradiance of $750 \text{ W}\cdot\text{m}^{-2}$. The temperature of the sample was roughly maintained at 35 °C.

For the linseed oil samples, we also performed thermal ageing with a heater fixed at 75 ° C in order to compare the modifications produced, during the same time, with two accelerated ageing processes. Some samples were analyzed after a natural ageing performed in a dark room at 25° C.

1.4 Methods

The egg and the oil samples were analysed with ATR-FTIR (Thermo-Nicolet) and spectrofluorometry (Horiba Jobin Yvon Fluoromax 2) described in detail in the Appendix A.

The excitation emission spectra (EES) were acquired exciting with monochromatic radiation between 220 nm and 400 nm (in steps of 10 nm) and the emission was analysed between 250 nm and 700 nm with a spectral resolution of 1 nm. The EE spectra were corrected for the detector

efficiency and the lamp emission spectral distribution. The corrected EE spectra are reported in the following contour maps with 200 different colours from the minimum values (in blue) to the maximum values (in red).

The fluorescence spectra were acquired exciting at 365 nm and measuring the emission spectrum in the 380-700 nm range with a step of 6 nm. The slits of the spectrometer were fixed at 3 nm band-pass for the excitation and 2.5 nm band-pass for the emission.

1.5 Results and discussion

1.5.1.1 Chicken's egg

1.5.1.2 Fluorescence excitation emission spectroscopy

Dried egg white and egg yolk exhibit not significantly different excitation emission spectra, as seen in the contour maps shown in Fig. 22.

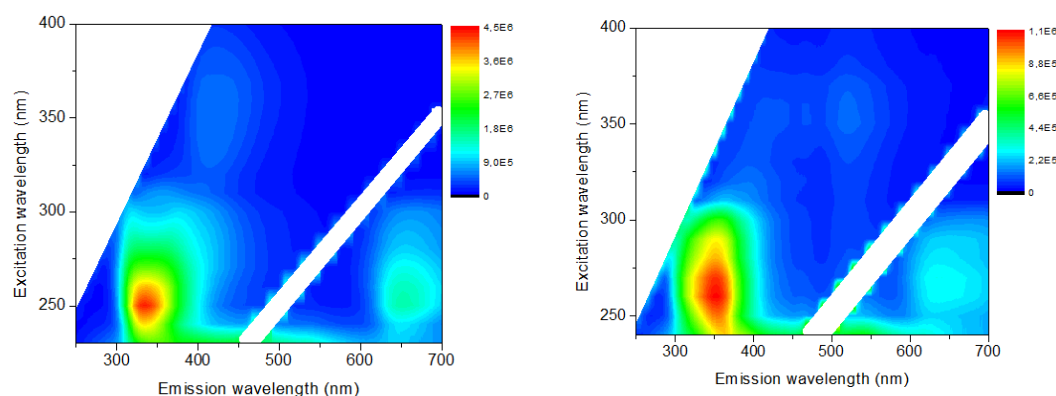


Fig. 22: Excitation Emission spectra of dried egg white (left panel) and egg yolk (right panel).

The positions of the emission maxima indicate the presence of multiple fluorophores. For this reason, the EE spectra are discussed in this section by dividing the matrix into two parts: one for the shortest excitation wavelengths ($\lambda < 325$ nm) and the second one for the highest wavelengths ($\lambda > 325$ nm).

In the case of egg white, the aromatic amino acids, such as tryptophan, tyrosine, phenylalanine, have a maximum of the fluorescence emission between 320 nm and 360 nm for excitation wavelengths between 220nm and 290 nm [Nevin A. *et al.* (2006-1), Karoui R. *et al.* (2006-1), Osticioli *et al.* (2008)]. Tryptophan dominates the fluorescence emission, that is centered at 340 nm for an excitation wavelength of 248 nm [Nevin A *et al.* (2008-2), Nevin A. (2006-2)].

The emissions of the amino acids found in egg white were also detected in egg yolk samples [Karoui R. *et al.* (2006-2)].

In both egg white and egg yolk, the short wavelength emission maximum generates a weak maximum in the emission spectra at approximately 650 nm as a consequence of the second-order diffraction of the grating.

High excitation wavelengths (320-375 nm) cause a weak fluorescence emission due to several degradation products of the egg proteins formed after the drying.

Both egg white and egg yolk present Maillard reaction products with the excitation/emission peak at 380/580 nm [Nevin A. *et al.* (2006-1), Nevin *et al.* (2007), Kurt *et al.* (2011), Nevin A. *et al.* (2009)]. It is necessary to mention that egg yolks also contain lipidic fractions, with notable cholesterol and unsaturated fatty acids, which could produce reactions with basic aminoacids generating several fluorophores following a similar pathway as fatty acid chains of linseed oil.

We cannot distinguish the emission of vitamin A (approximately at 410 nm), one of the most abundant yolk component, from the fluorescence emission of the Maillard products that are produced by the reactions between free glucose or sugars and amino acids [Nevin A. *et al.* (2006-1)].

The presence of riboflavin may induce fluorescence for excitation/emission at 360/530 nm [Plytycz B. *et al.* (2006)]. However, it is necessary to remember that the intensity recorded in this spectral range can be associated with auto-absorption phenomena (Part I, chap. 1, par. 1.3.1).

Considering the complexity of the fluorescence spectra of eggs at high excitation wavelengths, we acquired the emission spectra of egg white and egg yolk for the single excitation wavelength of 365 nm (excitation wavelength generally used for the fluorescence imaging of paintings). The aim of

acquiring these spectra is to isolate the single bands contributing to the measured fluorescence spectra. To do this we used a Gaussian curve-fitting deconvolution with the Origin software (for more detail see Part II, chapter 1, par. 1.2.4.2). We used a linear combination of two or three Gaussian bands, whose peak positions and full widths at half-maximum (FWHM) were fixed. The intensities were allowed to vary in order to match the line shape of the experimental spectra. The fitting program operated to determine the true absolute minimum value of the sum of squared deviations by an iterative process. The relative contributions of the single bands to the total fluorescence were calculated using the integral of the band areas derived from the Gaussian deconvolution.

The true absolute minimum value of the sum of squared deviations is defined as χ^2 and the coefficient of determination as r^2 . Although the fluorescence spectra of white egg and egg yolk, shown in Fig. 23 and Fig. 24 respectively, appear different, the curve-fitting deconvolution shows that the single bands contributing to the total spectra are emitted in the same range of wavelengths:

- for egg white, the fluorescence emission at about 410 nm can be ascribed to the oxidized Tyrosine, such as dityrosine, and to a mix of oxidized Tyrosine and vitamin A for the egg yolk [Nevin A. *et al.* (2008-1)].
- The fluorescence emission at approximately 435 nm can be assigned to tryptophan photo oxidation product derivatives, i.e. formylkynurenine, kynurenine and 3-OH-kynurenine [Nevin. A. *et al.* (2006)].
- The dihydroxyphenylalanine (DOPA), an oxidation product of tyrosine residues, probably shows a fluorescence maximum at about 450-480 nm [Smith G.J *et al.* (2000)].
- The fluorescence emissions at about 500 nm and 560 nm are connected to the contribution of riboflavin, that is the major constituent of egg yolk, and it is present also in egg white.
- The fluorescence of cross linking from fatty acid polymerization could be present at about 550 nm [Nevin A. *et al.* (2008-2)].

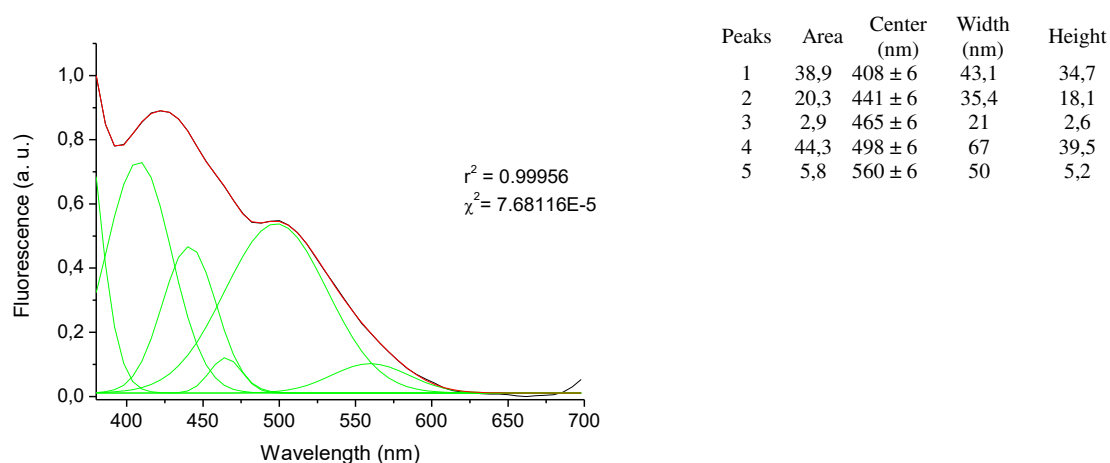


Fig. 23 : Fluorescence spectra of the dried egg white. The red curve was calculated using the integral of the band areas derived from the Gaussian spectra deconvolution (green curves).

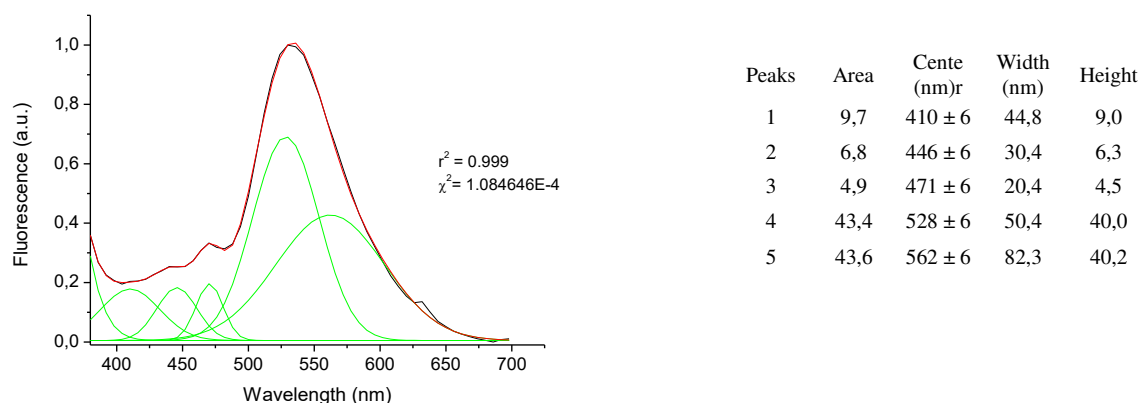


Fig. 24 : Fluorescence spectra of the dried egg yolk. The red curve was calculated using the integral of the band areas derived from the Gaussian spectra deconvolution (green curves).

In order to understand the chemical modifications due to the ageing, we carried out a photodegradation ageing under artificial sunlight at 35°C on both egg white and egg yolk for 222 hours. For the egg yolk, we performed EE spectra also after 1 hour and after 7 hours of photodegradation ageing. The EE spectra are shown in Fig. 25.

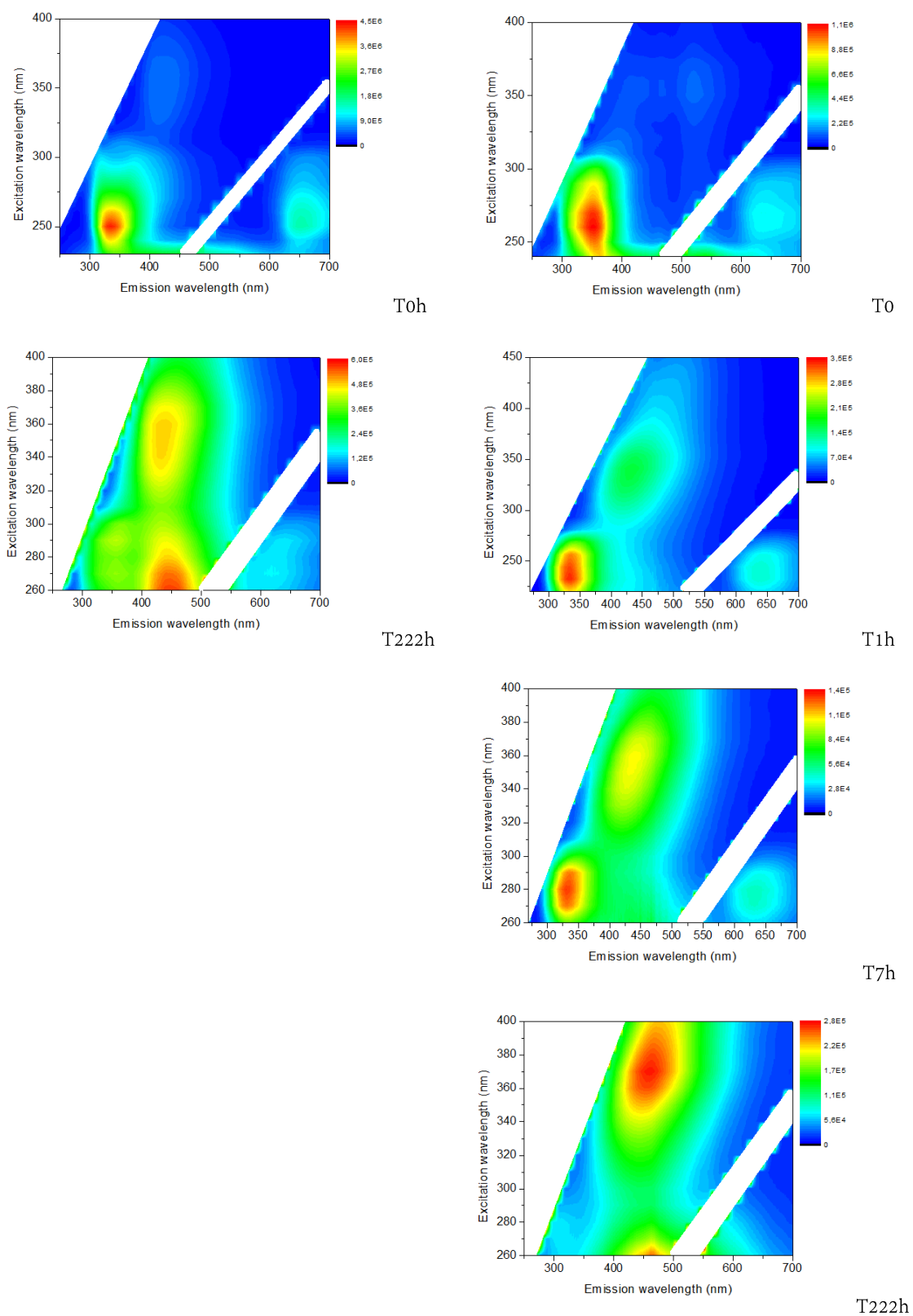


Fig. 25: EE spectra of egg white (left panel) and egg yolk (right panel) after photodegradation under sunlight at 35°C

For the egg white, the fluorescence emission of the amino acids at short excitation wavelengths is strongly reduced and the fluorescence emission at the highest excitation wavelengths increases. For the egg yolk, the high excitation wavelength emission maxima shift to high excitation/emission wavelengths after only few hours of ageing. The fluorescence emission of the amino acids disappears after 222 hours.

In order to assess the chemical degradation without the photochemical reactions, we carried out natural ageing for 10 days in a darkroom at 25°C on both egg white and egg yolk. The EE spectra are shown in Fig. 26. The degradation products of egg white and egg yolk are already present in samples naturally aged during a few days. In the case of egg yolk, we can distinguish the fluorescence emission of the vitamin A at 320/410.

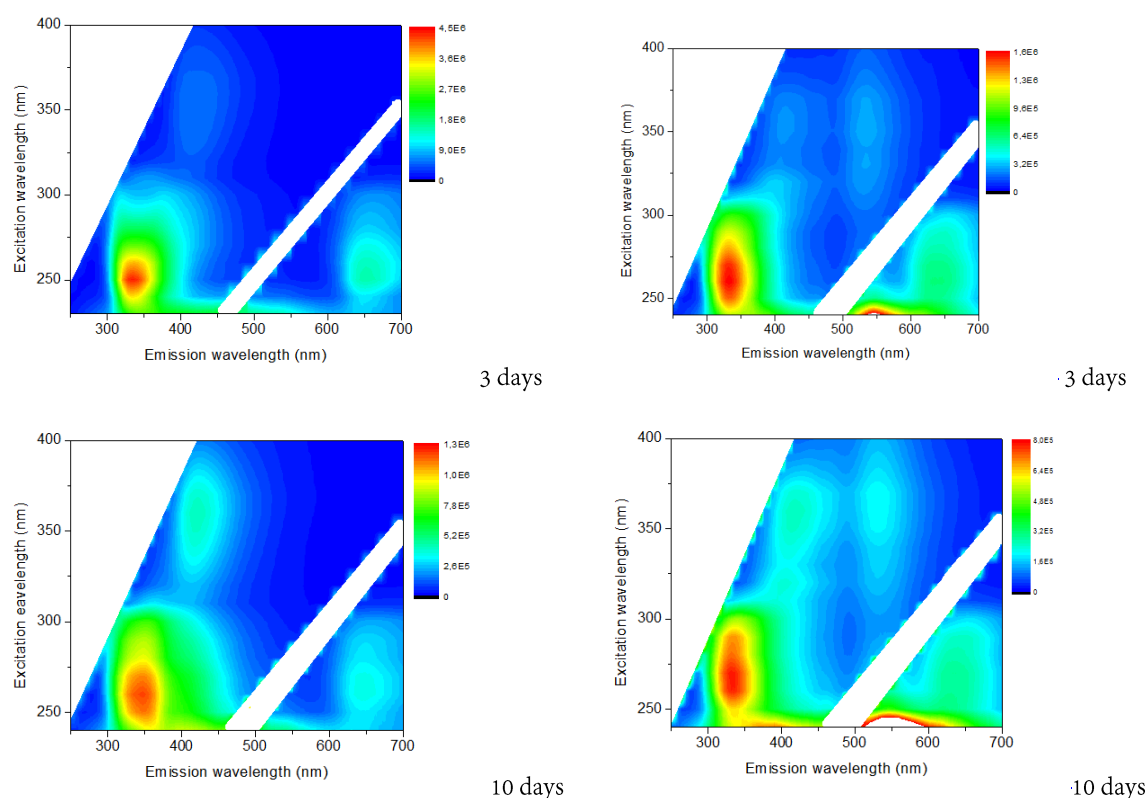


Fig. 26: EE spectra of dried egg white (left panel) and egg yolk (right panel) samples naturally aged for 3 days and for 10 days

Exciting at 365 nm, the fluorescence of riboflavin of the egg white disappears after 3 days. After further 5 days, the fluorescence peak at about 470-480 nm, probably due to the DOPA content, increases. The first fluorescence band shifts to high wavelengths with the natural ageing, Fig. 27 (left panel). This behaviour occurs also in the accelerated aged samples Fig. 27 (right panel). We cannot exclude the presence of additional weak fluorescence from multiple unidentified fluorophores. The maximum of the fluorescence emission of egg white is 422 nm after 10 days of natural ageing and at 440 nm after a photodegradation of 222 heures.

In the case of egg yolk samples, after a natural ageing, we note a strong increase of the fluorescence of the oxidised amino acids and a strong decrease of the riboflavin fluorescence, Fig. 28 (left panel). After an accelerated ageing of 65 hours, we noted a shift to long wavelengths of the first peak and a strong reduction of the intensity of the fluorescence of riboflavin, Fig. 28 (right panel). The maximum of the fluorescence emission of egg yolk is 416 nm after 10 days of natural ageing and at 464 nm after a photodegradation of 222 heures.

We can distinguish the fluorescence of egg white and egg yolk, also after 222 hours of photothermal ageing, since the maximum of the spectra of egg yolk is shifted to higher wavelengths than that of egg white, as shown in Fig. 29.

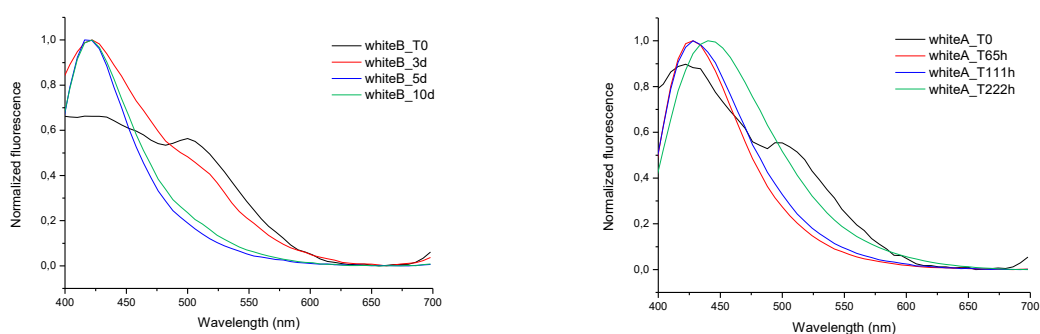


Fig. 27: Normalized fluorescence spectra of natural aged (left panel) photodegraded (right panel) egg white samples, exciting at 365 nm

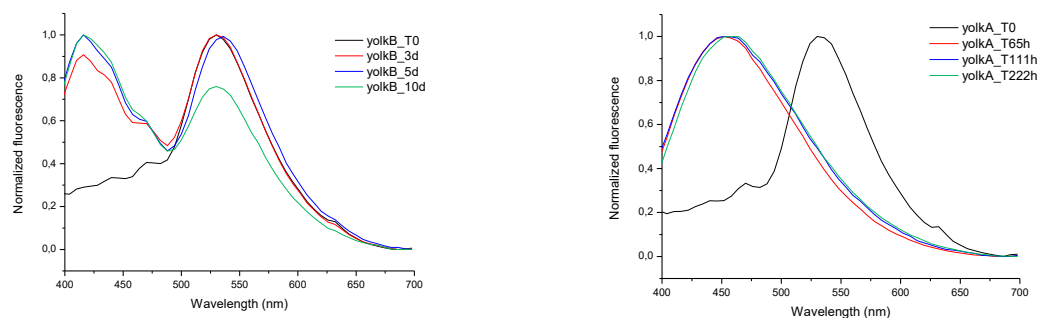


Fig. 28: Normalized fluorescence spectra of natural aged (left panel) photodegraded (right panel) egg yolk samples, exciting at 365 nm

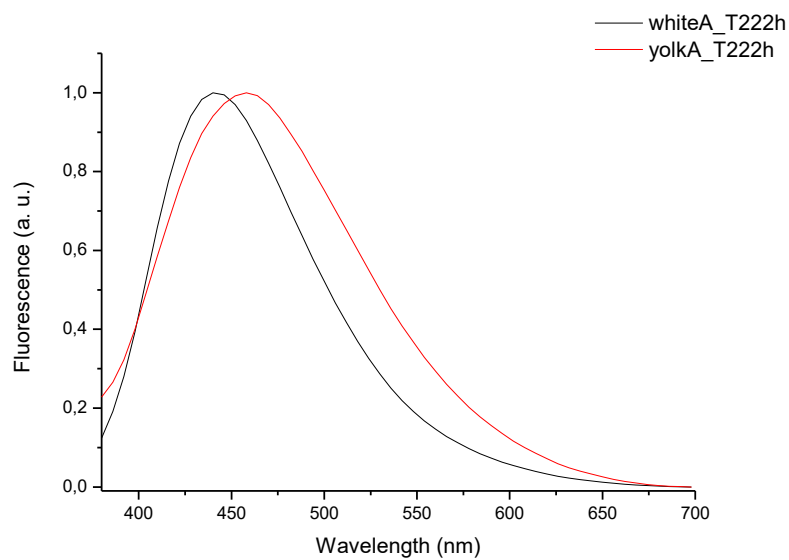


Fig. 29: Normalized fluorescence spectra of egg white and egg yolk samples after 222 hours of accelerated ageing

1.5.1.2 ATR-FTIR

Egg white and egg yolk are characterized by the presence of proteinaceous components and triglyceride units composed by unsaturated fatty esters. The ATR infrared absorption bands of the fresh samples are shown in Tab. 1.

Egg yolk can be easily distinguished from the egg white by the presence of a strong band at 1740 cm^{-1} (C=O stretching) and the bands at 2960 cm^{-1} , 2930 cm^{-1} and 2870 cm^{-1} (CH-stretching).

After the accelerated ageing, the band at 3009 cm^{-1} , assigned to unsaturated side chains, disappears, see Fig. 30. Moreover, the band at 1740 cm^{-1} and the two absorption bands of the amide I and amide II at 1650 cm^{-1} and 1550 cm^{-1} , respectively, change their spectral features.

Tab. 1: ATR-FTIR infrared band assignments based on the literature [Mazzeo R. (2008), Felder-Casagrande S. (1997), Meilunas R. J. et al. (1990)]. The bands with a wavenumber signed by * belong to the egg yolk spectra, those signed by + to the egg white spectra and those signed by ° to the dried egg yolk spectra.

wavenumber (cm^{-1})	IR vibration assignments
3293-86	N-H stretching
3070 ⁺	Amide II overtone
3006 [°]	ν (=C-H)
2962-54	$\nu_{\text{as}}\text{CH}_3$ stretching
2933-21	$\nu_{\text{as}}\text{CH}_2$ stretching
2854	$\nu_{\text{s}}\text{CH}_2$ stretching
1743-39*	C=O (ester) stretching
1639-52	Amide I (C=O) stretching
1548-35	Amide II(N-H) bending
1465-48	CH_3 asymmetric bending
1396-76	ν_{s} unprotonated carboxyl group on free fatty acid chains or CH_3 umbrella mode
1243-36	$\nu(\text{C-O})$
1166-53	$\nu(\text{C-O})$
1081-78	C–O–C (ester) stretching
1039-68	$\nu(\text{C-O})$
971 *	$\nu_{\text{as}}(\text{N-CH}_3)$

The ester bonds of the amide II bands (1236 cm^{-1} , 1166 cm^{-1} and 1090 cm^{-1}) change: the second band increases and the first one decreases, probably for the autoxidation of the lipid content in egg [Felder-Casagrande S. *et al.* (1997)].

The ATR-FTIR spectrum of the aged egg white does not show significant differences compared to the dried sample one, as shown in Fig. 31.

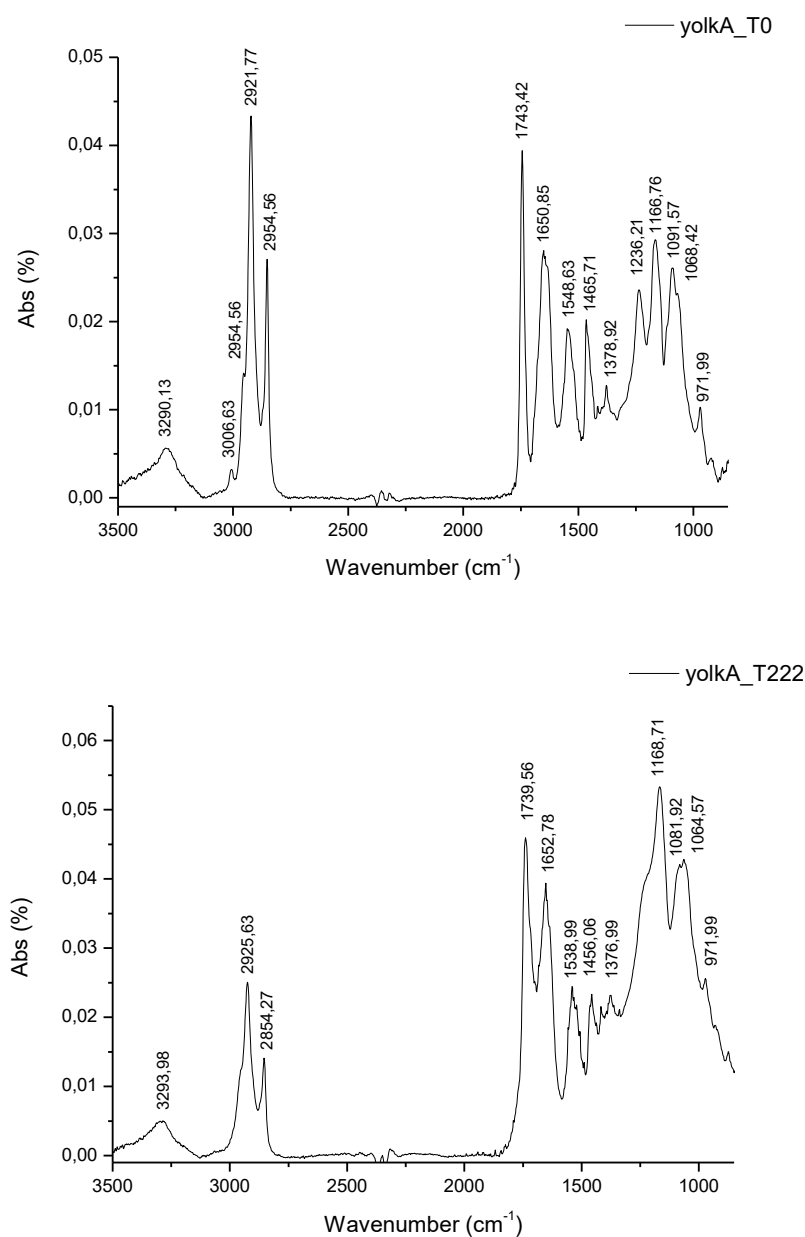


Fig. 30: ATR-FTIR spectra of dried egg yolk (top panel) and irradiated for 222 hours (bottom panel)

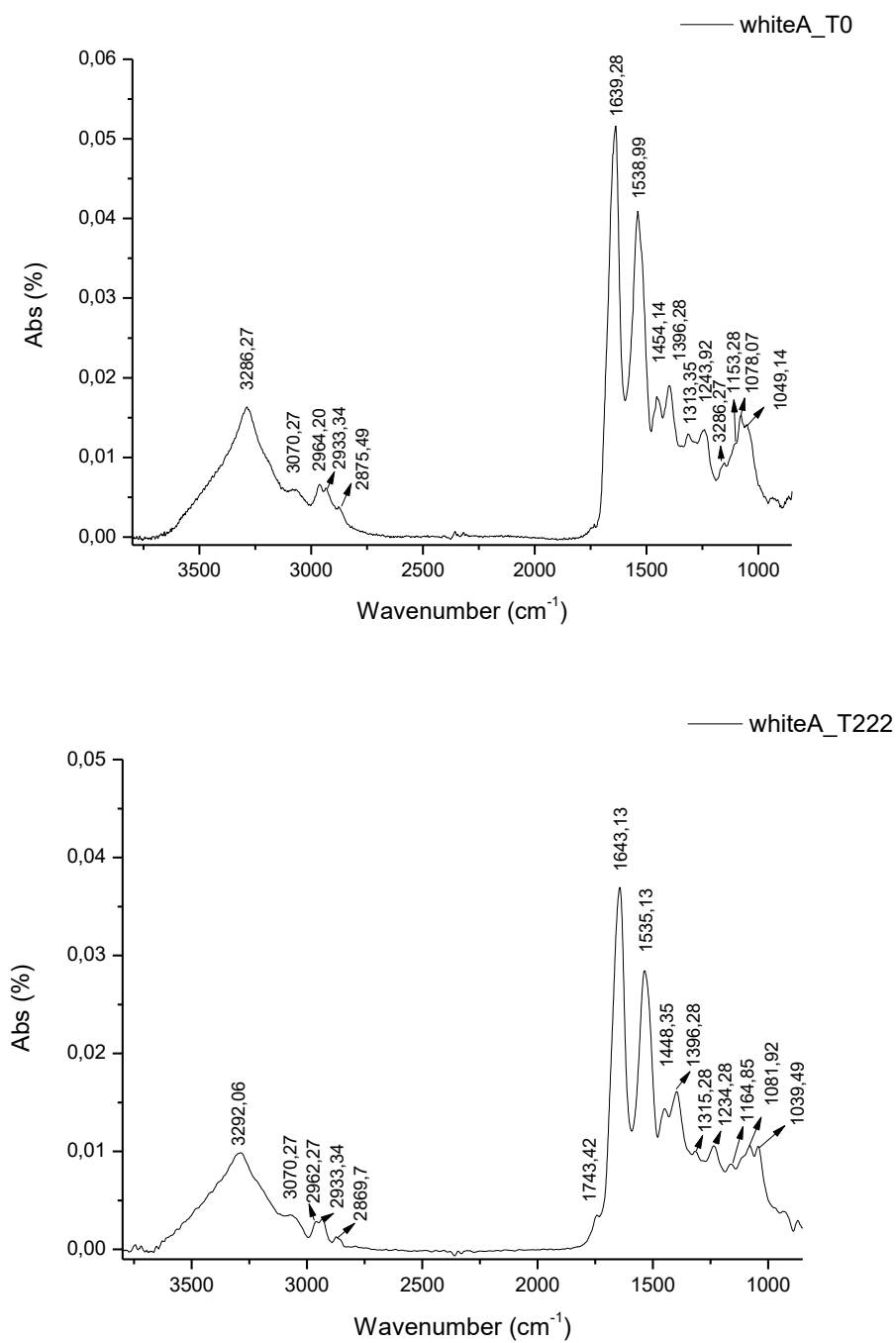


Fig. 31: ATR-FTIR spectra of dried egg white (top panel) and irradiated for 222 hours (bottom panel)

1.5.2. Linseed oil

1.5.2.1. Fluorescence excitation emission spectroscopy

The EE spectrum of the linseed oil dried in a heater for 1 month is shown in Fig. 32-a. It is characterized by two broad emission bands: the first one approximately at 360/450 nm and the second one at shorter wavelengths, approximately at 330/430 nm. This spectral feature can be attributed to the presence of multiple fluorophores.

After 15 hours of photodegradation, the broad band at higher excitation wavelengths disappears and the EE spectra show a single broad band at approximately 320/420 nm, Fig. 32-b. No more significant changes appear after 30, 90 and 155 hours, except for a small shift of the band to short excitation/emission wavelengths; after 322 hours the band is located approximately at 310/410 nm, Fig. 32 c-f. Finally, after 800 hours, the EE spectra show two maxima: one approximately at 360/440 nm and the other one approximately at 330/420 nm, Fig. 32-g.

Monitoring the fluorescence emission excited at 365 nm, we observe a shift of the emission band to short wavelengths, the maximum of the fluorescence spectra shifts from 452 nm to 436 nm, shown in the panel (h) of Fig. 32. This behaviour can be ascribed to the bleaching due to the strong light exposure [De la Rie (1982-2)].

The thermal degradation produces several different spectral features in the EE spectra of the linseed oil with respect to the spectra observed in the samples photodegraded under artificial sunlight, as shown in Fig. 33. After 15 hours the EE spectra become broader and shift to shorter excitation wavelengths. After 30, 90, 155, 320 and 800 hours the EE spectra show two distinct bands at 365/470 nm and 270/490 nm, respectively. The fluorescence spectra excited at 365 nm, presented in the panel (h) of Fig. 33, shift to long wavelengths, the maximum of the fluorescence spectra shift from 452 nm to 476 nm.

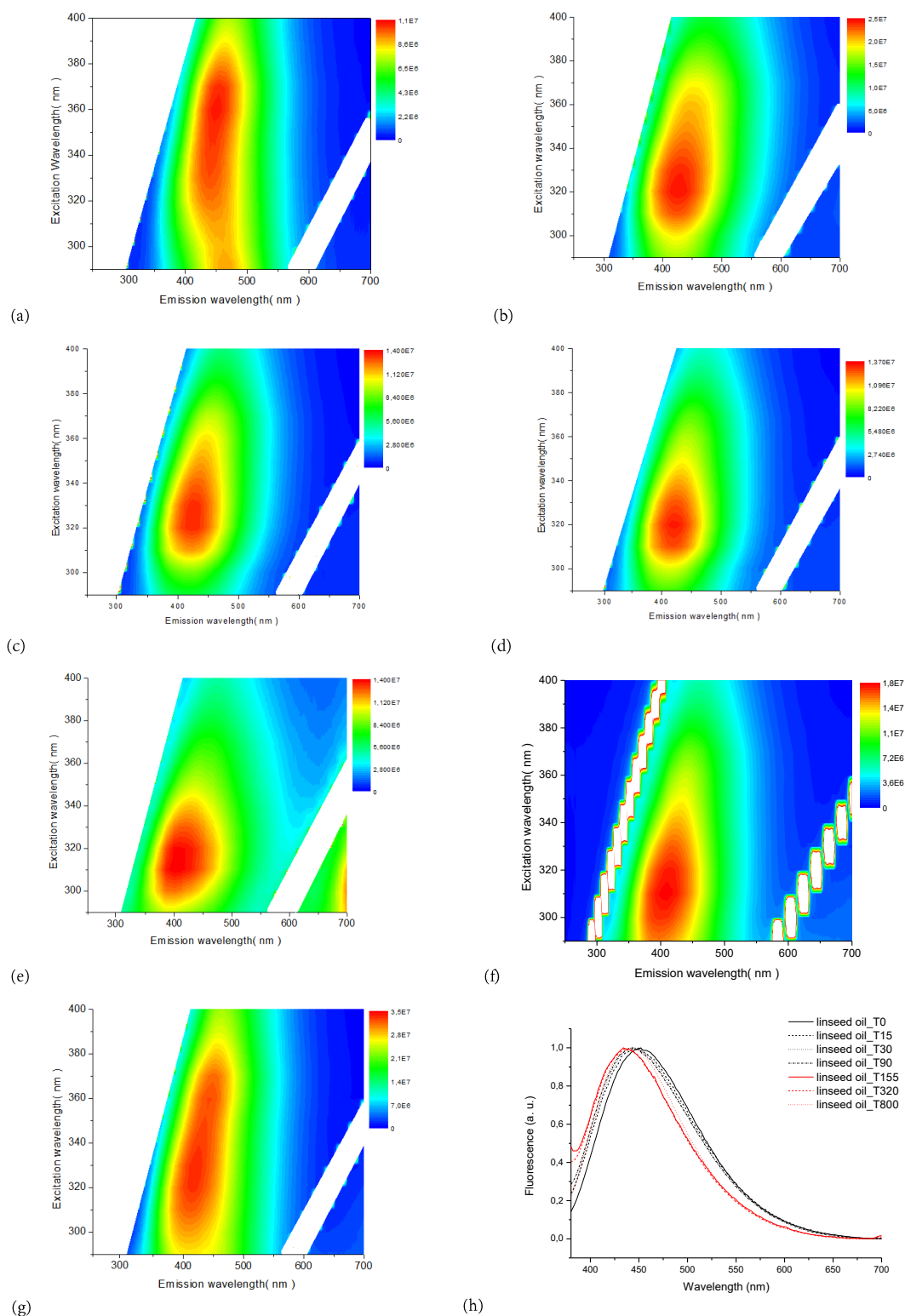


Fig. 32: Normalized excitation emission spectra of films of linseed oil. (a) dried, (b) irradiated for 15 hours, (c) irradiated for 30 hours, (d) irradiated for 90 hours, (e) irradiated for 155 hours, (f) irradiated for 320 hours, (g) irradiated for 800 hours. (h) Normalized fluorescence spectra excited at 365 nm.

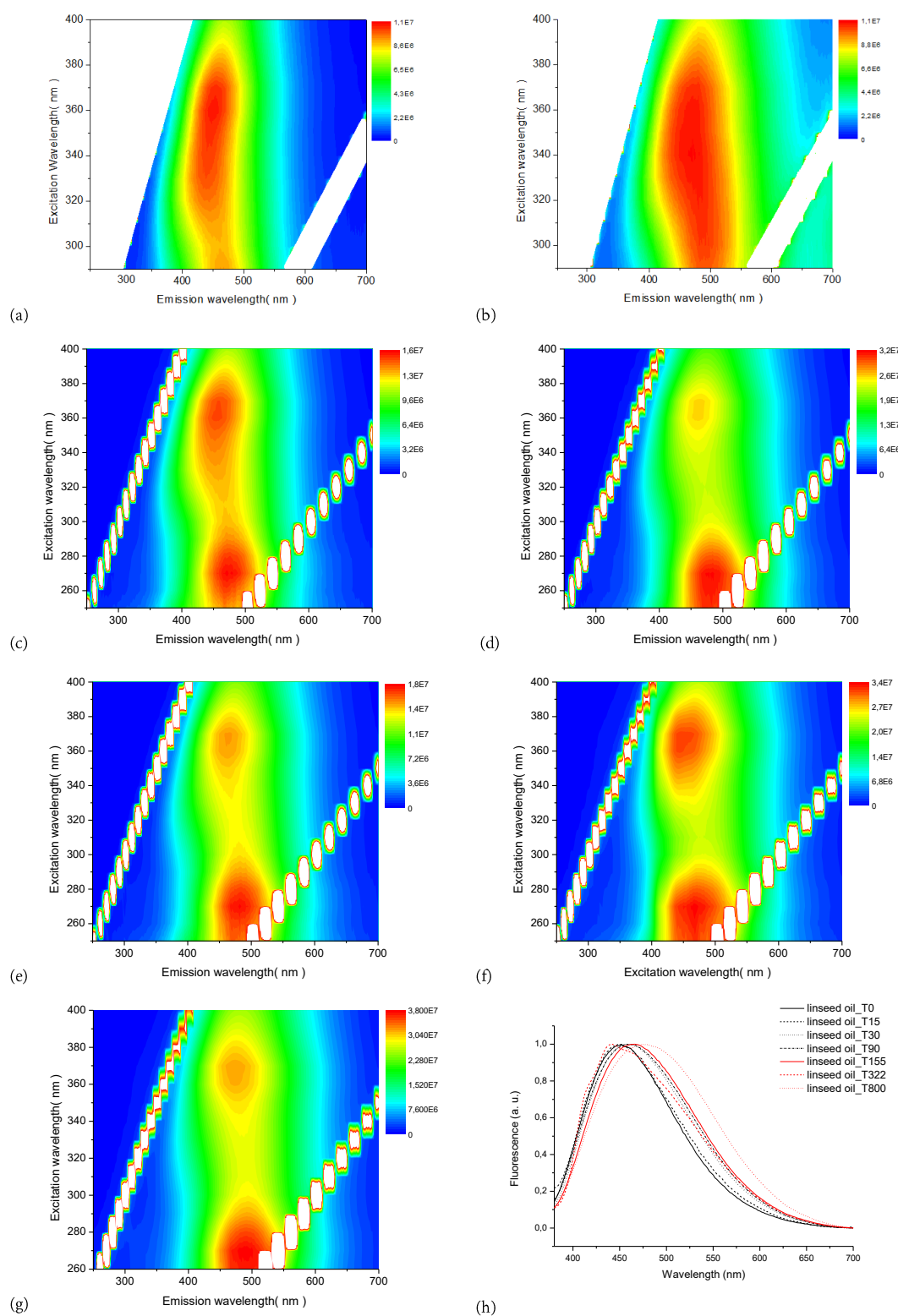


Fig. 33: Normalized excitation emission spectra of films of linseed oil heated at 75°C in dark: (a) dried, (b) heated for 15 hours, (c) heated for 30 hours, (d) heated for 90 hours, (e) heated for 155 hours, (f) heated for 320 hours, (g) heated for 800 hours. (h) Normalized fluorescence spectra excited at 365 nm.

1.5.2.2. ATR-FTIR

The assignment of the vibrational IR spectrum bands of “sticky” linseed oil, shown in Fig. 34, is summarized in Tab. 2. During the photodegradation, we assist to several spectral changes, shown in Fig. 35:

- the disappearance of the bands at 1637 cm^{-1} and 971 cm^{-1} , indicating the decrease of the unsaturated groups;
- the increase and the broadening of the carbonyl absorption band (≈ 1716 cm^{-1}) caused by the increase of the number of compounds containing this group;
- the decrease of the peaks at 2927 cm^{-1} and 2858 cm^{-1} ;
- the absorption of the –OH groups (3454 cm^{-1}) decreases after 320 hours but rises again after 800 hours; this spectral trend can indicate the formation of dicarboxylic acids in the oil [Lazzari M. et al. (1999)];
- a shift to small wavenumbers of the band at approximately 1740 cm^{-1} .

With the thermal ageing we noted the same changes of the spectral features as those described for the photo-ageing, but these chemical modifications present a slower kinetics, Fig. 36.

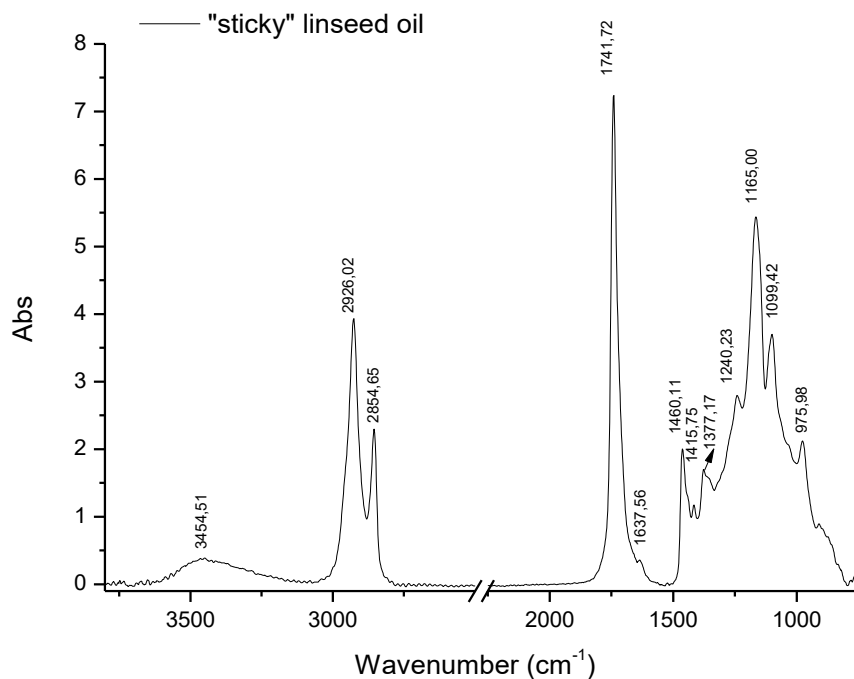


Fig. 34: ATR-FTIR spectrum of the “sticky” linseed oil

Tab. 2: ATR-FTIR infrared bands assignments based on the literature [Lazzari M. et al. (1999), Adam Oleszko et al. (2015)].

wavenumber (cm ⁻¹)	IR vibration assignments
3454	-OH
2926	ν_a (C-H) CH ₂ stretching
2854	ν_s (C-H) CH ₂ stretching
1741	ν C=O (ester) stretching
1637	ν C=C stretching
1460	δ (CH ₂) bending
1415	wag (CH ₂)-CH ₂ -CO-O-
1377	wag CH ₂ wagging
1240	ν_a (C-C-O)
1165	ν (C-O) or δ (CH ₂)
1099	ν_s (O-CH ₂ -C) stretching
976	ν_{as} (C=C): conformation trans

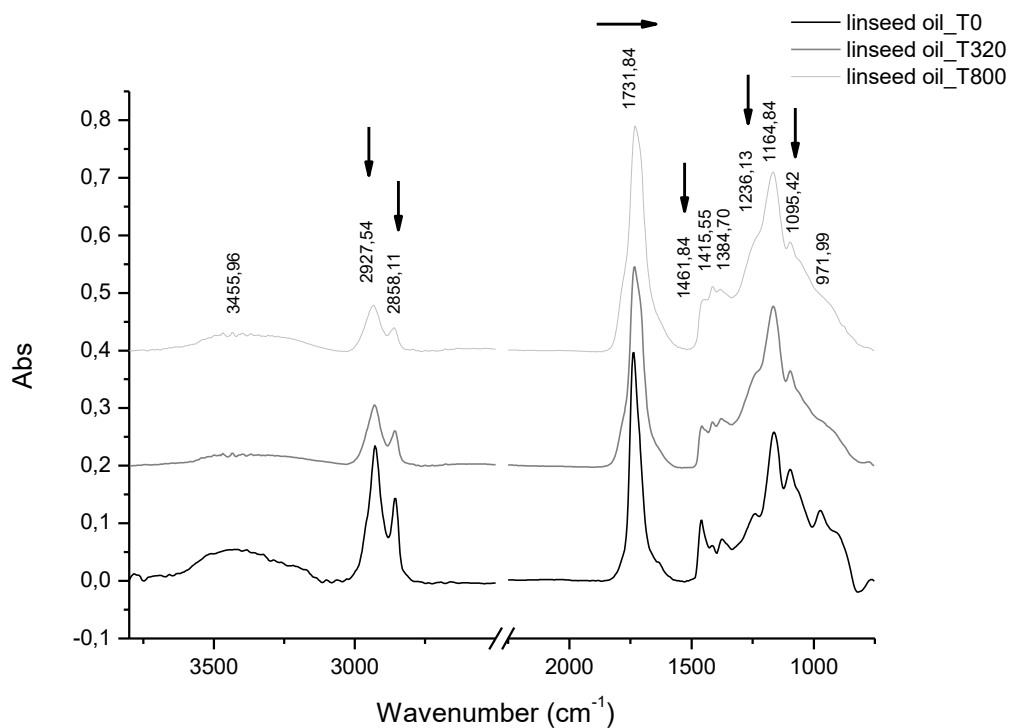


Fig. 35: ATR-FTIR spectra of the dried linseed oil (T0) and irradiated for 320 hours and 800 hours

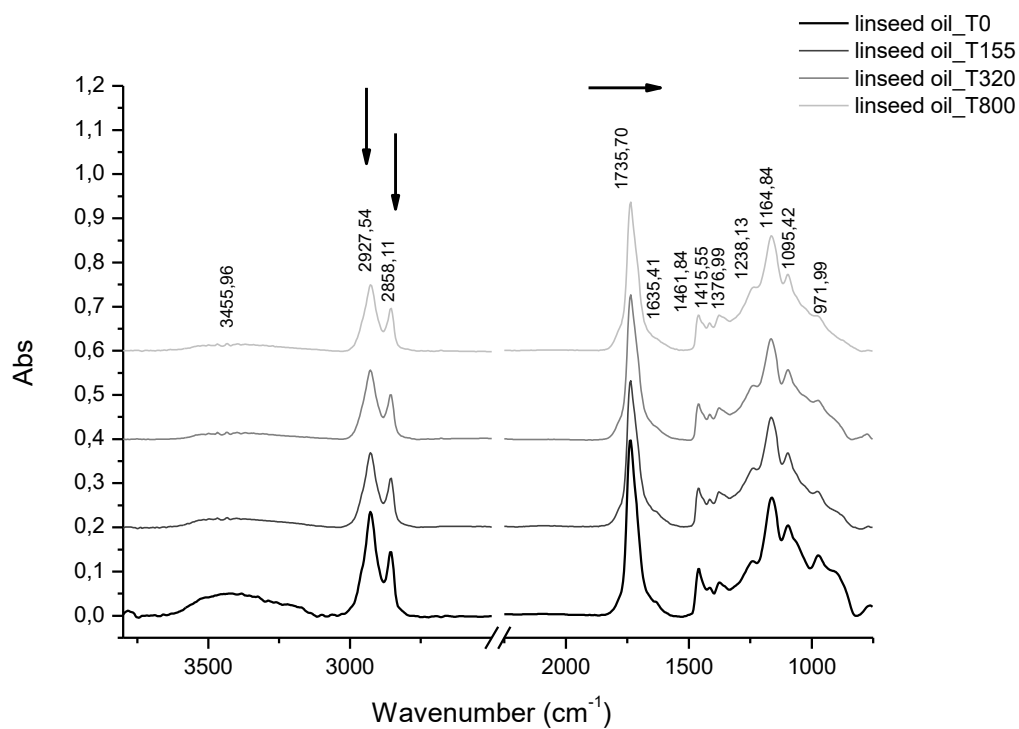


Fig. 36: ATR-FTIR spectra of the dried linseed oil (T0) and heated for 155 hours, 320 hours and 800 hours

1.6 Conclusions

The investigation of the ageing of egg white, egg yolk and linseed oil was performed by means of fluorescence excitation emission spectroscopy (EES) and ATR-FTIR. The EE spectra of egg white and egg yolk can be discriminated after the photodegradation under artificial sunlight. The wavelengths of the maxima of the fluorescence emission bands of egg yolk and egg white, excited at 365 nm, differ by about 20 nm. The ATR-FTIR spectra of egg white and egg yolk differ from each other in the range 1100 - 800 cm^{-1} , corresponding to the vibrational modes of C-O.

Photodegradation and thermal degradation of linseed oil show different behaviours in terms of the EE spectra and the ATR-FTIR spectra. After the photodegradation ageing, the EE spectrum is composed of two broad bands centred at about 330/420 nm and 360/430 nm, respectively. The EE spectrum obtained after the thermal ageing appears completely different, with two bands at 279/590 nm and 370/580 nm. This is due to the differences in the mechanisms involved in the accelerated ageing, photochemical reactions, on the one hand, thermal degradation in the other hand, which undergo various types of fluorophores. On the contrary, the infrared spectra did not show significant differences between the two accelerated ageing methods, most probably due to the similarity of the main degradation reactions. Nevertheless, the speed of the kinetics is significantly different and affects the intensity of the absorption bands. The accelerated photo-ageing produces an advanced state of degradation, observable through: (i) the strong decrease of the (C-H) CH_2 stretching band, (ii) the shift and broadening of the carbonyl band due to the formation of carboxylic acids.

Proteinaceous binders can be clearly distinguished from linseed oil by means of ATR-FTIR spectrometry. In fact, the bands at about 1730-35 cm^{-1} and 1164 cm^{-1} are only present in the oil samples. The possibility of discriminating the two binders media with fluorescence spectroscopy seems difficult because of their different behaviour according to the type of degradation (thermal or photodegradation). However, such result can be potentially interesting in order to have information on the method of fabrication but would need further research in the future.

Chapter 2

PIGMENTS AND PICTORIAL LAYERS

In this section, we will focus on advances and limitations of Fiber Optics Reflectance Spectroscopy (FORS), fluorescence spectroscopy and UV-VIS-NIR multispectral imaging used in order to identify the components of pictorial layers. We used swatches realized on purpose. We took into account different boundary conditions such as the presence of an underlying background and some changes in the experimental setups. We tested the use of different binders, pigment/binder ratios and pigment mixtures; finally, we focused on the possibility to distinguish mixtures of white pigments.

2.	Pigments and pictorial layers	
2.1.	UV-VIS-NIR spectroscopy and multispectral imaging for the pigments identification	61
2.1.1.	Introduction	61
2.1.2.	Materials	61
2.1.3.	Methods	63
2.1.4.	Results and discussion	63
2.1.4.1.	Reflectance spectra	63
2.1.4.2.	Reflectance spectra and the influence of the backgrounds	68
2.1.4.3.	Reflectance spectra and the influence of experimental setups	71
2.1.4.4.	Multispectral reflectance imaging	74
2.1.4.5.	Fluorescence spectra	89
2.1.4.6.	Multispectral UV-fluorescence imaging	96
2.1.4.7.	Multispectral Near Infrared imaging	98
2.1.5.	Conclusions	
2.2.	Study of the spectral behaviour of pigments mixed with oil and egg yolk in different percentages by means of UV-VIS spectroscopy and UV-VIS multispectral imaging	106
2.2.1.	Introduction	106
2.2.2.	Materials	106
2.2.3.	Methods	114

2.2.4.	Results and discussion	115
2.2.4.1.	Reflectance spectra	115
2.2.4.2.	Fluorescence spectra	124
2.2.4.3.	Correction of UV-fluorescence spectra	135
2.2.4.4.	Multispectral imaging	137
2.2.5.	Conclusions	141
2.3.	White pigment identification by means of reflectance and fluorescence spectroscopies and multispectral imaging	143
2.3.1.	Introduction	143
2.3.2.	Materials	145
2.3.3.	Methods	145
2.3.4.	Results and discussion	146
2.3.4.1.	Spectroscopic analysis	146
2.3.4.2.	Multispectral imaging	155
2.3.5.	Conclusions	159

2.1 UV-VIS spectroscopies and UV-VIS-NIR multispectral imaging for the pigment identification

2.1.1 Introduction

The identification of pigments and pictorial layers on artistic-historical artifacts can be performed by using non-destructive and micro-destructive methods. Taking into account the fundamental principle of the minimal damage, the non-destructive approaches are preferred for the investigation of cultural heritage.

In this study, we realized a database of pictorial reference samples to test the efficiency of FORS, fluorescence spectroscopy and multispectral imaging techniques for the identification of pictorial layers. This work is extremely important to identify the spectral features of a specific pigment or pictorial system (pigment with binder) for recognizing it in unknown pictorial materials.

In order to evaluate the efficiency of the FORS spectra methodology, we tested how the presence of either a white or a black background and the changes of the experimental setups can modify the shape of the reflectance curves obtained. Moreover, we applied the Principal Component Analysis (PCA) on the reflectance spectra in order to select a limited number (three) of multispectral reflectance images containing the relevant information.

Finally, we evaluated the transparency of our pictorial samples in the near-infrared range by means of multispectral images at 720 nm and at 1000 nm (long-pass filters) and at 800 nm and 900 nm (narrow-pass filters).

2.1.2 Materials

A large set of pictorial reference samples was manufactured in order to provide swatches ready for testing, simulating the pictorial layers occurring in real paintings. We have chosen forty-four

different materials, including both traditional and modern pigments as listed in Fig. 37. We mixed the pigments with egg yolk in 1:1 ratio, as suggested by Cennino Cennini [Cennino C. (1971)].

They were spread on microscope slides and also on a canvas that was properly prepared. The canvas was pure linen canvas and covered by a preparatory layer of lead white and egg yolk. On this layer we traced lines using four different materials: a) Lead tip (leaving material on the surface), b) a metal tip that produces an incision, c) charcoal, coal ink and d) iron gall ink.

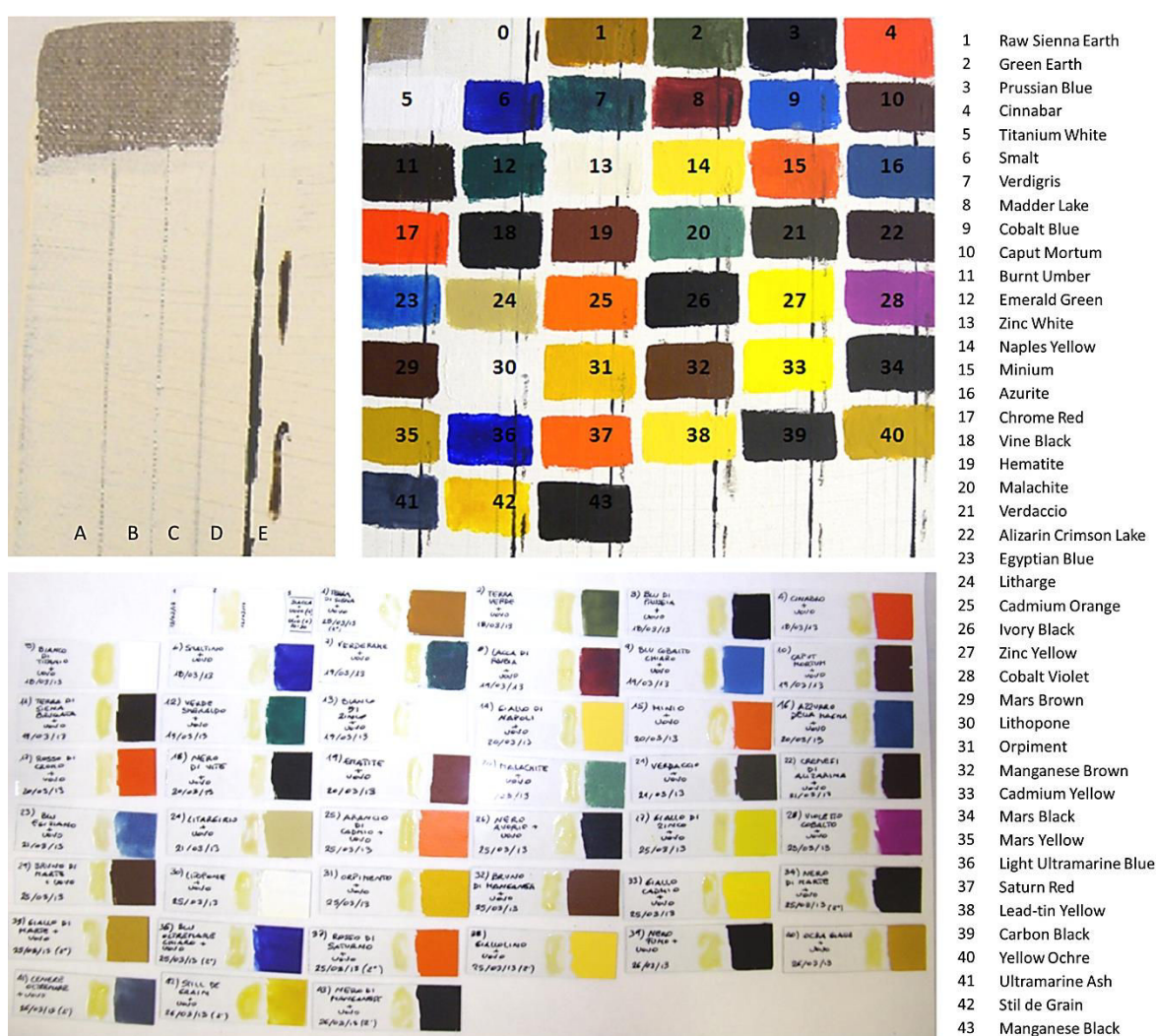


Fig. 37: Image of the lines realized on the lead white layer in order to simulate different ways of drawing (top left panel); the lines were performed with a Lead tip, leaving material on the surface (A), a metal tip that produces an incision (B), charcoal (C), coal ink (D) and iron gall ink (E) (left panel). The entire canvas covered by pigments/dyes mixed with yolk (top right panel); the numbers indicate the pigment/dyes listed on the table. The pigments/dyes mixed with yolk spread on microscope slides (bottom panel).

2.1.3 Methods

Reflectance measurements were carried out with Minolta CM-2300d and Avantes AvaSpec-2048 A-USB1 spectrophotometers. With the Avantes device, we used the spectralon SRS-99-010 (Labsphere) as diffuse reflectance standard.

The Avantes device, equipped with a UV LED (emitting at 365 nm), was also employed for the acquisition of the fluorescence spectra.

Multispectral imaging was performed with two CCD cameras:

- the QSI 583-w camera equipped with the Micro-Nikkor optical system;
- the EuroPixel HiSIS 23 E camera equipped with a Canon PH6x8 MACRO optical system.

We used the following band-pass interferential filters: 400 nm, 410 nm, 420 nm, 450 nm, 470 nm, 500 nm, 532 nm, 550 nm, 600 nm, 650 nm, 700 nm, 750 nm, 800 nm, 900 nm and two long-pass filters with cut-on wavelengths at 720 nm and 1000 nm.

Other details of the instrumental setups and the experimental conditions are reported in Appendix A.

2.1.4 Results and discussion

2.1.4.1 Reflectance spectra

The FORS spectra reported in this section were measured by placing a black support under the painted microscope slides to avoid any spectral contribution coming from the back of the microscope slides. The back support showed a flat spectrum with a reflectance of about 5 % in the entire spectral range. The FORS spectra shown in this paragraph were measured with a compact spectrometer (Minolta, CM-2300d).

In view of the following discussion, we must remember that absorption bands generally appear as minima in the reflectance spectra.

Similar hues present different FORS spectra, as shown from Fig. 38 to Fig. 43, depending on the chemical composition. Green pigments show specific spectral features (maxima and inflection points) that allow their discrimination as shown in, Fig. 38. Each absorption band can be explained by the energy required to do the electronic transitions. For example, the sample made with Emerald Green, that is a chromium-based compound, shows a strong absorption band centred in the UV region. This can be attributed to the metal-ligand charge transfer transition between the chromium and the oxygen anion [Brill T. B. (1980)]. Other absorption bands with maxima at 430 and 620-630 nm are related to the electron d-d transitions typical of chromium(III) in octahedral coordination. Verdigris shows an absorption band in the UV region due to a charge transfer electronic transition among the metal (Cu) and the ligand, and a broad absorption band from 550 to NIR due to the d-d transitions of Cu(II).

For the red, brown and orange hues, the spectral features are similar among them, as shown in Fig. 39: they all present an absorption band from about 360 nm to 550 nm. Cobalt Violet shows an absorption band from 500 nm to 570 nm. The red, brown and orange hues can be distinguished with the help of the positions of the inflection points and the presence of absorption bands between 600 and 700 nm (e. g. the electronic transitions of the Fe(III) ion of Hematite).

For the blue hue, despite the presence of the absorption band in the 550-670 nm range, Fig. 40-a, the associated pigments can be distinguished through the shift of the inflection points and the different behaviour in the NIR range, Fig. 40-b. Furthermore, some blue pigments show a specific spectral curve. For example, the reflectance of Cobalt Blue has three maxima between 350 nm and 550 nm and the Prussian Blue reflectance is very low.

For the yellow hues, we noticed a similar spectral behaviour for most of them; however, the positions of the inflection points could be useful to discriminate them, Fig. 41. Mars Yellow or Yellow Ocre (they present a similar chemical composition) can be discriminated from Zinc Yellow due to the different positions of the maxima.

We shall discuss in detail the spectral features of Lead white, Zinc White and Titanium White in Part II, chap. 2.3. We can add here that Litharge and Lithopone present inflection points at shorter wavelengths than the other white samples analysed, Fig. 42.

For the black pigments, we can notice a flat spectrum in the entire visible range, except for the Mars Black that contains Fe ions and shows an increase of reflectance for increasing wavelengths, Fig. 43.

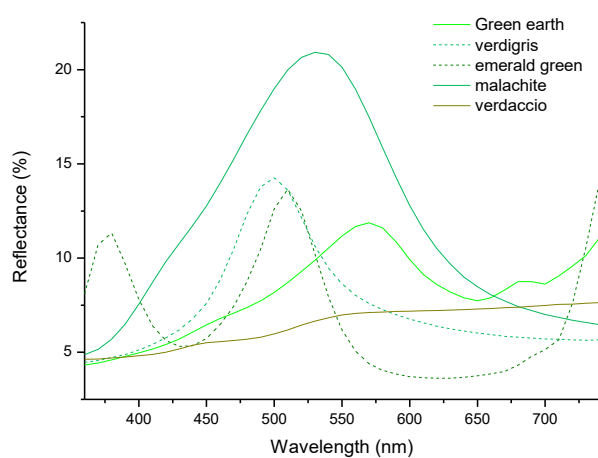


Fig. 38: Reflectance spectra of green pictorial layers spread on microscope slides (black background). Reflectance measurements carried out with the Minolta spectrometer.

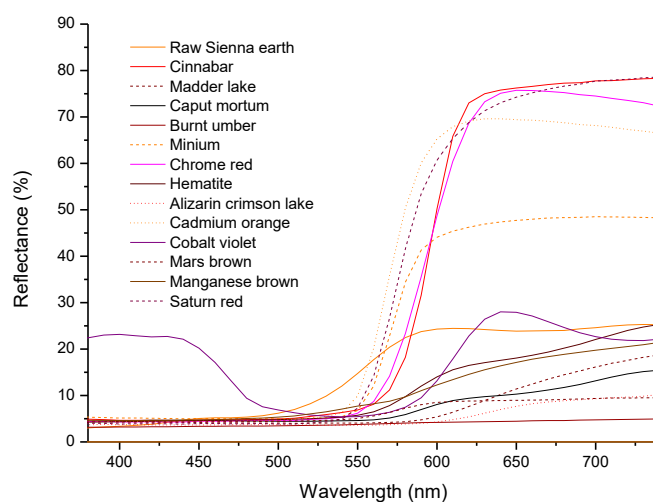


Fig. 39: Reflectance spectra of orange-red-brown pictorial layers spread on microscope slides (black background). Reflectance measurements carried out with the Minolta spectrometer.

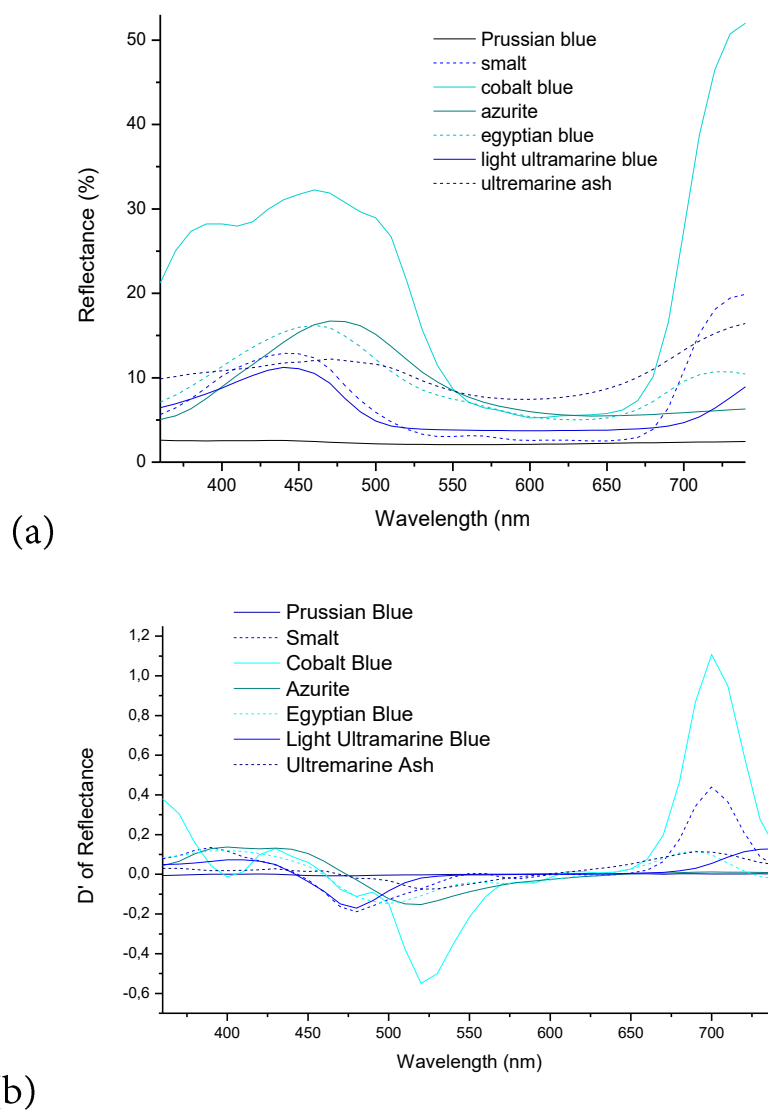


Fig. 40: Reflectance spectra (a) and their first derivative of blue pictorial layers spread on microscope slides (black background). Reflectance measurements carried out with the Minolta spectrometer.

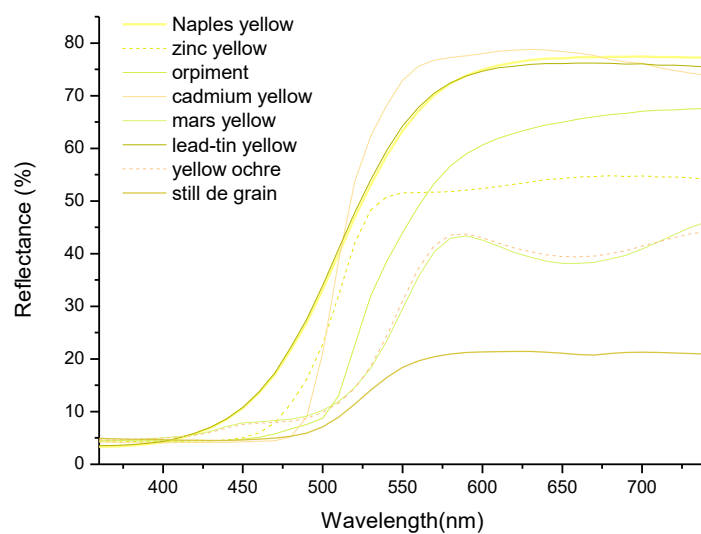


Fig. 41: Reflectance spectra of yellow pictorial layers spread on microscope slides (black background). Reflectance measurements carried out with the Minolta spectrometer.

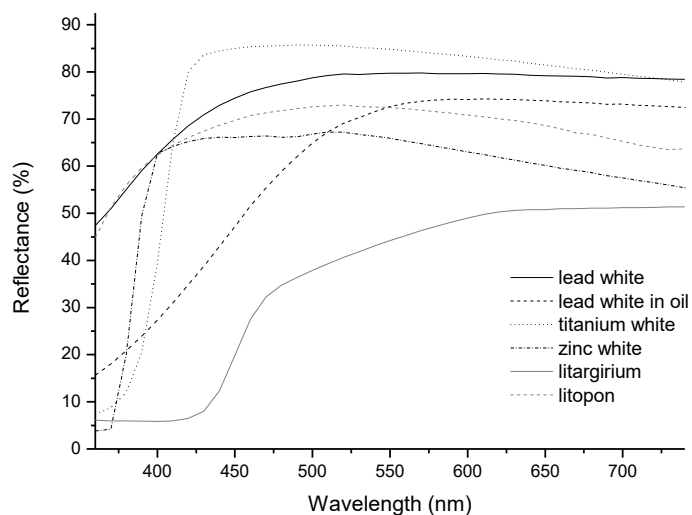


Fig. 42: Reflectance spectra of white pictorial layers spread on microscope slides (black background). Reflectance measurements carried out with the Minolta spectrometer.

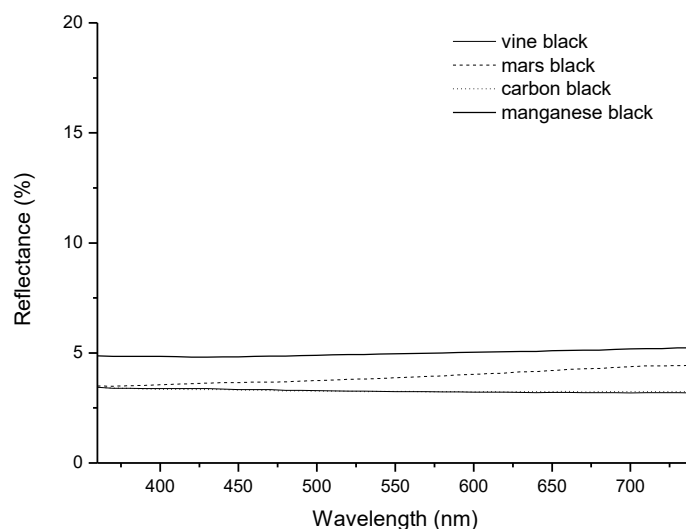


Fig. 43: Reflectance spectra of black pictorial layers spread on microscope slides (black background). Reflectance measurements carried out with the Minolta spectrometer.

2.1.4.2 Reflectance spectra and the influence of the backgrounds

In the previous paragraph, when discussing the spectral patterns of different pigments on a black background, we assumed that the measured reflected/diffused light was coming from the pictorial layers without relevant contribution of the back supports. In this section, we discuss the spectral behaviour of the same pictorial layer on different supports: microscope slide with white support and lead white layer on linen canvas. ; we give few representative examples in this section. All the data are reported in the Appendix B.

The FORS spectra of opaque pigments, with a high-covering power, such as Cinnabar and Cobalt Blue, do not change significantly although Cobalt Blue shows an increase of reflectance values in the IR, Fig. 44Fig. 29 and Fig. 4530. For Raw Sienna, Smalt and Stil de Grain placed on white layers, we assist to an increase of the reflectance value at the longest wavelengths, from Fig. 46 to Fig. 48Fig. 31-33. The strong reflectance increase is even more evident for transparent pigments like Stil de Grain and Smalt.

In order to locate more accurately the positions of the absorption bands and of the inflection points, we decided to calculate the first derivative of each spectrum (insets of the figures). The inflection points remain approximately in the same position, and the absorption bands do not change their positions or their intensities. This means that the absorption band is unaffected by the background layer.

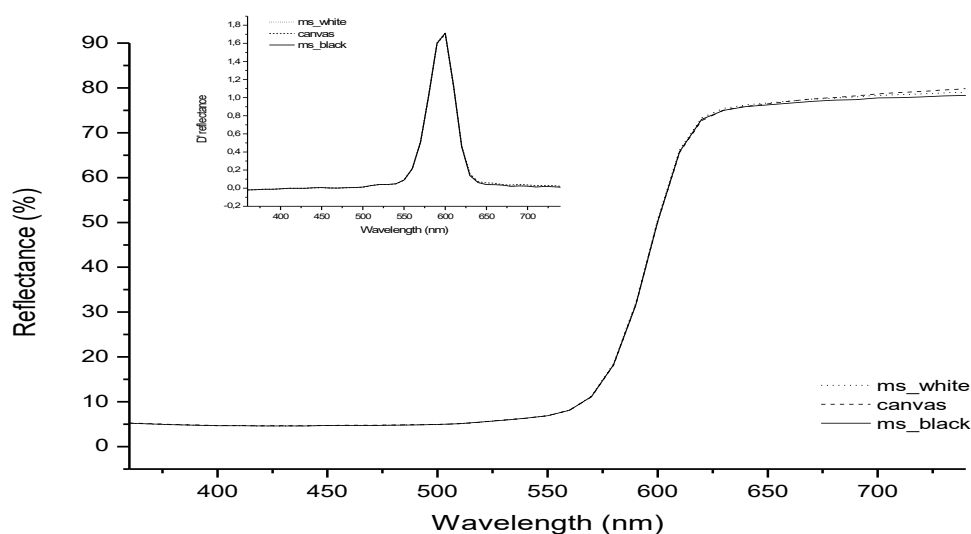


Fig. 44: Reflectance spectra of Cinnabar spread on microscope slides with a black support (solid line), white support (dashed line) and on a lead white layer (shot line). First derivate of the Reflectance spectra were shown in the top of the figure. Reflectance measurements carried out with the Minolta spectrometer.

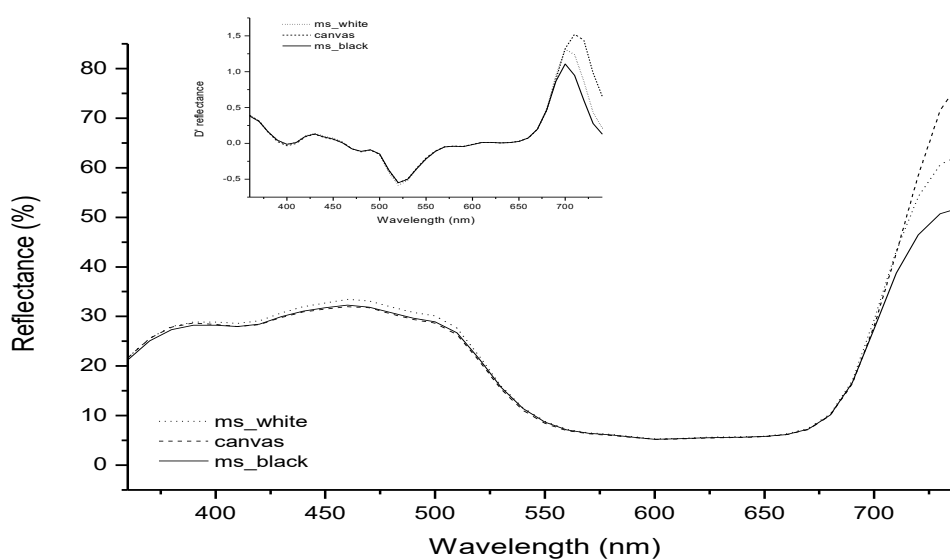


Fig. 45: Reflectance spectra of Cobalt Blue spread on microscope slides with a black support (solid line), white support (dashed line) and on a lead white layer (shot line). First derivate of the Reflectance spectra were shown in the top of the figure. Reflectance measurements carried out with the Minolta spectrometer.

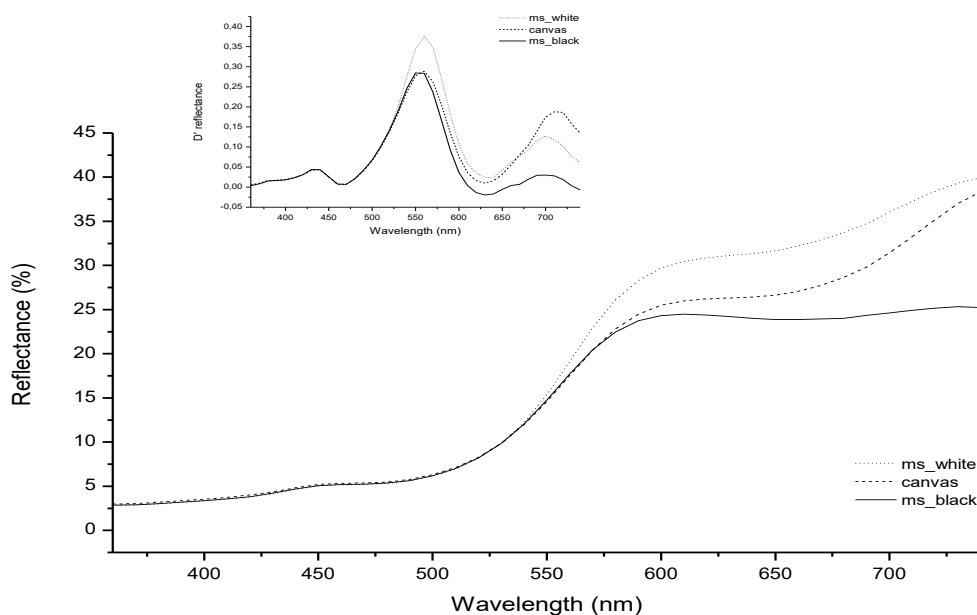


Fig. 46: Reflectance spectra of Raw Sienna Earth spread on microscope slides with a black support (solid line), white support (dashed line) and on a lead white layer (shot line). First derivate of the Reflectance spectra were shown in the top of the figure. Reflectance measurements carried out with the Minolta spectrometer.

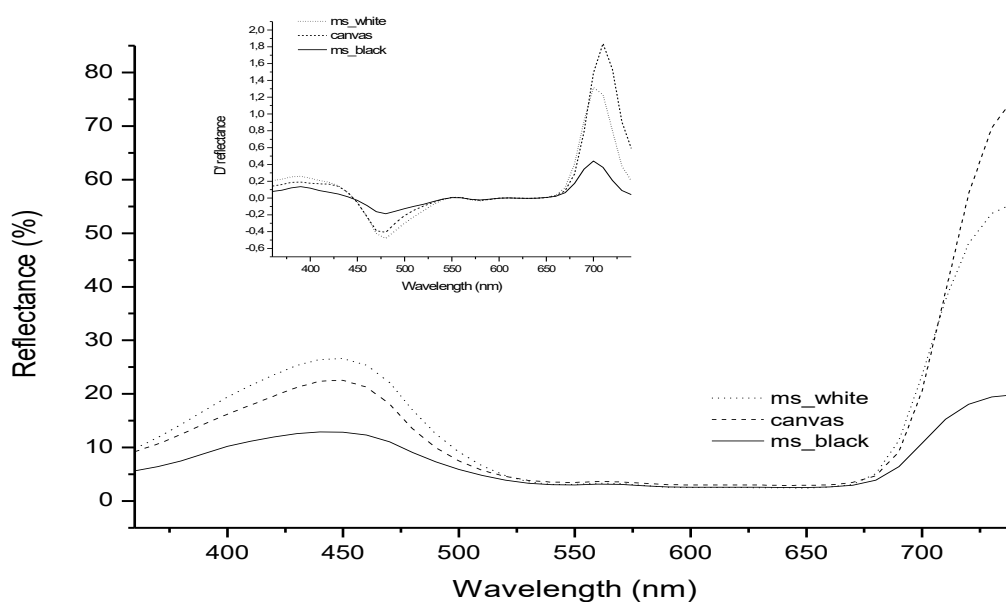


Fig. 47: Reflectance spectra of Smalt spread on microscope slides with a black support (solid line), white support (dashed line) and on a lead white layer (shot line). First derivate of the Reflectance spectra were shown in the top of the figure. Reflectance measurements carried out with the Minolta spectrometer.

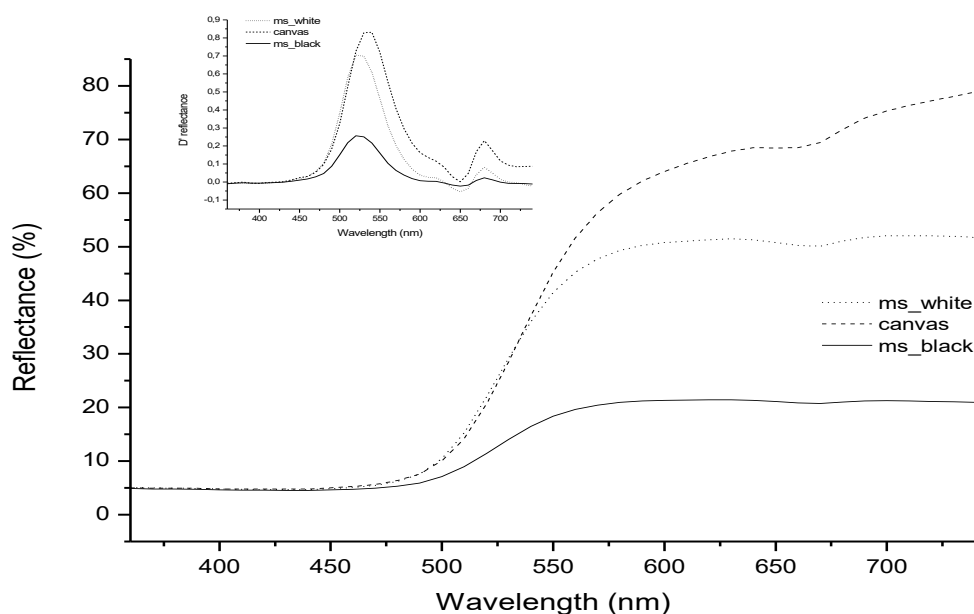


Fig. 48: Reflectance spectra of Stil de Grain spread on microscope slides with a black support (solid line), white support (dashed line) and on a lead white layer (shot line). First derivate of the Reflectance spectra were shown in the top of the figure. Reflectance measurements carried out with the Minolta spectrometer

2.1.4.3 Reflectance spectra the influence of the experimental setups

FORS analyses were performed with two different instrumental setups: Minolta and Avantes spectrometers, as described in the Appendix A. The main differences are: the illumination/acquisition geometry, the sample holder and the type of incident light. The Avantes spectrometer is equipped with optical fibers for illuminating the sample and for collecting the radiation; the geometry is $45^{\circ}/0^{\circ}$. An integrated sphere is included in the Minolta spectrometer, so the geometry is $\text{diff}/8^{\circ}$. Moreover, the radiation source of the Minolta is a xenon lamp while that of the Avantes spectrometer is a halogen lamp. We measured FORS on the same samples as those used in the previous sections, but, with the Minolta spectrometer, the spectra were measured on dried samples, while in the case of the Avantes spectrometer, the measurements were done after two years of storage in our laboratory for the paint on the canvas and in the dark for the others.

The shape of most of the reflectance spectra does not show significant changes between the two acquisition systems. We noted a discrepancy from 360 nm to 450 nm due to the different spectral distribution of the incident lights: the halogen lamp presents a very low emission in the “violet” and “blue” regions, supplying a weak reference signal; this one causes the apparent increase of the reflectance if all the spectra are not properly corrected. We can observe this phenomenon, for example, in the Zinc Yellow spectra in the Fig. 49.

For the Litharge, a weak shift occurs to lower wavelengths for the samples on the microscope slides and we noted a high increase of the reflectance baseline. Probably this is due to the light scattering that is more intense for the geometry 45/0° than for the diff/8° one. Also a change in the spectrum shape is visible: the second shoulder at about 630 nm disappears and the sample spread on the lead white layer shows a high decrease of reflectance, Fig. 50. Probably the change in colour is related to the light exposition; in fact, after the acquisition of the multispectral images, the sample spread on the microscope slides showed the same behaviour, Fig. 51.

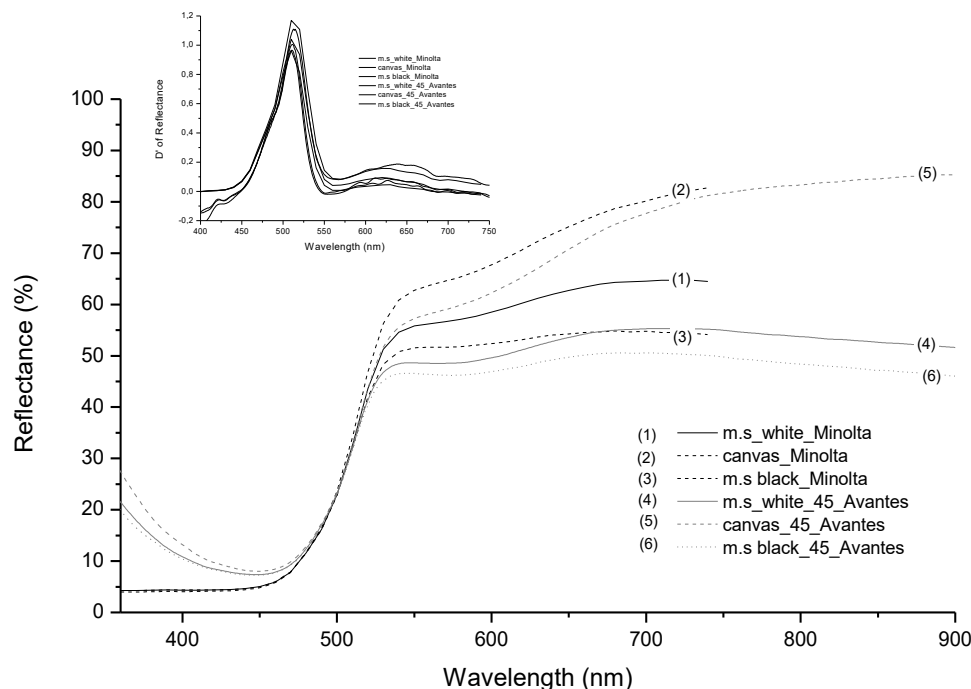


Fig. 49: Reflectance spectra of Zinc Yellow. Measurements carried out with the Minolta spectrometer: (1) pictorial layer spread on microscope slides with a white support, (2) pictorial layer spread on a lead white layer, (3) pictorial layer spread on microscope slides with a black support; measurements carried out with the Avantes spectrometer: (4) pictorial layer spread on microscope slides with a white support, (5) pictorial layer spread on a lead white layer, (6)

pictorial layer spread on microscope slides with a black support. First derivate of the Reflectance spectra were shown in the top of the figure.

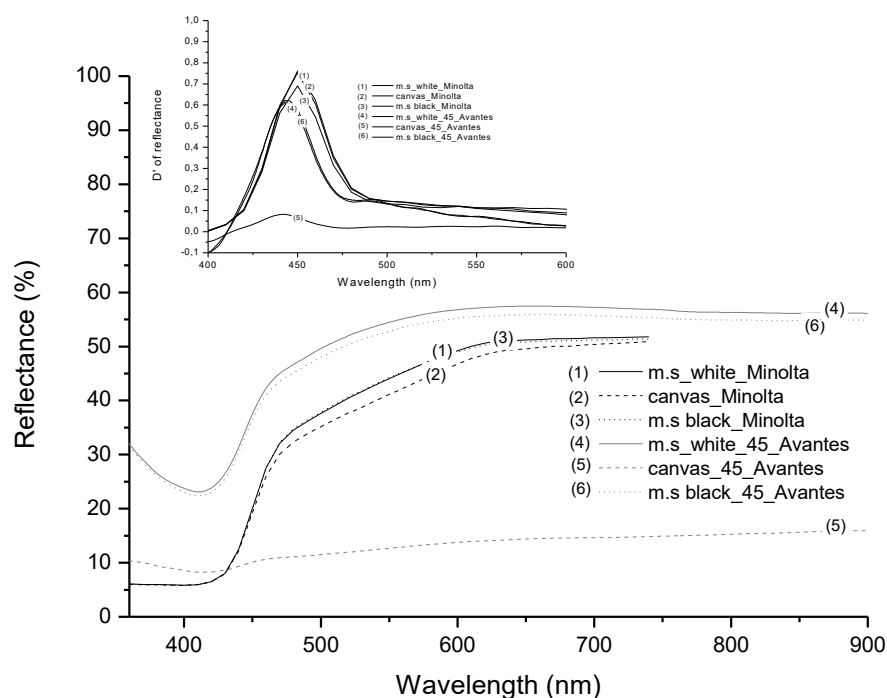


Fig. 50: Reflectance spectra of Litharge. Measurements carried out with the Minolta spectrometer: (1) pictorial layer spread on microscope slides with a white support, (2) pictorial layer spread on a lead white layer, (3) pictorial layer spread on microscope slides with a black support; measurements carried out with the Avantes spectrometer: (4) pictorial layer spread on microscope slides with a white support, (5) pictorial layer spread on a lead white layer, (6) pictorial layer spread on microscope slides with a black support. First derivate of the Reflectance spectra were shown in the top of the figure.

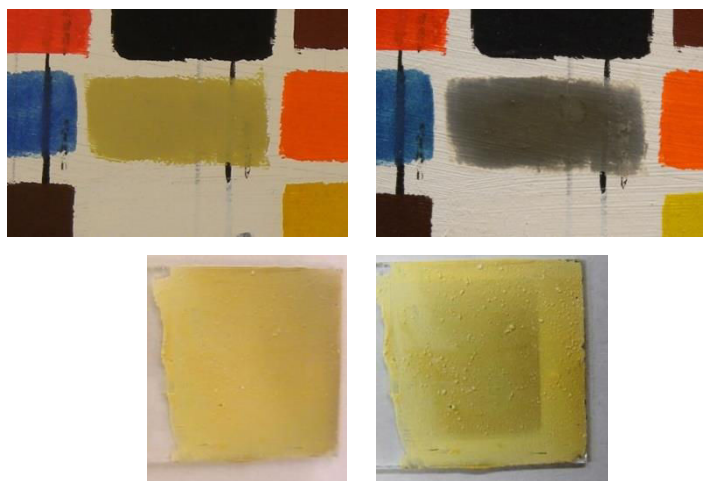


Fig. 51: Photography of the Litharge samples. Dried Litharge layer on the left side and after two years at right side. the figures on the top shows the pictorial layer above the lead white layer, on the bottom the sample spread on microscope slide.

1.1.3.4. Multispectral reflectance imaging

Multispectral reflectance imaging was performed by using 12 narrow-band filters with 400 nm, 410 nm, 420 nm, 450 nm, 470 nm, 500 nm, 532 nm, 550 nm, 600 nm, 650 nm, 700 nm, 750 nm transmission peaks. The photographic image and the reflectance images of the forty-four samples spread on lead white preparation are shown in Fig. 52 and Fig. 53, respectively.

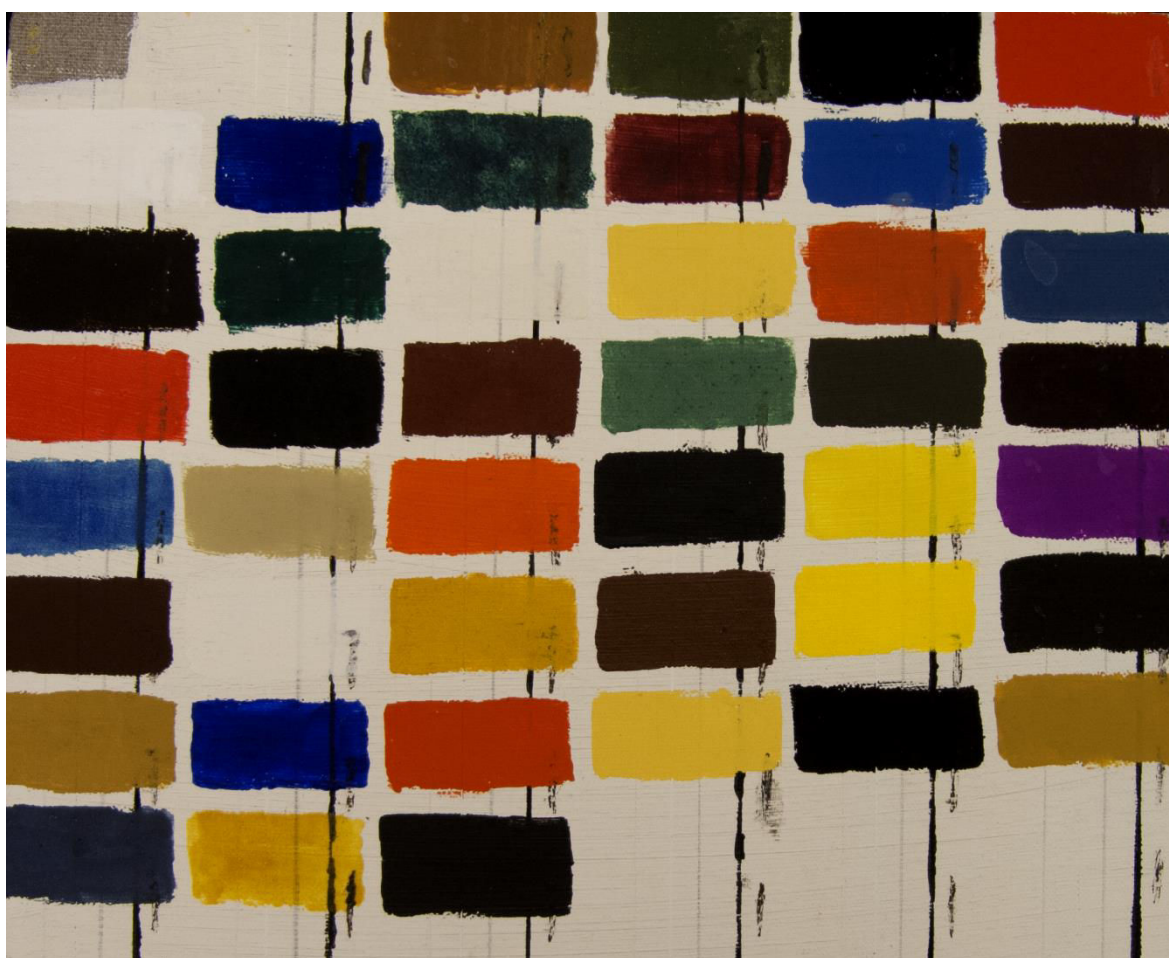


Fig. 52: Image of the forty-four dye and pigments mixed with egg yolk and spread on a lead white layer

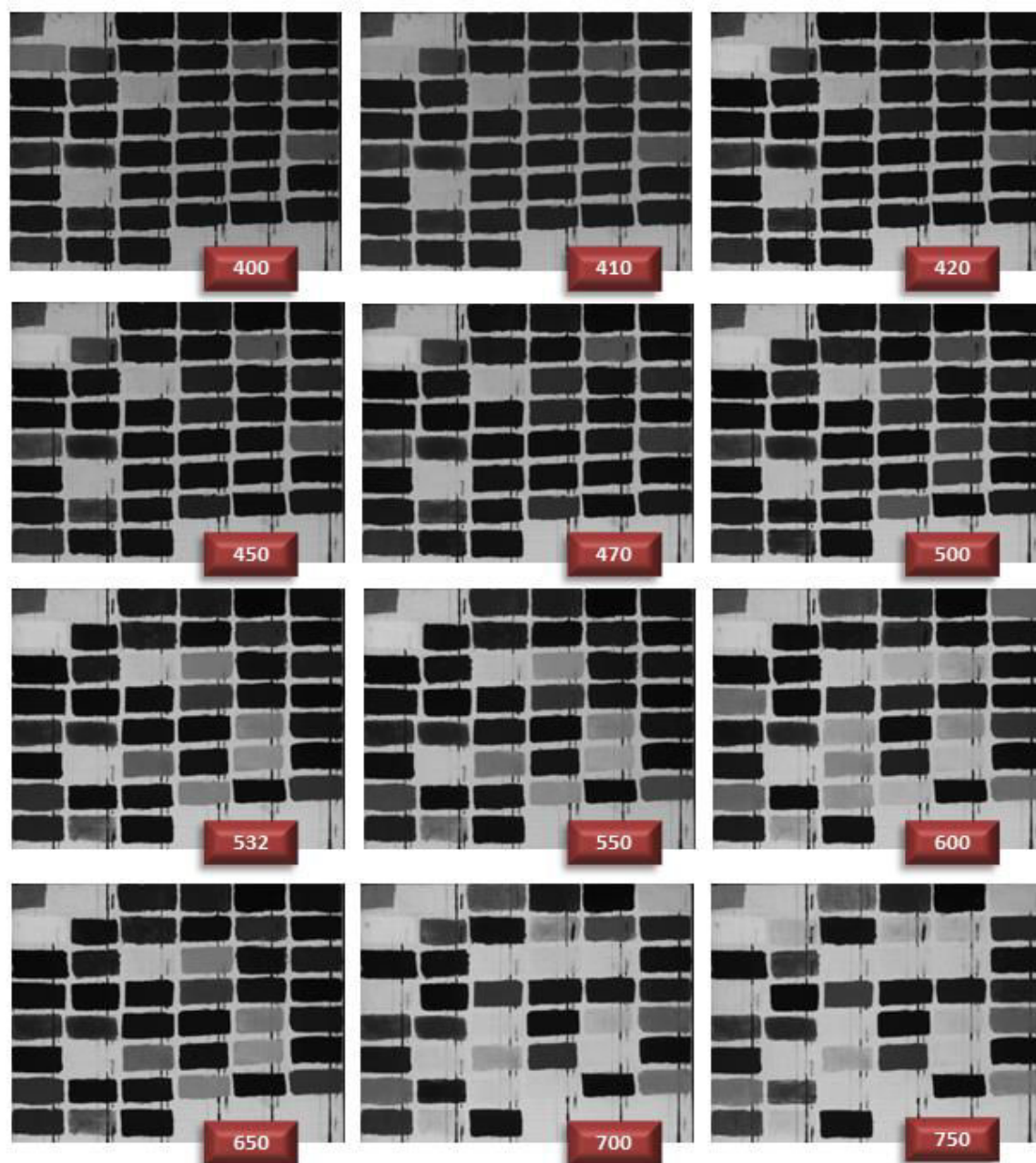


Fig. 53: Multispectral reflectance images of the forty-four pictorial layers spread on lead white preparation.

Despite the already limited number of images, we tried not to select more than three multispectral images for identifying pigments with the same hue and we recombined them into a “false” RGB image in order to emphasize the different spectral features. For this purpose we applied the Principal Component Analysis (PCA) on the reflectance spectra in order to select at most three wavelengths that contain the maximum variances in terms of reflectance percentage.

We performed the PCA on the reflectance spectra of the samples placed on the black support, acquired with the Minolta instrument.

For each reflectance spectrum we considered 31 wavelengths (from 400 nm to 700 nm at steps of 10 nm). For almost all the data, we decided not to include the reflectance values taken at long wavelengths (> 700 nm) in order to avoid any effect related to the transparency of some pictorial layers in this spectral range.

The PCA is performed on a data matrix in which each row represents a single spectrum (called *sample* or *observation*) and each column collects the reflectance values at a single wavelength (called *variable*). The aim of PCA is the reduction of the number of variables through an orthogonal linear transformation of the variables to a new coordinate system. The new axes are the principal components (called *eigenvectors*) and are ordered in decreasing order of variance (called *eigenvalues*). The first principal component (PC1) is the direction in the new space along which projections have the largest variance; the second greatest variance comes to lie on the second principal component (PC2) and so on. The variance plot shows how much variance in the dataset is explained by the PCs (i. e. PC1, PC2, PC3, etc.), an example is shown in Fig. 54.

Blue pigments

For the blue pigments, the eigenvectors of the PC1, PC2 and PC3 explain the 95% of the variance, as shown in Fig. 54.

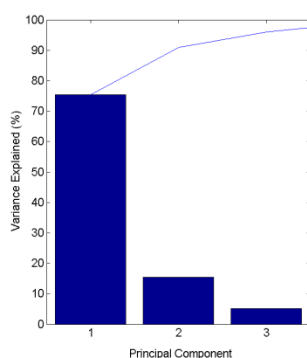


Fig. 54: Variance explained by different principal components. 1=PC1, 2=PC2 and 3=PC3.

The 3D-plot of the PC1, PC2 and PC3 shows that the wavelengths that mainly contribute to each component are : 500 nm to PC1, 700 nm to PC3, as shown in Fig. 55-a. By rotation of the 3D-plot, shown in Fig. 55-b, it is clear that 450 nm and 440 nm dominate the second principal component (PC2).

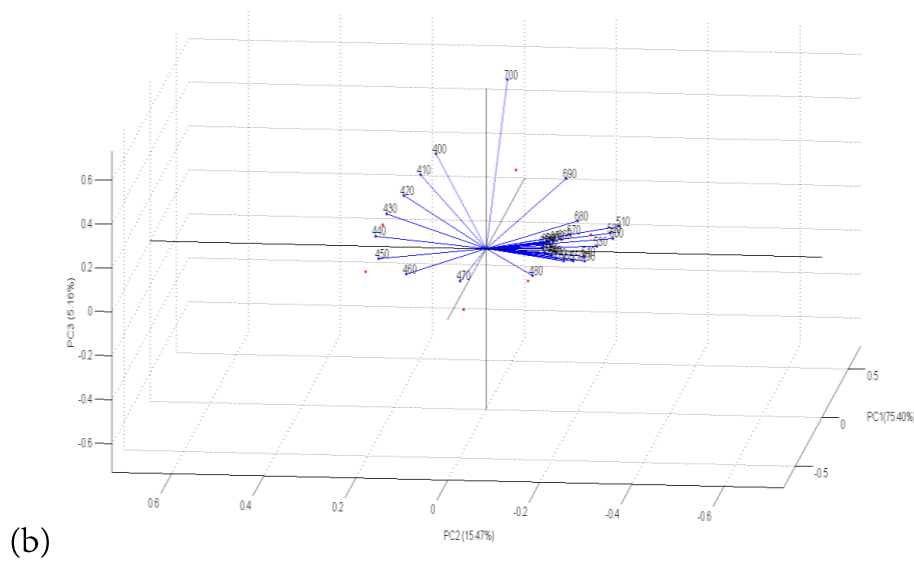
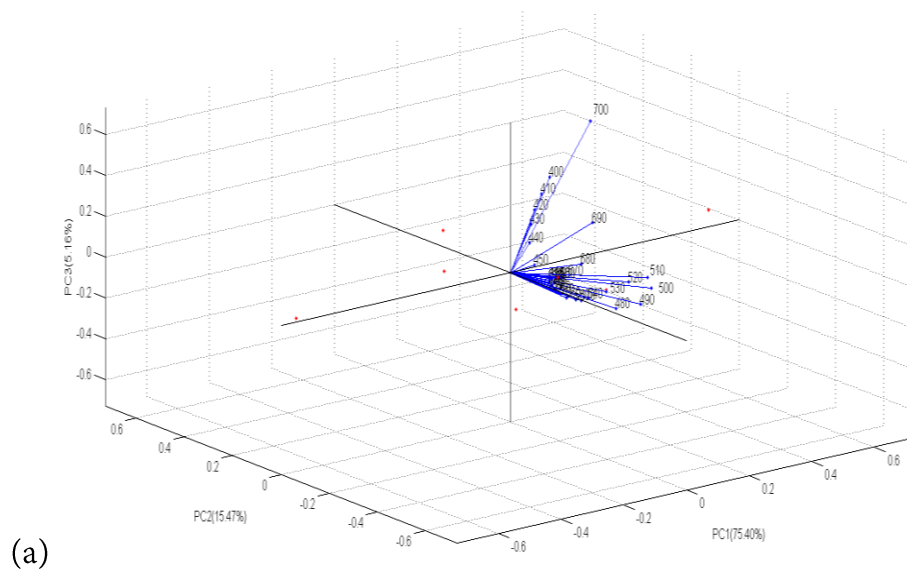


Fig. 55: The 3D-plot of the PC1, PC2 and PC3

Taking into account this result, we choose three images captured at 450 nm, 500 nm and 700 nm and we recombine them in a RGB image with this order: R=450, G=500 and B=700 nm, Fig. 56. It is really interesting that Cobalt Blue and Smalt, characterized by a similar chemical composition, show strong “false” colour differences. Cobalt Blue is a cobalt(II) oxide-aluminium oxide, $\text{CoO} \cdot \text{Al}_2\text{O}_3$, while Smalt is a glass containing SiO_2 (65%) + K_2O (15%) + Al_2O_3 (5%) + CoO (10%). Although, in principle they can be distinguished for the presence of Silica and Potassium oxide in Smalt, in paintings this is not always possible since these two compounds can be associated also to other pigments. With this image processing method, instead, it seems to be possible. Moreover, also ultramarine blue, $\text{Na}_{8-10}\text{Al}_6\text{Si}_6\text{O}_{24}\text{S}_{2-4}$, is clearly distinguished from Ultramarine Ash, although it presents a similar chemical composition; both are hardly detected with XRF due to the presence of elements with low atomic weight.

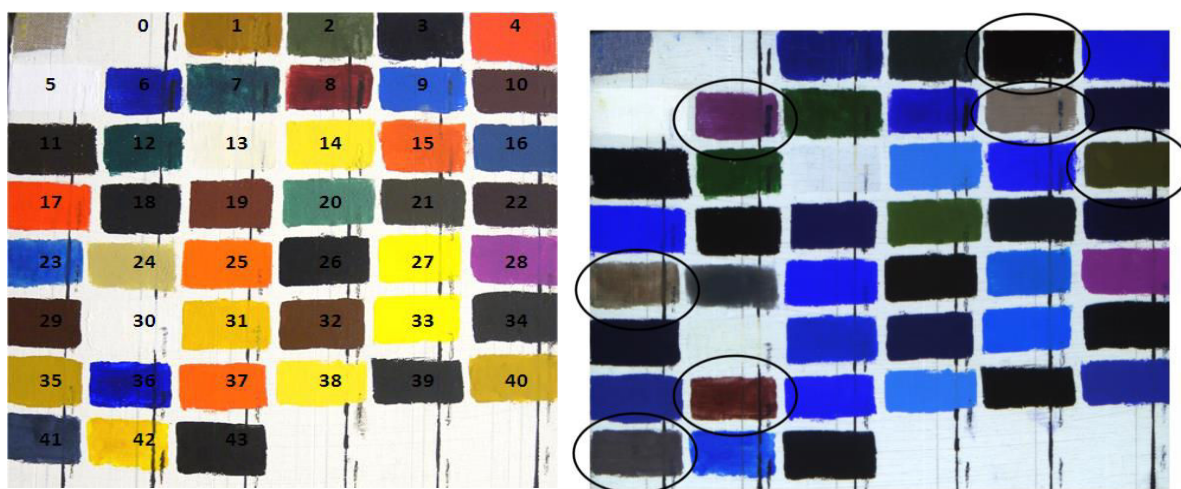


Fig. 56: Visible image (left panel) and “false” RGB image (right panel) of the pictorial layers spread on the lead white preparation. The “false” RGB image was obtained combining the images captured at 450 nm, 500 nm and 700 nm. The blue pigments are circled in black. Prussian Blue is in the position 3, Smalt in 6, Cobalt Blue in 9, Azurite in 16, Egyptian Blue in 23, ultramarine blue in 36 and Ultramarine Ash in 41.

Since this procedure could be influenced by the colour of a background layer, as we discussed in the previous sections, we followed the same acquisition procedure with the samples on microscope slides, changing the colour of the background support (in one case black in the other

one white). As shown in Fig. 57, the “false” RGB colour remains the same as in the image in Fig. 56. This means that the identification of the pigments with this method is independent with respect to whether there is white or black background, and thus it is not affected by a possible transparency of the tested material in the selected range (400-700 nm).

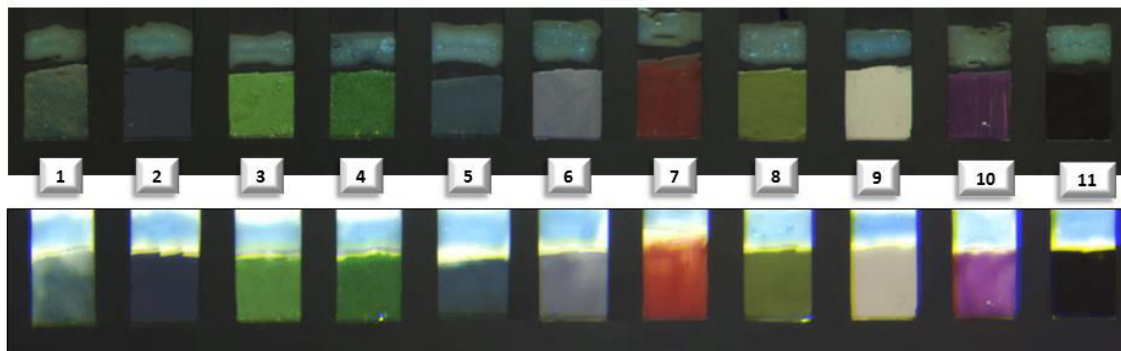


Fig. 57: “false” RGB images of the blue and green layers spread on microscope slide. Images obtained with a black and a white backgrounds, on the top and the bottom panels, respectively. The number corresponds to: 1 Egyptian Blue, 2 Verdaccio, 3 Malachite, 4 Verdigris, 5 Green Earth, 6 Ultramarine Ash, 7 ultramarine blue, 8 Azurite, 9 Cobalt Blue, 10 Smalt and 11 Prussian Blue.

Afterwards, some of the blue pigments were mixed with linseed oil to evaluate if it is possible to distinguish the pigments mixed with other binders by means of multispectral reflectance images. For this purpose we selected Prussian Blue, Ultramarine blue (Maimeri), Cobalt Blue, Ultramarine Ash, Smalt and Azurite; we added to the set also another Ultramarine blue pigment (Zecchi). We spread the pigment/oil mixtures on microscope slides trying to obtain a covering layer and a thin layer in the same swatch. The spectral behaviours of these pigments in either egg yolk or linseed oil are very similar, also changing the colour of the background support (in one case black in the other one white), except for the Smalt sample, Fig. 58. In fact, the reflectance spectra acquired on the entire set of Smalt samples laid on all the supports used, shown in Fig. 60, exhibits different ratios between the reflectance in the “blue” range and the “red-NIR range”. The values at 700 nm higher than those at 450 nm, explain the bluer aspect of the Smalt sample in oil shown in Fig. 58. Probably it is related to the thickness of the sample and/or to the binder used.

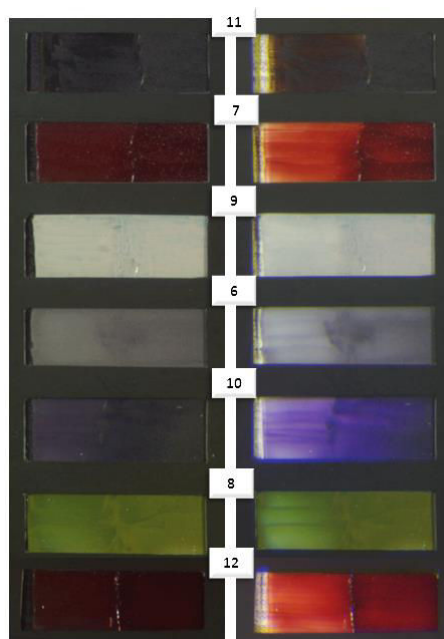


Fig. 58: “false” RGB images of the blue layers obtained mixing the pigment with oil, spread on microscope slide. Images obtained after lying the swatches on a black and a white backgrounds, on the left and the right panels, respectively. The number corresponds to: 11 Prussian Blue, 7 Ultramarine blue (Maimeri), 9 Cobalt Blue, 6 Ultramarine Ash, 10 Smalt, 8 Azurite, and 12 Ultramarine blue (Zecchi)

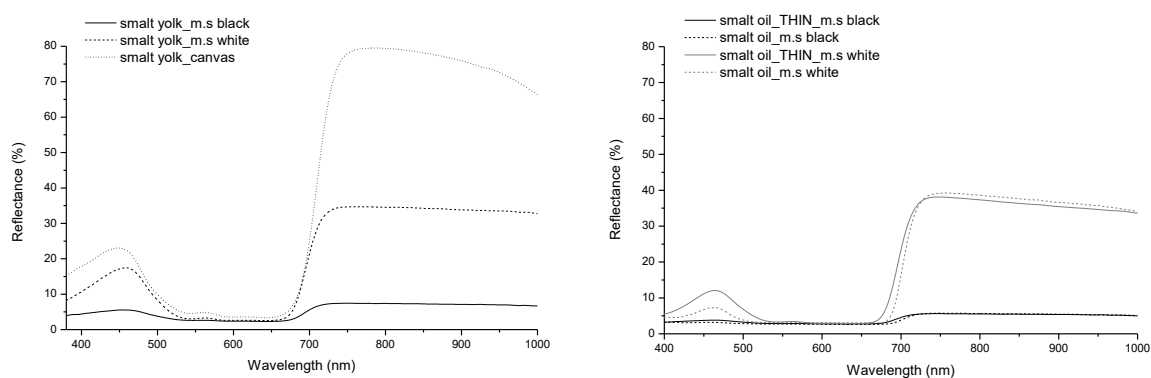


Fig. 59: FORS spectra of the Smalt pigment mixed in egg yolk (left panel) and linseed oil (right panel). The terms “m.s. white” is relative to the spectra obtained from the pictorial layer spread on microscope slide laid on a white support, “canvas” to the pictorial layer spread on a lead white layer, “m.s. black” to the pictorial layer spread on microscope slides laid on a black support, “THIN_m.s. black” is the spectra of a thin pictorial layer spread on microscope slides laid on a black support, “THIN_m.s. white” is the spectra of a thin pictorial layer spread on microscope slides laid on a white support.

Green pigments

By using the previous RGB recombination (450 nm, 500 nm and 700 nm), we can distinguish the “ferrous” green from the “cuprous” ones: Verdaccio and Green Earth appear blue while Malachite and Vergris are green-coloured, see Fig. 57. Despite this interesting result, we performed the PCA on the green pigments and we found that the first two principal components explain the 97.82% of the variance, as shown in Fig. 60 (left panel).

From the 2D-plot of the PC1 and PC2, we can notice that the maximum variance is at 540 nm for the PC1 and 500 nm for the PC2, all the other variables are located in the positive PC1-positive PC2 quadrant and are partially included in the bandwidth of the filters used, Fig. 60 (right panel).

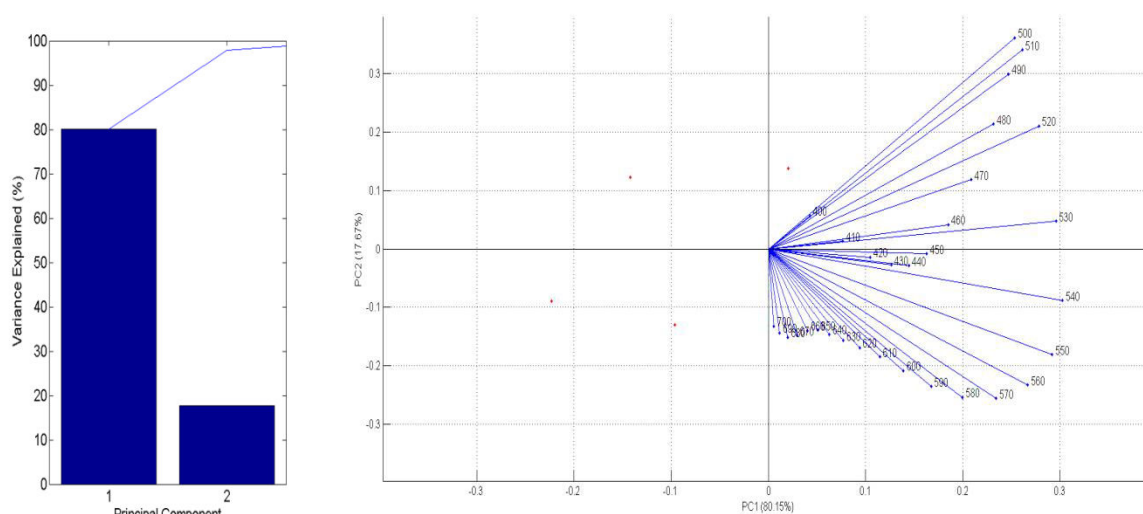


Fig. 60: Variance explained by different principal components. 1=PC1 and 2=PC2 (left panel). 2D-plot of the PC1 and PC2 (right panel)

To obtain the false RGB image, we also select the image at 470 nm, that contributes, in part, to the maximum variance. Recombining the images taken at 470 nm, 500 nm e 532 nm Vergris is clearly distinguished, as it appears as green colour, and Malachite too, as it appears as light blue, Fig. 61;

however the other green pigments are hardly distinguishable. This is probably related to the low spectral difference between the reflectance spectra of the samples, to our selection of the filters and to FWHM of the filters, as shown in Fig. 62, in which we report the transmittance of the filters and the reflectance spectra of the green pictorial layer in the same graph.

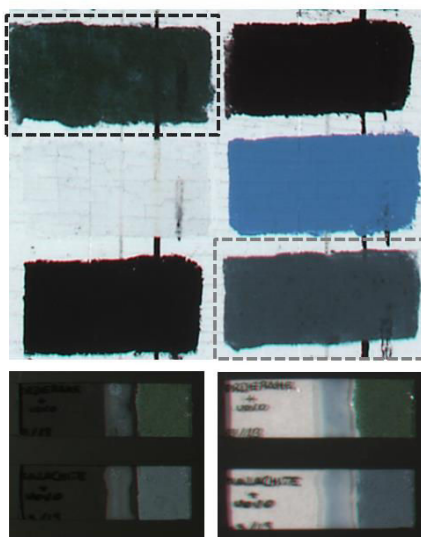


Fig. 61: “false” RGB images of the Verdigris and Malachite samples. On the top it is shown the “false” RGB image of the samples spread on the white lead layer in which Verdigris is the placed on top/left and Malachite on bottom/right. The “false” RGB images in the bottom panel are relative to the samples with a black background (left) and a white background (right).

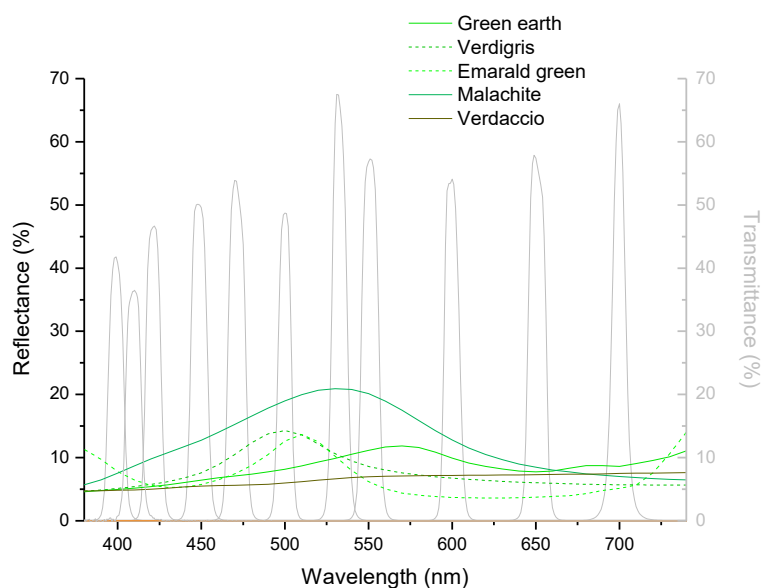


Fig. 62. Reflectance spectra of the green pictorial layers and the transmittance curves of the narrow-band filters employed

Yellow pigments

We performed the PCA of the yellow hue in the range 400-600 nm in order not to be influenced by the strong transparency of the yellow pigments at long wavelengths. We found that the first two principal components explain the 97.66% of the variance, Fig. 63.

We can notice that the maximum variance is at 550 nm for the PC1 and 490 nm for the PC2. To perform a false RGB image, we selected the images at 550 nm, 500 nm (that is the nearest to 490 nm) and also 532 nm, that contribute in part to the maximum variance. All the other variables are located in the positive PC1-positive PC2 quadrant and they are partially included in the bandwidth of the filters used.

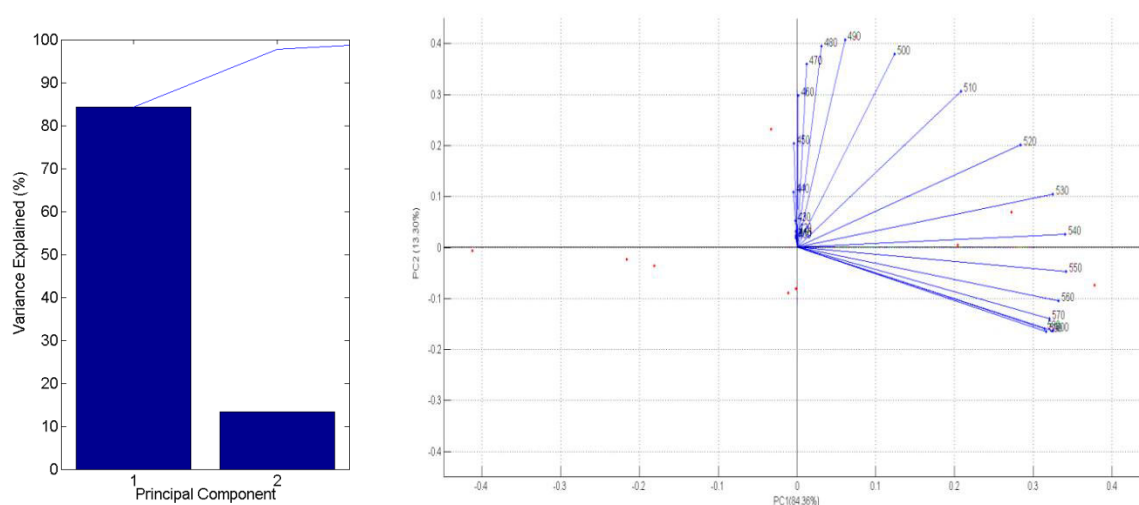


Fig. 63: Variance explained by different principal components. 1=PC1 and 2=PC2 (left panel) and the 2D-plot of the PC1 and PC2

In the future, it will be advisable to increase the number of filters and to use narrower band-pass ones in this region to improve the performances related to pigment identification. Nevertheless, in the “false” RGB image obtained from the combination of the filters at 550 nm, 532 nm and 500 nm, Fig. 48, the following specific spectral features can be noticed:

- The yellow pictorial layers prepared with pigments containing iron ions are well identified as brown hue.
- Lead-based pigments, like Lead-Tin and Naples Yellow appear light brown.
- Orpiment, Zinc and Cadmium Yellow can be confused. Litharge is the darkest due to its high state of degradation, as discussed in par. 1.1.4.3.
- Alike the green and the blue pigments, the yellow pigments spread on the microscope slides and put either on a black or on a white support, exhibit the same “false” RGB colours observed for the samples on canvas in Fig. 64, as shown in Fig. 65.

We also performed the PCA between 400 nm and 740 nm in order to evaluate if it is possible to discriminate better among the yellow pigments, including part of the NIR radiation. By analysing the 2-D plot of the PC1 and PC2 (97.87% of the variance), Fig. 66, we selected the images at 700 nm, 650 nm and 500 nm in this order to recombine the “false” RGB image, Fig. 67.

In this way, the Naples Yellow and Lead-Tin Yellow are discriminated well from Cadmium Yellow, Orpiment and Zinc Yellow, but it remains hard to distinguish between each other.

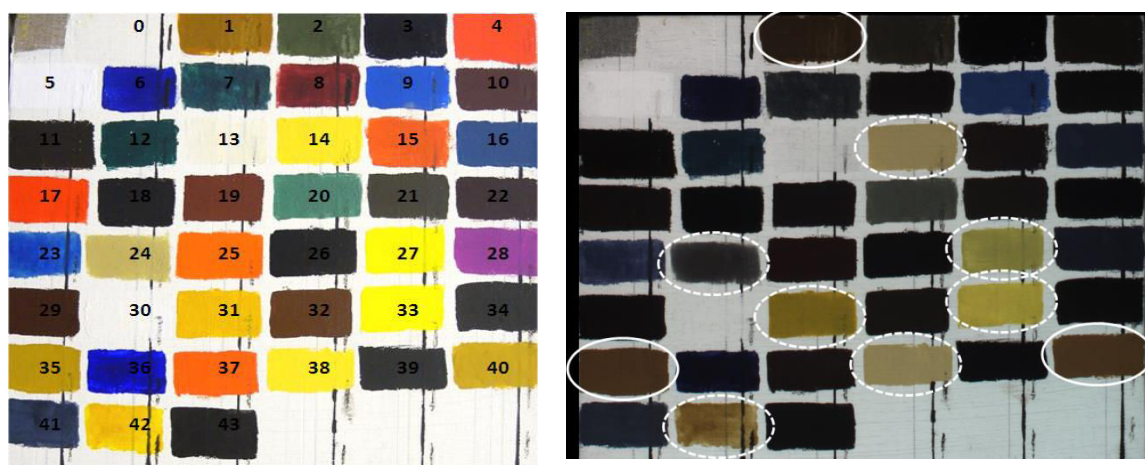


Fig. 64: Visible image (left panel) and “false” RGB image (right panel) of the pictorial layers spread on the lead white preparation. The “false” RGB image was obtained combined the images captured at 550, 532 and 500. The yellow pigments containing iron ions are circled in solid lines (Raw Sienna Earth in position 1, Mars Yellow in position 35 and Yellow Ocre in position 40), the other yellow samples are circle in dash lines (Naples Yellow 14, Litharge 24, Zinc Yellow 27, Orpiment 31, Cadmium Yellow 33, Lead-Tin Yellow 38, Stil de Grain 42) .

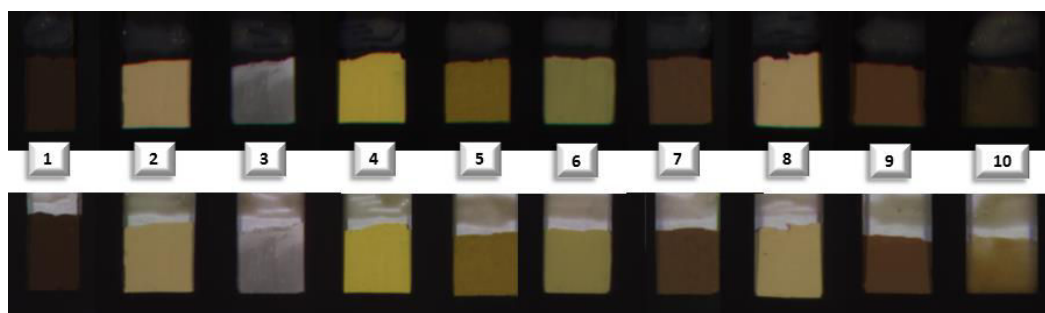


Fig. 65: “False” RGB images of the yellow layers spread on microscope slide. Images obtained with a black and a white backgrounds, on the top and the bottom panels, respectively. The number corresponds to: 1 Raw Sienna Earth, 2 Naples Yellow, 3 Litharge, 4 Cadmium Yellow, 5 Orpiment, 6 Zinc Yellow, 7 Mars Yellow, 8 Lead-Tin Yellow, 9 Yellow Ochre, 10 Stil de Grain.

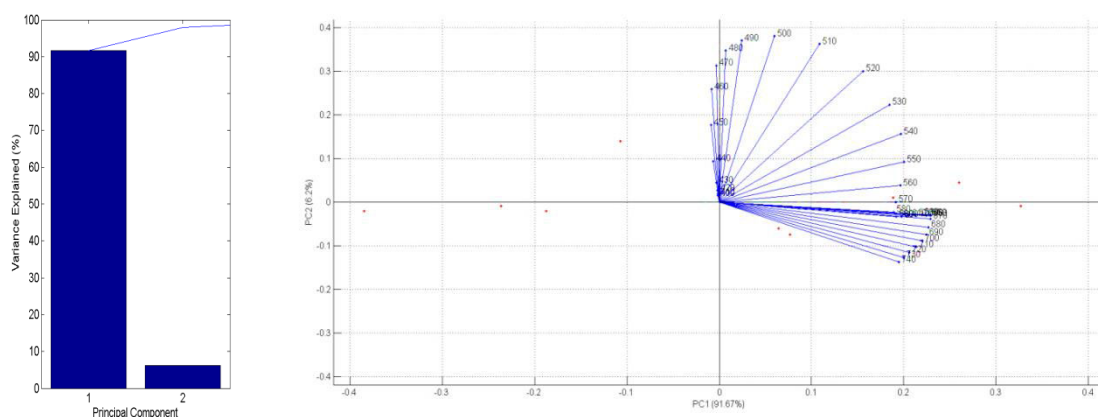


Fig. 66: Variance explained by different principal components. 1=PC1 and 2=PC2 (left panel). 2D-plot of the PC1 and PC2 (right panel).



Fig. 67: Visible image (left panel) and “false” RGB image (right panel) of the pictorial layers spread on the lead white preparation. The “false” RGB image was obtained combined the images captured at 700, 650 and 500. The pictorial layers circled correspond to Raw Sienna Earth in position 1, Naples Yellow 14, Litharge 24, Zinc Yellow 27, Orpiment 31, Cadmium Yellow 33, Mars Yellow in position 35, Lead-Tin Yellow 38, Yellow Ochre in position 40 and Stil de Grain in 42.

Red-orange and brown pigments

The PCA performed between 400 nm and 650 nm showed that the first two principal components explain the 97.78% of the variance, Fig. 68. The 2D-plot of PC1-PC2 displayed that the maximum variance is at 650 nm for the PC1 and 440 nm for the PC2, Fig. 68. We selected the images at 650 nm, at 450 nm (that is the filter with the wavelength nearest to 440 nm) and also 600 nm, that contribute in part to the maximum variance, to obtain the false RGB image shown in Fig. 69, in this order R=650 nm, G=600 nm and B=450 nm.

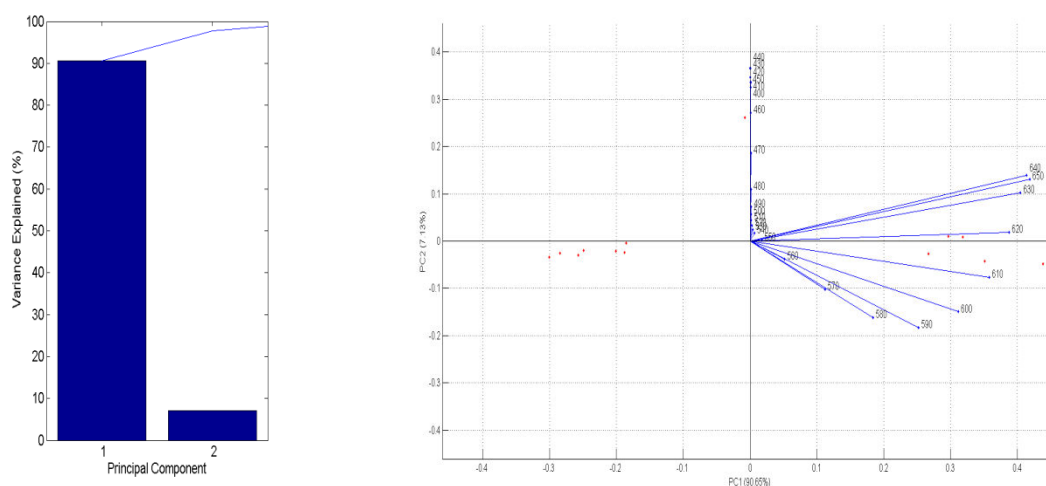


Fig. 68: Variance explained by different principal components. 1=PC1 and 2=PC2 (left panel) and the 2D-plot of the PC1 and PC2

The choice of these filters does not allow us to identify properly the red pigments. Probably this is due to the 50 nm steps for sampling the multispectral images and to the FWHM of the transmission of the filters, which does not permit a sufficiently selective recognition, as shown in Fig. 70, except for the violet hue.

Thus, as for the yellow samples, we tried to extend the wavelength range and we performed the PCA between 400 and 740 nm. By the observation of the PC1 and PC2 (97.51% of the variance),

Fig. 71, we selected and combined the images at 700 nm, 650 nm and 450 nm in this order, to obtain the “false” RGB image shown in Fig. 72.

However, the use of the broader wavelength range in the PCA analysis does not improve the identification of the red-orange hue swatches.

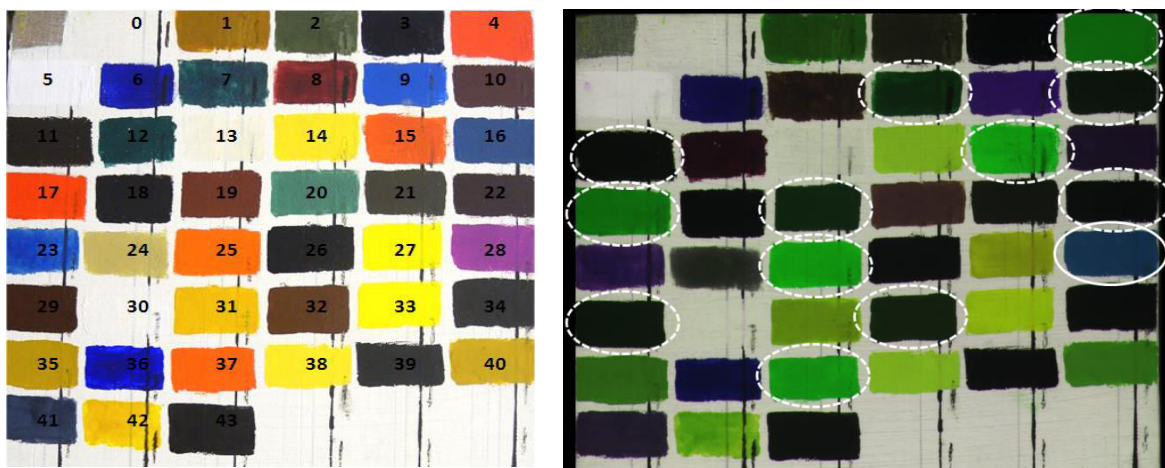


Fig. 69: Visible image (left panel) and “false” RGB image (right panel) of the pictorial layers spread on the lead white preparation. The “false” RGB image was obtained combined the images captured at 650, 600 and 450. The pictorial layers circled correspond to Cinnabar in the position 4, Madder Lake in the position 8, Caput Mortum in the position 10, Burnt Umber in the position 11, Minium in the position 15, Chrome Red in the position 17, Hematite in the position 19, Alizarin Crimson Lake in 22, Cadmium Orange in 25, Cobalt Violet in 28, Mars Brown in 29, Manganese Brown in 32, Saturn Red in 37.

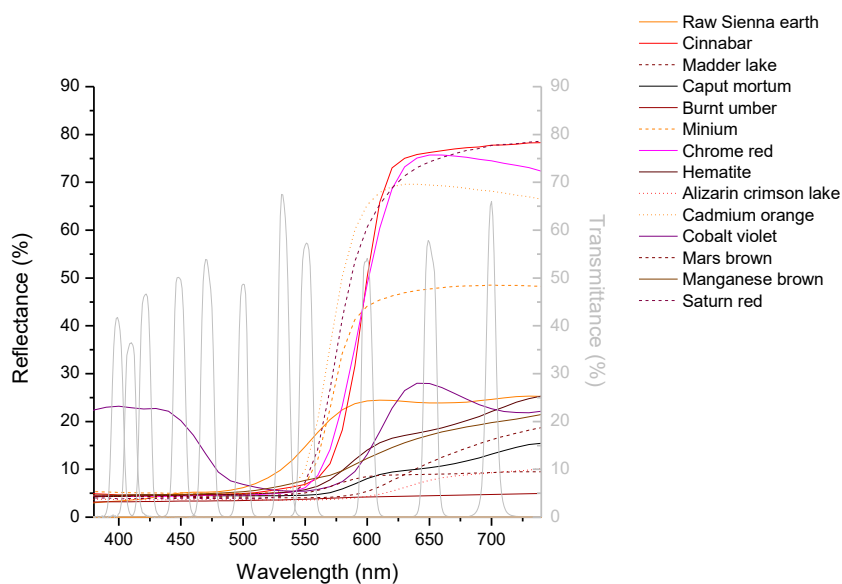


Fig. 70: Reflectance spectra of the red-orange-brown pictorial layers and the transmittance curves of the narrow-band filters employed

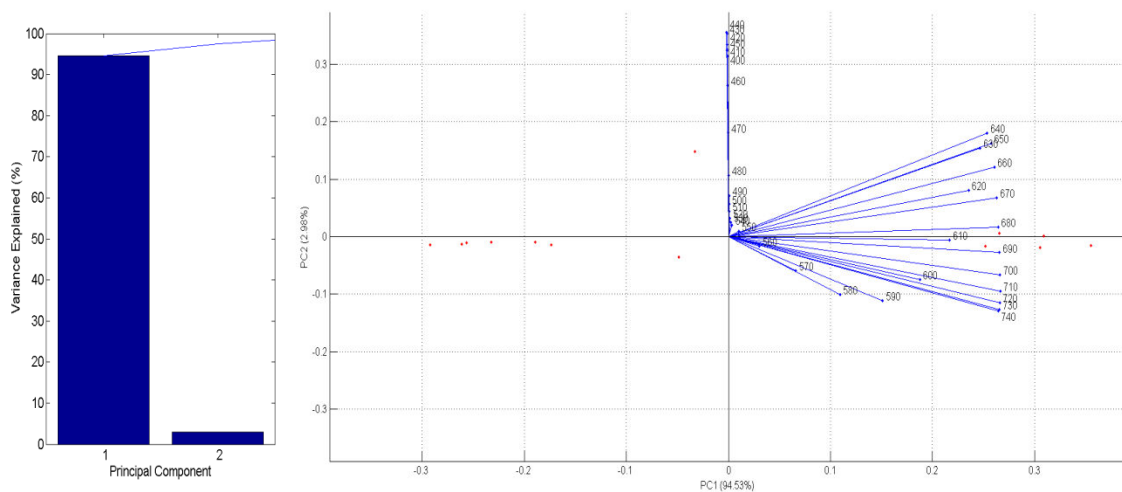


Fig. 71: Variance explained by different principal components. 1=PC1 and 2=PC2 (left panel) and the 2D-plot of the PC1 and PC2



Fig. 72: Visible image (left panel) and "false" RGB image (right panel) of the pictorial layers spread on the lead white preparation. The "false" RGB image was obtained combined the images captured at 700, 650 and 450. The pictorial layers circled correspond to Cinnabar in the position 4, Madder Lake in the position 8, Caput Mortum in the position 10, Burnt Umber in the position 11, Minium in the position 15, Chrome Red in the position 17, Hematite in the position 19, Alizarin Crimson Lake in 22, Cadmium Orange in 25, Cobalt Violet in 28, Mars Brown in 29, Manganese Brown in 32, Saturn Red in 37.

2.1.3.5. Fluorescence spectra

The entire set of pictorial layers was analysed by fluorescence spectroscopy with the Avantes spectrometer, exciting at 365 nm.

We compared the fluorescence spectra of the pictorial samples prepared on the lead-white layer and those laid on the black support and we found a decrease of the fluorescence intensity of the stratified layers, except for the blue pigments layers and other pictorial layers, such as Green Earth, Verdigris, Malachite, Verdaccio and Raw Sienna Earth. In this section we report two examples in Fig. 73, the other data are reported in Appendix C.

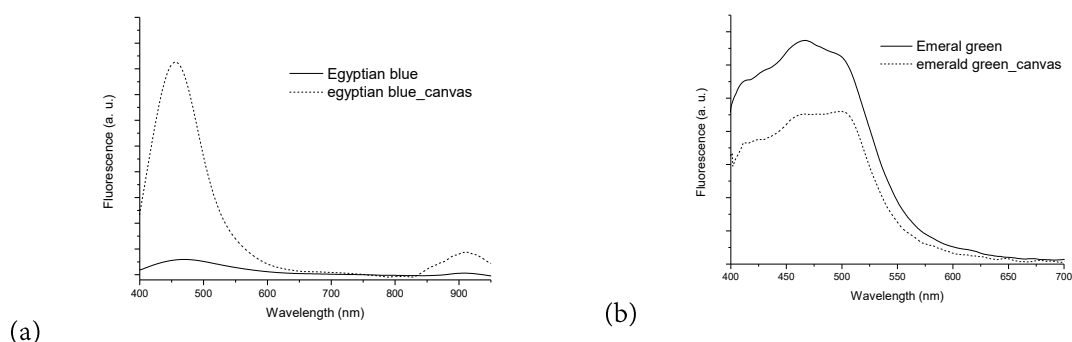


Fig. 73: Fluorescence spectra of Egyptian Blue (a) and Emerald Green (b) measured on a black support and on Lead White layer (canvas)

These trends are probably due to the UV and VIS transmittance of the upper layers: the UV radiation might penetrate over the upper layer and excites the Lead White layers, the induced fluorescence of this background can cross the upper layer and reaches the spectrometer. This means that UV radiation can excite the internal layers despite its low penetration depth. Likewise, the back fluorescence of the upper layer can illuminate the background and produces a diffused or reflected light. In this section we present the results obtained on the pictorial layers spread on the lead white layer, because this situation better simulates the stratigraphy of real paintings.

The fluorescence emission of the egg yolk has been discussed in the previous chapter, (Part II, chap. 1). This emission changes in relation with the ageing method, however the maximum of the

fluorescence spectra is at 416 for samples storage in darkness at 25°C for 10 days and at 464 nm for photodegraded samples after 222 hours.

The fluorescence spectra of the blue pictorial layers, presented in Fig. 74 Fig. 56, show a broad band with a maximum around 450 nm, that can be attributed to the binder and/or to the pigment-binder system. In fact, we suppose that this spectral behavior is probably a combination between the fluorescence emission of the binder and that of the blue pigments due to the fact that most of the blue pigments exhibit an intense fluorescence emission in this range. Some blue pigments can be, in such conditions, distinguished by the intensities of their fluorescence. However, such parameter is not pertinent for an identification on a painting as the intensity of a band is strongly influenced by several aspects: the type, the quantity, the ageing of the binders, and the thickness of the pigment layer.

However, among the selected blue pigments, we can perfectly discriminate the Egyptian Blue layer since its fluorescence spectrum shows a characteristic band at 911 nm.

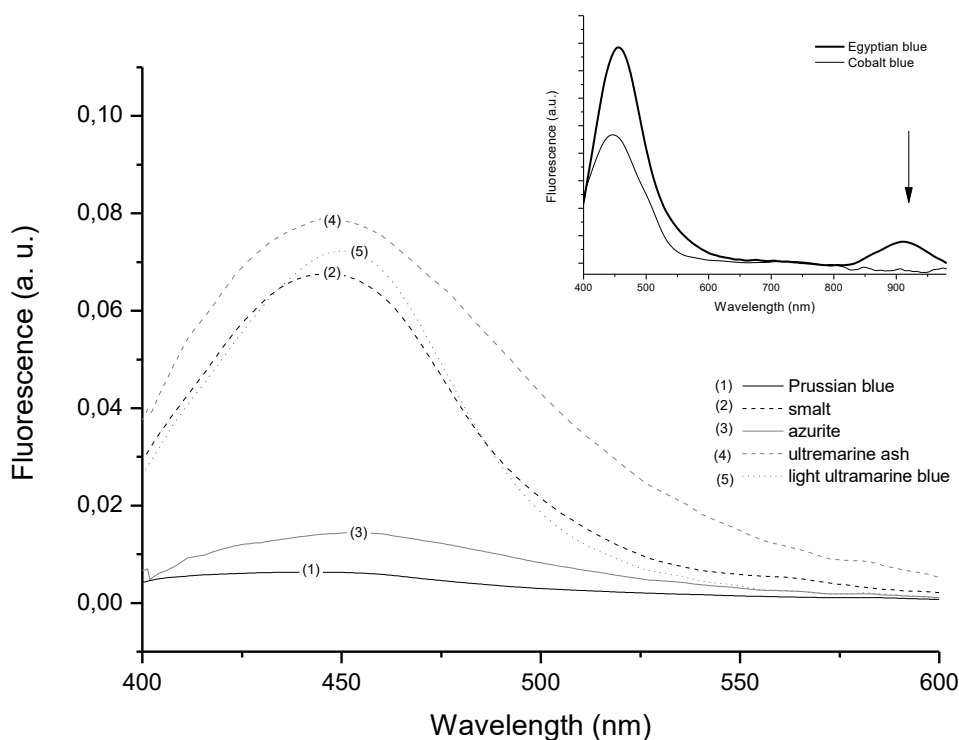


Fig. 74: Fluorescence spectra of blue pigments with egg yolk

The fluorescence spectra of the green pigments, presented in Fig. 75, show a broad band with a maximum around 450 nm, owing to the fluorescence of the binder. The Emerald Green spectrum is different with the presence of another strong band at about 470-500 nm.

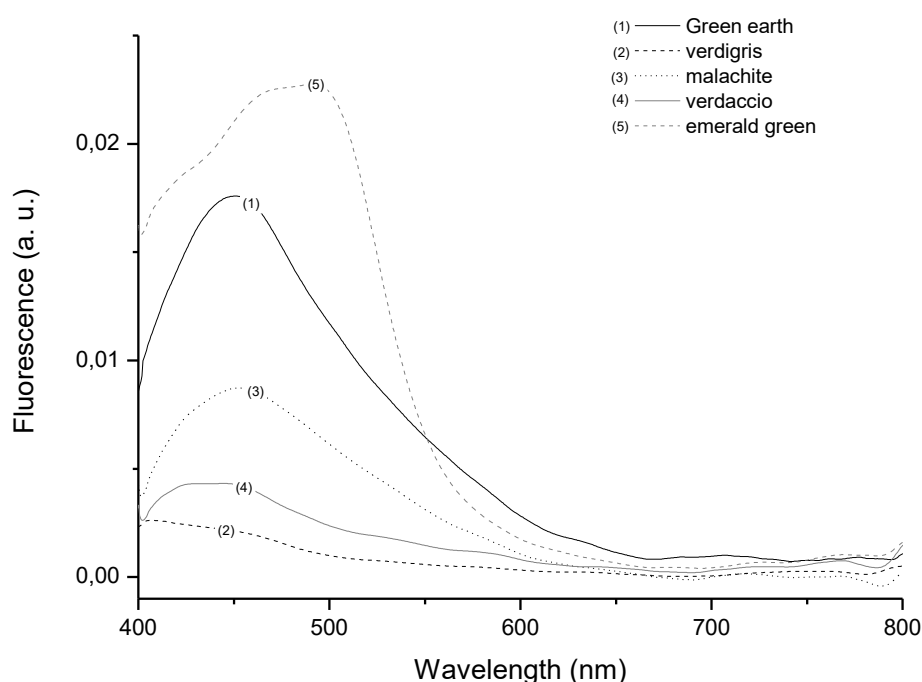


Fig. 75: Fluorescence spectra of green pigments with egg yolk, exciting at 365 nm

For the yellow, orange, red and brown pictorial layers it is hard to distinguish the true fluorescence emission from the reflected and/or scattered light by the coloured pigment [Verri G. et al. (2008)]. In fact, the fluorescence band at short wavelengths can be attributed to the binder while the second peak can be associated with the reflected and/or scattered light from the pigment due to interaction between the photons emitted from the binder and the surrounding pigment (Part I, chap.1.3.2), Fig. 76 and Fig. 77.

However, four pictorial layers exhibit spectral features that can be assigned to the fluorescence of the pigment. The fluorescence spectrum of Stil de Grain, which is a dye, shows a strong band at about 550 nm and a shoulder at 450 nm (probably the fluorescence of the binder), Cadmium Yellow and Cadmium Orange present a fluorescence band in the IR with a maximum at about 850 nm, Fig. 60. and 61. These two pigments can be distinguished for the shape of the IR fluorescence band, since its FWHM for Cadmium Yellow is higher than that of Cadmium Orange, Fig. 78 and Fig. 79. Finally, the Cobalt Violet fluorescence spectrum presents two peaks at 440 nm (strong) and 620 nm (weak), Fig. 79.

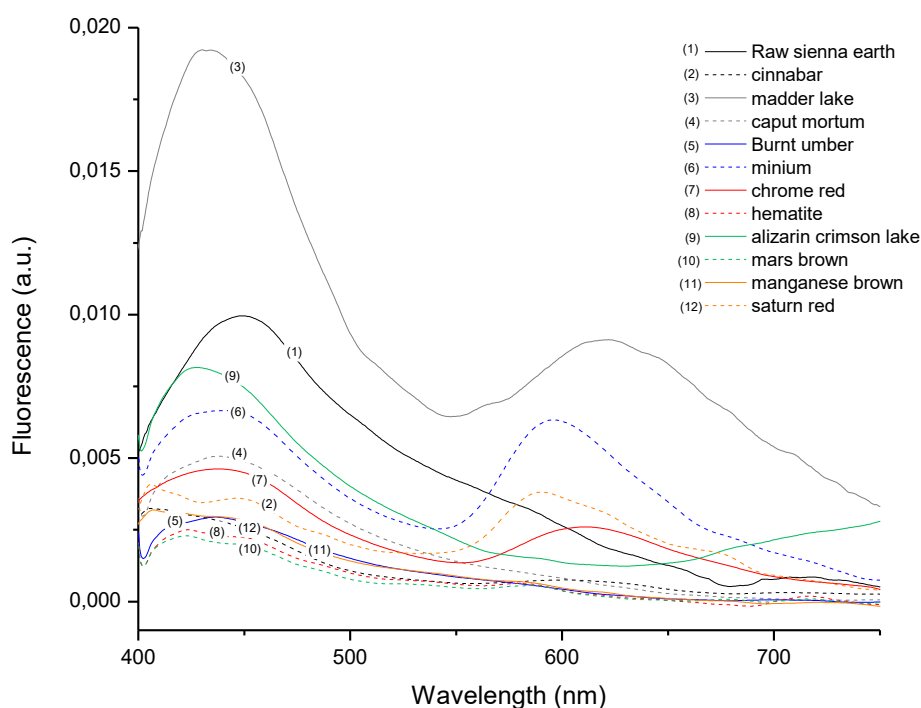


Fig. 76: Fluorescence spectra of orange, red and brown pigments with egg yolk

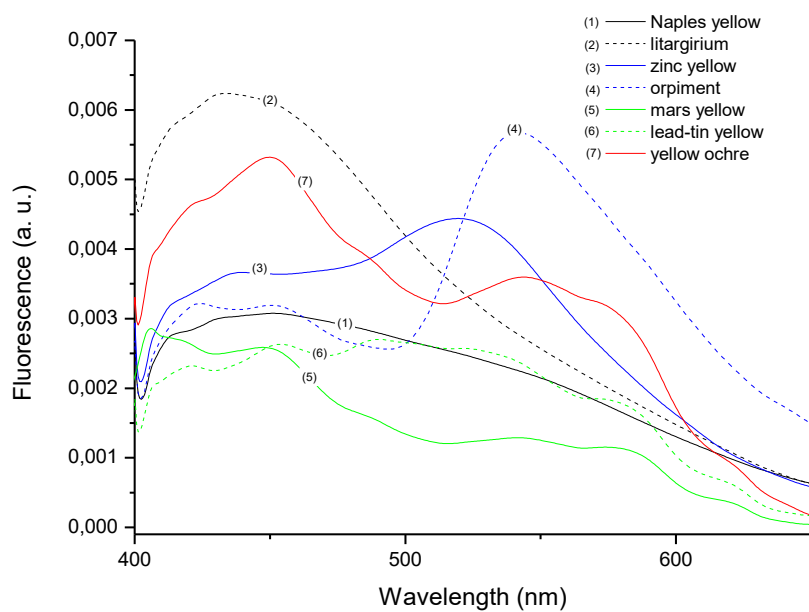


Fig. 77: Fluorescence spectra of yellow pigments with egg yolk

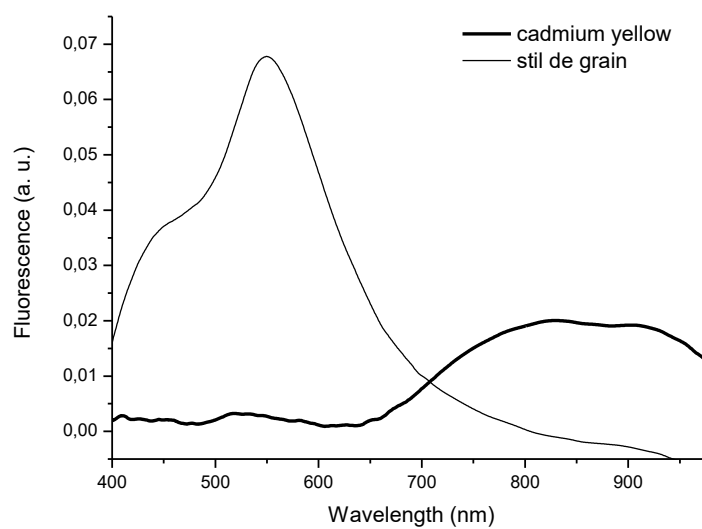


Fig. 78: Fluorescence spectra of Cadmium Yellow and Stil de Grain pigments with egg yolk

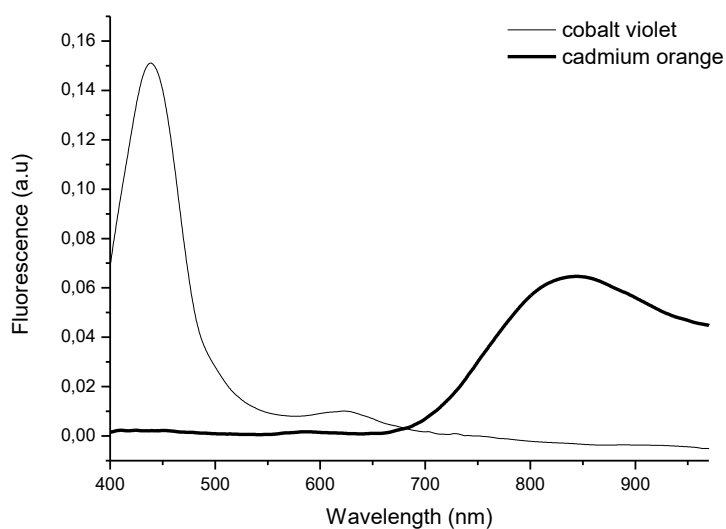


Fig. 79: Fluorescence spectra of Cobalt Violet and Cadmium Orange pigments with egg yolk

The fluorescence spectra of white pigments are shown in Fig. 80. The fluorescence spectra of Lithopone and Lead white mixed with egg yolk show a similar spectral behaviour with a broad band the maximum of which is at 450 nm. The fluorescence spectrum of Zinc White exhibits a weak band peaking at 425 nm and a second, stronger one at 520 nm; that of Titanium White shows a broad band between 400 nm and 470 nm, Fig. 80. We will discuss in detail Zinc White, Lead white and Titanium White in the paragraphs 2.2 and 2.3 in this chapter.

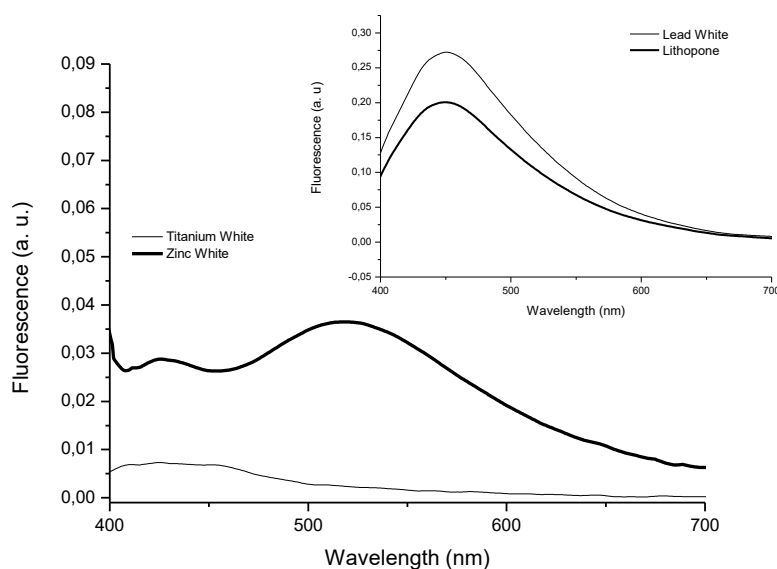


Fig. 80: Fluorescence spectra of lead white, Lithopone, titanium and zinc pigments with egg yolk, exciting at 365 nm.

Some black pigments exhibit a broad band in the fluorescence spectra, peaking at 435 nm for the Vine Black and Ivory Black about 440 nm, that we assign to the fluorescence of the binder, Fig. 81. The other black pigments present a weak maximum at 410 nm.

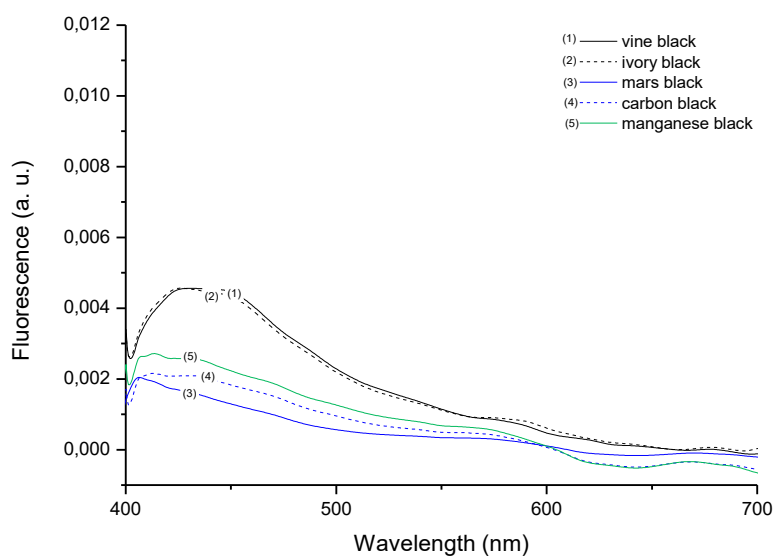


Fig. 81: Fluorescence spectra of black pigments in egg yolk

2.1.3.6. Multispectral UV-fluorescence imaging

We acquired the images of the fluorescence at 450 nm, 470 nm, 500 nm, 532 nm, 550 nm, 600 nm, 650 nm, 700 nm, 750 nm, and 800 nm, shown in Fig. 82. Most of the fluorescence emissions, that we measured with the spectrometer, are hardly detectable with the CCD system, due to the long working distance and the low fluorescence intensity emitted from the pictorial layers.

Cadmium Yellow and Cadmium Orange, corresponding to the numbers 33 and 25 respectively, are the only samples exhibiting an intense fluorescence at 750-800 nm. The Egyptian Blue presents a fluorescence band with a maximum in the IR region at 900 nm, that cannot be detected in our multispectral images.

Among the pictorial layers emitting in the visible range, the white pictorial layers exhibit an intense fluorescence up to 600 nm, with the exception of Titanium White (number 5 in the Fig. 82), which appears dark. The other fluorescent pictorial layers are well recognized by combining two sets of images in two “false” RGB images: the first one obtained from the images taken at 450 nm, 470 nm and 500 nm and the second one merging the images taken at 500 nm, 532 nm and 550 nm. We can individuate the fluorescence of Smalt, Cobalt Blue, Emerald Green, Egyptian Blue, violet blue, ultramarine blue, Ultramarine Ash and Stil de Grain as shown in Fig. 83, however Smalt and Ultramarine blue are hardly distinguishable.

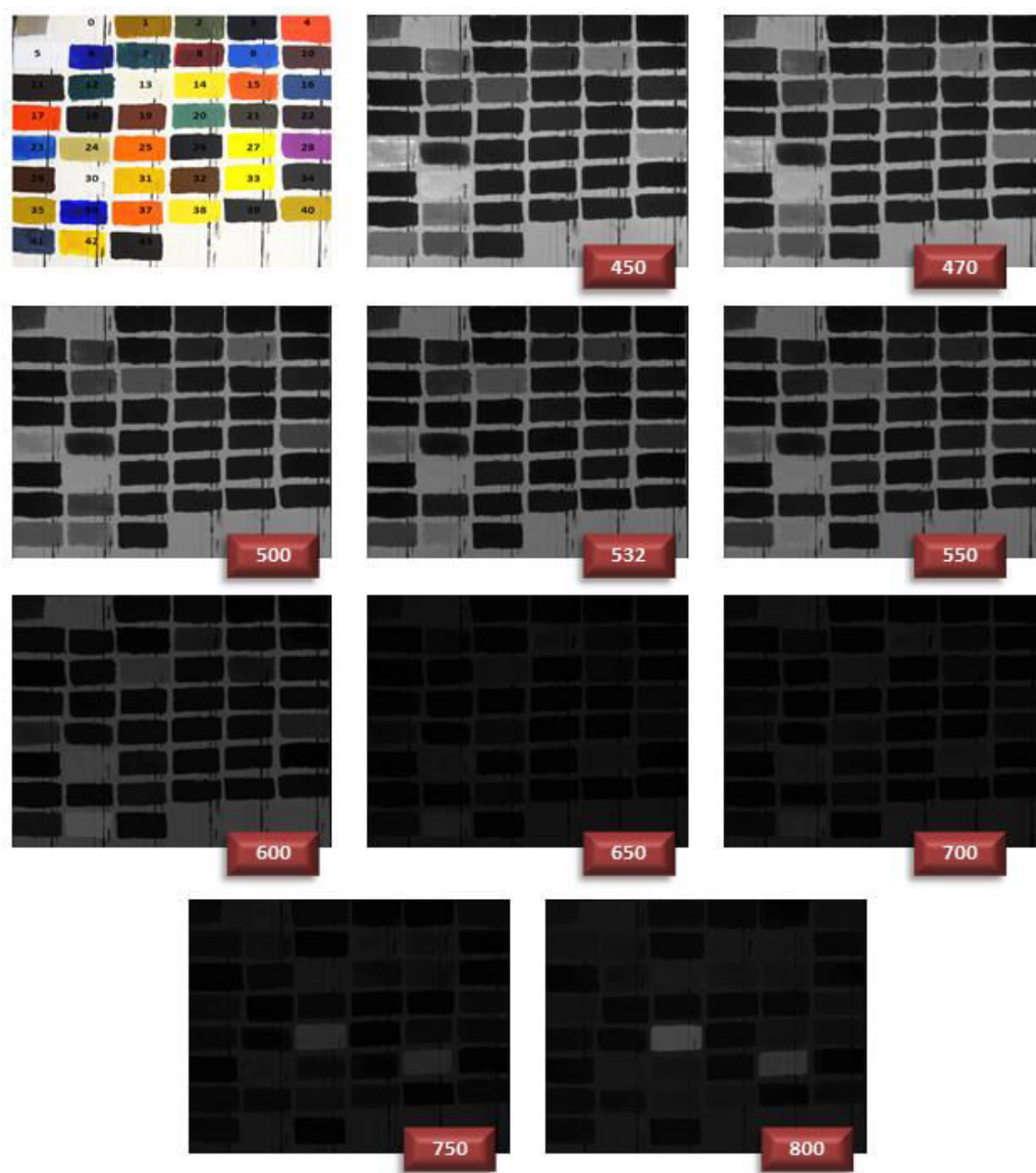


Fig. 82: Visible image and Multispectral UV fluorescence images of the forty-four pictorial layers

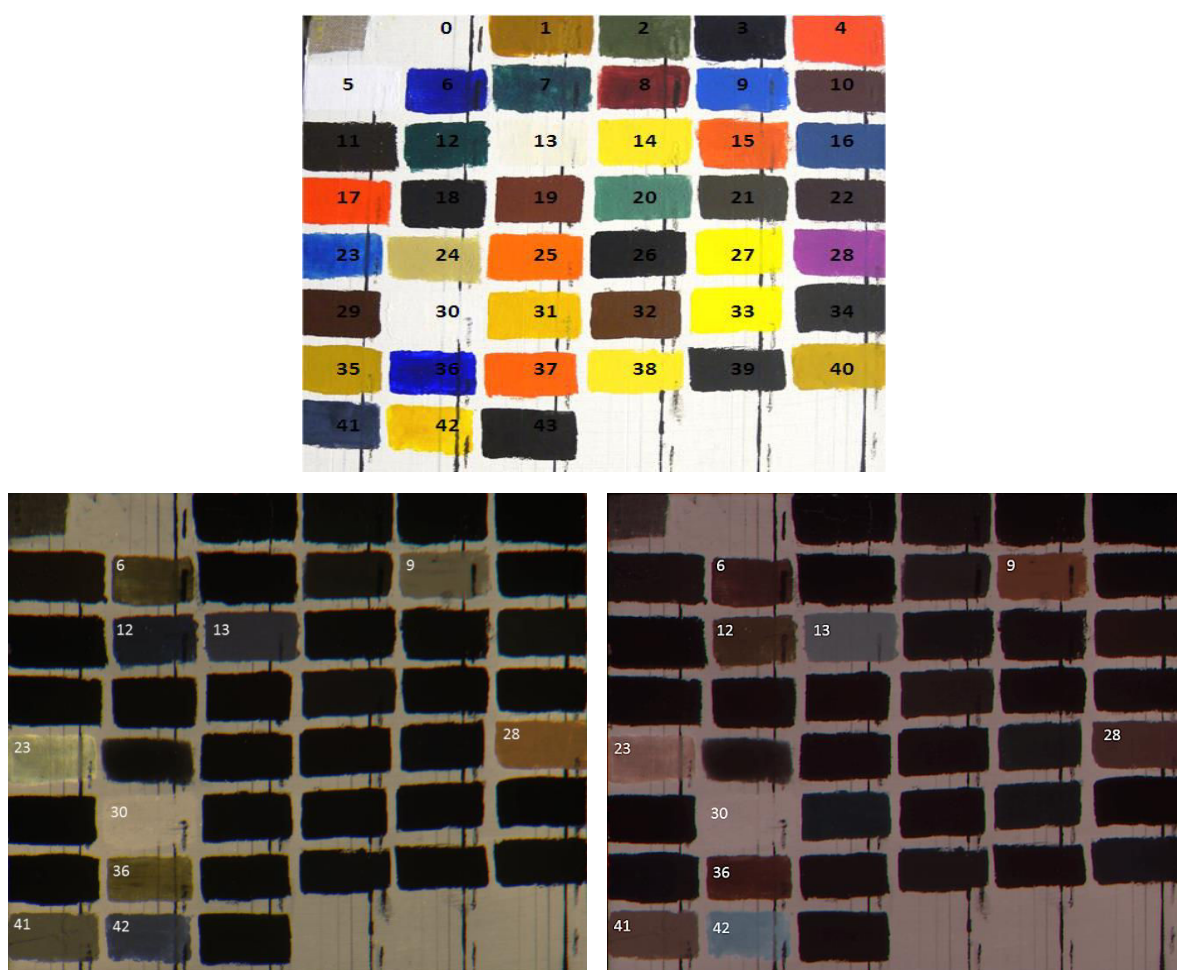


Fig. 83: Visible image (top panel) and “false” RGB images of the fluorescence emission of the pictorial layers spread on the lead white preparation (bottom panel). The “false” RGB image shown in the left panel was obtained combined the images captured at 450 nm, 470 nm and 500 nm and that in the right panel is the combination of fluorescence the images taken at 500 nm, 532 nm and 550 nm. The pictorial layers correspond to Smalt in the position 6, Cobalt Blue in the position 9, Emerald Green in the position 12, Zinc White in the position 13, Egyptian Blue in the position 23, violet blue in the position 28, Lithopone in the position 30, ultramarine blue in the position 36, Ultramarine Ash in the position 41 and Stil de Grain in the position 42.

2.1.3.7. Multispectral near-infrared imaging

Multispectral Near Infrared Imaging was performed on the forty-four pictorial layers spread on the lead white layer onto which we traced lines with different materials: Lead tip, a metal tip that produces an incision besides leaving a dark trace, charcoal, coal ink and iron gall ink, as shown in Fig. 37.

We performed reflectography infrared imaging by using four filters: two long-pass filters at 720 nm and 1000 nm, respectively, and two narrow-band filters at 800 nm and 900 nm. The images are shown in Fig. 84 where also the visible image obtained with a band-pass filter that cuts both UV and IR radiations is presented for comparison.

The results are summarized in Tab.3, in which we report for each pigment which lines can be observed when changing the filters used to acquire the images. In most cases, the inks are easily distinguished due to the high contrast between their high absorbance and the high reflectance of the back layer; the visualization of other materials is strongly dependent on the transparency of the upper-layer.

As expected, we can visualize better the under-drawings at longer wavelengths; this aspect is related to the increase of the penetration power of the IR radiation. However, some pigments remain highly absorbent such as Prussian Blue, Verdigris, Caput Mortum, Burnt Umber, Azurite, Vine Black, Hematite, Malachite, Verdaccio, Ivory Black, Mars Brown, Mars Black, Carbon Black and Manganese Black.

Comparing the image taken with the long-pass filter at 720 nm with those taken with narrow-pass filters (we can consider the long-pass filter at 1000 nm as a band-pass filter due to the sensitivity drop at about 1050 nm of the CCD sensor), we can state that the visualization of the traced lines is more detailed with a selection of narrow spectral intervals rather than an integrated image of a large VIS-IR range used for the contribution of the residual visible part of the spectrum and for blurring effect due to the variation of the focal length of the optical system.

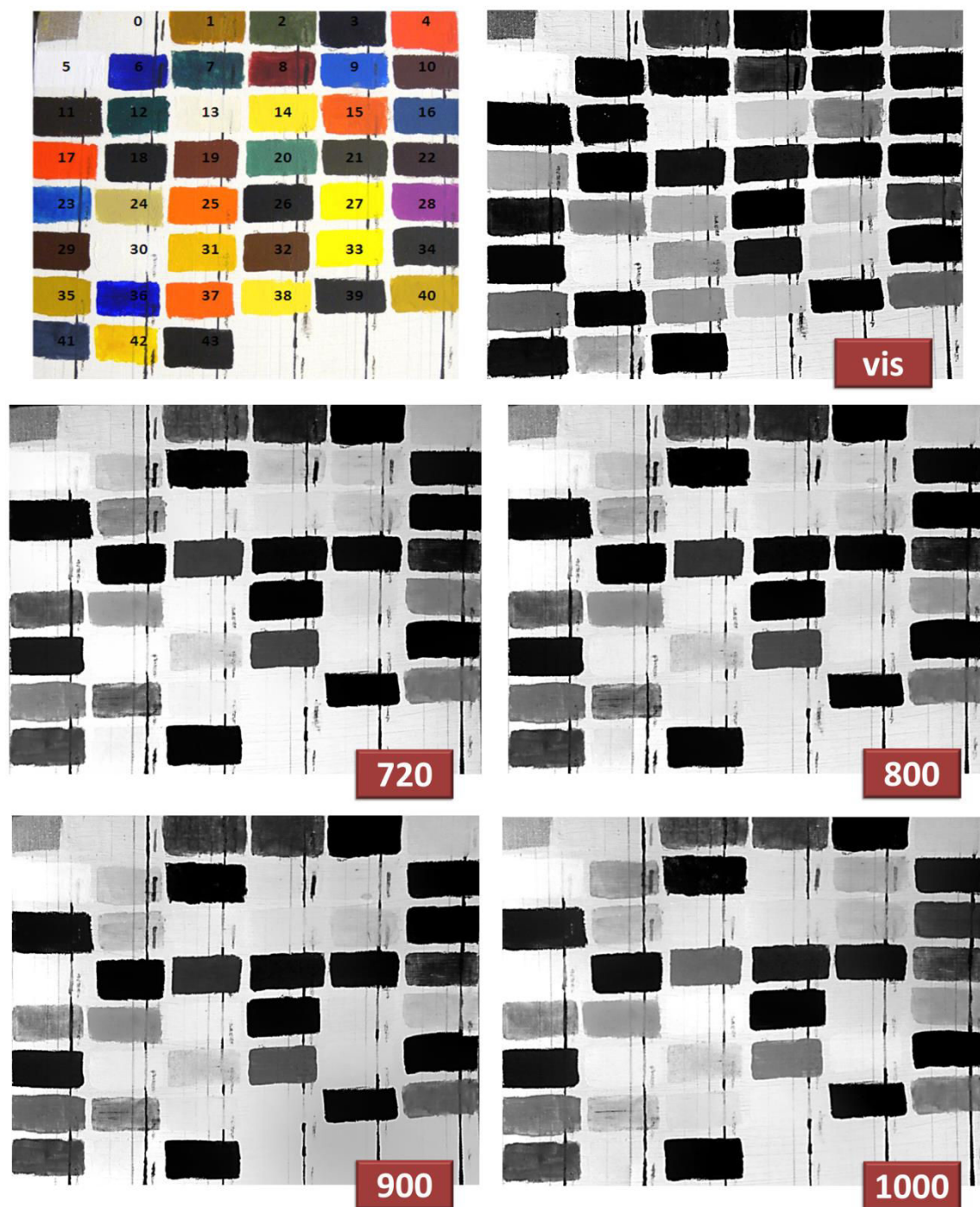


Fig. 84: Visible image and Multispectral NIR images of the forty-four pictorial layers

Tab. 3: Visibility of lines under the pictorial layers by using different filters. “A” corresponds to the metal Lead tip line, “B” to the incision, “C” to the charcoal line, “D” to the coal ink and “E” to the iron gall ink. the “w” indicates a week visualization.

		VIS	720 nm	800 nm	900 nm	1000 nm
1	Raw Sienna Earth	D, E	B, C, D, E	B, C, D, E	B, C, D, E	B, C, D, E
2	Green Earth	D, E	B(w), C(w), D, E	B(w), C(w), D, E	B(w), C(w), D, E	B, C, D, E
3	Prussian Blue	n. o.	n. o.	n. o.	n. o.	n. o.
4	Cinnabar	D(w), E	D(w), E	B(w), C(w), D (w), E (w)	B(w), C(w), D (w), E (w)	B(w), C(w), D (w), E (w)
5	Titanium White	B(w), C(w), D (w), E (w)	B, C, D, E	B, C, D, E	A, B, C, D, E	A, B, C, D, E
6	Smalt	D(w), E(w)	C, D, E	B(w), C, D, E	A(w), B, C, D, E	A(w), B, C, D, E
7	Verdigris	n. o.	n. o.	E(w)	E(w)	D(w), E(w)
8	Madder Lake	B(w), C(w), D, E	B, C, D, E	B, C, D, E	B, C, D, E	B, C, D, E
9	Cobalt Blue	B(w), C(w), D, E	B, C(w), D, E	B, C, D, E	A, B, C, D, E	A, B, C, D, E
10	Caput Mortum	n. o.	n. o.	n. o.	n. o.	n. o.
11	Burnt Umber	n. o.	n. o.	n. o.	n. o.	n. o.
12	Emerald Green	n. o.	C, D, E	B(w), C, D, E	C, D, E	C, D, E
13	Zinc White	A(w), B, C, D, E	A(w), B, C, D, E	A(w), B, C, D, E	A(w), B, C, D, E	A(w), B, C, D, E
14	Naples Yellow	C(w), D(w), E(w)	A(w), C(w), D(w), E(w)	C, D, E	A(w), C, D, E	A(w), C, D, E
15	Minium	B, C, D, E	A, B, C, D, E	A, B, C, D, E	A, B, C, D, E	A, B, C, D, E
16	Azurite	n. o.	n. o.	n. o.	n. o.	n. o.
17	Chrome Red	A, B, C, D, E	A, B, C, D, E	A, B, C, D, E	A, B, C, D, E	A, B, C, D, E
18	Vine Black	n. o.	n. o.	n. o.	n. o.	n. o.
19	Hematite	n. o.	n. o.	n. o.	n. o.	n. o.
20	Malachite	n. o.	n. o.	n. o.	n. o.	n. o.
21	Verdaccio	n. o.	n. o.	n. o.	n. o.	n. o.
22	Alizarin Crimson Lake	n. o.	D, E	D, E	B(w), C, D, E	A, B(w), C, D, E
23	Egyptian Blue	B, C, D, E	B, C, D, E	B, C, D, E	B, C, D, E	B, C, D, E
24	Litharge	C, D, E	C, D, E	C, D, E	C, D, E	C, D, E
25	Cadmium Orange	B, C, D, E	A, B, C, D, E	A, B, C, D, E	A, B, C, D, E	A, B, C, D, E
26	Ivory Black	n. o.	n. o.	n. o.	n. o.	n. o.
27	Zinc Yellow	B, C, D, E	A(w), B, C, D, E	A(w), B, C, D, E	A(w), B, C, D, E	A(w), B, C, D, E
28	Cobalt Violet	C(w), D, E	C, D, E	A, B, C, D, E	A, B, C, D, E	A, B, C, D, E
29	Mars Brown	n. o.	n. o.	B	B	B
30	Lithopone	C, D, E	C, D, E	C, D, E	C, D, E	C, D, E
31	Orpiment	B, C, D, E	A(w), B, C, D, E	A(w), B, C, D, E	A(w), B, C, D, E	A(w), B, C, D, E
32	Manganese Brown	B(w)	B(w)	B(w)	B(w)	B(w), E(w)
33	Cadmium Yellow	B, C, D, E	B, C, D, E	B, C, D, E	B, C, D, E	B, C, D, E
34	Mars Black	n. o.	n. o.	n. o.	n. o.	E(w)
35	Mars Yellow	E(w)	E(w)	B(w), D(w), E(w)	B(w), D(w), E(w)	B(w), D(w), E(w)

36	Light Ultramarine Blue	C(w), D, E	A(w).B, C, D, E	A(w).B, C, D, E	A(w).B, C, D, E	A(w).B(w), C, D, E
37	Saturn Red	B, C, D, E	B, C, D, E	A(w), B, C, D, E	A(w), B, C, D, E	A(w), B, C, D, E
38	Lead-Tin Yellow	C, D, E	A(w), C, D, E	A(w), C, D, E	A(w), C, D, E	A(w), C, D, E
39	Carbon Black	n. o.	n. o.	n. o.	n. o.	n. o.
40	Yellow Ocre	D(w), E(w)	A(w), B(w), C(w), D, E	A(w), B(w), C, D, E	A(w), B(w), C, D, E	A(w), B(w), C, D, E
41	Ultramarine Ash	D(w), E(w)	B(w), C(w), D, E	B(w), C(w), D, E	B(w), C(w), D, E	B(w), C(w), D, E
42	Stil de grain	A(w), C, D, E	A, C, D, E	A, C, D, E	A, C, D, E	A, C, D, E
43	Manganese Black	n. o.	n. o.	n. o.	n. o.	n. o.

Furthermore, we observe that the lines can be highly contrasted if the upper pictorial layer is completely or highly transparent and its reflectivity is low. Instead we have low contrast when the IR radiation is not completely absorbed by the superficial layer and reaches only partially the internal layer. For example this is the case of Egyptian Blue. A second situation occurs when the pictorial layer has a very high reflectance in the IR, such as Cinnabar, so that a small amount of the radiation can reach the back layer and the underdrawing is hardly visible.

This aspect was verified acquiring IR images of the several pictorial layers spread on microscope slides placed on a black support. In Fig. 85 some of the most significant examples are shown: the pictorial layer with Smalt, Fig. 85-A, the Alizarin Crimson Lake, Fig. 85-C, and Raw Sienna Earth, Fig. 85-D, become more transparent with increasing wavelength. On the contrary, the layers that contain Cinnabar, Fig. 85-B, and Cobalt Blue, Fig. 85-E, show a high reflection power in the IR. Finally, Ivory Black, Fig. 85-F, does not permit any IR transmission due to its high absorptivity.

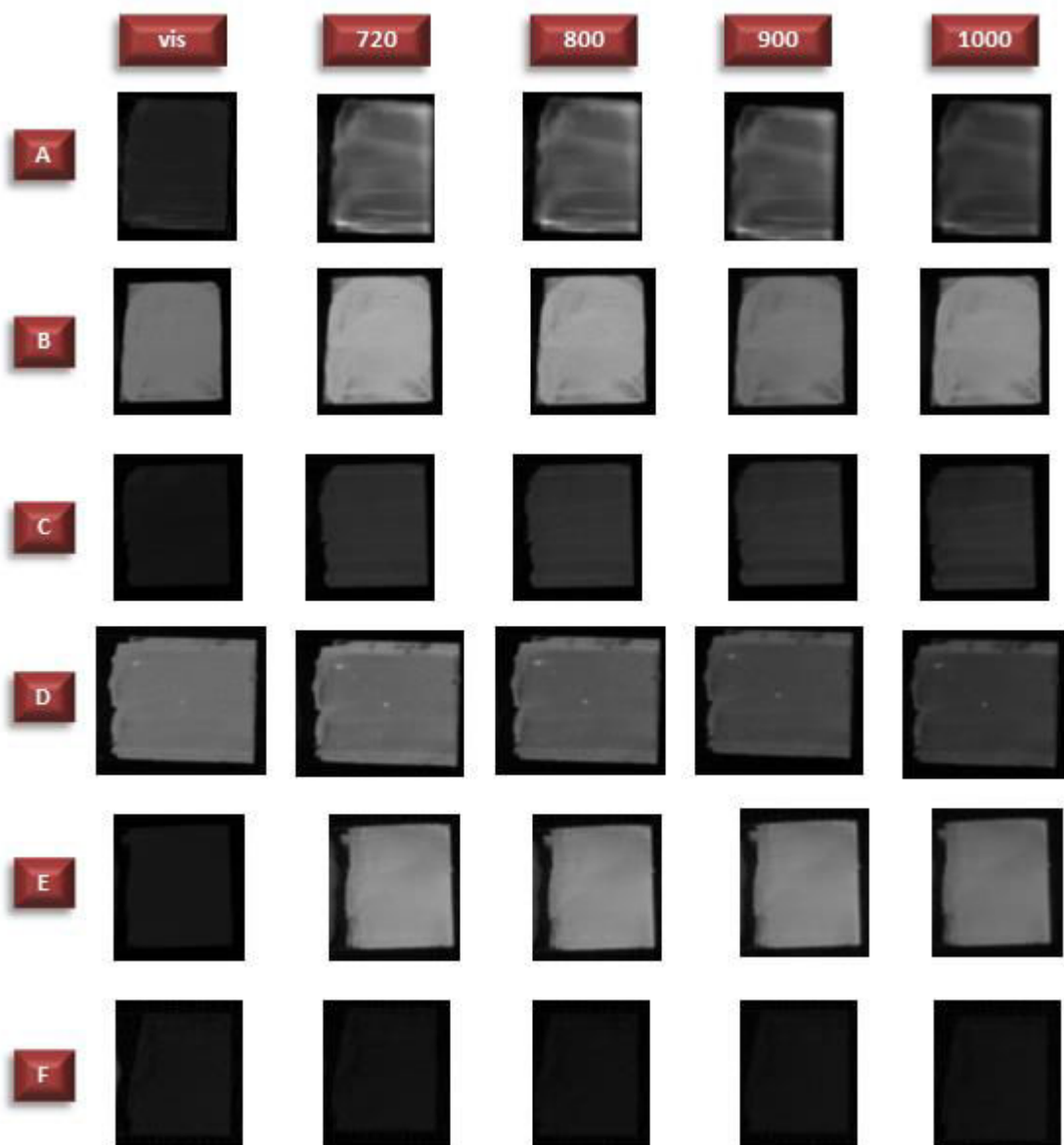


Fig. 85: Visible and IR images of pictorial layers: A=Smalt , B=Cinnabar, C=Alizarin Crimson Lake, D=Raw Sienna Earth, E=Cobalt Blue, F=Ivory Black.

We also tested the permanence of the lines traced under the pictorial layers, taking their IR image at 800 nm after two years, using a CCD camera with higher resolution than the previous one. In Fig. 86 we can notice that the line traced with the Lead tip has disappeared. Moreover, the image

presented in the bottom panel of Fig. 86 shows that the blackening of Litharge (indicated with a circle in the Fig.) has compromised the visualization of the under-drawings.

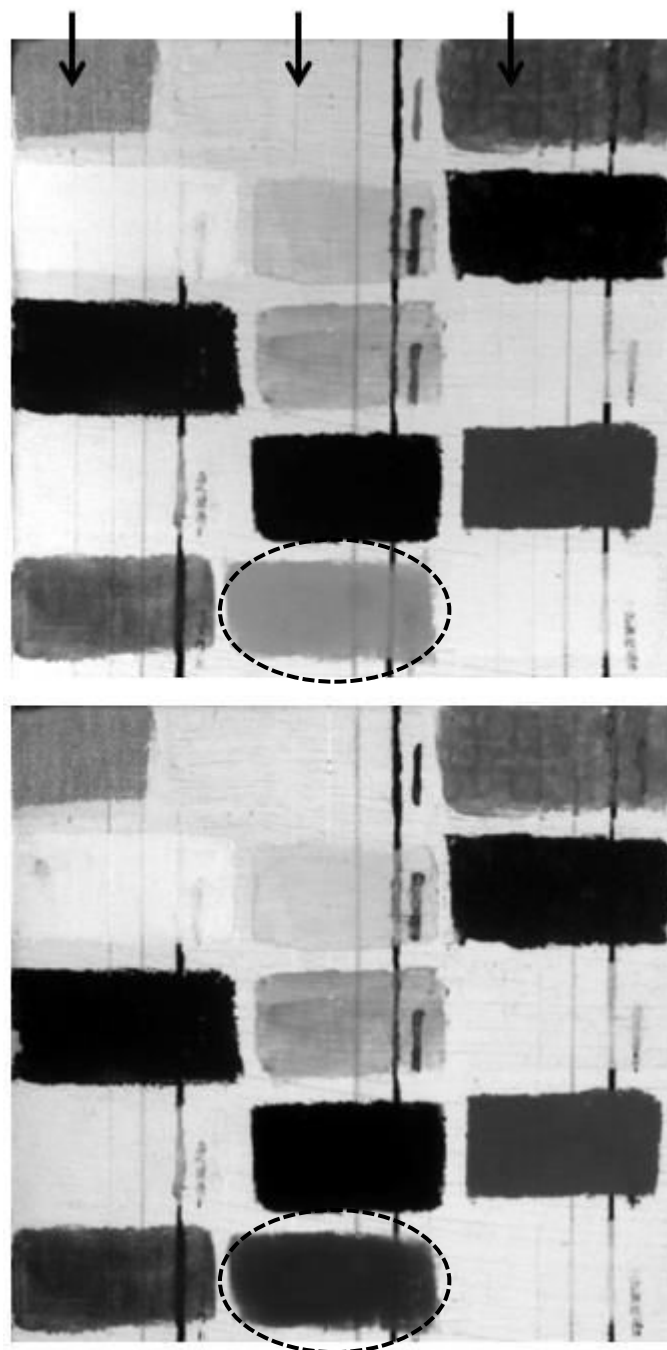


Fig. 86: Detail of the NIR image at 800 nm of the forty-four pictorial layers. Image after the drying of the sample (top panel) and image after two years. The Lead tip lines were indicated with the black narrows. Litharge layer is circled

2.1.5 Conclusions

The FORS spectra, the fluorescence spectroscopy and the UV-VIS-NIR multispectral imaging can be useful tools for the identification of sample pictorial layers formed by mixing a pigment and a binder. We observed that the reflectance structures of a pictorial layer do not change significantly in the presence of an underlying white layer, except for the intensity of the reflectance values.

PCA applied to the FORS spectra can be used for the selection of the significant multispectral images that contain the maximum variance of the spectral features. Moreover, if the PCA has indicated the wavelengths corresponding exactly to our filters, we obtained a good discrimination of the pictorial layers by means a “false” RGB combination.

Fluorescence spectra and multispectral UV fluorescence imaging were performed in order to recognize specific spectral features. All the blue pictorial layers showed an intense fluorescence emission at about 450 nm, that is probably a combination between the fluorescence emission of the binder and the blue pigments due to the fact that most of the blue pigments exhibit an intense fluorescence emission in this range. For the yellow, orange, red and brown pictorial layers it is hard to distinguish the true fluorescence emission from the reflected and/or scattered light of the pigment due to interaction between the photons emitted from the binder with the surrounding pigment. This phenomena can influence all the fluorescence emissions of the pictorial layers. Egyptian Blue, Cadmium Orange and Cadmium Yellow show an intense NIR fluorescence emission.

The use of band-pass NIR filters for the visualization of under-drawing was investigated, obtaining better results compared to ones obtained with long-pass filters.

2.2 Study of the spectral behaviour of pigments mixed with oil and egg yolk in different percentages by means of UV-VIS spectroscopy and UV-VIS multispectral imaging

2.2.1 Introduction

The reflectance and the fluorescence measurements are good scientific tools to recognize the pigments due to their specific spectral features that can be employed as fingerprints (Part II, chap. 1.1). However, a work of art is composed by mixtures of pigments and binders that can influence the spectral response and thus compromise the success of the identification.

Binders undergo important effects on the pictorial layer fluorescence: (i) the emission of a fluorescence signal by the excitation of their own fluorophores, which can be important in the case of non-fluorescent pigments, (ii) the modification of the pigment fluorescence.

In this part, we study the effect of the type and quantity of binder on the spectral behaviour of selected pictorial layers (reflectance and the fluorescence emission). Taking into account that it is impossible to test all the possible mixtures of pigments and binders, we selected ten pigments and two binders: linseed oil and egg yolk. We measured their reflectance and fluorescence spectra, and employed multispectral imaging techniques in order to map specific spectral features useful for the identification of pigments and binders. Moreover, we applied to the ultraviolet-induced fluorescence spectra the correction procedure suggested by [Verri G. et al. 2008] to extract the "true" fluorescence emission (Part I, chap. 1). This approach employed on some multispectral fluorescence images produced good results.

2.2.2 Materials

We realized a first set of samples mixing nine different pigments with either linseed oil or egg yolk in different mass ratios. For obtaining a good spreading power we also added distilled water. The pigments employed and the ratio of the pigment to the binder are reported in the following figures

showing the pictorial materials: Raw Sienna Earth Fig. 87; Burnt Sienna Earth in Fig. 88; Ercolano Red Ochre in Fig. 89; Yellow Ochre in Fig. 90; Minium in Fig. 91; Green Earth in Fig. 92; light Ultramarine Blue in Fig. 93; Lead White in Fig. 94; Zinc White in Fig. 95.

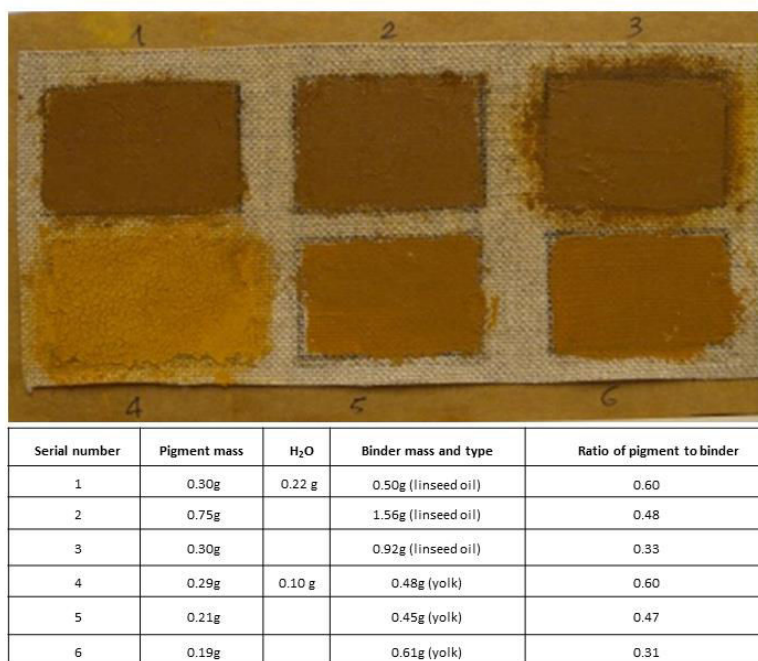


Fig. 87: Samples of Raw Sienna Earth mixed with linseed oil or egg yolk.

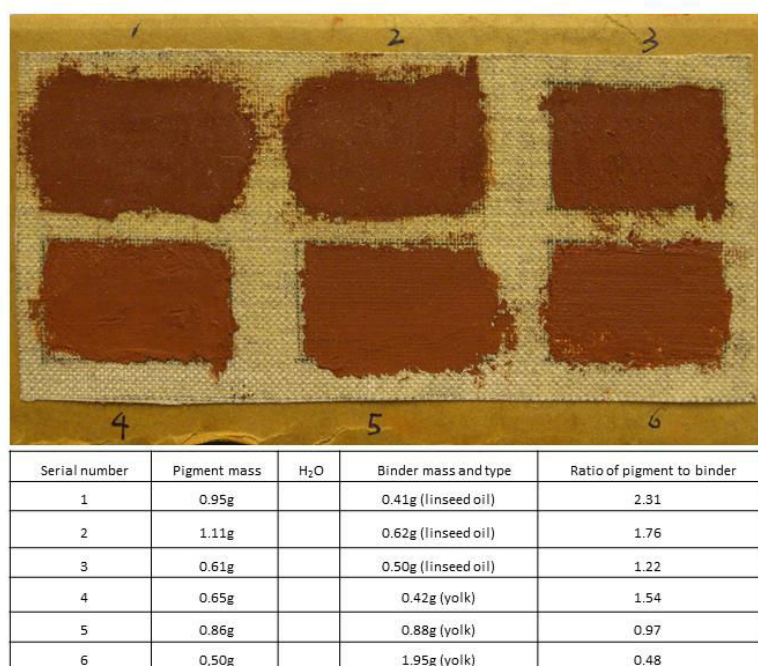


Fig. 88: Samples of Burnt Sienna Earth mixed with linseed oil or egg yolk.

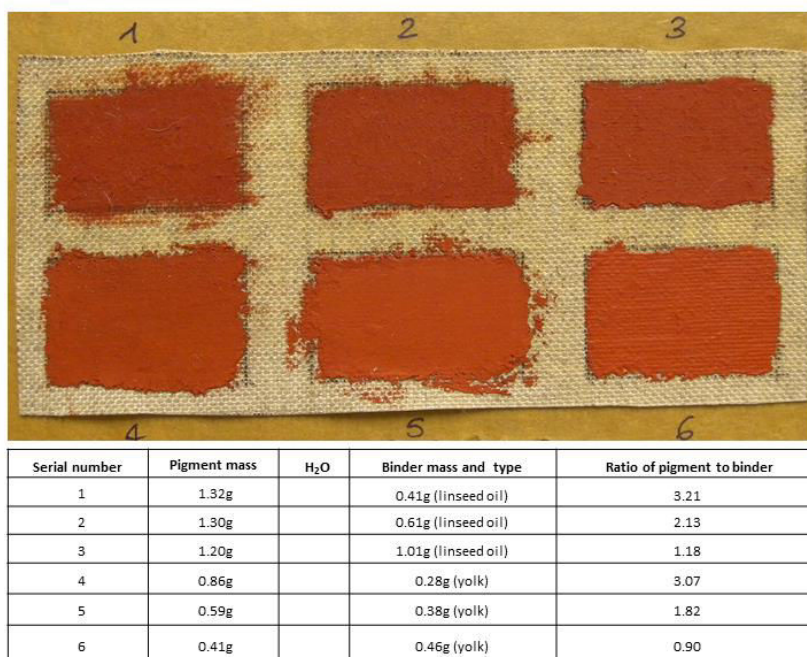


Fig. 89: Samples of Ercolano Red Ochre mixed with linseed oil or egg yolk.

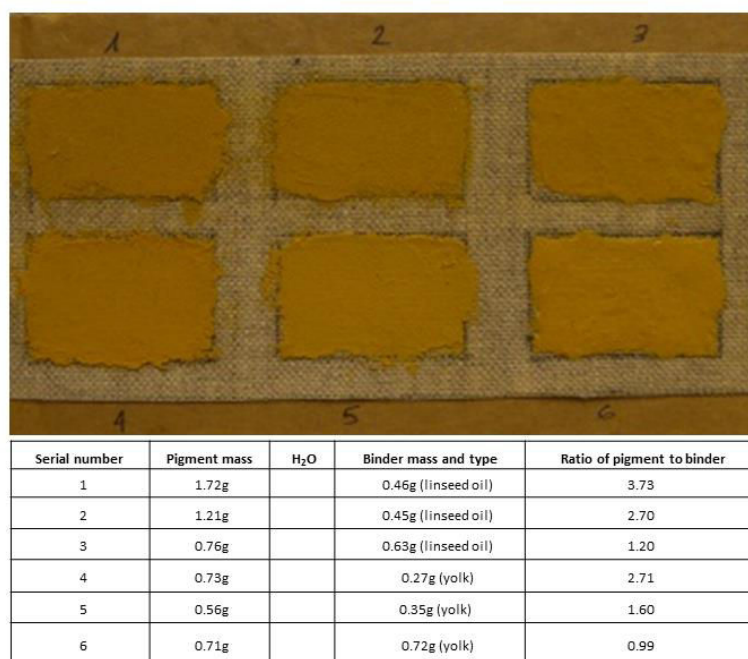
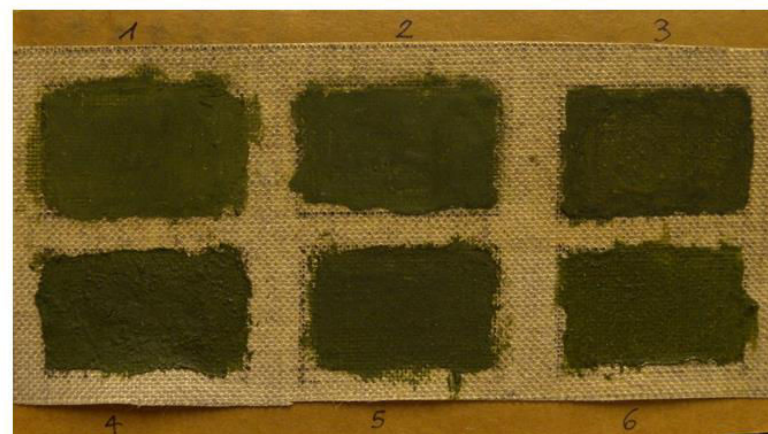


Fig. 90: Samples of Yellow Ochre mixed with linseed oil or egg yolk.



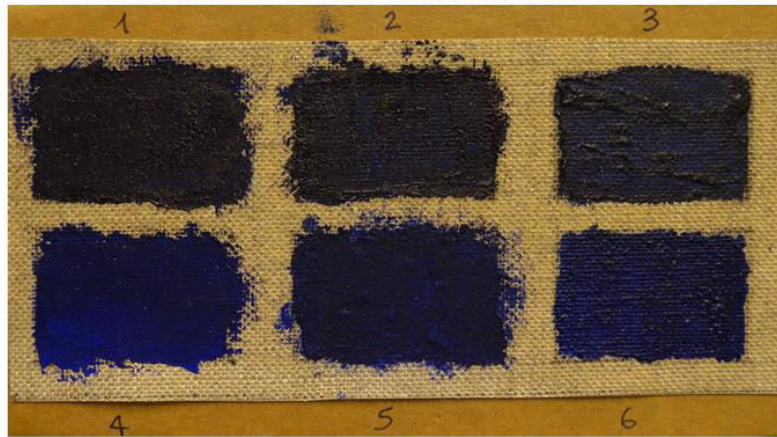
Serial number	Pigment mass	H ₂ O	Binder mass and type	Ratio of pigment to binder
1	0.82g		0.18g (linseed oil)	4.55
2	0.75g		0.20g (linseed oil)	3.75
3	0.75g		0.30g (linseed oil)	2.5
4	0.93g		0.29g (yolk)	3.20
5	0.81g		0.39g (yolk)	2.08
6	0.64g		0.64g (yolk)	1.0

Fig. 91: Samples of Minium mixed with linseed oil or egg yolk.



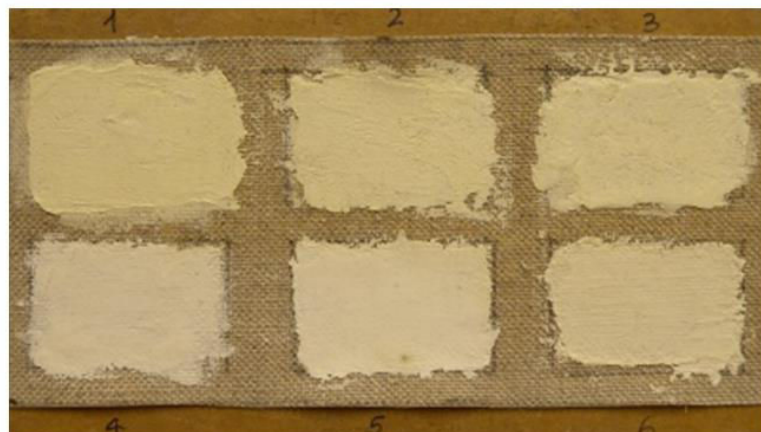
Serial number	Pigment mass	H ₂ O	Binder mass and type	Ratio of pigment to binder
1	1.49g	0.3g	0.92g (linseed oil)	1.62
2	0.98g	0.2g	0.78g (linseed oil)	1.26
3	0.75g		0.75g (linseed oil)	1
4	0.90g		1.26g (yolk)	0.71
5	0.51g		1.08g (yolk)	0.47
6	0.31g		1.04g (yolk)	0.30

Fig. 92: Samples of Green Earth mixed with linseed oil or egg yolk.



Serial number	Pigment mass	H ₂ O	Binder mass and type	Ratio of pigment to binder
1	0.62g		0.40g (linseed oil)	1.41
2	0.61g		0.58g (linseed oil)	1.05
3	0.50g		0.81g (linseed oil)	0.62
4	0.56g		0.39g (yolk)	1.44
5	0.30g		0.40g (yolk)	0.75
6	0.24g		0.60g (yolk)	0.40

Fig. 93: Samples of light Ultramarine Blue mixed with linseed oil or egg yolk.



Serial number	Pigment mass	H ₂ O	Binder mass and type	Ratio of pigment to binder
1	1.85g	0.3g	0.30g (linseed oil)	6.17
2	1.45g	0.3g	0.21g (linseed oil)	5.48
3	2.31g		0.70g (linseed oil)	3.30
4	1.08g		0.27g (yolk)	4.0
5	0.90g		0.34g (yolk)	2.65
6	1.01g		0.55g (yolk)	1.83

Fig. 94: Samples of Lead White mixed with linseed oil or egg yolk.



Fig. 95: Samples of Zinc White mixed with linseed oil or egg yolk.

A second set of samples was obtained mixing different pigments and varying quantities of pigments and binders, as follow:

- mixtures of Lead White and Raw Sienna Earth, shown in Fig. 96;
- mixtures of Lead White, Raw Sienna Earth and Green Earth, shown in
-
- Fig. 97: Samples obtained mixing Lead White, Raw Sienna Earth and Green Earth with linseed oil or egg yolk.
- ;
- mixtures of Lead White and Zinc White, shown in Fig. 98;
- mixtures of Lead White and Hematite, Zinc White and Hematite and a mixture of Lead White and Zinc White with Hematite, shown in Fig. 99;
- mixtures of Lead White, Zinc White and Hematite, shown in Fig. 100.



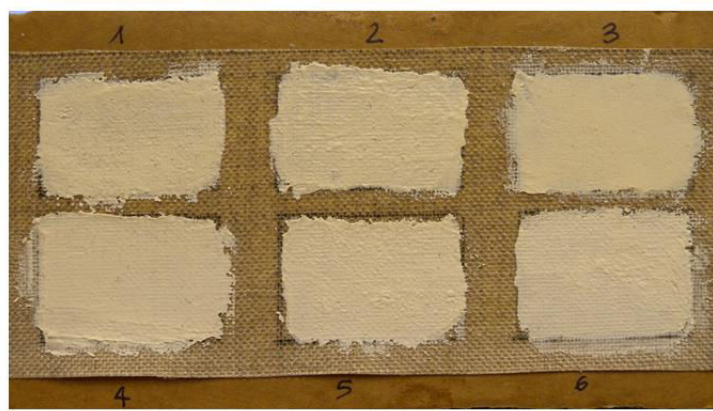
Serial number	Mixed pigment mass	Binder mass	Volume ratio between raw sienna earth and lead white
1	1.76g	0.48g (linseed oil)	10:90
2	1.74g	0.58g (linseed oil)	30:70
3	1.15g	0.52g (linseed oil)	50:50
4	0.70g	0.57g (linseed oil)	70:30
5	0.43g	0.47g (linseed oil)	90:10
6	1.76g	0.79g (yolk)	10:90
7	1.74g	1.05g (yolk)	30:70
8	1.15g	0.95g (yolk)	50:50
9	0.70g	1.05g (yolk)	70:30
10	0.43g	0.91g (yolk)	90:10

Fig. 96: Samples obtained mixing Lead White and Raw Sienna Earth with linseed oil or egg yolk.



Serial number	mixtures of raw sienna earth and lead white (mass)	green earth mass	Binder mass	Volume ratio between raw sienna earth and lead white
1	0.53g	0.10g	0.31g (linseed oil)	50:50
2	0.52g	0.20g	0.30g (linseed oil)	50:50
3	0.53g	0.30g	0.31g (linseed oil)	50:50
4	0.51g	0.10g	0.61g (linseed oil)	90:10
5	0.51g	0.20g	0.60g (linseed oil)	90:10
6	0.53g	0.30g	0.62g (linseed oil)	90:10

Fig. 97: Samples obtained mixing Lead White, Raw Sienna Earth and Green Earth with linseed oil or egg yolk.



Serial number	Pigment mass	Binder mass	Volume ratio between lead white and zinc white
1	1.05g	0.41g (linseed oil)	70:30
2	1.06g	0.51g (yolk)	70:30
3	0.99g	0.40g (linseed oil)	50:50
4	0.98g	0.53g (yolk)	50:50
5	0.92g	0.42g (linseed oil)	30:70
6	0.93g	0.54g (yolk)	30:70

Fig. 98: Samples obtained mixing Lead White and Zinc White with linseed oil or egg yolk.



Serial number	Pigment mass	Volume	Hematite mass	Binder mass
1	Zinc white 0.71 g	1ml	0.01g	0.35g
2	Lead white 1.09 g	1ml	0.01g	0.36g
3	(50:50) mixture of lead white and zinc white 0.89 g	1ml	0.01g	0.35g

Fig. 99: Samples obtained mixing Zinc White and Hematite (1), Lead White and Hematite (2), a mixture of Lead White and Zinc White with Hematite(3), with linseed oil.



Fig. 100: Samples obtained mixing Lead White, Zinc White and Hematite with linseed oil or egg yolk.

2.2.3 Methods

The reflectance measurements were performed with the Avantes AvaSpec-2048 A-USB1 spectrophotometer, using the spectralon SRS-99-010 (Labsphere) as the diffuse reflectance standard. The same Avantes spectrophotometer, equipped with a UV LED emitting at 365 nm, was employed for the acquisition of the UV fluorescence spectra. For each sample we acquired two fluorescence spectra.

The multispectral imaging was performed with the QSI 583-w camera, equipped with the Leica optical system. The images were taken using the following narrow band interferential filters: 380 nm, 390 nm, 400 nm, 410 nm, 420 nm, 450 nm, 470 nm, 500 nm, 532 nm, 550 nm, 600 nm, 650 nm, 680 nm, 700 nm, and 750 nm.

2.2.4 Results and discussion

2.2.4.1 Reflectance spectra

The reflectance spectra of all the samples constituted by a single pigment show slight differences, except for the percentage of reflectance. This means that, despite the quantity and the type of binders, the spectral features do not change significantly, as shown in Fig. 101, Fig. 102, Fig. 103, Fig. 104, Fig. 105, Fig. 106, Fig. 107, Fig. 108, Fig. 109. We do not find a specific pattern connected to the increase or decrease of the pigment/binder ratios. The samples of Ultramarine, Raw Sienna Earth and Burnt Sienna Earth mixed with egg yolk showed a higher reflectance than those mixed with linseed oil.

One of the samples, Raw Sienna Earth in egg yolk (n° 4), showed a strong craquelures, that produced a strong increase of the reflectance, shown in Fig. 105.

The reflectance spectra of Zinc White differ significantly from those of Lead White between 370 nm and 450 nm, see Fig. 108 and Fig. 109. This means that they can be distinguished well from each other.

Both the Ultramarine Blue and the Lead White in linseed oil samples display a shift to long wavelengths of the inflection point, probably due to the yellowing of the pictorial layer, see Fig. 106 and Fig. 109.

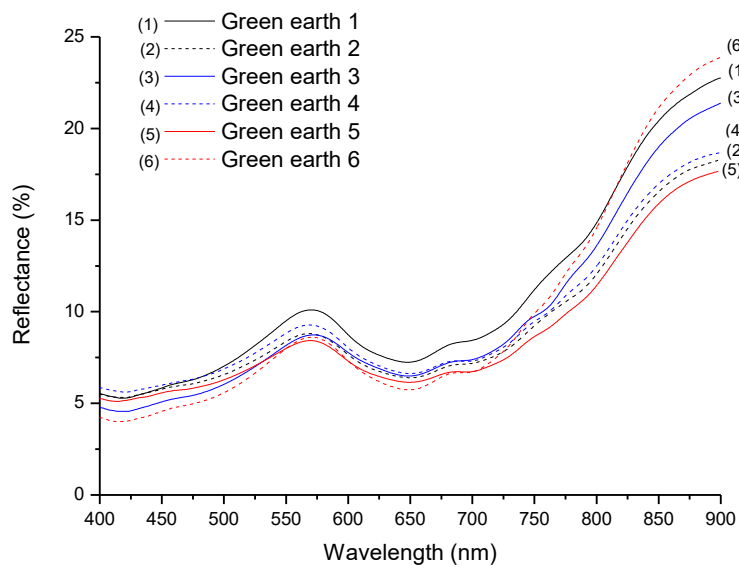


Fig. 101: Reflectance spectra of the samples of Green Earth mixed with linseed oil (solid lines) or egg yolk (dash lines). The samples from 1 to 3 and from 4 to 5 present an augmentation in the amount of the binder: linseed oil and egg yolk respectively.

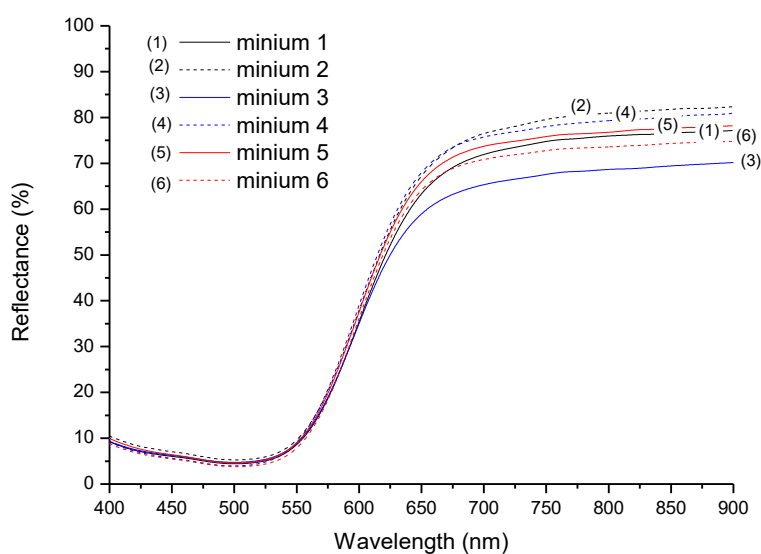


Fig. 102: Reflectance spectra of the samples of Minium mixed with linseed oil (solid lines) or egg yolk (dash lines). The samples from 1 to 3 and from 4 to 5 present an augmentation in the amount of the binder: linseed oil and egg yolk respectively.

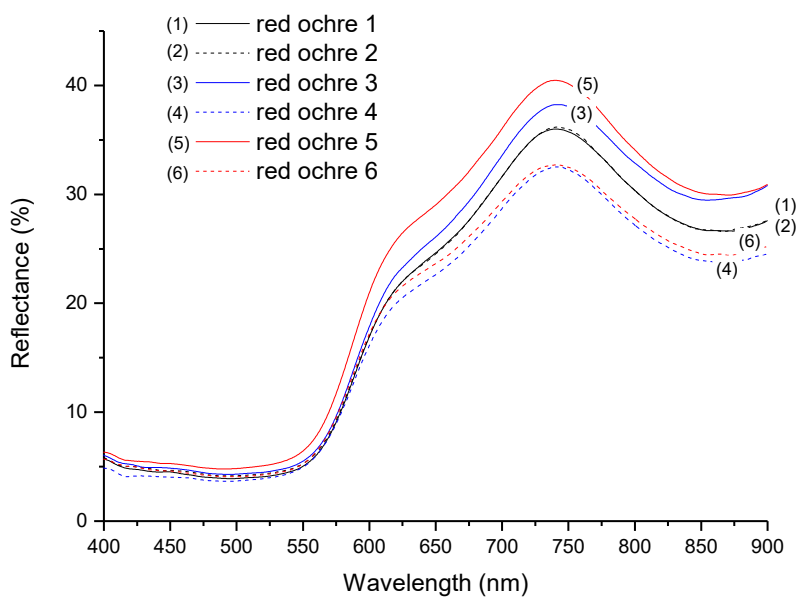


Fig. 103: Reflectance spectra of the samples of Ercolano Red Ochre mixed with linseed oil (solid lines) or egg yolk (dash lines). The samples from 1 to 3 and from 4 to 5 present an augmentation in the amount of the binder: linseed oil and egg yolk respectively.

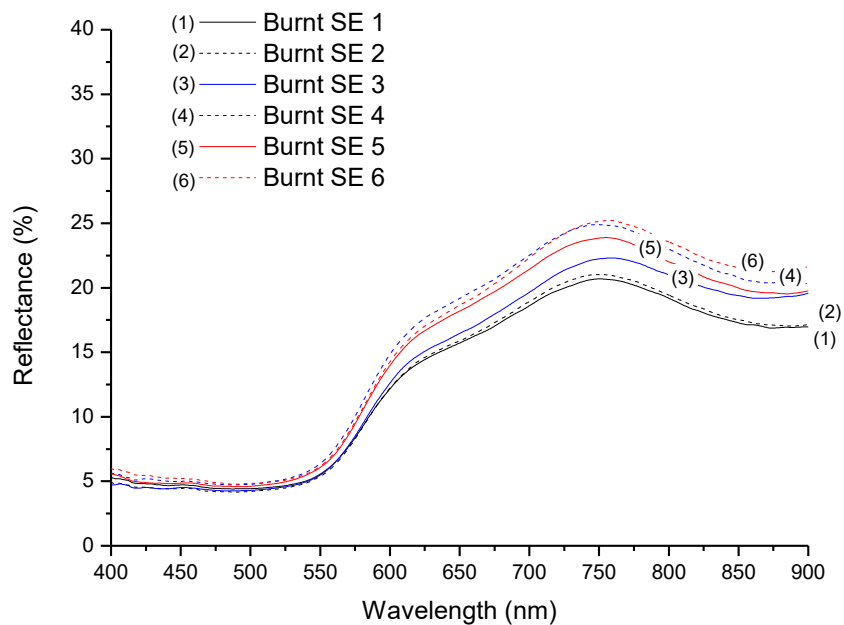


Fig. 104: Reflectance spectra of the samples of Burnt Sienna Earth mixed with linseed oil (solid lines) or egg yolk (dash lines). The samples from 1 to 3 and from 4 to 5 present an augmentation in the amount of the binder: linseed oil and egg yolk respectively.

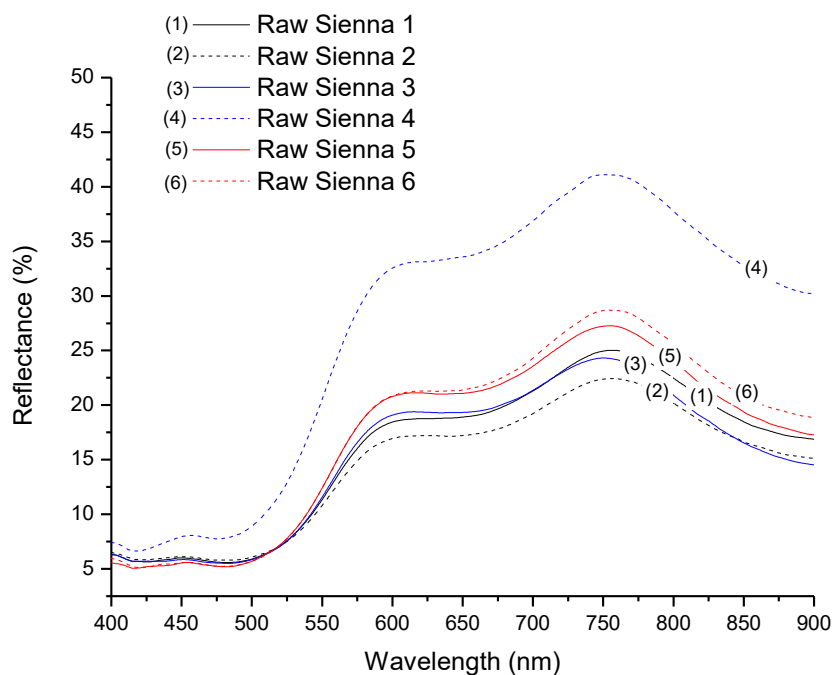


Fig. 105: Reflectance spectra of the samples of Raw Sienna Earth mixed with linseed oil (solid lines) or egg yolk (dash lines). The samples from 1 to 3 and from 4 to 5 present an augmentation in the amount of the binder: linseed oil and egg yolk respectively.

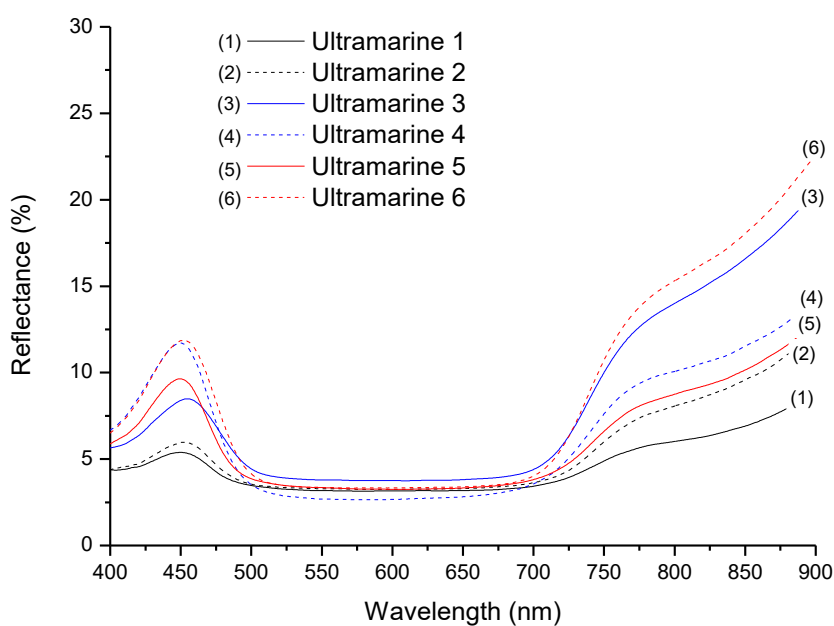


Fig. 106: Reflectance spectra of the samples of light Ultramarine Blue mixed with linseed oil (solid lines) or egg yolk (dash lines). The samples from 1 to 3 and from 4 to 5 present an augmentation in the amount of the binder: linseed oil and egg yolk respectively.

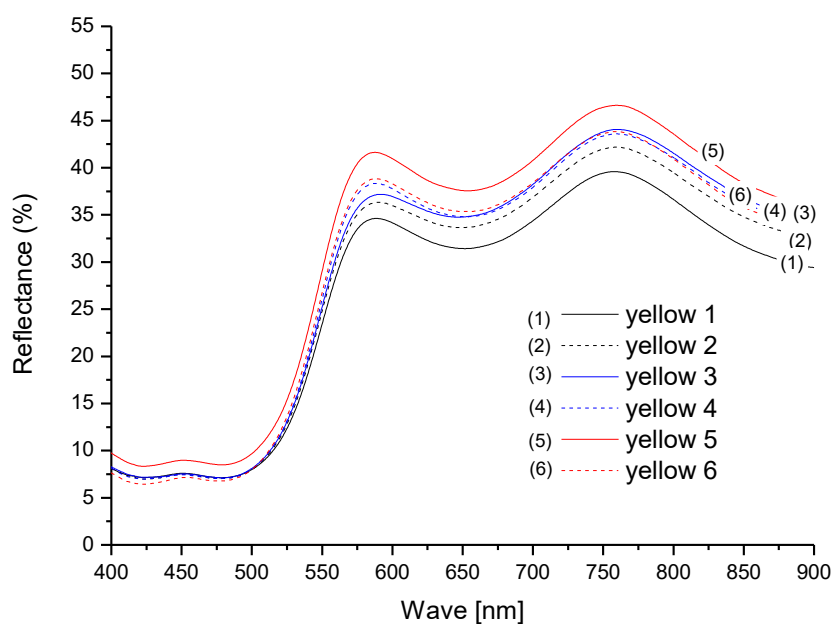


Fig. 107: Reflectance spectra of the samples of Yellow Ochre mixed with linseed oil (solid lines) or egg yolk (dash lines). The samples from 1 to 3 and from 4 to 5 present an augmentation in the amount of the binder: linseed oil and egg yolk respectively.

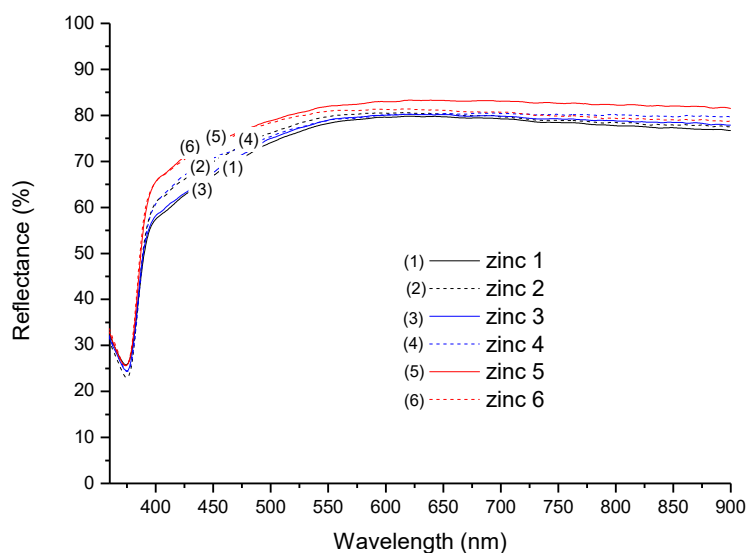


Fig. 108: Reflectance spectra of the samples of Zinc White mixed with linseed oil (solid lines) or egg yolk (dash lines). The samples from 1 to 3 and from 4 to 5 present an augmentation in the amount of the binder: linseed oil and egg yolk respectively.

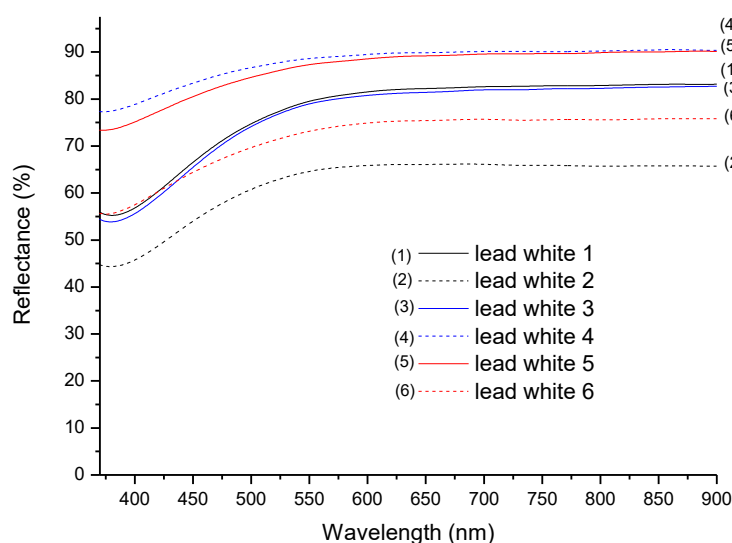


Fig. 109: Reflectance spectra of the samples of Lead White mixed with linseed oil (solid lines) or egg yolk (dash lines). The samples from 1 to 3 and from 4 to 5 present an augmentation in the amount of the binder: linseed oil and egg yolk respectively.

The intensity of the reflectance spectra of the mixtures of Lead White and Raw Sienna Earth increases with the percentage of Lead White. The reflectance spectra is, thus, a combination of the spectra of the two pigments. As a result, the weak shoulder at about 460 nm is more pronounced and the band at about 755 nm becomes less marked (cf. Fig. 110). Furthermore, the inflection point around 550 nm shifts towards shorter wavelengths with an increase of Lead White, as clearly shown in the first derivative spectra presented in Fig. 111.

The two blends 50:50 and 90:10 of Raw Sienna Earth and Lead White, mixed with Green Earth and linseed oil as a binder, show different inflection points at about 525 nm and 550 nm, respectively. The reflectance spectra of the samples with the highest quantity of Raw Sienna Earth are weaker at long wavelengths and show a second, and have a well-pronounced band at 750 nm. Despite the low quantity of Green Earth, all the reflectance spectra show weak bands between 650 nm and 800 nm, typical of the Green Earth pigment, see Fig. 112.

The reflectance spectra of the samples prepared mixing Lead White and Zinc White, presented in Fig. 113, show the spectral features of the Zinc White samples with an additional shoulder at 400 nm and an inflection point at about 380 nm.

The reflectance spectra of Zinc White mixed with other pigments, such as Hematite, show a peak at about 390-400 nm, as shown in Fig. 114.

The reflectance spectra of the mixtures of Lead White, Zinc White and Hematite display a decrease of the reflectance with the increase of the amount of Hematite as shown in Fig. 115.

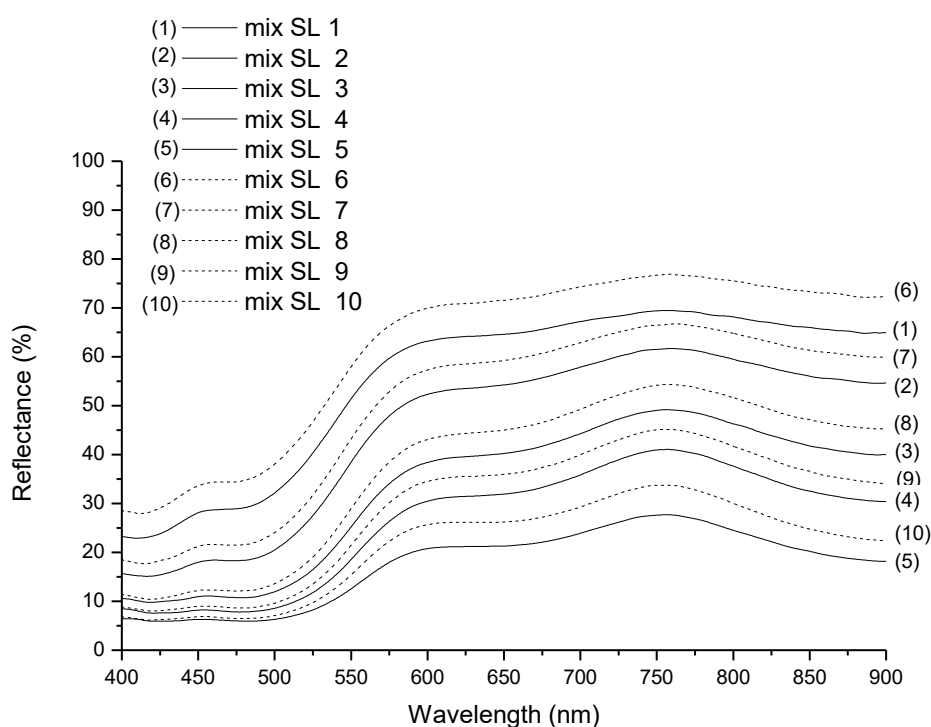


Fig. 110: Reflectance spectra of the samples of Lead White and Raw Sienna Earth mixed with linseed oil (solid lines) or egg yolk (dash lines). The samples from 1 to 5 are mixed with linseed oil while those from 6 to 10 are mixed with egg yolk. The Lead White and Raw Sienna Earth ratios are 10:90 (1 and 6), 30:70 (2 and 7), 50:50 (3 and 8), 70:30 (4 and 9) and 90:10 (5 and 10).

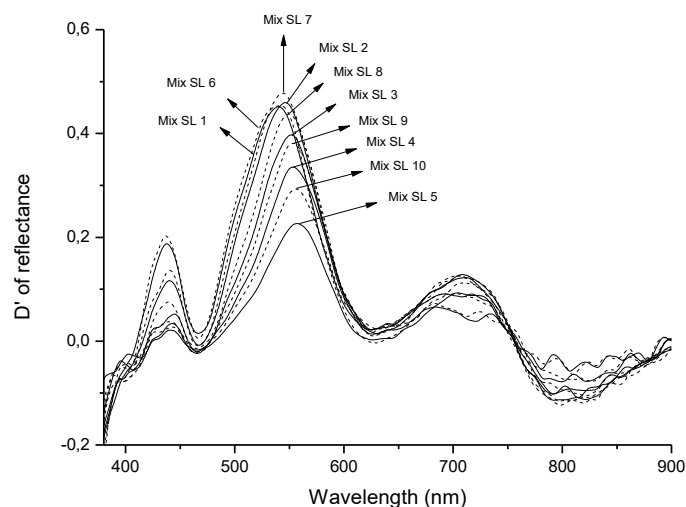


Fig. 111: First derivate of the reflectance spectra of the samples of Lead White and Raw Sienna Earth mixed with linseed oil (solid lines) or egg yolk (dash lines). The samples from 1 to 5 are mixed with linseed oil while those from 6 to 10 are mixed with egg yolk. The Lead White and Raw Sienna Earth ratios are 10:90 (1 and 6), 30:70 (2 and 7), 50:50 (3 and 8), 70:30 (4 and 9) and 90:10 (5 and 10).

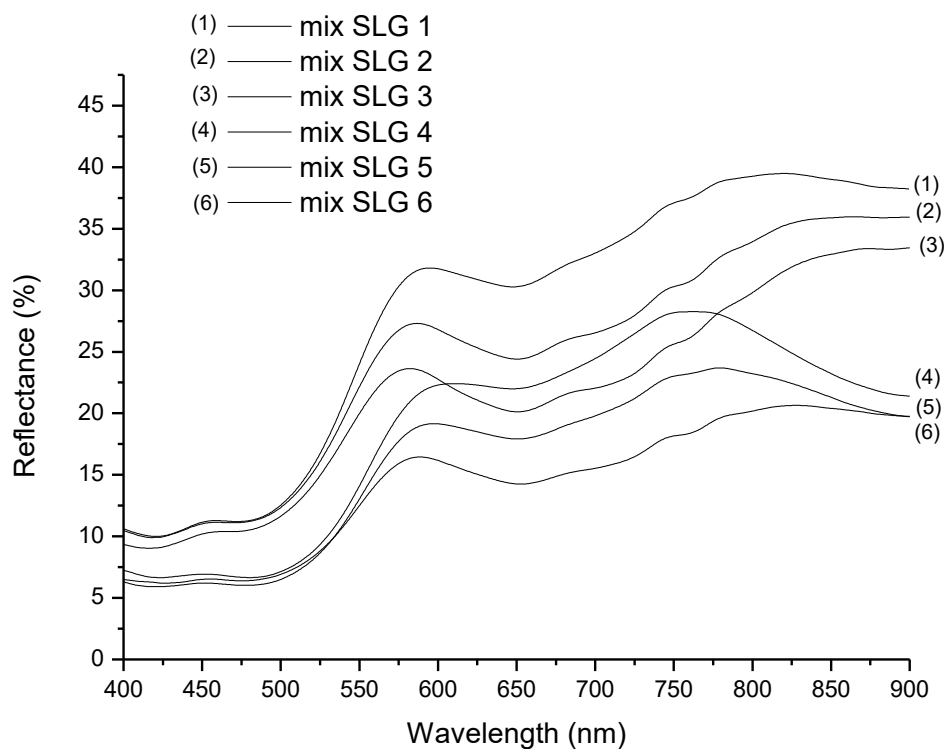


Fig. 112: Reflectance spectra of the samples of Raw Sienna Earth, Lead White and Green Earth mixed with linseed oil or egg yolk . The samples from 1 to 3 are mixtures of Raw Sienna and Lead White 50:50 and increasing quantities of Green Earth mixed with linseed oil while those from 4 to 6 are mixtures of Raw Sienna and Lead White 90:10 and increasing quantities of Green Earth mixed with egg yolk

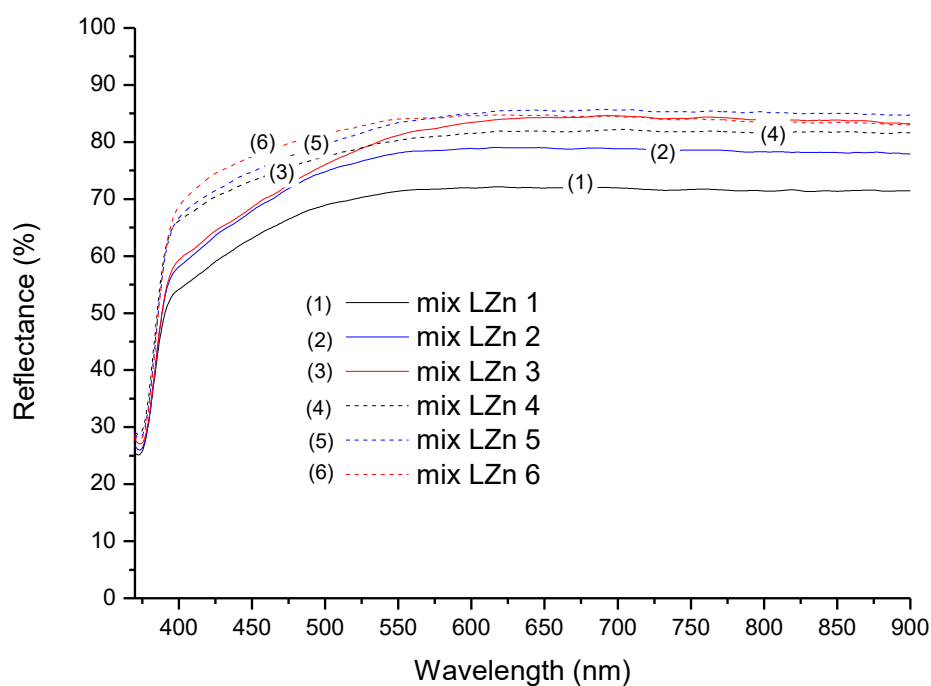


Fig. 113: Reflectance spectra of the samples of Lead White and Zinc White with linseed oil (solid lines) or egg yolk (dash lines). The sample from 1 to 3 are mixed in linseed oil while those from 4 to 6 are mixed with egg yolk. The Lead White and Zinc White ratios are 70:30 (1 and 4), 50:50 (2 and 5) and 30:70 (3 and 6).

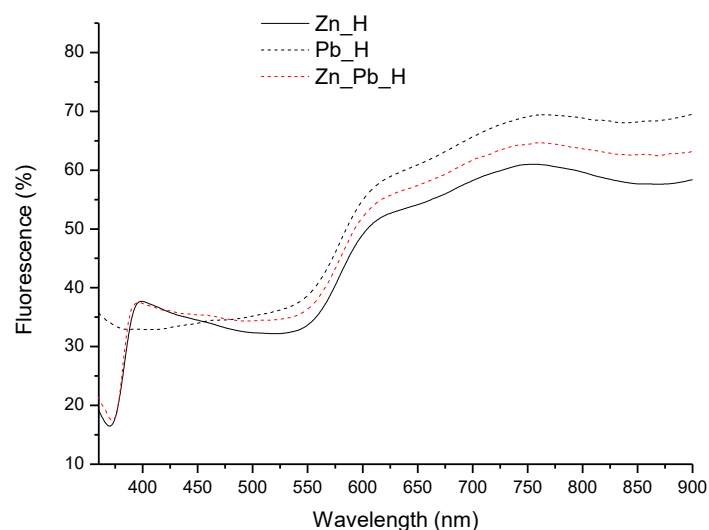


Fig. 114: Reflectance spectra of the samples of Lead White, Zinc White and Hematite with linseed oil. The sample 1 are constituted by Zinc White and Hematite, the sample 2 are constituted by Lead White and Hematite and the sample 3 by a mixture of Lead White and Zinc White 50:50 with Hematite.

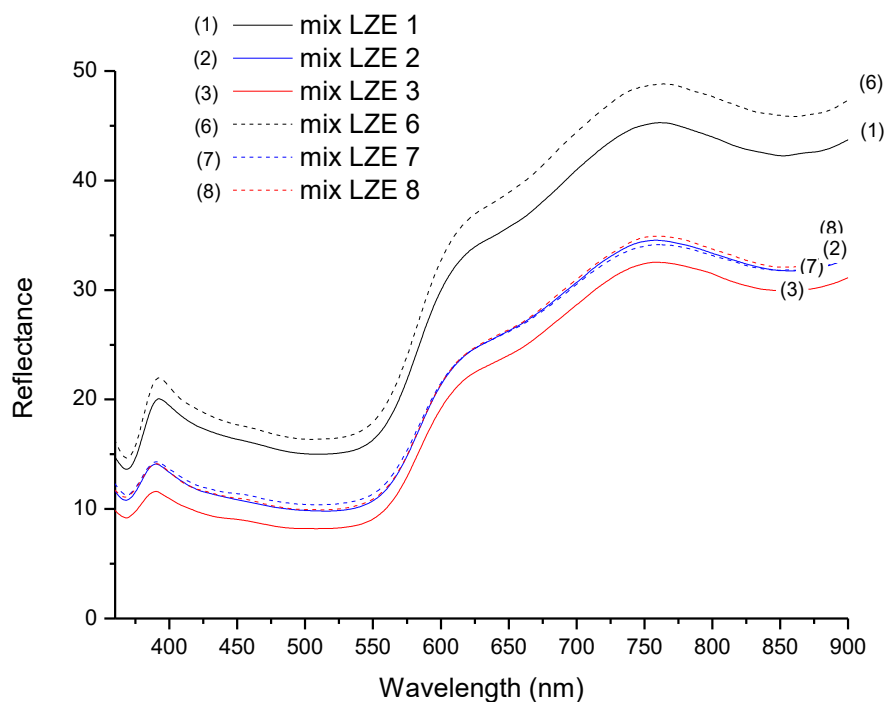


Fig. 115: Reflectance spectra of the samples of Lead White, Zinc White and Hematite with linseed oil (solid lines) or egg yolk (dash lines). The samples from 1 to 3 are mixtures of Raw Sienna and Lead White 50:50 and increasing quantities of Hematite mixed with linseed oil while those from 4 to 6 are mixtures of Raw Sienna and Lead White 50:50 and increasing quantities of Hematite mixed with egg yolk.

2.2.4.2 Fluorescence spectra

Our experiments showed that the intensity of the fluorescence emission is deeply dependent of the localisation of the analysis. Such result is related to the impossibility to spread a completely uniform pictorial layer.

The fluorescence of the samples of Raw Sienna Earth and Burnt Sienna Earth, Fig. 116, Ercolano Red Ochre and Yellow Ochre, Fig. 117, and Minium,

Fig. 118, exhibit two bands. We used the Gaussian curve-fitting deconvolution of the Origin Lab software to a discrimination of the contributions of the single bands to the fluorescence spectra; the deconvoluted bands are reported as the green curves in figures. We assign the first band to the fluorescence of the binder and the second one can be associated with the reflected and/or scattered light from the pigment due to interaction between the photons emitted from the binder with the

surrounding pigment, as discussed in Part I, chap. 1.3.2, as shown in Fig. 116 and Fig. 117. Furthermore, the second band occurs approximately at 540-560 nm for the Raw Sienna Earth and Yellow Ochre, and at about 570-600 nm for the Burnt Sienna Earth, Ercolano Red Ochre and Minium. The above values agree with the inflection points of the reflectance spectra of the corresponding pictorial layers in Fig. 87, Fig. 90, Fig. 88, Fig. 89 and Fig. 91, respectively.

For the red-yellow hues, we noted that it is difficult to distinguish the fluorescence of either binder, because the first band appears approximately at the same position, 430-450 nm, for both egg yolk and linseed oil samples.

We cannot establish a spectral trend of the fluorescence spectra with the decrease of the ratio between the pigment and the binders mass, probably due to the heterogeneity of the pictorial samples.

As shown in Fig. 119, in the case of the Green Earth samples we can distinguish the presence of linseed oil as a binder from that of egg yolk from their fluorescence spectra since the oil samples present a strong emission at longer wavelengths. The deconvolution of the spectra, presented in Fig. 120, has allowed to identify two bands: the first one at 432-433 nm for the egg yolk samples and at 438-442 nm for the linseed oil samples and a second one at 481-493 nm for the egg yolk samples and at 519-531 nm for the linseed oil samples.

In the case of light Ultramarine Blue samples, the fluorescence spectra of the samples mixed with the egg yolk are definitely different from those mixed with linseed oil: in fact, in the latter case, the main fluorescence band shifts to longer wavelengths and broadens, as shown in Fig. 121. The same behaviour has been observed for the Lead White samples, in which the fluorescence of the egg yolk samples presents a maximum at 436 nm, while that of the linseed oil samples the maximum is at 456 nm, as shown in Fig. 122.

From the fluorescence of the Zinc White samples we cannot distinguish the presence of the egg yolk as a binder from that of the linseed oil, see Fig. 123.

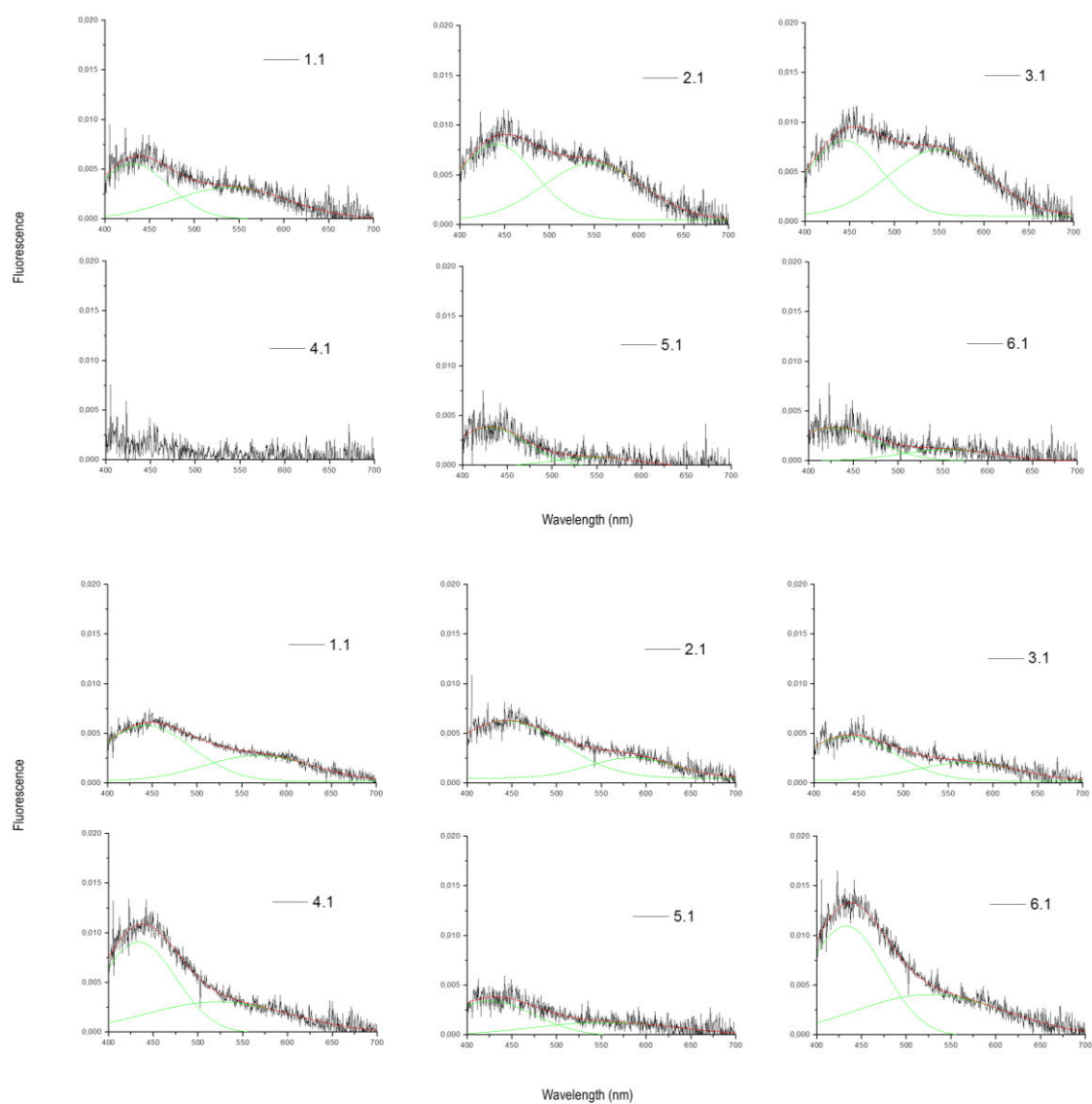


Fig. 116: Fluorescence spectra of the Raw Sienna Earth (top panel) and Burnt Sienna Earth (bottom panel) samples. The spectra 1.1, 2.1, 3.1 correspond to one measurement area of the samples 1, 2 and 3 (mixture with linseed oil). The spectra 4.1, 5.1, 6.1 correspond to one measurement area of the samples 4, 5 and 6 (mixture with egg yolk).

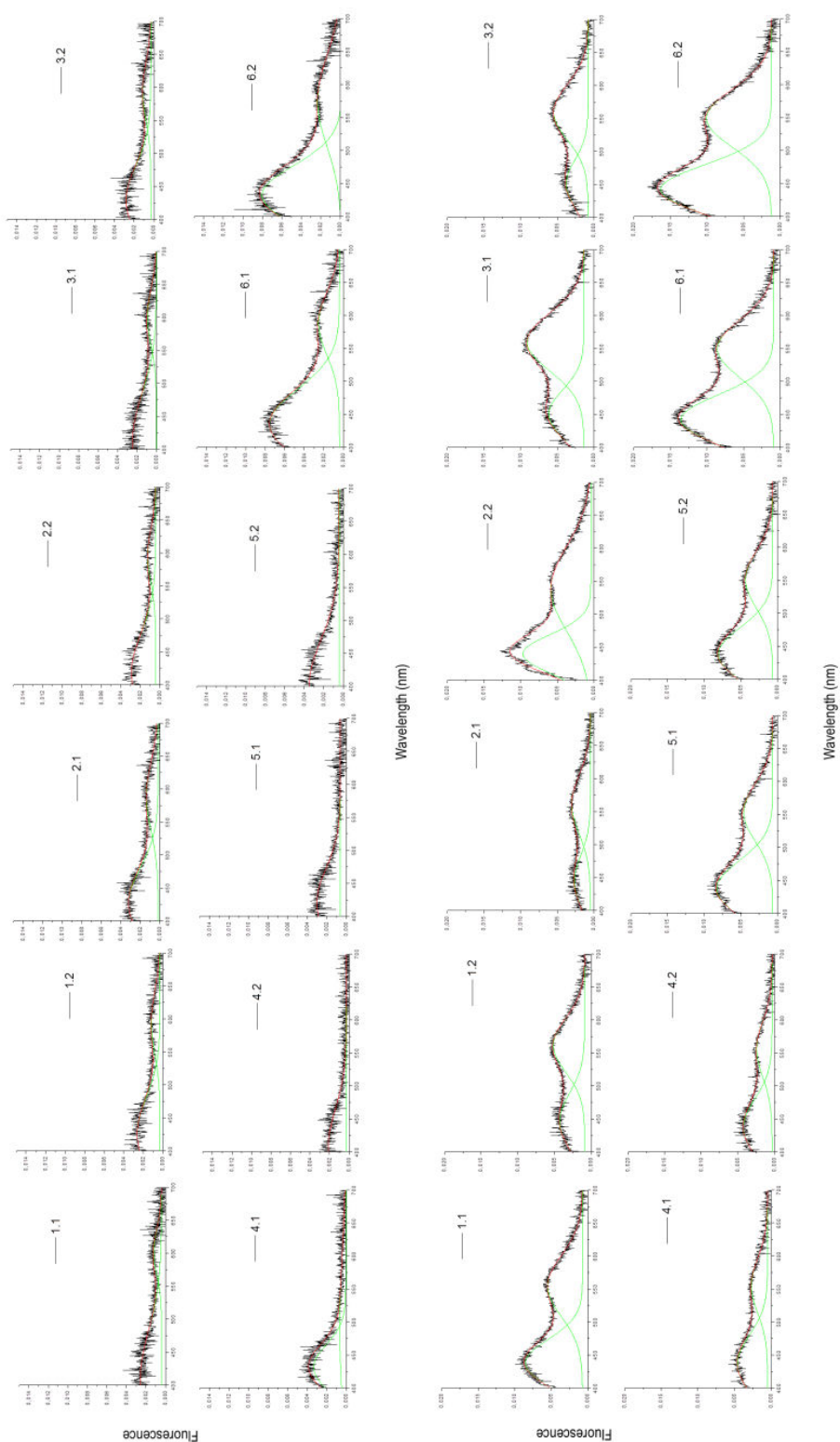


Fig. 117: Fluorescence spectra of the Ercolano Red Ochre (top panel) and Yellow Ochre (bottom panel) samples. The spectra 1.1, 1.2, 2.1, 2.2, 3.1, 3.2 correspond to two measurement areas of the samples 1, 2 and 3 (mixture with linseed oil). The spectra 4.1, 4.2, 5.1, 5.2, 6.1, 6.2 correspond to two measurement areas of the samples 4, 5 and 6 (mixture with egg yolk).

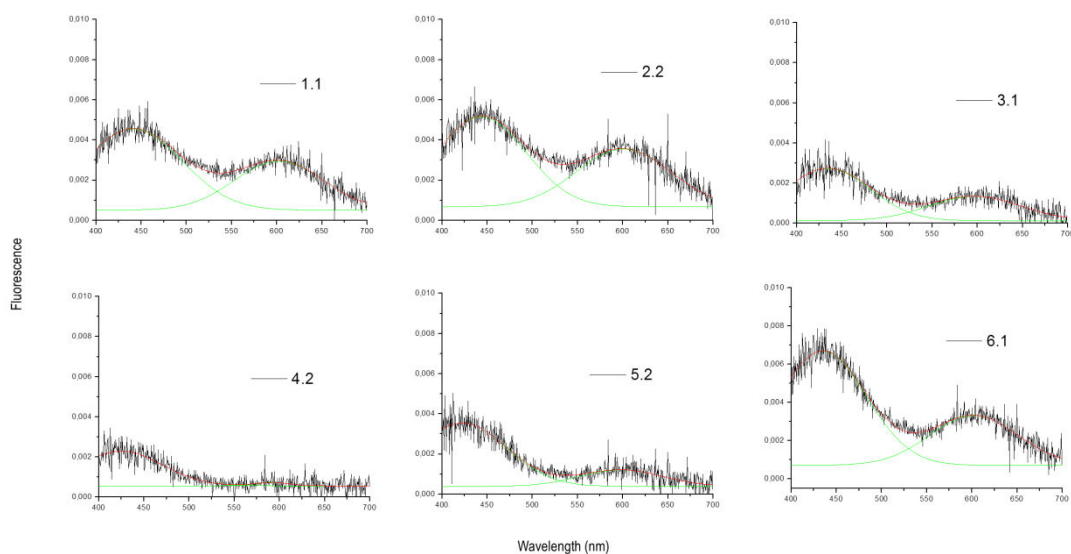


Fig. 118: Fluorescence spectra of the Minium samples. The spectra 1.1, 2.2, 3.1 correspond to one measurement area of the samples 1, 2 and 3 (mixture with linseed oil). The spectra 4.2, 5.2, 6.1 correspond to one measurement area of the samples 4, 5 and 6 (mixture with egg yolk).

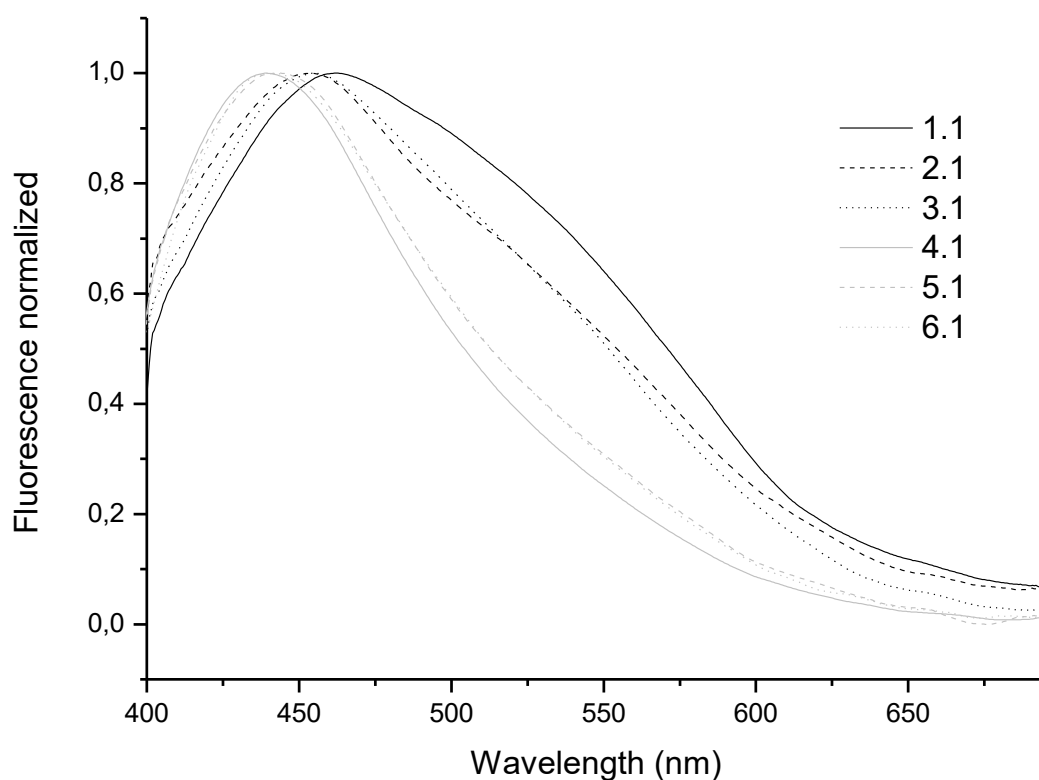


Fig. 119: Normalized fluorescence spectra of the Green Earth samples. The spectra 1.1, 2.1, 3.1 correspond to one measurement area of the samples 1, 2 and 3 (mixture with linseed oil). The spectra 4.1, 5.1, 6.1 correspond to one measurement area of the samples 4, 5 and 6 (mixture with egg yolk).

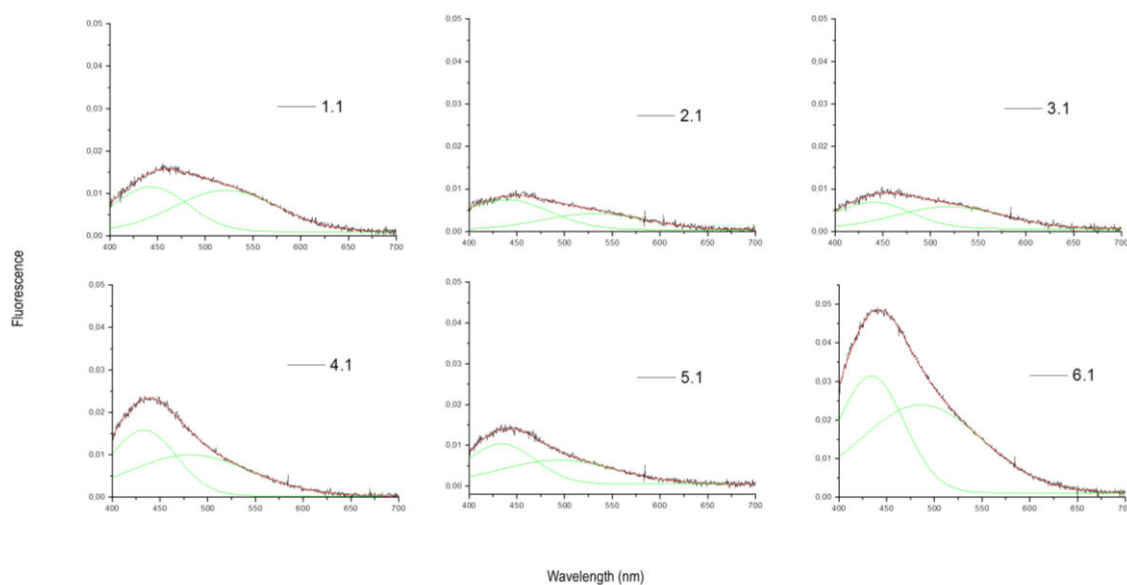


Fig. 120: Fluorescence spectra of the Green Earth samples. The spectra 1.1, 2.1, 3.1 correspond to one measurement area of the samples 1, 2 and 3 (mixture with linseed oil). The spectra 4.1, 5.1, 6.1 correspond to one measurement area of the samples 4, 5 and 6 (mixture with egg yolk).

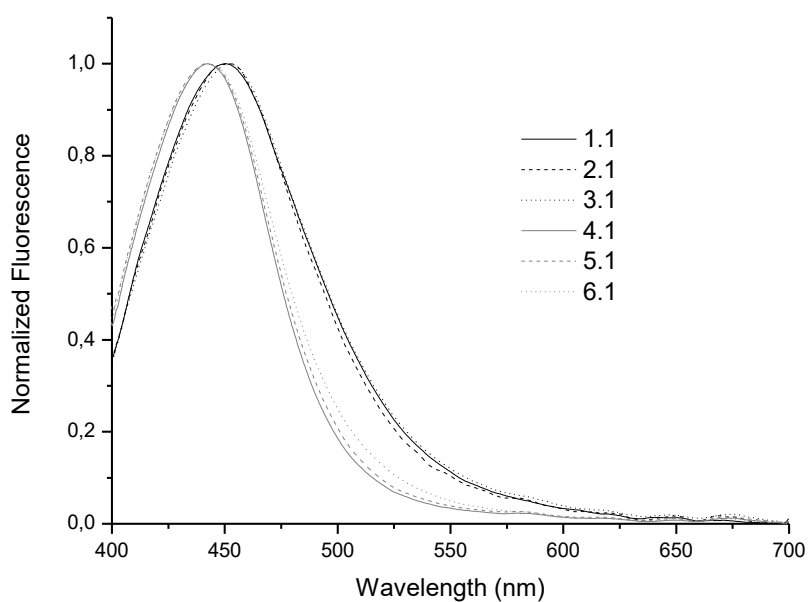


Fig. 121: Normalized fluorescence spectra of the light Ultramarine Blue samples. The spectra 1.1, 2.1, 3.1 correspond to one measurement area of the samples 1, 2 and 3 (mixture with linseed oil). The spectra 4.1, 5.1, 6.1 correspond to one measurement area of the samples 4, 5 and 6 (mixture with egg yolk).

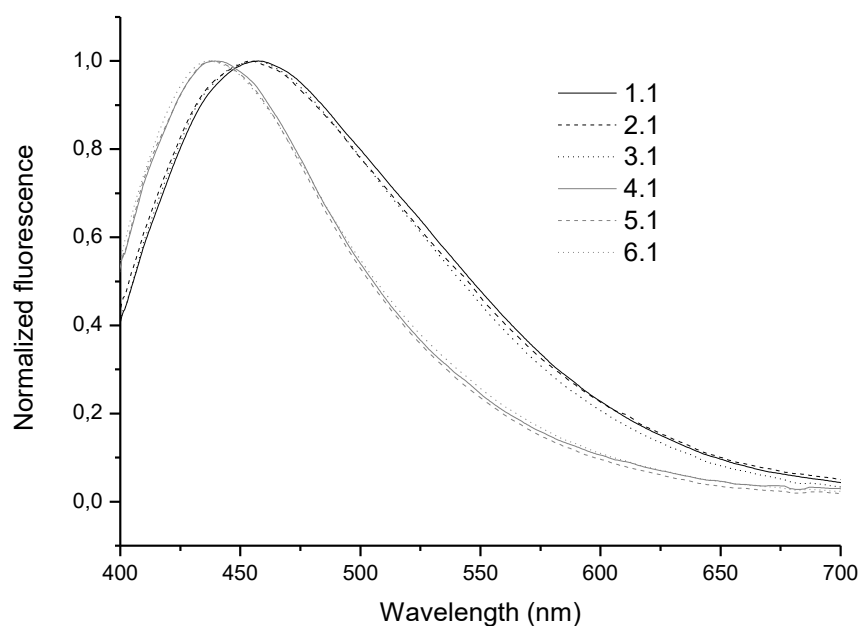


Fig. 122: Normalized fluorescence spectra of the Lead White samples. The spectra 1.1, 2.1, 3.1 correspond to one measurement area of the samples 1, 2 and 3 (mixture with linseed oil). The spectra 4.1, 5.1, 6.1 correspond to one measurement area of the samples 4, 5 and 6 (mixture with egg yolk).

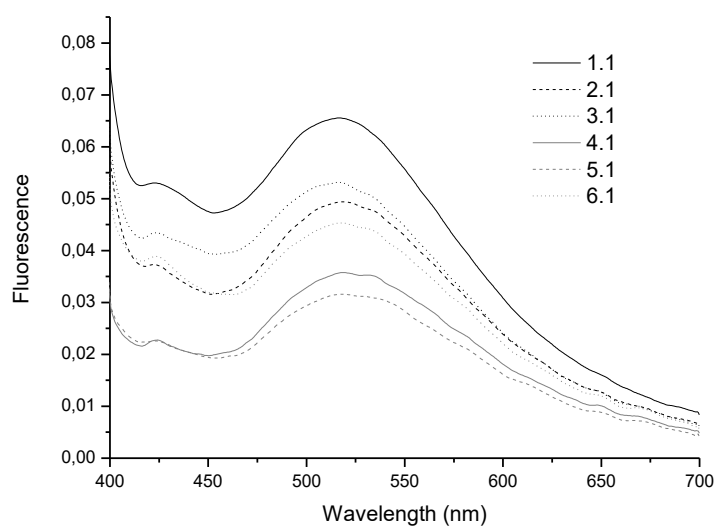


Fig. 123: Fluorescence spectra of the Zinc White samples. The spectra 1.1, 2.1, 3.1 correspond to one measurement area of the samples 1, 2 and 3 (mixture with linseed oil). The spectra 4.1, 5.1, 6.1 correspond to one measurement area of the samples 4, 5 and 6 (mixture with egg yolk).

The fluorescence spectra of the mixtures of Lead White and Raw Sienna Earth, presented in Fig. 124-a, show two broad bands and a shoulder. A high percentage of Lead White produces an intense peak at about 400-450 nm. We performed the deconvolution of the spectra of the samples of Raw Sienna Earth mixed with Lead White 10:90 blended either with linseed oil (spectrum n° 1 in the inset) or with egg yolk (spectrum n° 6 in the inset). Their fluorescence spectra are constituted by three bands at 430 nm, 450nm and 525 nm (spectrum n° 1); the last one shifts to 511 nm in the spectrum n° 6, see Fig. 124-b, Fig. 124-c The first band is assigned to the fluorescence emission of the binders, the other two peaks at longer wavelengths are probably caused by the reflected or scattered light of the Raw Sienna Earth. The deconvoluted bands centred at 430 nm and 450 nm are reported in Fig. 124-d.

The spectral features of the fluorescence spectra of the mixture of Lead White, Raw Sienna Earth and Green Earth are similar to those of the previous samples: they show a shoulder at a shorter wavelength, a band at about 450 nm and a second, broad band at longer wavelengths than above, see Fig. 125.

The fluorescence spectra of the white pigment mixtures, shown in Fig. 126, have the same behaviour as the fluorescence spectra of the Zinc White samples. This means that the presence of Lead White cannot be detected when it is mixed with Zinc White by means of UV fluorescence spectrometry. We can only ascertain that the low wavelength peak at about 425 nm is more pronounced compared with that of the Zinc White samples. Furthermore, a slight shift of the second broad band occurs between the linseed oil samples and the egg yolk samples. We will discuss in detail the white pigment mixtures in the next paragraph.

The fluorescence spectra of both mixtures of Lead White with Hematite and Zinc White with Hematite, presented in Fig. 127, show the fluorescence emission of Lead White and of Zinc White in linseed oil, respectively, and an additional third peak at long wavelengths due to the reflected and/or scattered light of the Hematite pigment.

The samples with a blend of Lead White and Zinc White mixed with Hematite displayed the spectral features of the Zinc White sample with addition of a third peak due to the reflected and/or

scattered light of the Hematite, shown in Fig. 128. Moreover, the fluorescence emission of these samples decreases with increasing the amount of Hematite.

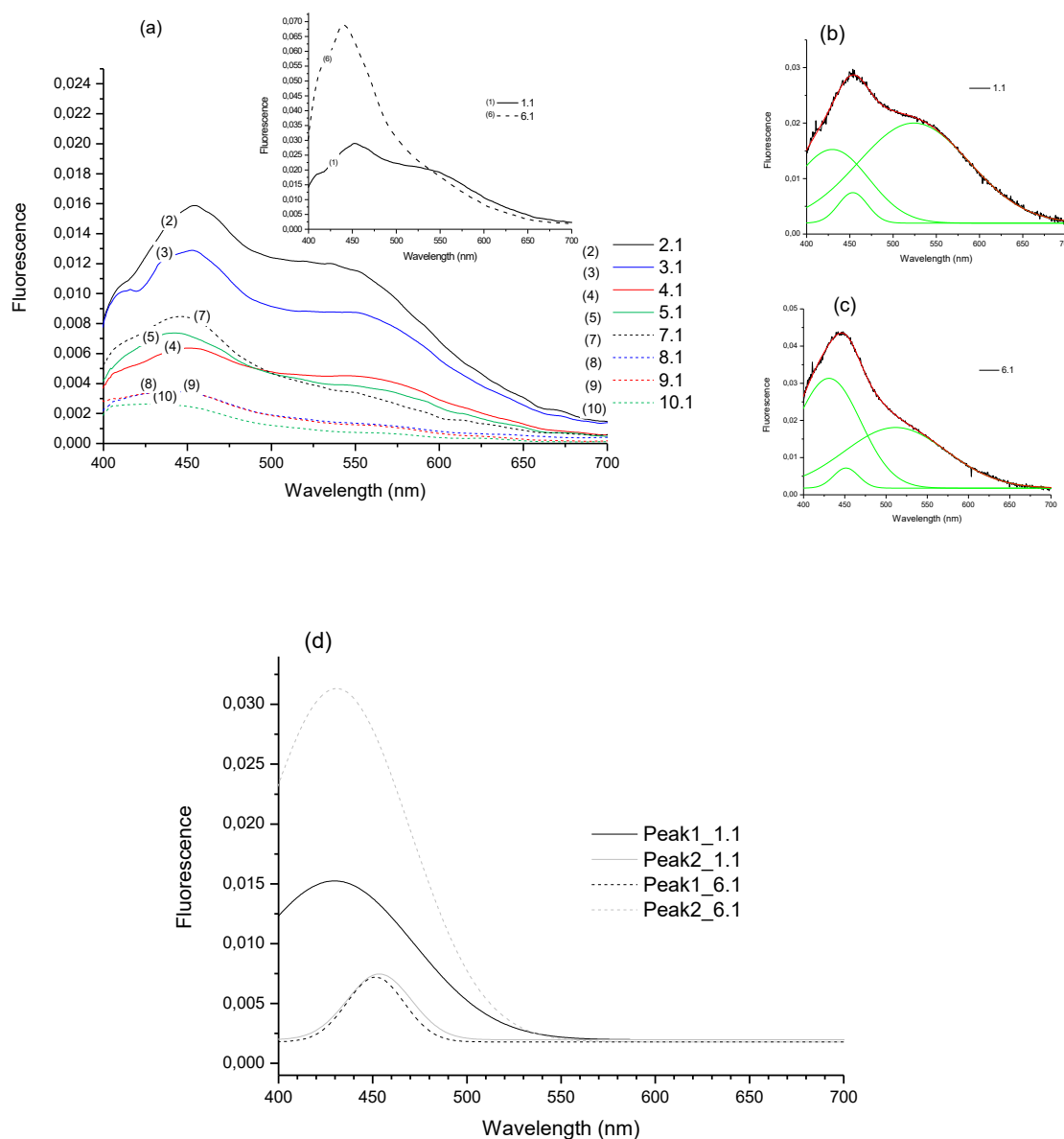


Fig. 124: a) Fluorescence spectra of the Lead White and Raw Sienna Earth samples. The spectra 1.1 (shown in the inset), 2.1 and 3.1, 4.1, 5.1 correspond to one measurement area of the samples 1, 2, 3, 4 and 5 (mixture with linseed oil). The spectra 6.1 (shown in the inset), 7.1, 8.1, 9.1 and 10.1 correspond to one measurement area of the samples 6, 7, 8, 9, and 10 (mixture with egg yolk). b) Deconvolution of the fluorescence spectrum of the sample 1.1. c) Deconvolution of the fluorescence spectrum of the sample 6.1. d) Deconvoluted bands centred at 430 nm and 450 nm obtained from the spectra of the samples 1.1 and 6.1.

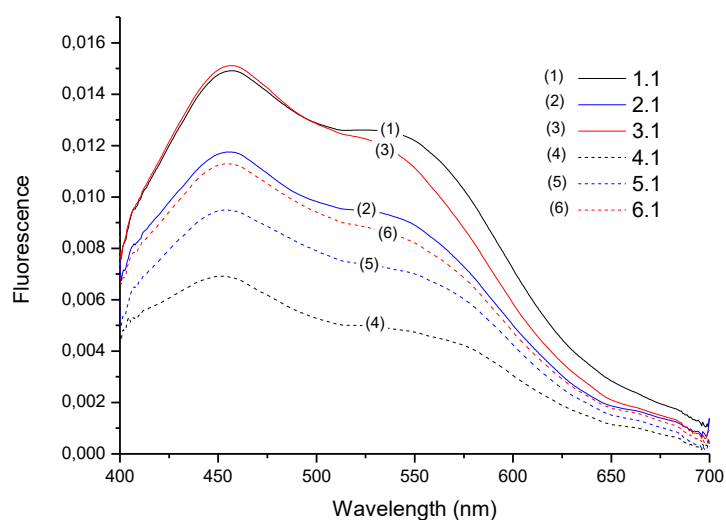


Fig. 125: Fluorescence spectra of the Lead White, Raw Sienna Earth and Green Earth samples. The spectra 1.1, 2.1, 3.1 correspond to one measurement area of the samples 1, 2 and 3 (mixture with linseed oil). The spectra 4.1, 5.1, 6.1 correspond to one measurement area of the samples 4, 5 and 6 (mixture with egg yolk)

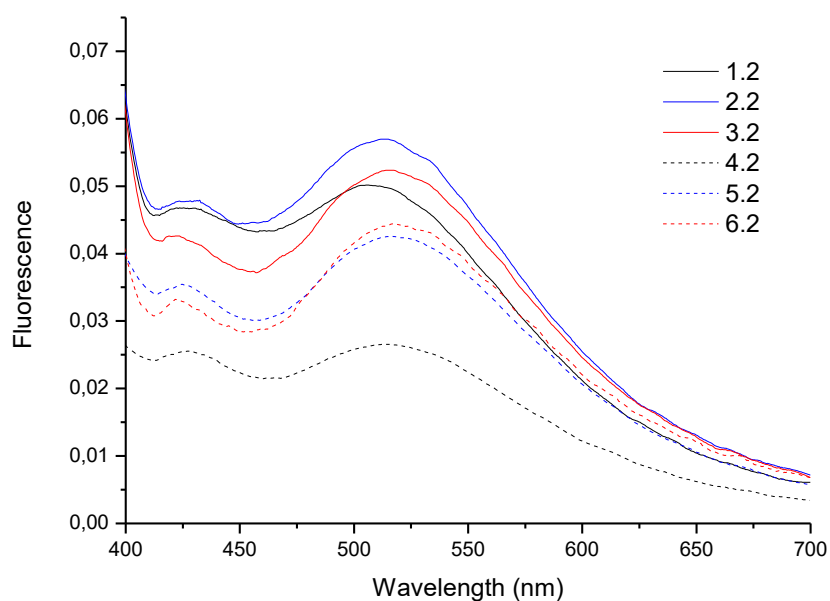


Fig. 126: Fluorescence spectra of Lead White and Zinc White samples. The spectra 1.2, 2.2, 3.2 correspond to one measurement area of the samples 1, 2 and 3 (mixture with linseed oil). The spectra 4.2, 5.2, 6.2 correspond to one measurement area of the samples 4, 5 and 6 (mixture with egg yolk).

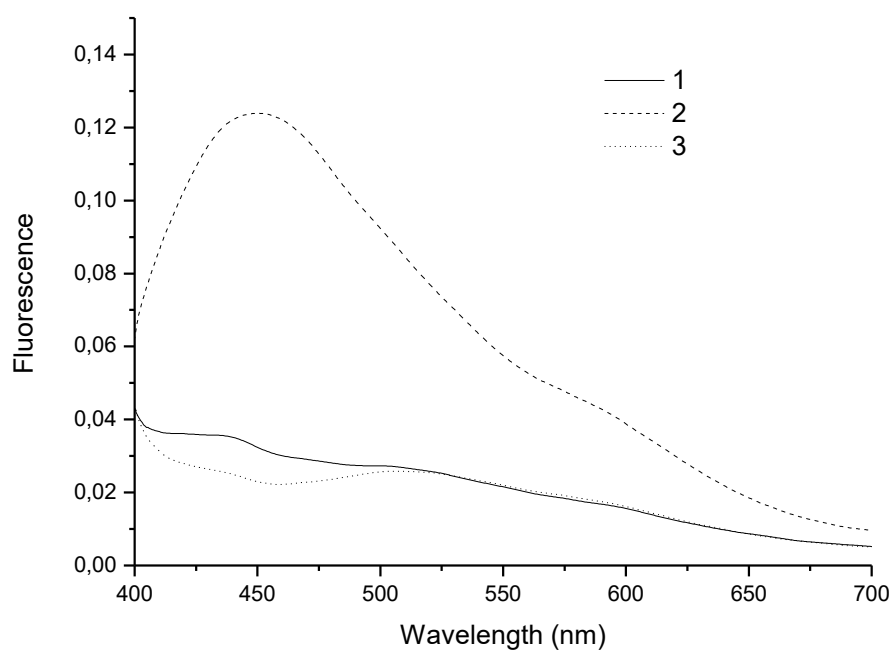


Fig. 127: Fluorescence spectra of the Zinc White and Hematite sample (1), the Lead White and Hematite sample (2) and the mixture of Lead White, Zinc White and Hematite (3). All the samples are mixed with linseed oil.

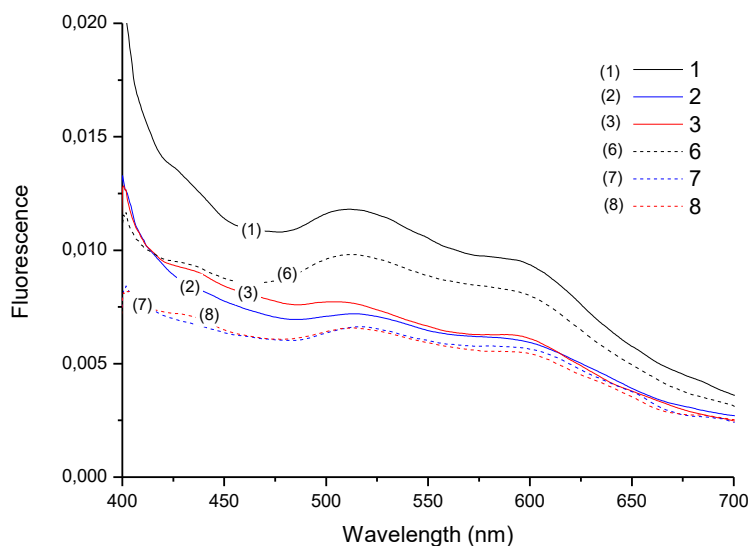


Fig. 128: Fluorescence spectra of samples prepared mixing Lead White, Zinc White and Hematite. The spectra 1, 2, 3 correspond to one measurement area of the samples 1, 2 and 3 (mixture with linseed oil). The spectra 6, 7, 8 correspond to one measurement area of the samples, 6, 7 and 8 (mixture with egg yolk).

2.2.4.3 Correction of UV-fluorescence spectra

We corrected the measured fluorescence spectra of four selected sets of samples for the auto-absorption, reflection and scattering effects taking into account the Kubelka-Munk theory [Verri G. et al. (2008)], according to the method presented in detail in Part I, chap. 1, par. 1.3.2.

The correction of the fluorescence of the Lead White samples presented in Fig. 129-a, showed that the auto-absorption, reflection and scattering effects are quite irrelevant in this case, since the corrected fluorescence spectra are very close to the acquired ones, Fig. 129-b; the correction just reduced the wavelength difference between the maxima of the linseed oil and the egg yolk samples fluorescence's.

The corrected fluorescence spectra of the Yellow Ochre samples, shown in Fig. 130-a, change significantly with respect to the acquired ones, Fig. 130-b. The spectra of the samples prepared with linseed oil display a broader band than the egg yolk samples; in addition the fluorescence emission increases with increasing the quantity of the binders.

The correction algorithm has produced good results also on the samples with the white pigments mixed with the Hematite, as shown in Fig. 131-a and Fig. 132-a. In fact we can confirm that the third band present in the measured fluorescence spectra at long wavelengths is due to the auto-absorption effects of the Hematite, since it disappears in the corrected spectra, Fig. 131-b and Fig. 132-b.

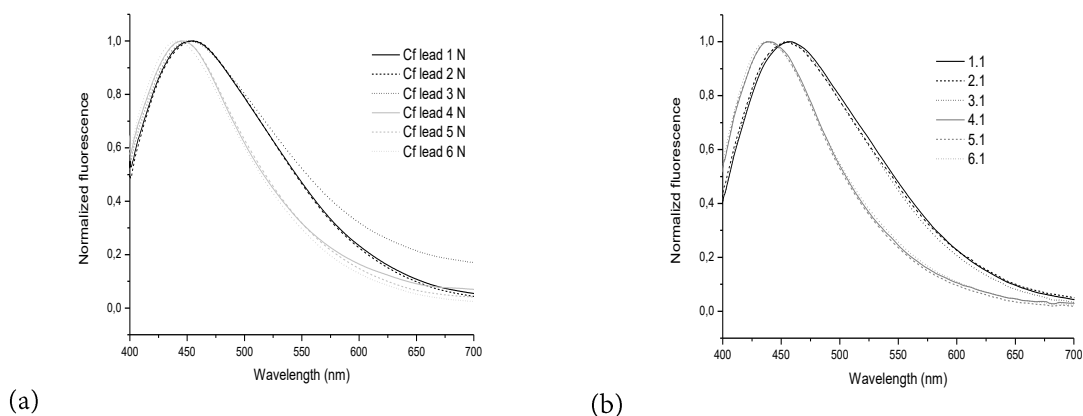


Fig. 129: Corrected fluorescence spectra (a) and fluorescence spectra (b) of the Lead White samples. The spectra 1, 2, 3 correspond to one measurement area of samples 1, 2 and 3 (mixture with linseed oil). The spectra 4, 5, 6 correspond to one measurement area of samples 4, 5 and 6 (mixture with egg yolk). The spectra are normalized to the maximum value.

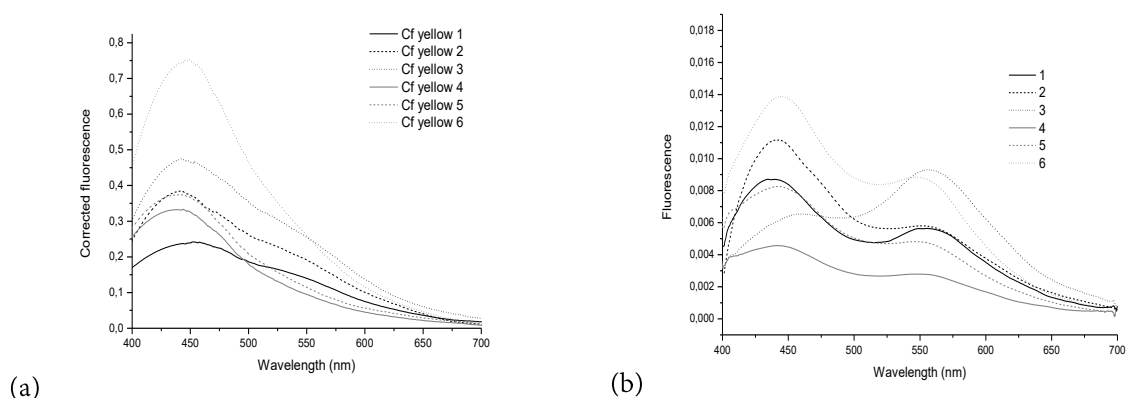


Fig. 130: Corrected fluorescence spectra (a) and fluorescence spectra (b) of the Yellow Ochre samples. The spectra 1, 2, 3 correspond to one measurement area of samples 1, 2 and 3 (mixture with linseed oil). The spectra 4, 5, 6 correspond to one measurement area of samples 4, 5 and 6 (mixture with egg yolk).

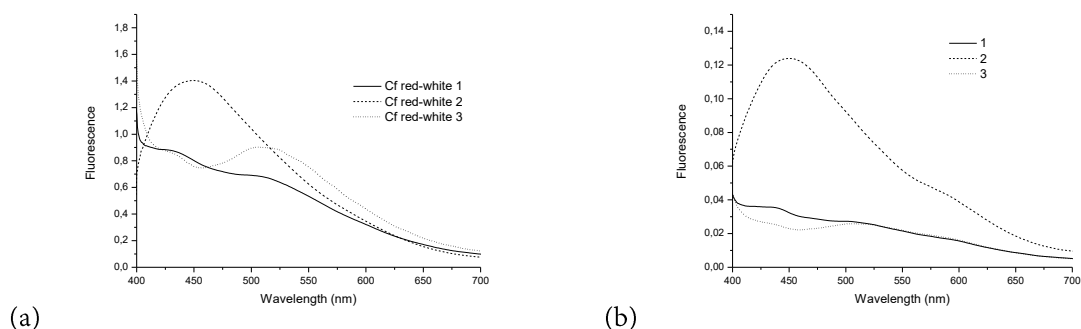


Fig. 131: Corrected fluorescence spectra (a) and fluorescence spectra (b) of the Zinc White and Hematite sample (1), the Lead White and Hematite sample (2) and the mixture of Zinc White, Lead White and Hematite sample (3) .

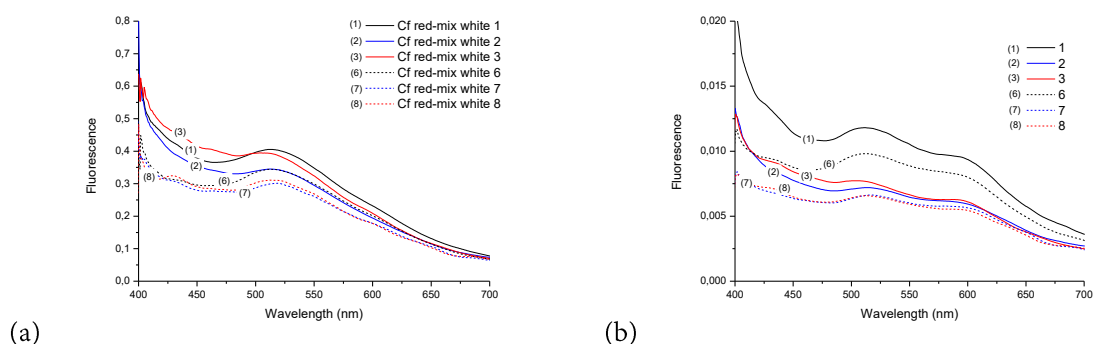


Fig. 132: Corrected fluorescence spectra of the mixtures of Lead White, Zinc White and Hematite samples. The spectra 1, 2, 3 correspond to one measurement area of samples 1, 2 and 3 (mixture with linseed oil). The spectra 6, 7, 8 correspond to one measurement area of samples 6, 7 and 8 (mixture with egg yolk).

2.2.4.4 Multispectral imaging

We acquired the multispectral reflectance imaging and the multispectral UV-fluorescence imaging of all the samples. In this section we report the main results pertinent to the samples with Zinc White because we can identify the presence of this pigment from the reflectance spectral features. In Fig. 133 present the multispectral reflectance images of the mixtures of Lead White and Zinc White, presented in Fig. 98, taken with the filters at 380 nm, 390 nm, 400 nm, 410 nm,

420 nm, 450 nm, 470 nm, 500 nm, 532 nm, 550 nm, 600 nm, 650 nm, 680 nm, 700 nm, and 750 nm. We can notice that the samples containing Zinc White show a darker image than the Lead White samples with the filter at 380 nm. In fact the reflectance spectra are weaker in the UV region, as shown in Fig. 108 and Fig. 113. We can notice the same behaviour for the samples with Zinc White and Hematite and Zinc White with Lead White and Hematite shown in Fig. 134. By means of the 'false' RGB combination of the filters at 380 nm, 400 nm and 410 nm, shown in Fig. 135, we have emphasized this aspect: the blue colour indicates the presence of Zinc White while the light red the presence of Lead White alone.

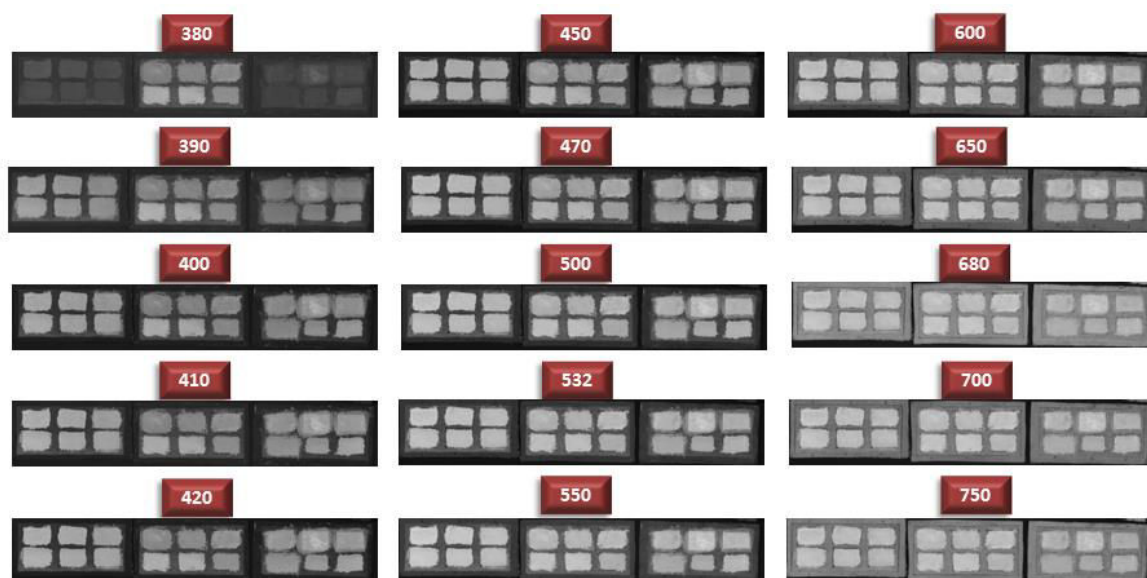


Fig. 133: In the left of each panel: multispectral reflectance images of the mixtures of Lead White and Zinc White samples. In the centre of each panel: multispectral reflectance images of Lead White samples. In the right of each panel: multispectral reflectance images of Zinc White samples.

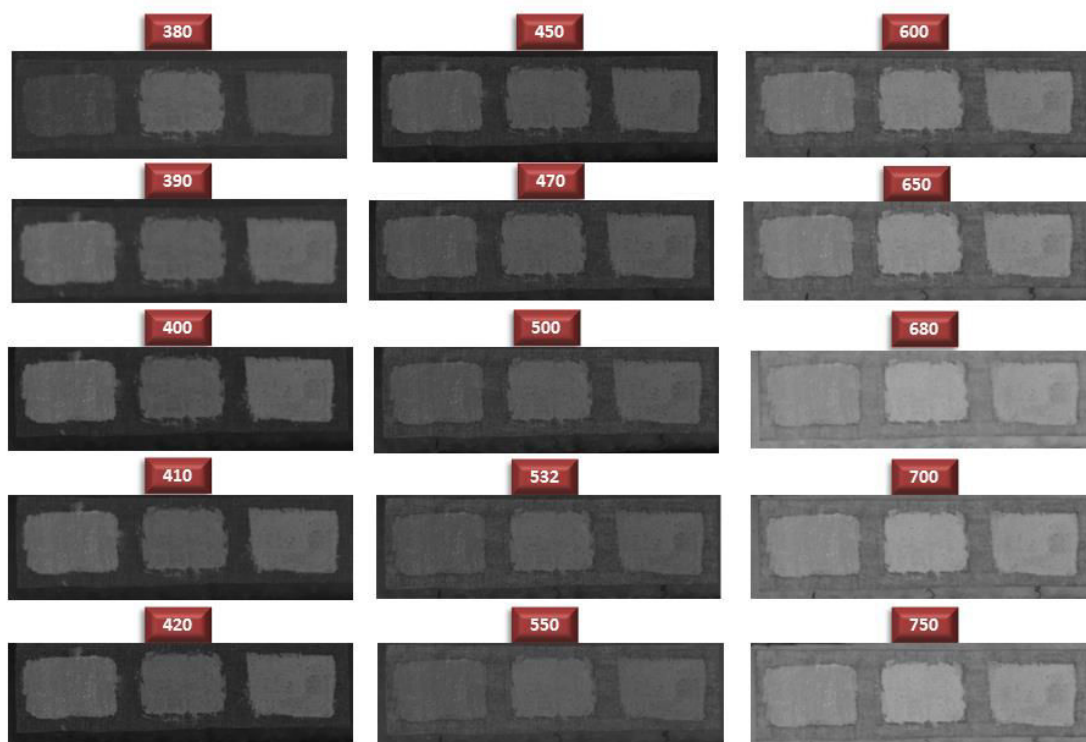


Fig. 134: Multispectral reflectance images of the Zinc White with Hematite, Lead White with Hematite and the mixtures of Lead White, Zinc White and Hematite samples.



Fig. 135: From left to right: 'False' RGB combination of the multispectral reflectance images at 380 nm, 400 nm and 410 nm of the Zinc White with Hematite, Lead White with Hematite and the mixtures of Lead White, Zinc White and Hematite samples.

We applied the correction of the UV-fluorescence spectra employed in the previous paragraph onto the multispectral UV fluorescence images in order to verify the possibility to isolate the “true” fluorescence phenomena also on the images. We applied this algorithm on the sample with Zinc White and Hematite (n°3) and on the sample containing Lead White, Zinc White and Hematite (n°1) and we obtained good results, reported in this section as the reconstruction of the fluorescence spectra obtained from the multispectral UV-fluorescence images, Fig. 136 and Fig.

137. It is clear that the correction algorithm produces a decrease of the fluorescence spectra at long wavelengths as in the fluorescence spectra acquired with the spectrometer. This means that the correction employed on fluorescence spectroscopy can be used also for the multispectral UV fluorescence imaging.

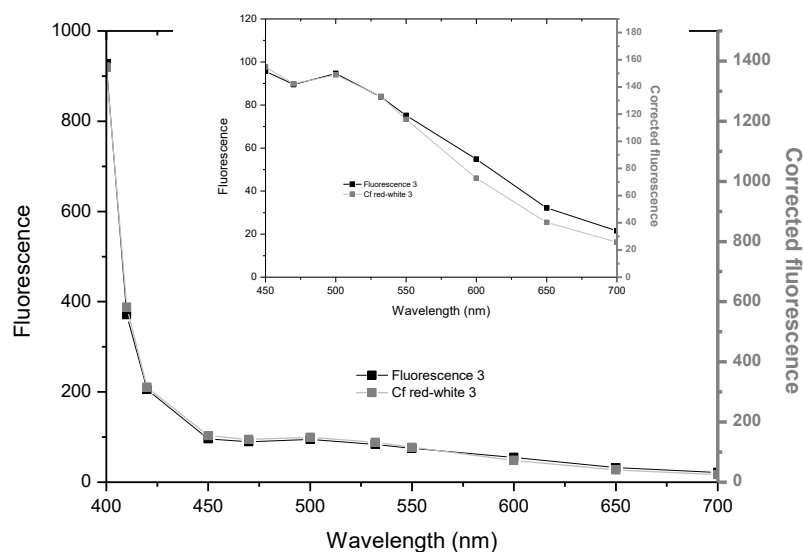


Fig. 136: Reconstruction of the fluorescence spectra of the multispectral UV-fluorescence images of a mixture of Zinc White and Hematite (sample n° 3).

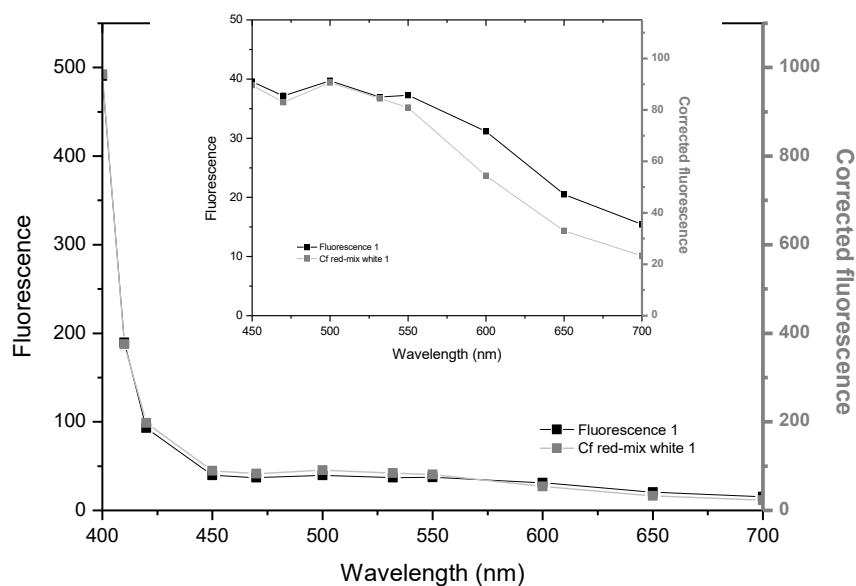


Fig. 137: Reconstruction of the fluorescence spectra of the multispectral UV-fluorescence images of a mixture of Lead White, Zinc White and Hematite (sample n° 1).

2.2.5 Conclusions

The potentiality of FORS, fluorescence spectroscopy and multispectral reflectance and UV-fluorescence imaging were investigated on ad hoc prepared pictorial layers. The spectral features of simple pictorial layers constituted by a pigment and a binder (either egg yolk or linseed oil) mixed in different ratios and those of complex pictorial layers composed of two or more pigments and a binder (either egg yolk or linseed oil) in different ratios were analysed with the aim of finding the fingerprints for recognizing all the materials with which they are made.

FORS spectra are almost ineffective for recognizing the binders for most samples, except for the Ultramarine Blue and the Lead White samples. The reflectance of Ultramarine Blue pigment in linseed oil samples shows a band with a maximum at about 450 nm, shifted to long wavelengths with respect to egg yolk ones; the reflectance of Lead White mixed with linseed oil is higher than that of egg yolk mixtures at short wavelengths.

We also found that the addition of a small quantity of a pigment can change significantly the reflectance curve of a pictorial layer; instead, the addition of Lead White, the reflectance of which appears almost flat in the entire visible range, is ineffective.

Fluorescence spectroscopy can be useful to recognize some pigments present in the mixtures, such as Zinc White, or the binders (egg yolk or linseed oil) only in the case of a few pictorial layers, such as Green Earth, Ultramarine Blue and Lead White. The deconvolution of the fluorescence spectra revealed the presence of some emission bands due to the auto-absorption phenomenon. We applied the correction procedure suggested by Verri et al. (2008), to eliminate the auto-absorption features from the emission spectra in order to identify the fluorescent species. By obtaining the “true” fluorescence we have a good distinction between the egg yolk binder from the linseed oil binder.

Multispectral reflectance imaging was useful for the identification of Zinc White in mixtures using the “false” RGB combination of the images taken at 380 nm, 400 nm and 410 nm.

The correction procedure applied for the UV-fluorescence spectra was also applied on the multispectral UV-fluorescence images, obtaining good results.

2.3 White pigment identification by means of multispectral imaging

2.3.1 Introduction

White pigments are the most widely employed pictorial materials encountered in easel paintings since they are used to obtain the light hues. Although they were generally associated with coloured pigments, the artists often mixed them in order to improve the aesthetic qualities of the painting. For example, when Zinc White is added to Lead White, the pictorial layers preserve good optical properties due to the stability of Zinc White to photo-ageing processes [Feller R. L. (1985)].

From ancient times to the present, Lead White, Zinc White and Titanium White are the most important white pigments used for paintings. Among them, Lead White has been the most important white pigment. It has been used through the ages and it has been the only white pigment employed in the European easel paintings until the nineteenth century, when zinc oxide replaced it.

The Lead White pigment is a basic lead(II) carbonate, $\text{PbCO}_3 \cdot \text{Pb(OH)}_2$, and it has been used both in mixtures with other pigments and in the “imprimatura” (canvas primer). In the pictorial layer execution, Lead White was ground in oil and in egg tempera (the latest procedure was often used in the early Italian panel painting [Roy A. ed., (1986)]) and it presents a high hiding power due to its high refractive index, even in oil.

Despite the common use in the modern paintings, Lead White was slowly abandoned starting from the 1780 when Zinc White was introduced. The most important reason for abandoning Lead White is its high toxicity.

The Zinc White pigment is a zinc oxide, ZnO , known since antiquity. However, it appears in paintings only at the end of the eighteenth century. It presents approximately the same refractive index of Lead White, but it has less hiding power in oil due to the lower spreading capacity in oil [Feller R. L. (1985)].

In the 1920's also Titanium White was introduced. Titanium White is a titanium dioxide, TiO_2 , that can have two crystallographic forms, anatase and rutile. In the beginning, Rutile was employed as a white pigment and it showed to possess a better hiding power than anatase; the latter one was widely used since 1937 due to the difficulty of producing synthetic rutile [Bacci M. et al. (2007)].

From this short introduction, it appears clear that the identification of a specific white pigment or a white pigment mixture is fundamental for the authentication of paintings. The diagnostic methods used for the pigment identification can be divided into two categories: non-destructive and micro-destructive. The non-destructive diagnostic methods are preferred by art historians because the methodological approach does not include any sampling.

Probably XRF spectroscopy is the most specific analysis used, but, despite its low costs and ease of use, reveals very small portions of the painting (1-2 mm maximum).

The reflectance and UV-fluorescence spectroscopies have been used for pigment identification [Bacci M. et al. (2007), Clementi C. et al. (2012)], but the application on white pigment mixtures is still quite unexplored. However, these two techniques have the same limitations as XRF: the analysed spot can be at maximum 1 mm of diameter.

Another approach could be the use of the UV fluorescence photography but, in this case, it is difficult to distinguish small differences of fluorescence due to the small sensitivity of the color camera in the short wavelength region.

In recent years multispectral and hyperspectral imaging methods are replacing traditional UV-VIS spectroscopy and UV-fluorescence photography due to the possibility to map pigments with the acquisition of spectral images of UV-fluorescence and reflectance.

The aim of this section is to characterize the spectral features of white pigment mixtures in different binders (egg yolk and linseed oil) in order to understand if it is possible to isolate the spectral features of the pure pigments. The results achieved will be used for the selection of the multispectral images required for mapping the white pigments and for recognizing the egg yolk binder from the linseed oil one.

2.3.2 Materials

We realized six "pure" pictorial samples using three white pigments: Lead White, Zinc White and Titanium White mixed with two different binders: egg yolk and linseed oil.

For this study we used the Lead White pigment produced by Kremer pigmente, the Zinc White and the Titanium White (rutile) pigments produced by Zecchi (Florence, Italy).

Eighteen samples were realized mixing two white pigments with different ratios (30:70, 50:50 and 70:30 % in volume). Each "pure" and each mixed sample ($0.40\text{g} \pm 0.1\text{g}$) was combined with linseed oil ($0.20\text{g} \pm 0.03\text{g}$) for the oil samples or with egg yolk ($0.04 \pm 0.02\text{g}$) and distilled water in order to obtain a good spreading property. For the Lead White in egg yolk, we prepared two samples with different quantities of the binder. All the samples were spread on the microscope slides shown in Fig. 138, where Pb yolk ++ labels the sample with the highest quantity of egg yolk. All the samples were analysed immediately after drying and then after two months of storage in the darkness.

2.3.3 Methods

Reflectance measurements were carried out with both spectrophotometers: a Minolta CM-2300d and an Avantes AvaSpec-2048 A-USB1. We used two different devices complementary to each other. We used a barium sulfate pellet as diffuse reference sample.

We acquired the fluorescence spectra excited at $365 \pm 2\text{ nm}$ by means of a Horiba FluoroMax-2 spectrometer. The sample surfaces were placed at 45° with respect to the excitation source and to the collection position.

The multispectral imaging was performed with the QSI 583-w camera equipped with the Micro-Nikkor optical system and the following narrow-band interferential filters: 380 nm, 390 nm, 400 nm, 410 nm, 420 nm, 450 nm, 470 nm, 500 nm, 550 nm, and 600 nm.

1		10		1	Pb70Zn30 yolk	14	Pb50Ti50 oil
2		11		2	Pb50Zn50 yolk	15	Pb30Ti70 oil
3		12		3	Pb30Zn70 yolk	16	Ti70Zn30 oil
4		13		4	Pb70Ti30 yolk	17	Ti50Zn50 oil
5		14		5	Pb50Ti50 yolk	18	Ti30Zn70 oil
6		15		6	Pb30Ti70 yolk	19	Pb yolk ++
7		16	*	7	Ti70Zn30 yolk	20	Pb yolk
8		17		8	Ti50Zn50 yolk	21	Ti yolk
9		18		9	Ti30Zn70 yolk	22	Zn yolk
19				10	Pb70Zn30 oil	23	Pb oil
20		23		11	Pb50Zn50 oil	24	Ti oil
21		24		12	Pb30Zn70 oil	25	Zn oil
22		25		13	Pb70Ti30 oil	*	Barium sulfate

Fig. 138: Samples analyzed

2.3.4 Results and discussion

2.3.4.1 Spectroscopic analysis

The reflectance spectra and their first derivatives of the “pure” white pigments mixed with egg yolk or linseed oil are reported in Fig. 139 and Fig. 140, respectively.

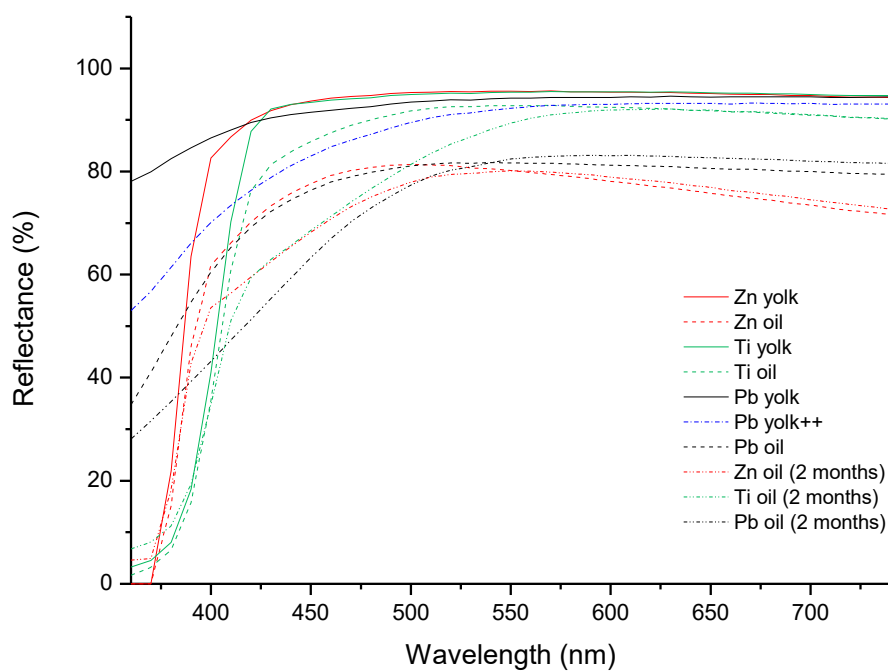


Fig. 139: Reflectance spectra of Zinc White, Lead White and Titanium White mixed with egg yolk or linseed oil. The acquisitions were performed with the Minolta instrument

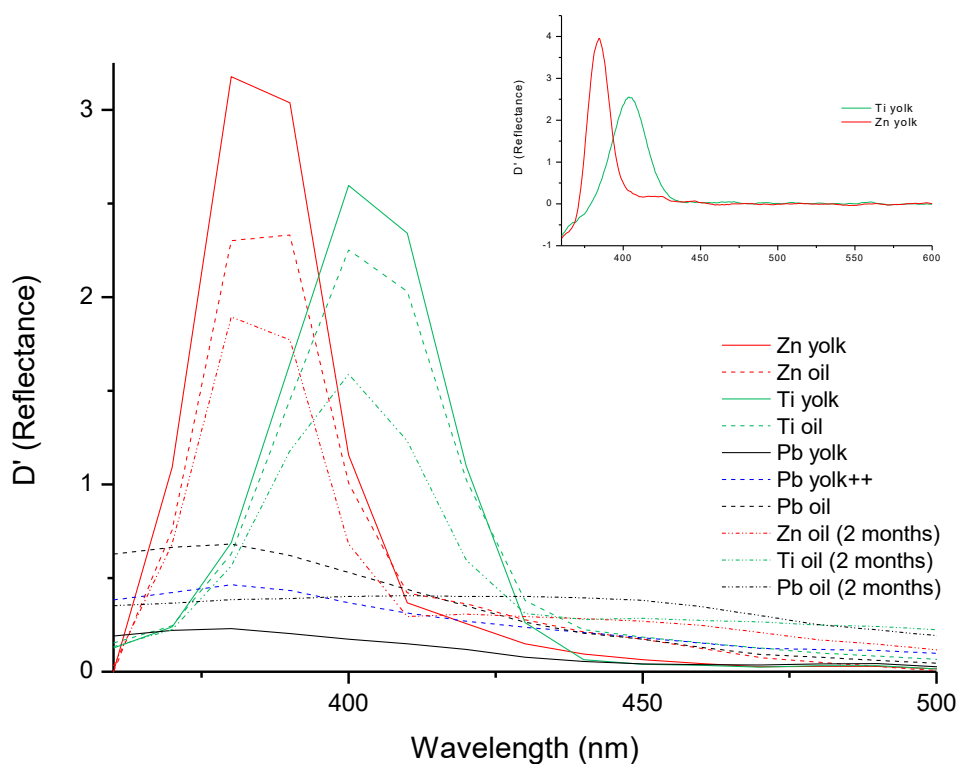


Fig. 140: First derivative of the reflectance spectra of Zinc White, Titanium White, Lead White mixed with egg yolk or linseed oil calculated from the acquisitions with the Minolta instrument. Top panel: first derivative of the reflectance spectra of zinc and Titanium White in yolk calculated from the measurements with the Avantes device.

Zinc White

The reflectance spectra of Zinc White have a step-like shape, with an inflection point at $384,2 \pm 0.8$ nm, that remains roughly in the same position regardless of the binder used, see Fig. 140. An absorption band present in the UV range, Fig. 139, lead to a yellower tone of this pigment with respect to Lead White.

In the visible range, the reflectance of the samples with oil are lower than that ones with egg yolk. After 2 months the reflectance spectrum of the samples with oil presents two shoulders: one at about 400 nm (the same shoulder present in the reflectance of other samples) and a second weak one at about 470 nm. This suggests a yellowing of the sample due to the absorption of blue light.

The fluorescence emission of Zinc White, shown in Fig. 141, presents a narrow UV emission band with the maximum at about 380 nm, and a broader band situated in the range 460-580 nm (centered at 500 nm). The fluorescence spectra do not change considerably between the oil and the egg yolk samples.

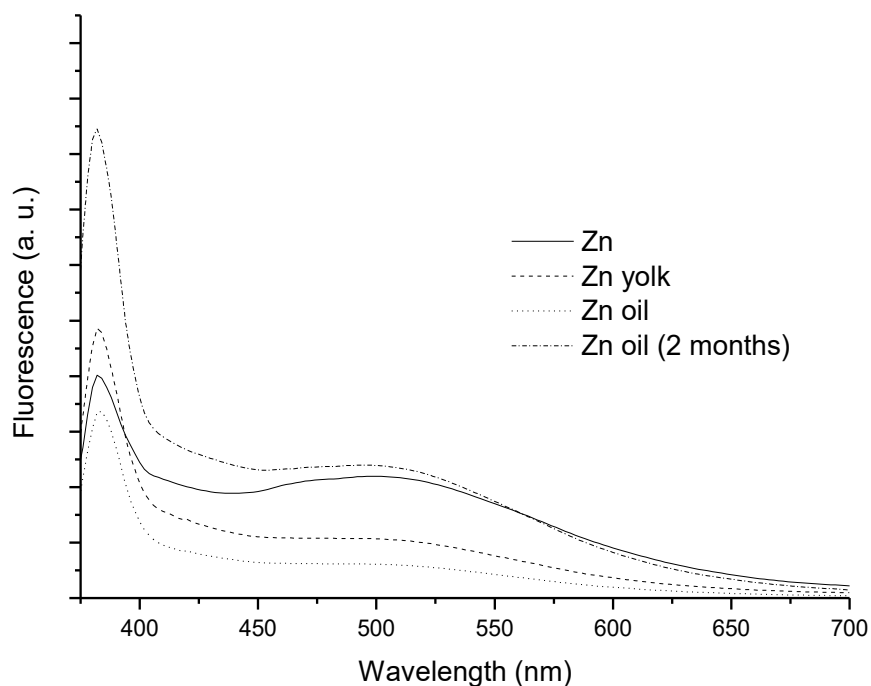


Fig. 141: Fluorescence emission of Zinc White powder and Zinc White in egg yolk or linseed oil

Titanium White

The reflectance spectra of Titanium White, Fig. 139, have a step-like shape with the inflection point at $403,6 \pm 0,8$ nm, that remains roughly in the same position regardless of the binders used, see Fig. 140. As in the case of the Zinc White pigment, also the Titanium White absorbs in the UV range, giving a yellower tone than Lead White. Although their similar reflectance shapes, it is possible to distinguish Titanium White from Zinc White thanks to a shift of 20 nm of the inflection point.

The fluorescence emission of Titanium White is characterized by a broad band from 400 nm to 500 nm with two weak peaks at 412 nm and 466 nm. The intensity ratio between these two fluorescence emissions decreases in oil and after 2 months of natural ageing the first peak becomes a shoulder and the second one a strong peak, see Fig. 142.

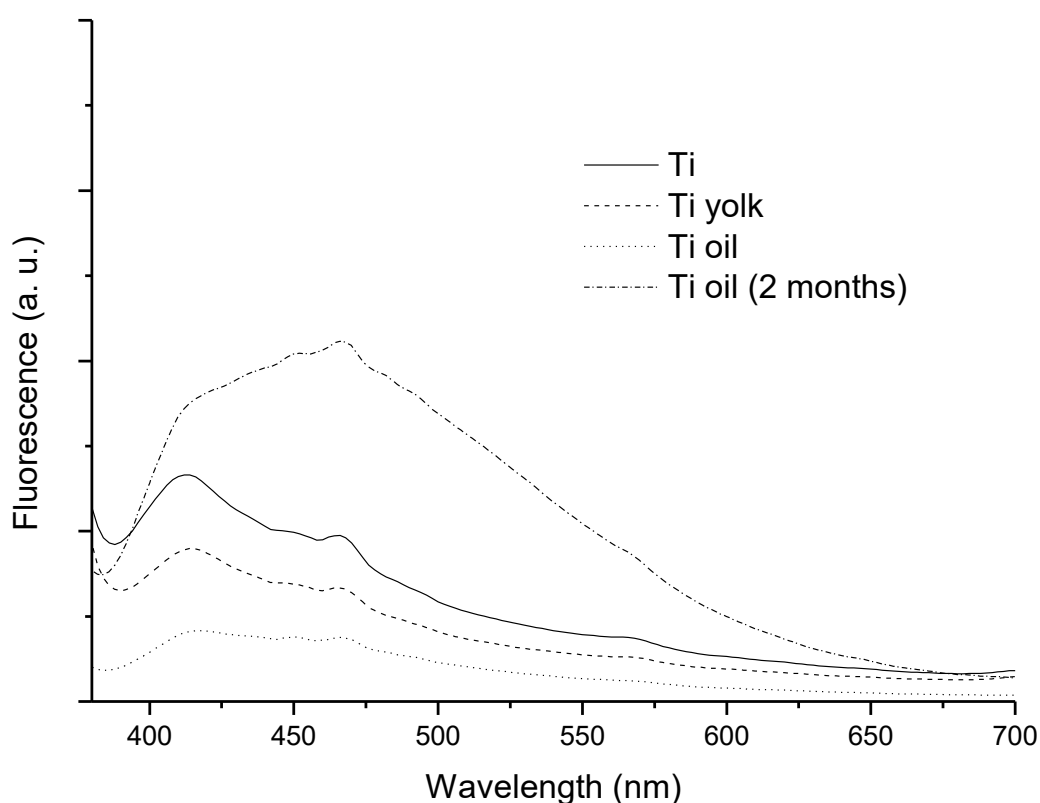


Fig. 142: Fluorescence emission of Titanium White powder and Titanium White in egg yolk or linseed oil

Lead White

The reflectance spectra of Lead White shows high reflectance values at short wavelengths, Fig. 139. The Lead White reflectance of oil samples is lower than that of egg yolk samples. After 2 months, the inflection point in the reflectance spectrum of Lead White in oil samples presents a strong shift towards longer wavelengths.

The fluorescence emission of Lead White powder is quite flat in the entire visible range, implying

a white fluorescence emission, see

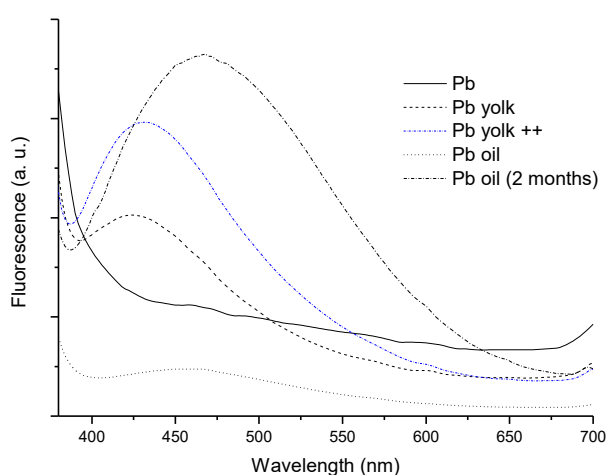


Fig. 143. The presence of the egg yolk induces a fluorescence emission band centred at 420 nm, the fluorescence intensity increases adding more binder. When Lead White is dispersed in linseed oil, the broad band maximum shifts towards long wavelengths, up to about 468nm. After 2 months of natural ageing, we observed an increase of the fluorescence intensity.

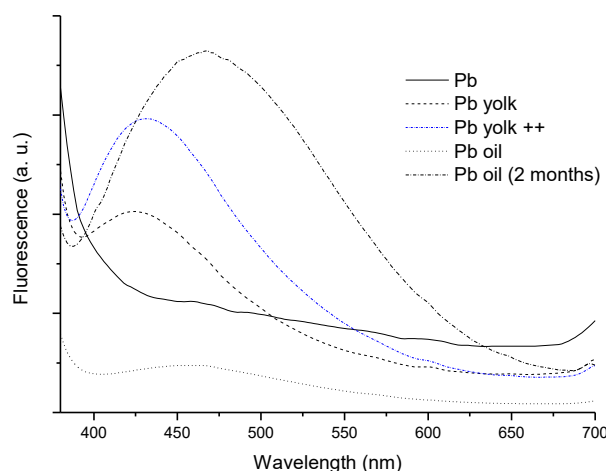


Fig. 143: Fluorescence emission of Lead White powder and Lead White in egg yolk or linseed oil

Lead and Zinc White

The reflectance spectra of the lead and Zinc White mixture present the same spectral features of Zinc White, also in the Pb/Zn ratio of 70/30 (% in volume), see Fig. 144. The reflectance of the sample with the Pb/Zn ratio 70/30 is lower than that of the other ones, in particular it is above that of the oil samples. The Pb/Zn ratios 50/50 and 30/70 reflectance's present an inversion of the reflectance curves at 480 nm (for the dried oil samples) and at 530 nm (for oil aged samples): in fact the curve of the Pb/Zn ratio 50/50 in dried oil presents a lower reflectance at $\lambda < 480$ nm than the one of the Pb/Zn ratio 30/70 and it occurs the contrary for $\lambda > 480$ nm. The same behaviour is shown by the curves of the aged oil samples.

In spite of the presence of Lead White, we observed an absorption band in the UV range, alike “pure” Zinc White samples.

The fluorescence emission of the lead and Zinc White mixtures shows a spectral behaviour similar to that of the Zinc White samples. The broad band at long wavelengths is less distinguishable in egg yolk samples, Fig. 145.

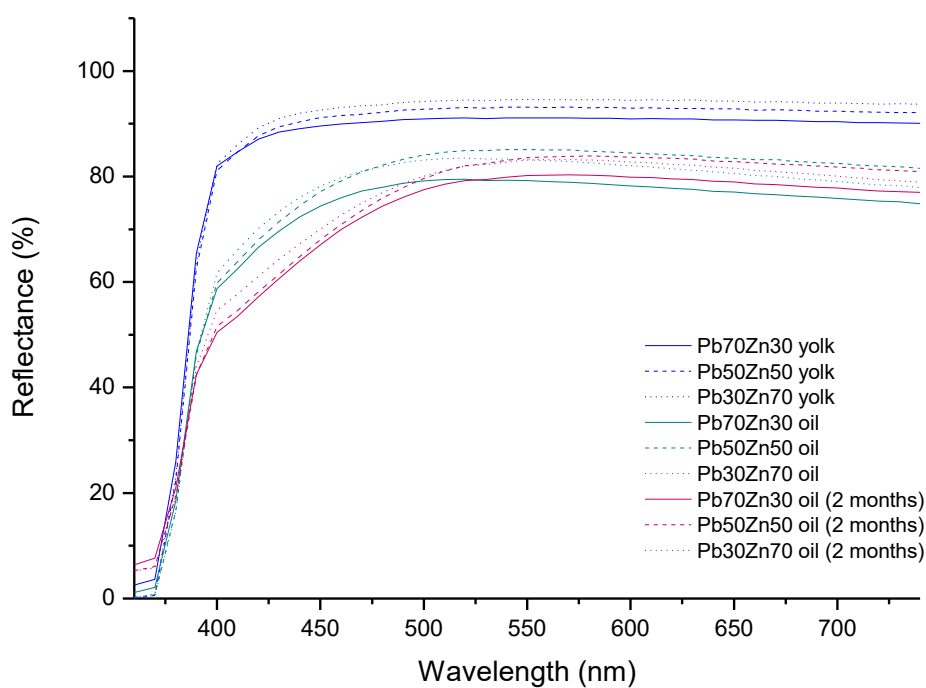


Fig. 144: Reflectance spectra of mixtures of Lead White and Zinc White with egg yolk or linseed oil.

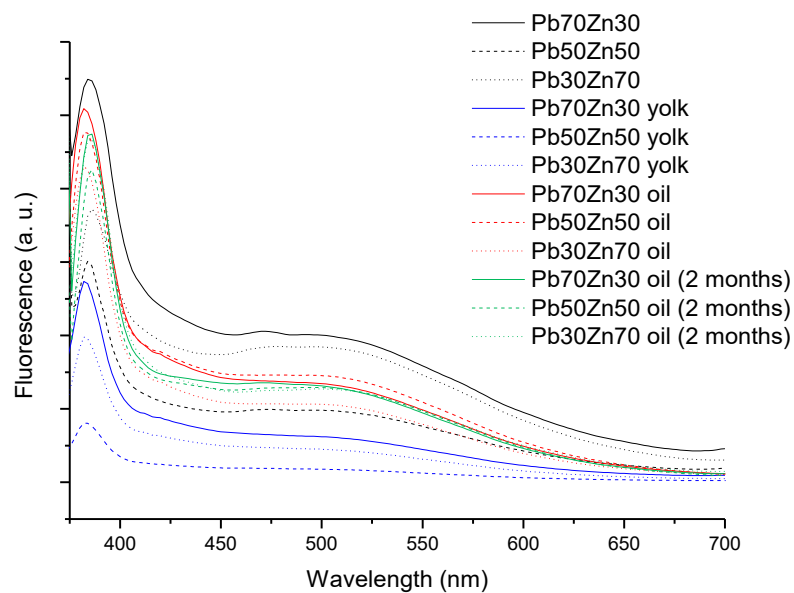


Fig. 145: Fluorescence emission of Lead White and Zinc White with egg yolk and linseed oil

Lead and Titanium White

The reflectance spectra of the lead and Titanium White mixtures present the same spectral features of the Titanium White, also for the Pb/Zn ratio 70/30 (% in volume), Fig. 146. In spite of the presence of Lead White, an absorption band is present in the UV range, alike “pure” Titanium White samples. The oil samples present a reduction of the reflectance in the blue region.

The fluorescence spectra revealed that the fluorescence emission at 466 nm increases in the aged oil samples, alike the “pure” Titanium White, for this reason we can distinguish samples prepared with egg yolk from those prepared with linseed oil, Fig. 147.

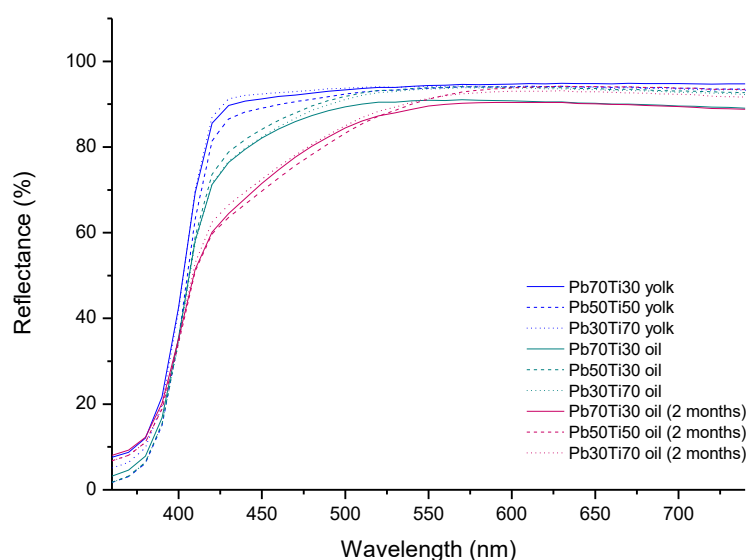


Fig. 146: Reflectance spectra of Lead White and Titanium White with egg yolk or linseed oil.

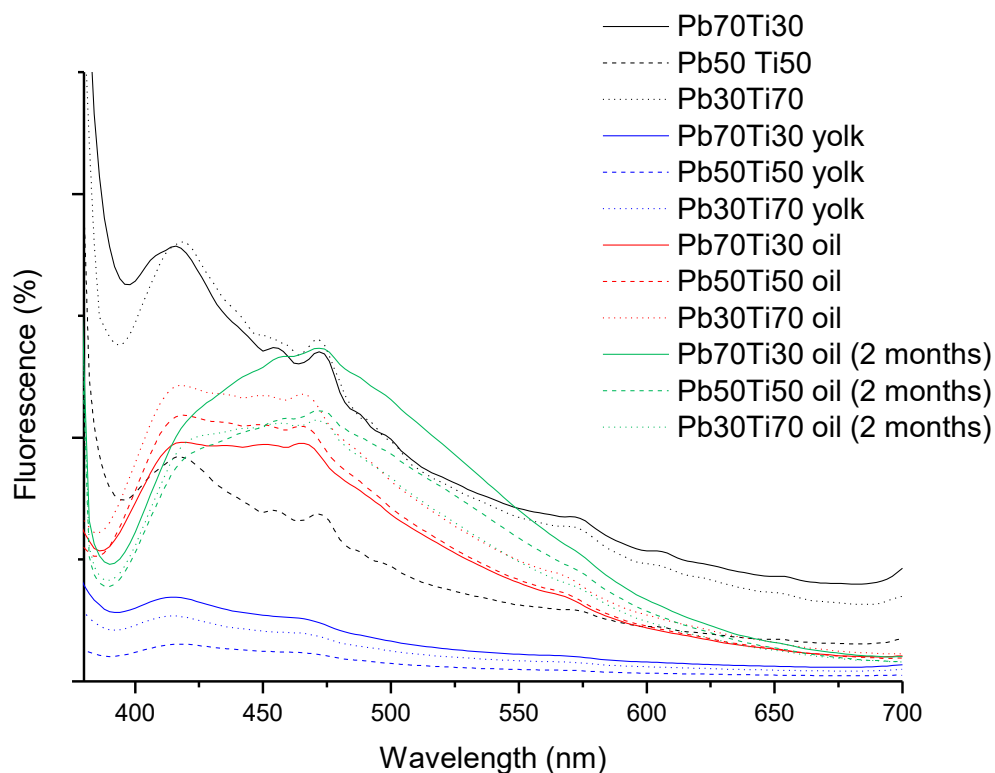


Fig. 147: Fluorescence spectra of Lead White and Titanium White with egg yolk or linseed oil.

Titanium and Zinc White

The reflectance spectra of Zinc White and Titanium White mixtures, shown in Fig. 148, present the same spectral features as the reflectance spectrum of Titanium White, implying that if Titanium White is combined with Lead White or Zinc White, we cannot recognize the last ones with the reflectance measurements.

On the contrary, the fluorescence spectra show the spectral features of both Zinc White and Titanium White. For the 2 months aged oil samples we do not observe substantial difference, which instead appears in the Titanium White in oil, Fig. 149.

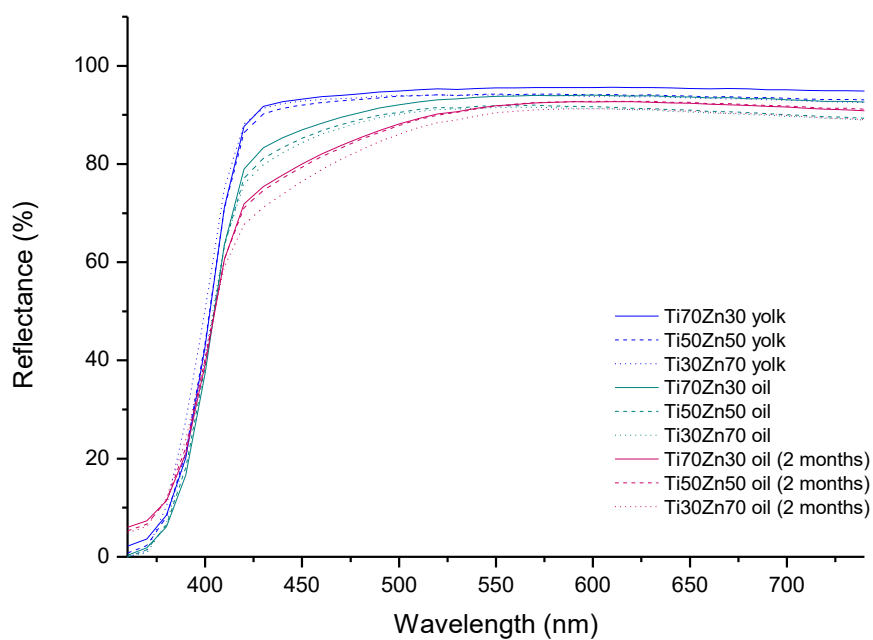


Fig. 148: Reflectance spectra of mixtures of Titanium White and Zinc White with egg yolk or linseed oil.

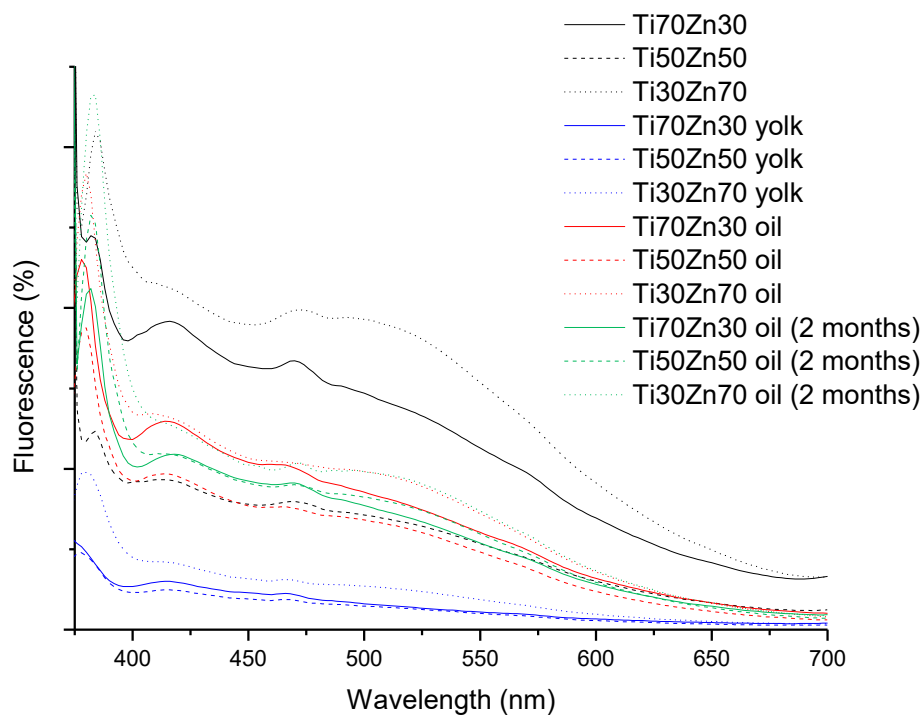


Fig. 149: Fluorescence emission of mixtures of Titanium White and Zinc White with egg yolk or linseed oil.

2.3.4.2 Multispectral images

Multispectral Reflectance Imaging

The multispectral reflectance images were acquired on the egg yolk and oil samples after 2 months of natural ageing. On the basis of the results of the reflectance measurements and the observation of the multispectral acquisitions, we selected three reflectance images obtained using the filters at 380 nm, 400 nm and 420 nm that containing the significant differences in the reflectance values, Fig. 150. We can observe that, at 380 nm, the samples that contain Titanium White and Zinc White show lower reflectance values than the “pure” Lead White samples. The mixtures of Lead White and Zinc White displayed high reflectance values at 400 nm, while at 420 nm there is no difference between the white samples. In general, the reflectance of the oil samples appears less intense.

In the combined “false” RGB image obtained using the three selected images reported above, we can evidence the presence of the “pure” Zinc White and of Zinc White in mixtures with Lead White as the light blue-green hue. Lead White in oil and in egg yolk assumes a light blue hue. All the Titanium White samples present a blue false colour.



Fig. 150: Multispectral images at 380 nm, 400 nm and 420 nm of the white mixtures (left panel) and “false” RGB combination of the same images. The yolk samples are framed in blue in the multispectral images and in red in the “false” RGB image.

Multispectral fluorescence imaging

Although Zinc White is well recognized by its fluorescence band in the UV range peaking at about 380 nm, it is well also identified by using the visible fluorescence emission. On the basis of the results of the fluorescence spectra and the observation of the multispectral fluorescence acquisitions, we selected three fluorescence images, obtained using the filters at 420 nm, 470 nm and 532 nm. Observing the “false” RGB image shown in Fig. 151, obtained combining these images, we can say:

- the egg yolk samples can be distinguished from the oil ones;

- the “pure” Zinc White and the mixture of Lead-Zinc White samples are well identified as brown hue;
- Titanium White as well as Titanium White mixed with Lead White in egg yolk samples are not detected; the same pigments in oil showed the same fluorescence emission as Titanium in oil;
- Lead White presents a different behaviour in oil or in yolk, and we can notice that the high quantity of egg yolk (Pb ++) produces an intense “false” RGB colour;
- the samples with Titanium White mixed with Zinc White showed an increase of the lightness for increasing Zinc White both in yolk and oil samples.



Fig. 151: "false" RGB combination of the fluorescence images taken at 420 nm (R), 470 nm (G) and 532 nm (B) of the white samples and their mixtures. The yolk samples are framed in blue rectangles.

2.3.5 Conclusions

The spectral features of white pigments and white pigments mixtures have been evaluated and discussed through the combined use of reflectance measurements, UV-fluorescence measurements and multispectral imaging.

We found that the reflectance measurements are effective to recognize Lead White in oil from Lead White in egg yolk, Zinc White in oil from Zinc White in egg yolk, and the presence of Zinc White when mixed with Lead White. The samples containing Titanium White, despite the high content of Zinc White or Lead White, maintain the spectral features of the “pure” titanium samples. With the fluorescence spectra in the visible range we can well distinguish not only the samples that contain Zinc White but also we can distinguish in which binder it has been mixed.

The presence of Lead White in mixtures does not significantly influence the reflectance and the fluorescence spectra.

In the “false” RGB images obtained combining the reflectance images taken at 380 nm, 400 nm and 420 nm, we can recognize if the Zinc White pigment is mixed with Titanium White or with Lead White.

The “false” RGB combination of the fluorescence images taken at 420 nm, 470 nm and 532 nm discriminate if Zinc White and its mixtures with other white pigments are blended with linseed oil or with egg yolk. The Titanium White and its mixtures appear black but they show a weak fluorescence in oil. Lead White can be detected only if it is mixed with linseed oil or yolk egg without mixing with other white pigments.

Chapter 3

Spirit and oil varnishes

In this chapter we discuss the assessment of the artificial ageing of spirit and oil varnishes prepared from mastic, dammar and colophony. Fluorescence excitation emission, UV-VIS and ATR-FTIR spectroscopies were measured to monitor changes of the optical and chemical properties of varnish samples prepared in the laboratory. Photodegradation and thermal ageing have been employed in order to compare the degradation products produced by the two techniques. We tested the multispectral fluorescence imaging to see if it is possible to discriminate between oil and spirit varnishes and among the resins.

3.	Spirit and oil varnishes	161
3.1	Introduction	162
3.2	Materials	165
3.3	Accelerated ageing	165
3.4	Methods	166
3.5	Results and discussion	167
3.5.1	ATR-FTIR	167
3.5.1.1	Photo-thermal effects	171
3.5.1.2	Thermal ageing	171
3.5.2	Spectrofluorimetry	175
3.5.2.1	Mastic	175
3.5.2.2	Dammar	181
3.5.2.3	Colophony	187
3.5.3	UV-VIS Absorption spectra and yellowing	193
3.5.4	Multispectral fluorescence imaging	202
3.6	Conclusions	207

3.1 Introduction

Natural resins of vegetal origin were commonly used in easel painting since ancient times. They were applied mainly as a transparent coating for protective and aesthetic purposes. Teophilus, in the 11th century [Theophilus P. (1979)], and Cennino Cennini in the 15th century [Cennini C. (1971)], described various methods used by the artists for preparing paint varnishes.

For painting, we can divide the varnishes into two groups: *oil varnishes*, that were obtained boiling natural resins such as sandarac, rosin or mastic, in drying oils (linseed or walnut oil) and *spirit varnishes* or *essential oil varnishes*, that became more common after the 16th century; they were solutions of natural resins in a volatile solvent, usually oil of turpentine.

Resins are complex mixtures of terpenoids derived from isoprene. They can be distinguished by the number of carbon atoms in the molecule into sesquiterpenic (terpenic compounds with 15 carbon atoms), diterpenic (terpenic compounds with 20 carbon atoms) and triterpenic (terpenic compounds with 30 carbon atoms).

Triterpenoid resins, such as mastic and dammar, were the most popular varnishes in the past for artists and restorers due to their excellent adhesive properties, their good solubility in solvents and for their yellowing lower than one of varnishes made with diterpenoid resins, such as colophony.

Many scientists have studied the ageing of varnishes, in particular they have focused on the research of biomarkers to recognize a specific varnish and/or resin and its degradation products [Mallégol J. et al. (2001), Nevin A. et al. (2009), Azemard C. et al. (2014)]. The research performed so far lead us to identify the “autoxidation” as the main degradation pathway [Feller L. R. (1994)]. The formation of peroxy radicals, caused by the combination of the oxygen present in the air with free radicals, induces the extraction of hydrogen atoms from the terpenes, the consequences of this process is described in the Part II, chap. 1 .

Autoxidation can be attributed to the exposition of the varnishes to light and heat, but it seems to occur also in the darkness [Colombini M. P. et al. (2000), Dietemann et al. (2001)]. Generally, a strong oxidation is positively correlated with the radicals concentration in natural varnishes.

However, dammar, that induce more radicals than mastic, shows a stronger oxidation process. This fact can be explained taking into account the total chemical composition of varnishes and/or resins [Dietemann *et al.* (2009)].

The most commonly adopted analytical approach to investigate natural resinous materials is the liquid or gas chromatography/mass spectrometry (GC/MS) [Van der Doelen G. A. *et al.* (1998), Van der Berg K. J. *et al.* (2000), Peris-Vicente J. *et al.* (2009), Bonaduce I. *et al.* (2016)]. Such analytical technique allows to identify the chemical markers, giving the molecular fingerprints of an organic material and/or information on the conservation and the fabrication techniques of the sample, depending on the type of marker (i) biomarker molecules are stable and preserved intact over the centuries, (ii) degradation markers come from ageing reactions of the biomarker either due to ageing or fabrication technique (intense heating for example). However, not all the GC/MS analyses permit the individuation of the polymeric or insoluble fractions, already present in the resin or formed during the ageing. To overcome this aspect, spectroscopic techniques, such as FTIR and Raman spectroscopy, can be used. These techniques are useful to recognize the oxidation cross-linking reactions or hydrolysis, depending on the resin typology [Prati (2011)] and can be performed *in situ*. Fluorescence spectroscopy and imaging could be proposed as alternative non-destructive methods for the analysis of varnishes. This is due to the formation of several fluorophores during the ageing, different and specific for each varnish. Thus, the ageing plays a crucial role in the nature and the intensity of the fluorescence of a varnish. In this way, Fluorescence imaging provides a specific advantage for mapping differences in varnishes, retouching and repainting, but, the most often, the fluorescence signal cannot be linked to a specific compound or chemical function.

In the scientific literature, a wide range of research have been done on the artificial and natural ageing of the varnishes. De la Rie R. (1988) used a Fadeometer equipped with a xenon arc containing a borosilicate inner filter and a sodalime outer filter to block the shortest UV wavelengths. The lamps were operated at 3000 watts and the samples were irradiated at 0.90 W/m²/nm and were maintained at a relative humidity of 51%. Dieteman P. *et al.* (2000) studied

the terpens treated with the tetrahydrofuran (THF) and irradiated with daylight for 300 hours. Van der Doelen et al. (2000) irradiated triterpenoid solutions with 13000-13500 lx by using fluorescence tubes. Nevin A. et al. (2009) proposed a photodegradation with daylight and 50×10^6 lux/h at 35°C, that should simulate the natural ageing of 100 years in a museum environment. Thoury M. et al. (2007) used a climatic camera heated at 70°C for 168 and 336 hours. Scientists also applied mixed accelerated ageing methods, irradiating and heating the samples [Felder-Casagrande et al. (1997), Dieteman P et. al (2001), Dietemann P. et al. (2003)].

Hence, it cannot exist a standard, certified procedure to produce an absolute artificial ageing. Reactions change according to the type of ageing method involved: intense heating (thermal degradation), irradiation (direct or photoinduced photochemical reactions), alone or in association. Furthermore, even for a same type of ageing, many parameters occur: for a same photochemical experiment, the degradation products obtained in laboratory can vary depending on the wavelengths of irradiation, the intensity of the photonic flow of each wavelength, the temperature and the relative humidity. As natural oxidations and/or other reactions can occur simultaneously or during the night and can differ from artificial to natural ageing.

The aim of this work is to assess the optical and chemical changes of the varnishes by thermal and photochemical ageing methods. For the photochemical ageing, we choose the Suntest as irradiation apparatus because it reproduces very well the sunlight and have a system of regulation of the temperature. Spirit and oil varnishes of mastic, dammar and colophony were submitted to light and heating up to 800 hours, separately. Optical and chemical changes were monitored by means of ATR-FTIR spectroscopy, spectrofluorimetry and UV-VIS spectroscopy after 15, 30, 90, 155, 320 and 800 hours of accelerated ageing.

We also focused on the fluorescence emission excited at 365 nm, that is the wavelength of the UV radiation commonly used for the fluorescence imaging of paintings. UV multispectral imaging was tested to distinguish the varnish samples.

3.2 Materials

We have chosen three resins: colophony (Kremer Pigmente GmbH & Co KG), mastic (The Chios gum mastic growers association), and dammar (EMIGA, S.A.). Linseed oil was purchased from Lefranc & Bourgeois; the turpentine spirit was produced by TALENS.

For preparing the spirit varnishes, the resins were grinded and then added to the solvent, heated and stirred for a few minutes. Oil varnishes were realized by adding the powdered resins into boiling linseed oil in the 1:2 weight ratio. The mixtures were stirred until the total dissolution and, finally, they were filtered. All the samples were spread on quartz slides trying to obtain a thin (fewer than 10 microns) and homogenous layer. Then all the samples were stored at 35°C for one month in the darkness to reach a complete drying.

3.3 Accelerated ageing

We used two accelerated degradation methods: photochemical ageing and thermal ageing.

The photochemical ageing was done irradiating the samples in a Suntest CPS+photoreactor (Atlas) equipped with a xenon lamp and a filter that prevents the transmission of wavelengths shorter than 290 nm. The lamp was supplied to have an irradiance of $750 \text{ W}\cdot\text{m}^{-2}$. The temperature of the sample was roughly maintained at 35 °C.

Thermal ageing was performed with a heater set at 75 °C. In order to compare the modifications produced with the two accelerated ageing methods, we used the same time intervals in both methods.

3.4 Methods

The varnishes were analysed with ATR- Infrared Imaging Microscopy (Nicolet iN 10 MX, Thermo-Scientific), Spectrofluorometry (Horiba Jobin Yvon Fluoromax 2), UV-VIS spectroscopy (Cary 100, Agilent), and Multispectral imaging. The details are given in the see Appendix A.

The ATR-spectra were obtained averaging 64 scans collected for 16 s each; the spectral resolution was 4 cm^{-1} . The area analysed was $150 \times 150\text{ }\mu\text{m}^2$.

The excitation emission (EE) spectra were acquired exciting between 260 nm and 400 nm at steps of 10 nm; the emission was collected between 250 nm and 700 nm at steps of 1 nm. The slits were fixed at 3 nm band-pass for the excitation and 2.5 nm band-pass for the emission. The EE spectra were corrected for the detector efficiency and for the lamp emission spectrum, and they are presented in the figures as contour maps with 200 different colours from the minimum value (in blue) to the maximum value (in red).

The fluorescence spectra were acquired at steps of 6 nm exciting at 365 nm. The slits were fixed at 3 nm band-pass for the excitation and 2.5 nm band-pass for the emission.

The multispectral imaging was performed with a QSI 583-w camera equipped with a Leica optical system and the following narrow band interferential filters: 450 nm, 470 nm, 500 nm, 532 nm, 550 nm, 600 nm. The fluorescence emission was induced by two UV sources made with three LEDs emitting at 365 nm. The multispectral images were corrected as reported in Part I, chap. 2.

3.5 Results and discussion

3.5.1 ATR-FTIR

The spirit varnishes present the same spectral features that the resins alone due to the total evaporation of the solvent. Thus, we can assign the absorption bands directly to the resins. The

ATR-FTIR spectra of the dried spirit varnishes are reported in Fig. 152, Fig. 153 and Fig. 154. The three resins show two CH stretching broad bands at 2939-2942 cm^{-1} and 2854-2869 cm^{-1} , that are the convolution of several narrow absorption bands (CH_3 , CH_2 , tertiary CH, CH_2 vinyl) identified by Azemard C. et al. (2014).

The band at 1689 cm^{-1} for colophony and at 1700 cm^{-1} for the triterpenes is attributed to the C=O bonds.

The absorption band at 1640 cm^{-1} is assigned to the linear C=C stretching vibrations in unsaturated polymers; in colophony this vibration band occurs at 3080 cm^{-1} . The 3080 cm^{-1} band is the main feature that has been used for the identification of fresh diterpenic resins. All the resins show two bands at 1454-1457 cm^{-1} and 1376-1384 cm^{-1} related to the CH_3 , CH_2 bending and a band at 1172-1176 cm^{-1} due to the stretching of the C-C bond or to C-H aromatic rings.

Oil varnishes are well identified thanks to the characteristic absorption bands of the linseed oil approximately at 1164 cm^{-1} [$\delta(\text{CH}_2)$ or $\nu(\text{C-O-C})$], 1100 cm^{-1} [$\nu_a(\text{O-CH}_2\text{-C})$], 975-80 cm^{-1} (residual unsaturation after curing), 725 cm^{-1} (C=C) [Lazzari M. et al. (1999), Mallégol J. et al. (1999), Mallégol J. et al. (2000), Mallégol J. et al. (2001)], Fig. 155, Fig. 156 and Fig. 157.

3.5.1.1 Photochemical effects

The degradation processes follow a similar evolution for all varnishes, as shown in the ATR-FTIR spectra reported in Fig. 152, Fig. 153, Fig. 154, Fig. 155, Fig. 156 and Fig. 157.

We can summarize the main spectral changes as follows:

- the absorbance between 3200 and 3600 cm^{-1} increases due to the formation of OH bonds;
- the absorbance between 1330 and 800 cm^{-1} increases for the presence of more C-O stretching bonds;
- the absorbance of the 1172-1176 cm^{-1} bands increases;

- all the C-H vibrational bands drastically decrease and an absorbance band, approximately at 2977 cm^{-1} , appears, probably due to the increase of one or more of the convoluted CH bands;
- the C=C bands at 725 cm^{-1} disappear;
- the band approximately at 1700 cm^{-1} shifts to higher wavenumbers only for the spirit varnishes. It becomes broader and presents a shoulder approximately at 1645 cm^{-1} (C=C band). In oil samples the 1700 cm^{-1} band shifts slightly to lower wavenumbers as in the linseed oil samples (Part II, chap. 1).

All these effects can be attributed to various types of oxidation, loss of volatile compounds and/or to the cross-linking processes that produce a decrease of the C=C and C-H bonds.

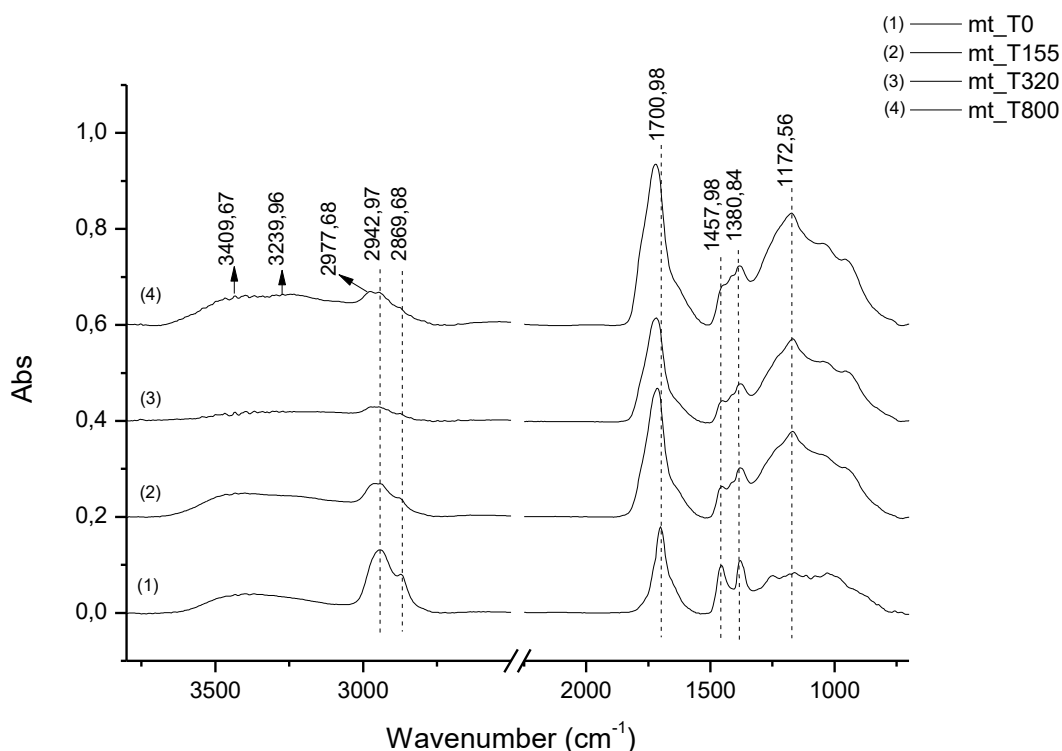


Fig. 152: ATR-FTIR spectra of the mastic in turpentine: dried (T0) and irradiated for 155, 320 and 800 hours.

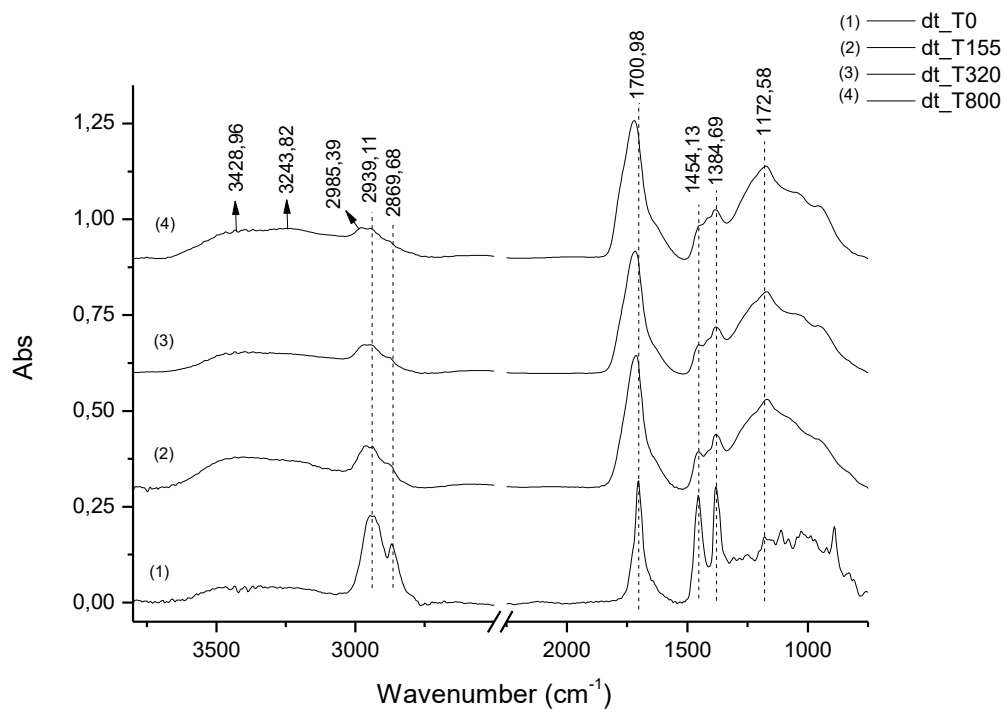


Fig. 153: ATR-FTIR spectra of the dammar in turpentine: dried (T0) and irradiated for 155, 320 and 800 hours.

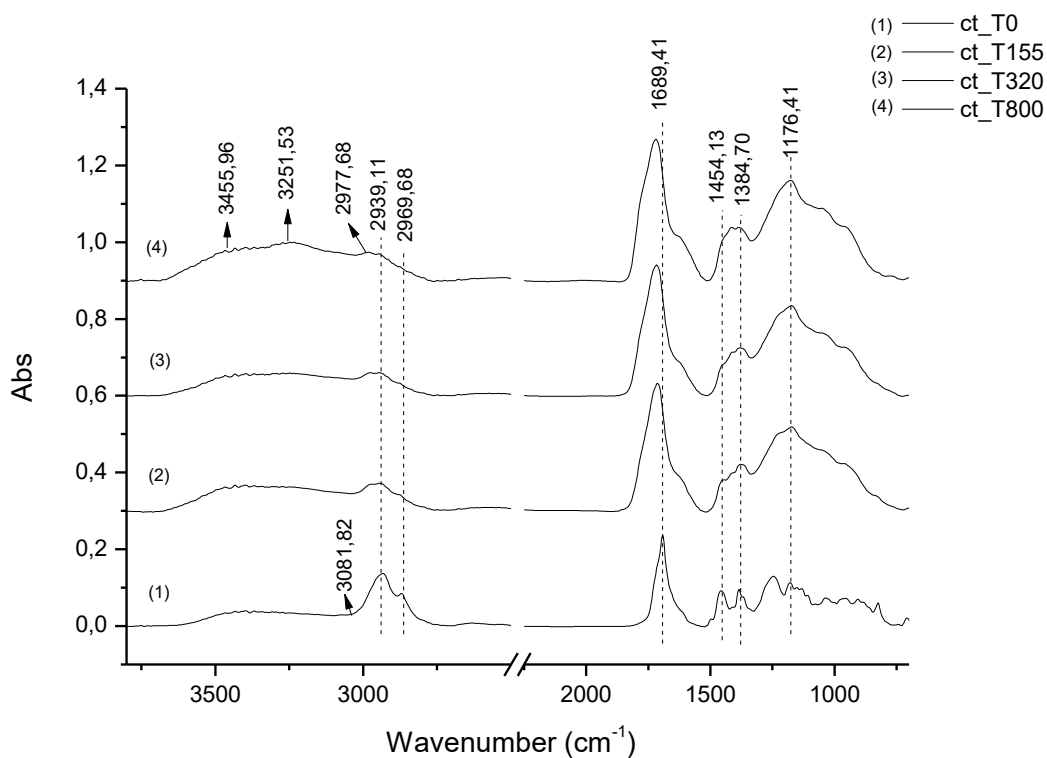


Fig. 154: ATR-FTIR spectra of the colophony in turpentine: dried (T0) and irradiated for 155, 320 and 800 hours.

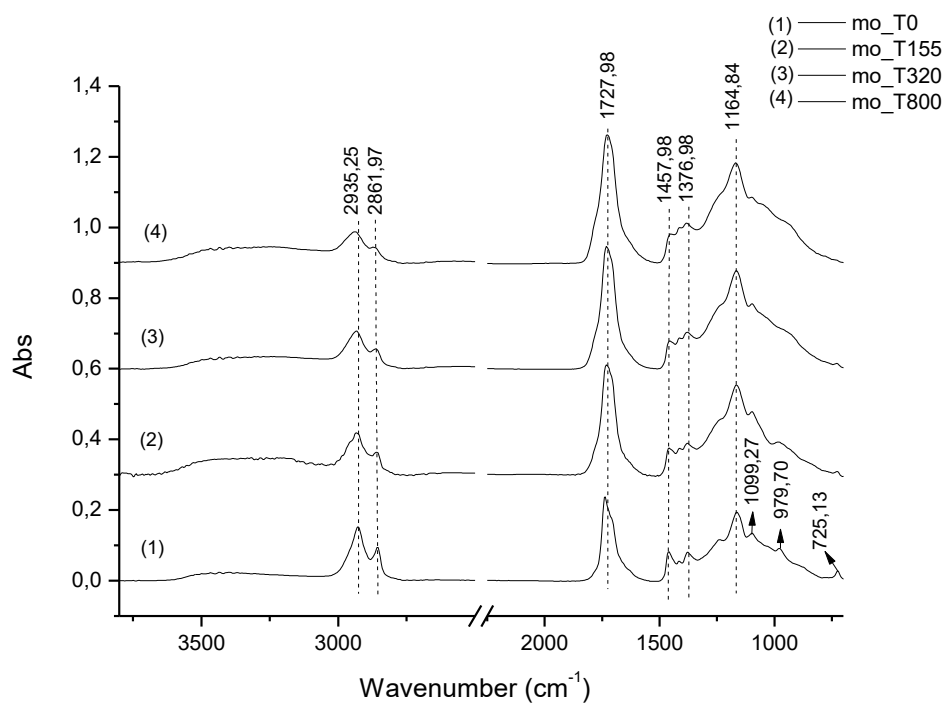


Fig. 155: ATR-FTIR spectra of the mastic in linseed oil: dried (T0) and irradiated for 155, 320 and 800 hours.

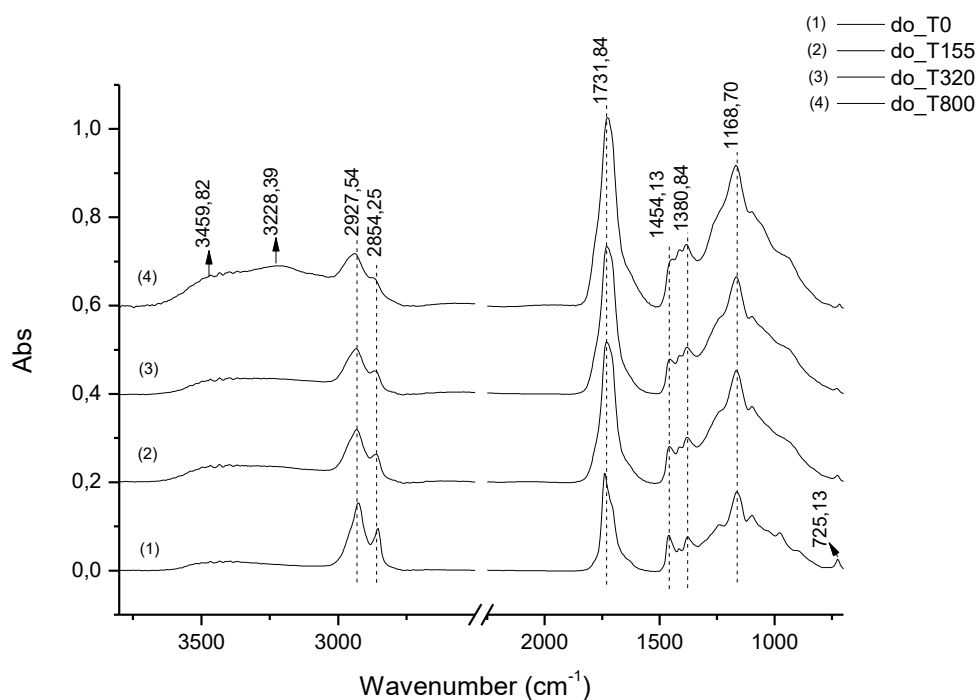


Fig. 156: ATR-FTIR spectra of the dammar in linseed oil: dried (T0) and irradiated for 155, 320 and 800 hours.

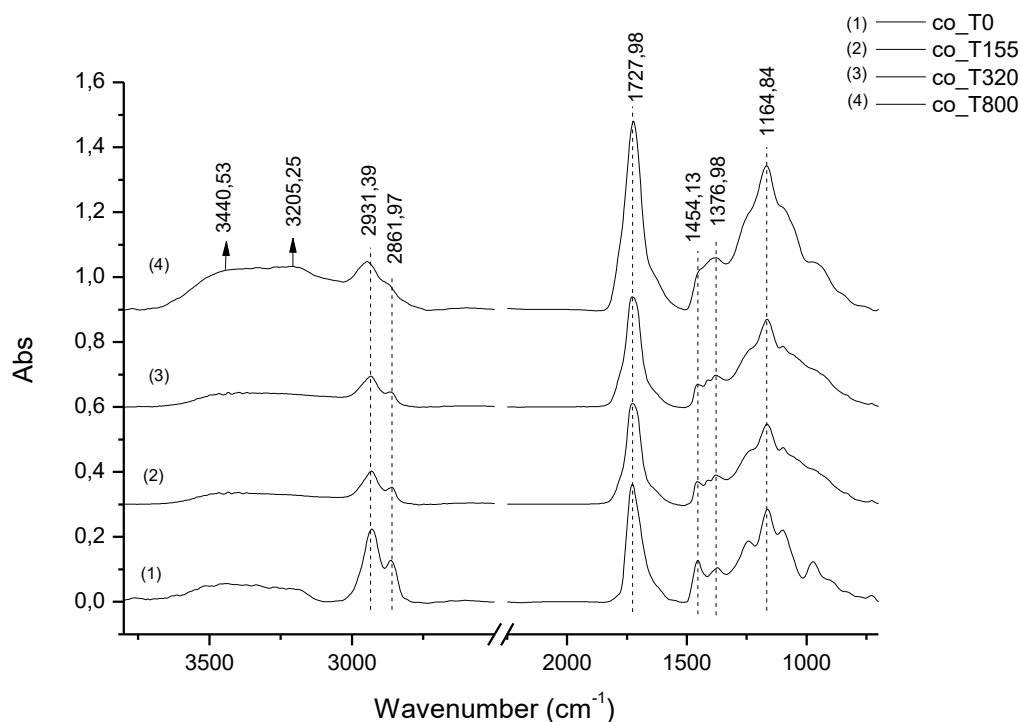


Fig. 157: ATR-FTIR spectra of the colophony in linseed oil: dried (T0) and irradiated for 155, 320 and 800 hours.

3.5.1.2 Thermal effects

The ATR-FTIR spectra of the thermally aged samples are quite similar to those of the dried varnishes: in fact they do not change considerably after 155, 320 and 800 hours of heating, as shown in Fig. 158, Fig. 159, Fig. 160, Fig. 161, Fig. 162, Fig. 163. We can notice only a slight broadening and a shift to lower wavenumbers of the band at 1700 cm^{-1} for the spirit varnishes, and an increase of the band at $1160\text{--}1164\text{ cm}^{-1}$ for the oil varnishes. The band at 725 cm^{-1} remains in the same position after the thermal ageing.

Aged spirit colophony does not show significant spectral modifications; the peak at $1160\text{--}1174$ does not increase with the thermal process.

These results suggest that the oxidation process occurs only photochemically and not during heating. In fact, only the photochemical ageing induces an almost complete destruction of the original allyl groups present in the resins and an increase of the oxidized species.

The main absorption bands characteristic of dried and aged varnishes are summarized in Tab. 4.

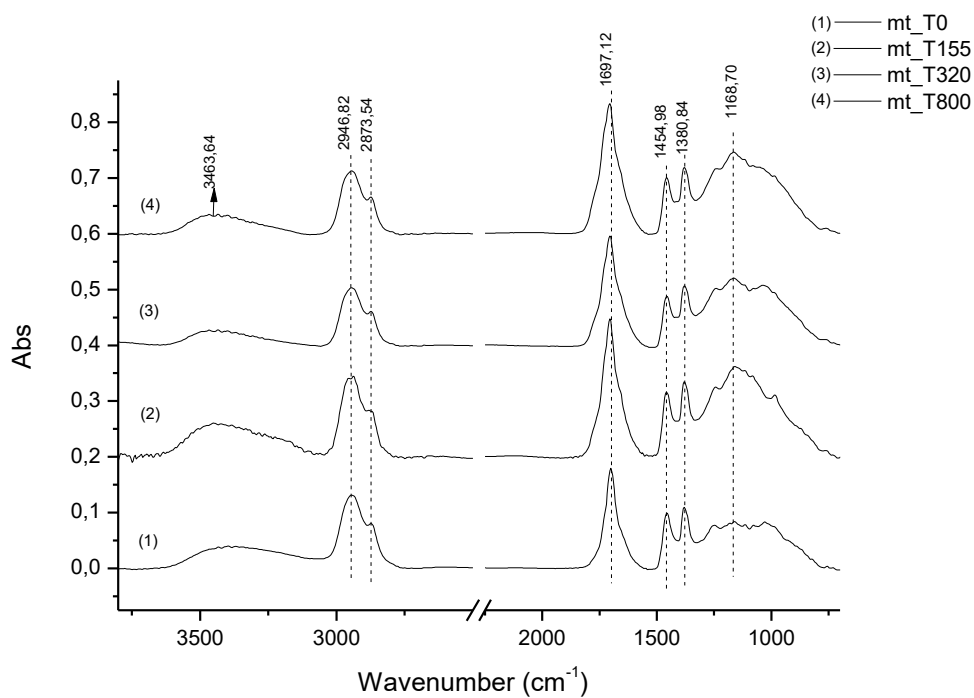


Fig. 158: ATR-FTIR spectra of the mastic in turpentine: dried (T0) and heated for 155, 320 and 800 hours.

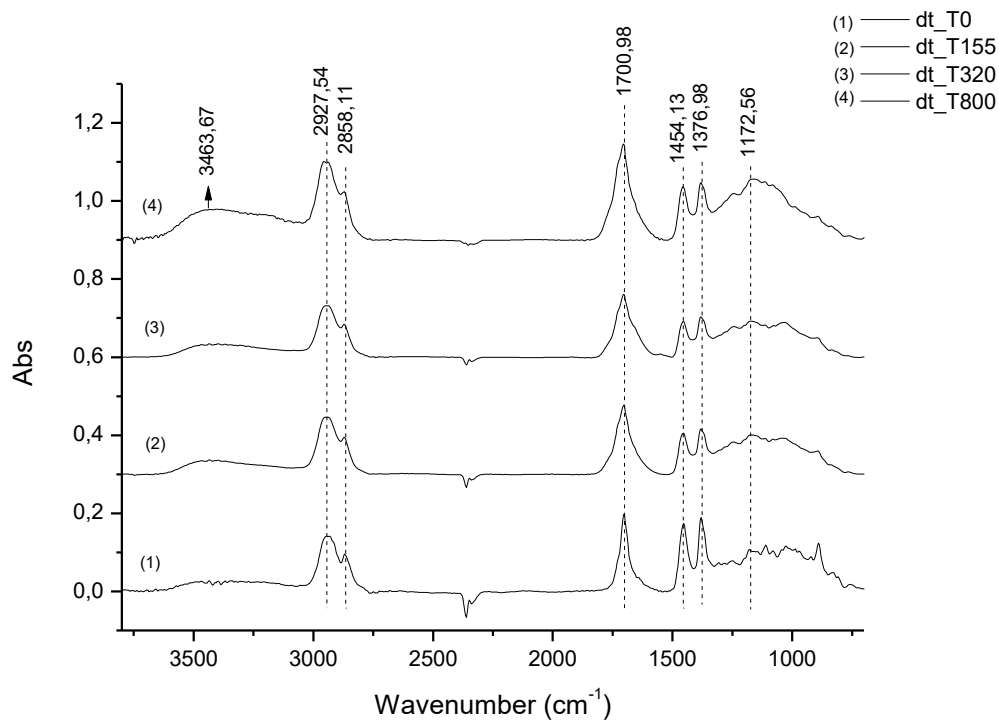


Fig. 159: ATR-FTIR spectra of the dammar in turpentine: dried (T0) and heated for 155, 320 and 800 hours.

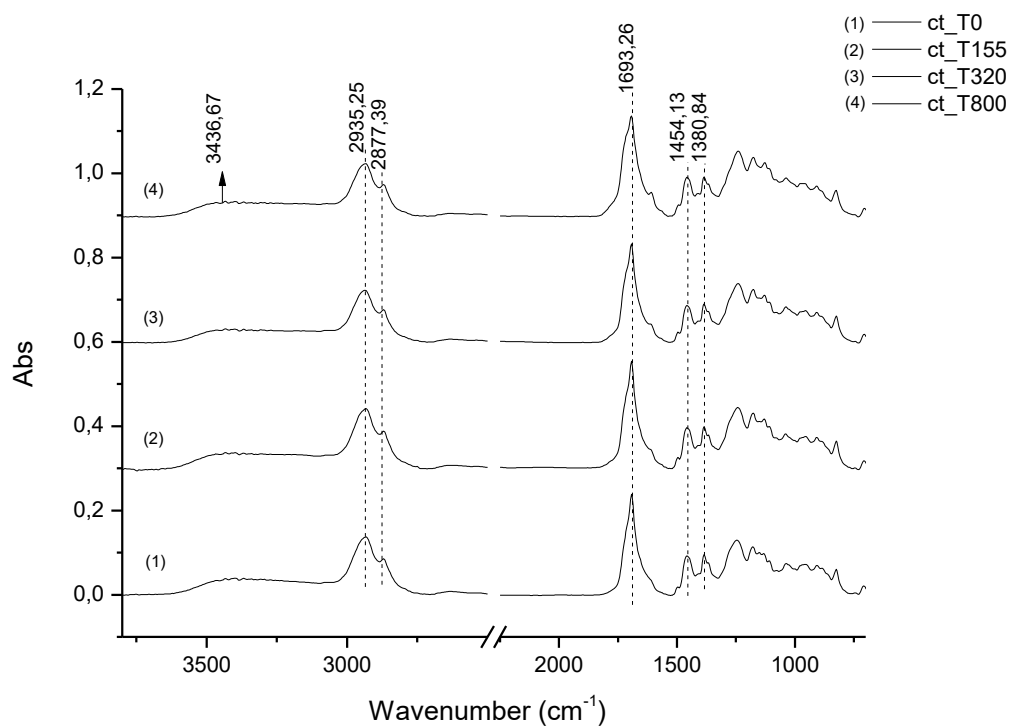


Fig. 160: ATR-FTIR spectra of the colophony in turpentine: dried (T0) and heated for 155, 320 and 800 hours.

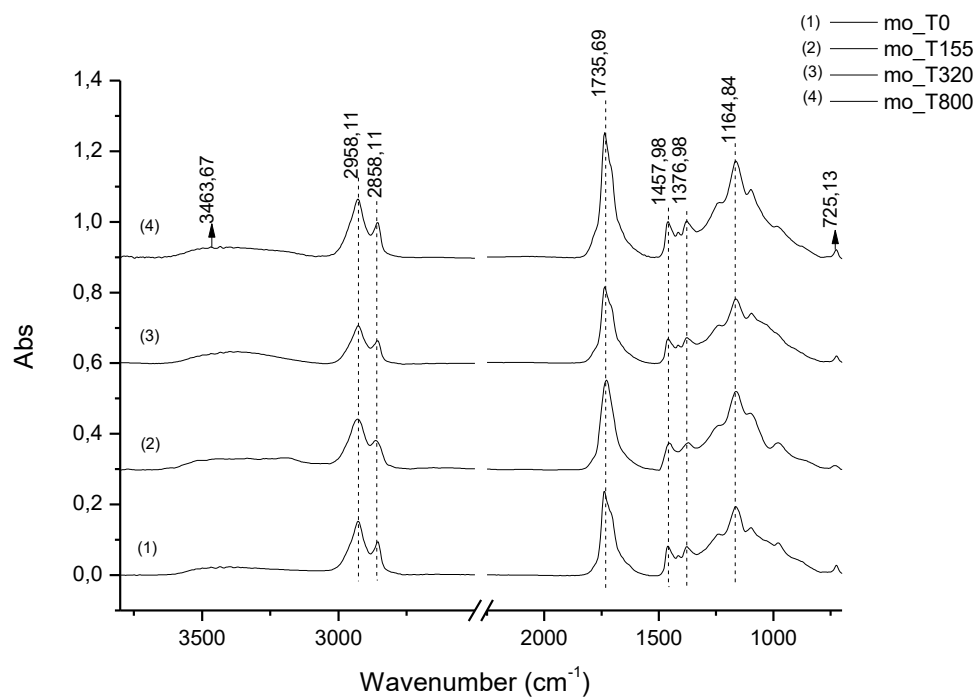


Fig. 161: ATR-FTIR spectra of the mastic in linseed oil: dried (T0) and heated for 155, 320 and 800 hours.

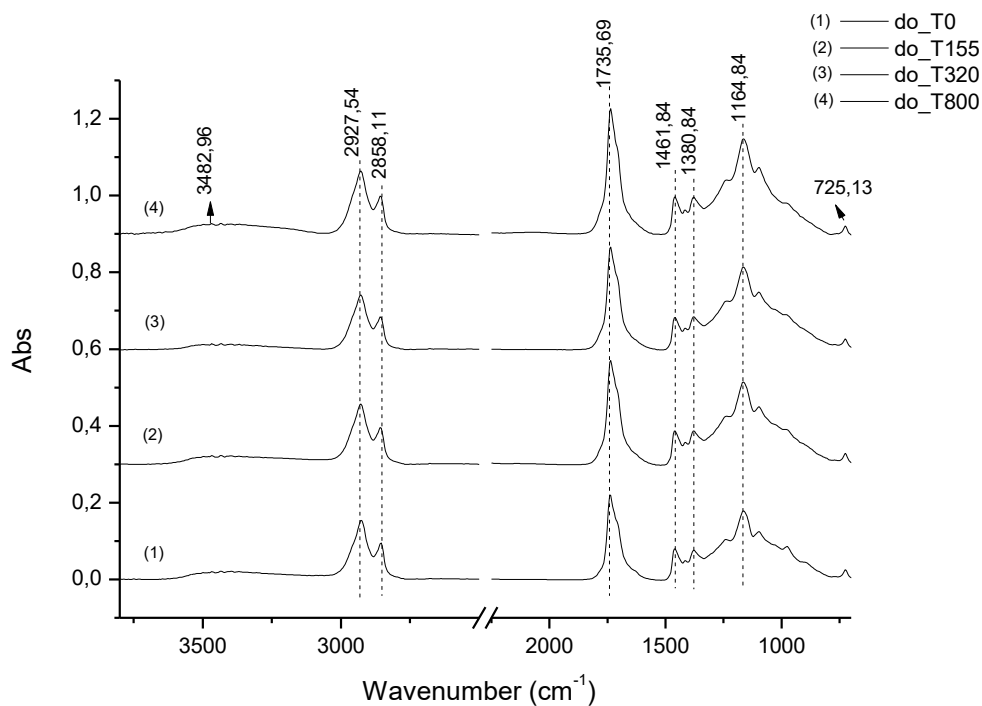


Fig. 162: ATR-FTIR spectra of the dammar in linseed oil: dried (T0) and heated for 155, 320 and 800 hours.

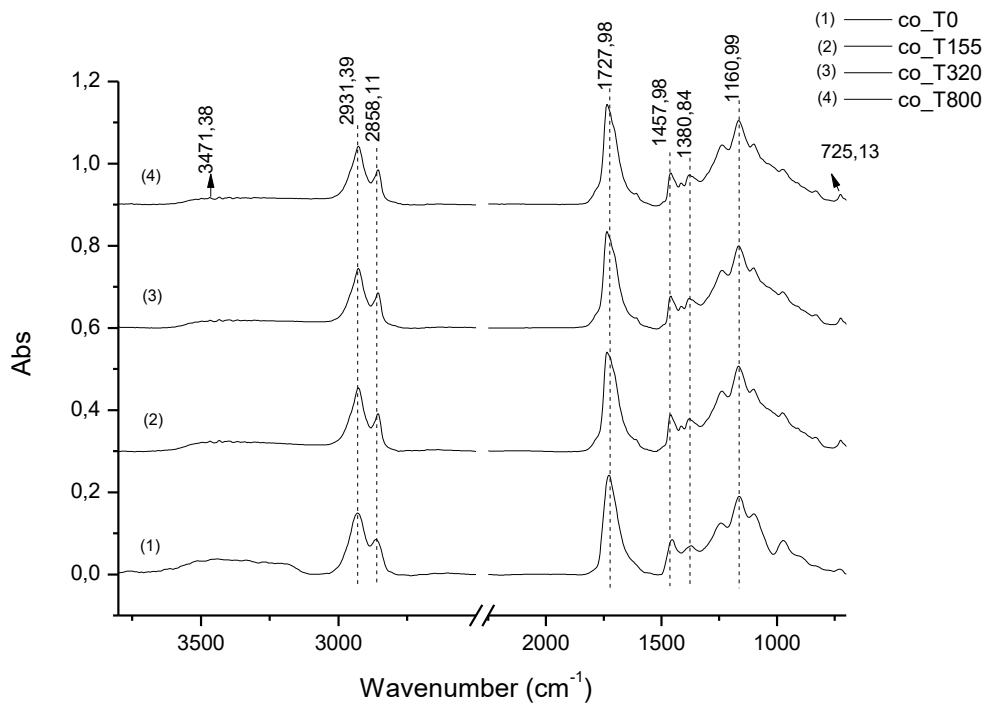


Fig. 163: ATR-FTIR spectra of the colophony in linseed oil: dried (T0) and heated for 155, 320 and 800 hours.

Tab. 4: ATR-FTIR bands assignments for mastic, dammar and colophony: D (dried), P (800 hours of photochemical ageing), T (800 hours Thermal ageing), s (shoulder). The references for the bands assignments are: Mazzeo R. et al. (2008), Edward H. G. L. et al. (1996), Nevin A. et al. (2009), Lazzari M. et al. (1999).

Absorption bands (cm ⁻¹)	Spirit varnishes									Oil varnishes									Assignment
	Mastic			Dammar			Colophony			Mastic			Dammar			Colophony			
3600-3200	D	P	T	D	P	T	D	P	T	D	P	T	D	P	T	D	P	T	O-H stretching
3080					P	T	D	P	T	D	P	T	D	P	T	D	P	T	ν (=C-H)
2940	D	P	T	D	P	T	D	P	T	D	P	T	D	P	T	D	P	T	ν_{as} (CH ₂)
2870	D	P	T	D	P	T	D	P	T	D	P	T	D	P	T	D	P	T	ν_{as} (CH ₂)
1700	D	P	T	D	P	T	D	P	T	D	P	T	D	P	T	D	P	T	ν (C=O)
1646	D(s)	P(s)		D(s)	P(s)	T(s)	D(s)	P(s)	T(s)	D(s)	P(s)		D(s)	P(s)	T(s)	D(s)	P(s)	T(s)	ν (C=C)
1457	D	P	T	D	P	T	D	P(s)	T	D	P	T	D	P	T	D	P	T	δ_{as} (CH ₂), CH ₂ scissoring
1411		P(s)			P(s)			P	T	D	P	T						T	COOH
1380	D	P	T	D	P	T	D	P	T	D	P	T	D	P	T	D	P	T	CH ₃ umbrella mode
1249	D	P(s)		D		T	D		T	D	P(s)	T	D	P(s)	T	d	P(s)	T	ν_d (C-C-O)
1203-1199	D			D						D	P		D			D			δ (CH) and δ (OH)
1180-1170	D	P	T	D	P	T	D	P	T								P		ν (C-O)
1164-1160	D	P	T				D			D	P	T	D	P	T	D		T	δ (CH ₂) or ν (C-O-C)
1114-1095	D		T	D		T	D					T	D	P	T		P(s)	T	ν_{as} (O-CH ₂ -C)
1030	D		T	D		T	D		T										ν (C-O-C)
980	D		T	D						D	P(s)	T	D		T	D		T	residual unsaturation
890						T										D(s)	P		ν (C-C-OH)
725	D											T	D	P	T	D		T	C=C

3.5.2. Spectrofluorimetry

3.5.2.1 Mastic

The EE spectra of the mastic samples are reported in Fig. 164, Fig. 165, Fig. 166 and Fig. 167.

The EE spectra of the dried spirit mastic show a fluorescence band with a maximum at 320/450 nm and a second fluorescence emission around 460 nm, hardly identified as a band, excited between 350 nm and 390 nm. After 15 hours of photochemical ageing, the main band shifts slightly to shorter excitation/emission wavelengths. After 30, 155, 320 and 800 hours of ageing, the position of this band does not change any more, but the intensity of the second fluorescence emission increases. The maximum of the main fluorescence band of mastic, excited at 365 nm, shifts to long wavelengths with ageing: from 450 nm to 460 nm for the mastic in turpentine; the band also becomes broader, probably for the fluorescence of multiple fluorophores.

The oil-mastic sample presents a fluorescence band at about 365/460 nm and another one approximately at 450 nm when excited at 310-350 nm. After 15 hours of photoageing, the intensity of the first band is reduced and that of the second one increases; in addition, the second

band shifts to 330/430 nm excitation/emission wavelengths. After additional 15 hours, the second emission band shifts to shorter wavelengths, 320/440 nm; after 90 hours its shift to lower excitation/emission wavelengths increases, the maximum being at 310/430 nm, then it remains in the same position after 155 and 320 hours. The EE spectra, measured after 800 hours of ageing, show a broadening and a shift of the maximum at 320/415 nm.

The maximum of the fluorescence spectrum excited at 365 nm occurs at about 450 nm for the dried samples, but it shifts to short wavelengths after the photodegradation of the oil varnish. At 800 hours ageing the maximum of the spectrum is located at 440 nm. Instead, the spirit varnish exhibits a shift of the fluorescence maximum to long wavelengths (460 nm).

The thermal ageing induces fluorescence emission at different excitation/emission wavelengths compared to the photochemically aged samples. For the spirit mastic we observe, after 15 hours, two fluorescence emissions, one at 370/450 nm and the other at 330/450 nm. After additional 15 hours, the fluorescence emission at the shortest wavelengths decreases and the second fluorescence emission shifts to longer emission wavelengths (370/460 nm). At 90, 155, 320 and 800 hours, the fluorescence bands broaden and shift slightly to higher excitation/emission wavelengths. The fluorescence spectrum excited at 365 nm presents a maximum at 448 nm for dried samples and for those aged for 15 hours, then the maximum shifts to 456 nm after additional 15 hours; it remains fixed at 460 nm after 90 and 155 hours of ageing; then it shifts to 464 nm and to 476 nm after 320 hours and 800 hours of ageing, respectively.

In the EE spectra of the oil samples we observe the broadening of the band at 365/460 nm and a weak fluorescence at shorter excitation/emission wavelengths, disappearing during the ageing.

Exciting at 365 nm, after 15 hours we observe a fluorescence emission band at 454 nm. The maximum of the band shifts to 464 nm in the spectra measured on samples aged for 30, 90, 155, and 320 hours; finally, after 800 hours of ageing, the fluorescence emission band presents an overall broadening and its maximum has shifted to 478 nm.

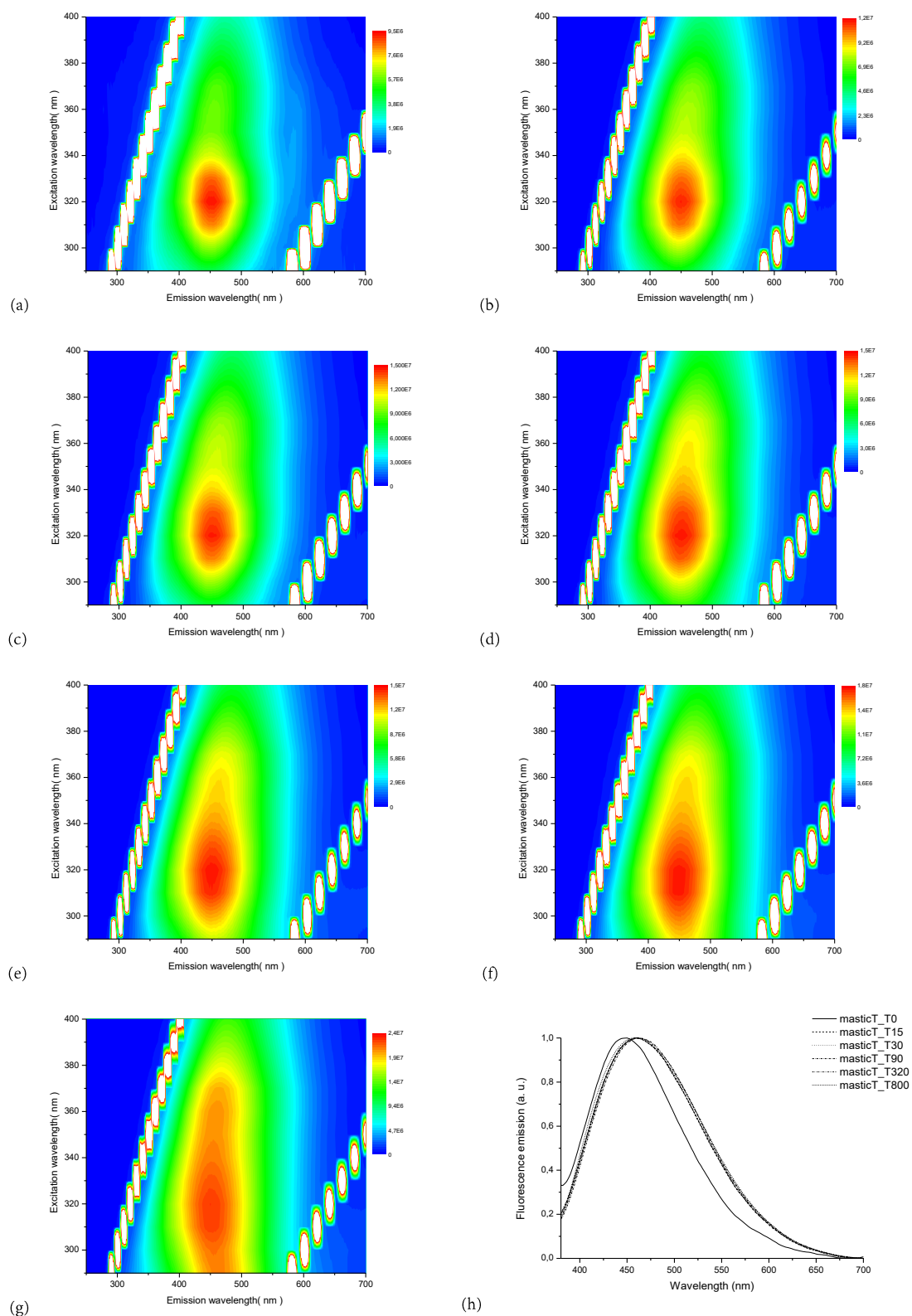


Fig. 164: Evolution of normalized excitation emission spectra of films of mastic in turpentine irradiated with artificial sunlight at 35°C: dried (a), irradiated 15 hours (b), 30 hours (c), 90 hours (d), 155 hours (e), 320 hours (f) and 800 hours (g). Normalized emission fluorescence spectra for $\lambda_{ex} = 365$ nm (h).

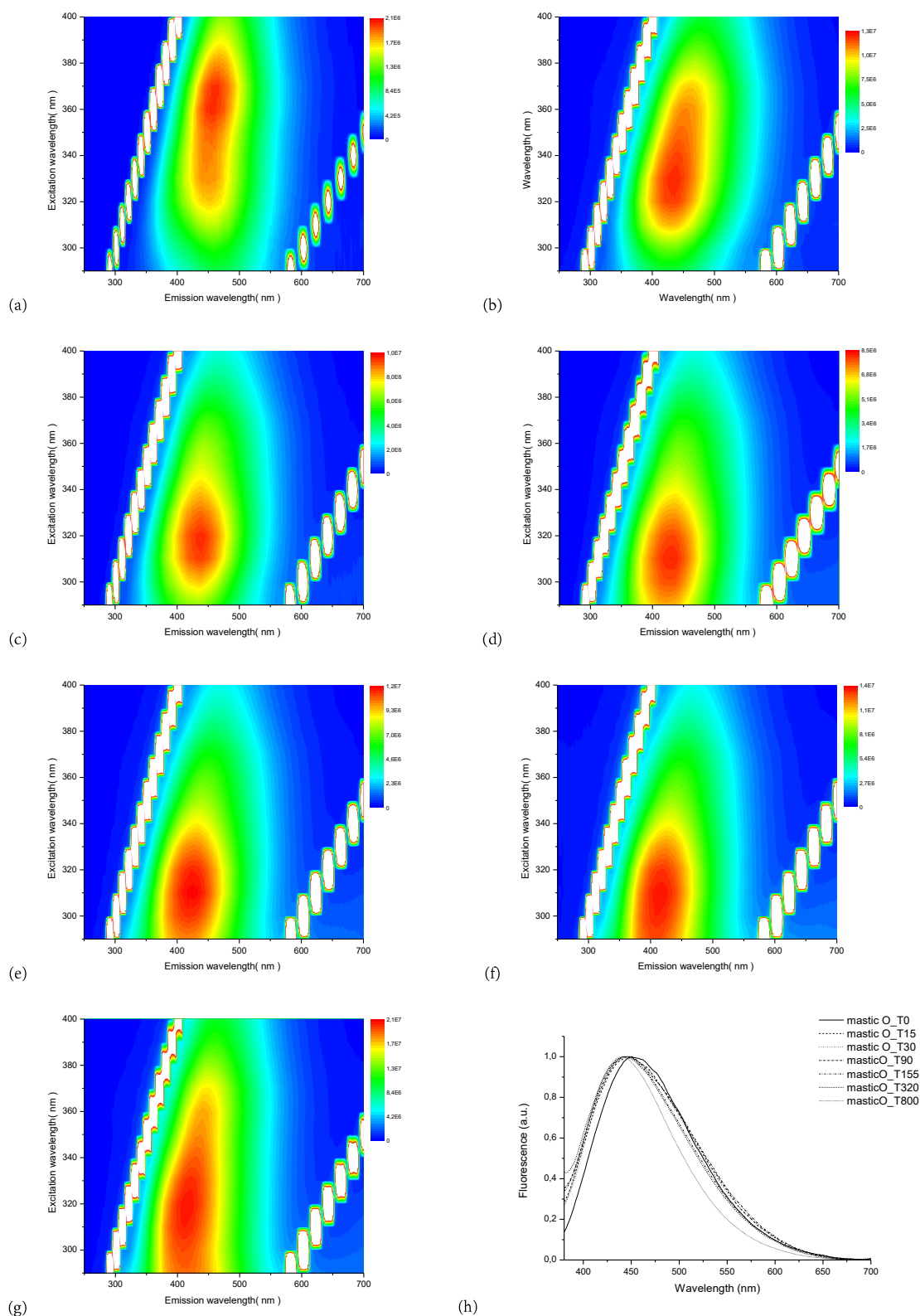


Fig. 165: Evolution of normalized excitation emission spectra of films of mastic in linseed oil irradiated with artificial sunlight at 35°C: dried (a), irradiated during 15 hours (b), 30 hours (c), 90 hours (d), 155 hours (e), 320 hours (f) and 800 hours (g). Normalized emission fluorescence spectra for $\lambda_{\text{ex}} = 365$ nm (h).

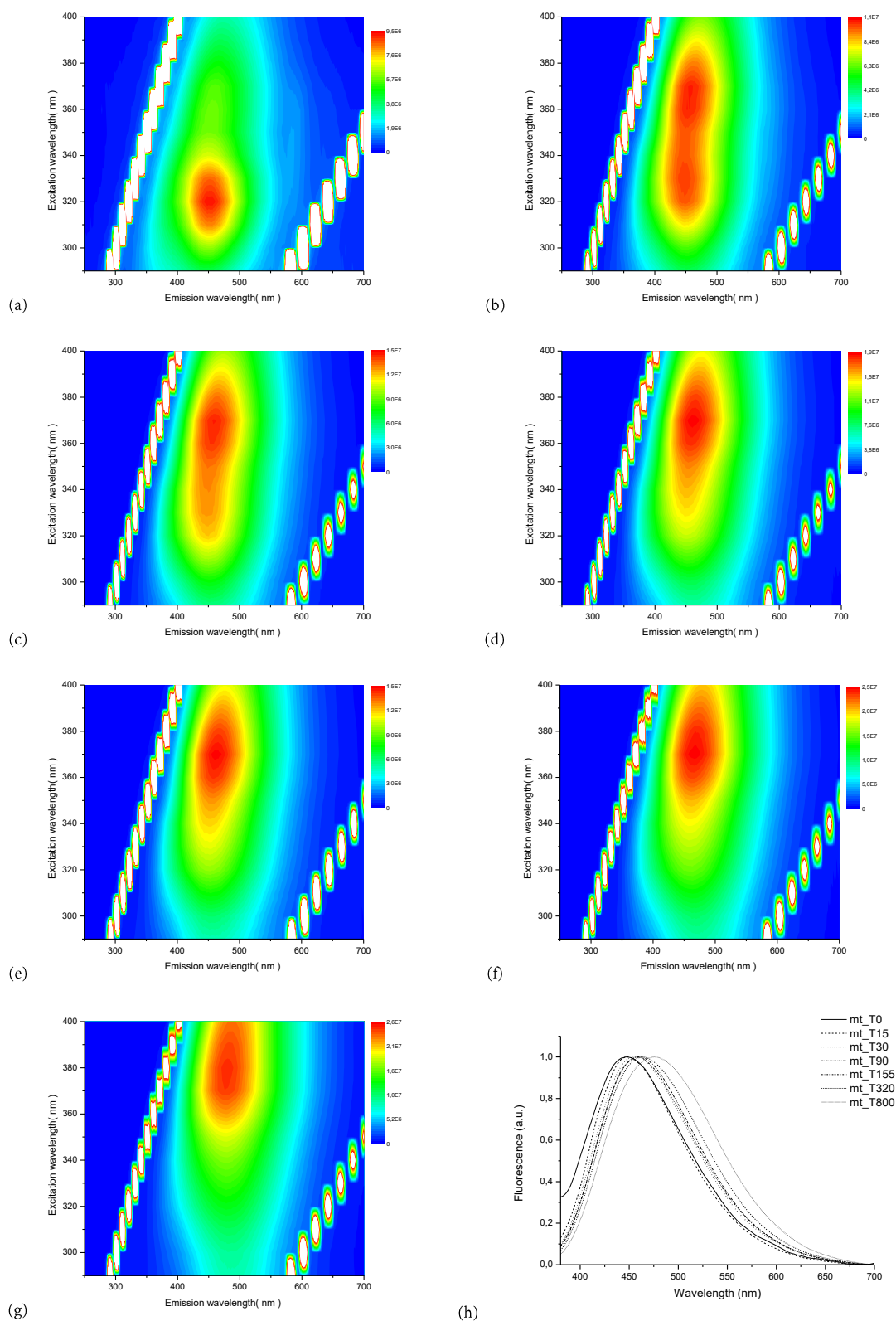


Fig. 166: Evolution of normalized excitation emission spectra of films of mastic in turpentine aged with the thermal method: dried (a), heated at 15 hours (b), 30 hours (c), 90 hours (d), 155 hours (e), 320 hours (f) and 800 hours (g). Normalized emission fluorescence spectra for $\lambda_{ex} = 365$ nm (h).

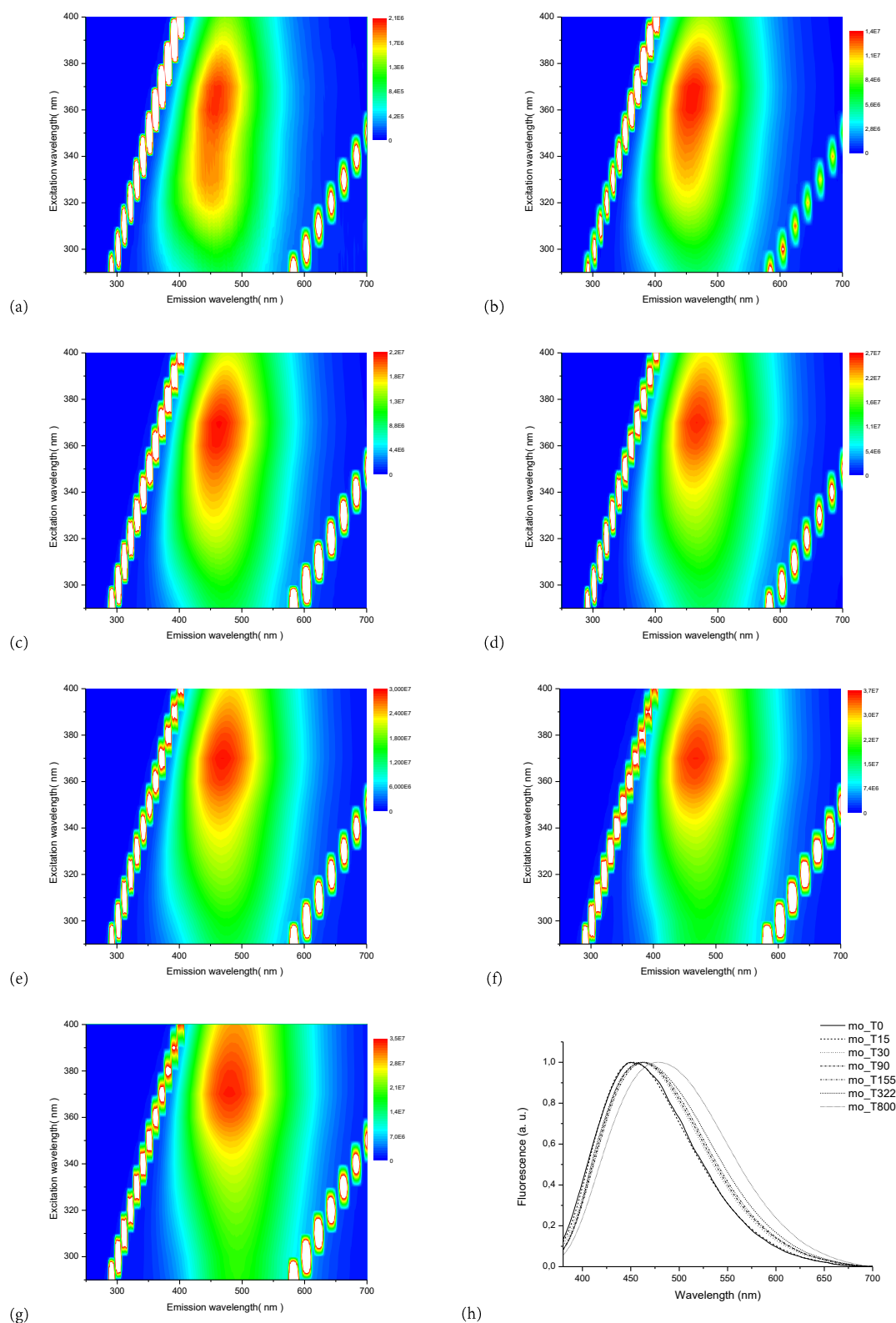


Fig. 167: Evolution of normalized excitation emission spectra of films of mastic in linseed oil aged with the thermal method: dried (a), heated at 15 hours (b), 30 hours (c), 90 hours (d), 155 hours (e), 320 hours (f) and 800 hours (g). Normalized emission fluorescence spectra for $\lambda_{ex} = 365$ nm. (h).

3.5.2.2 Dammar

The EE spectra of the dammar samples are reported in Fig. 168, Fig. 169, Fig. 170 and Fig. 171.

The EE spectra of the dried dammar show a broad emission band between 390 - 490 nm for excitation wavelengths between 295 nm and 380 nm. After the photoageing, the fluorescence emission is dominated by a band centred on 320/450 nm. After 800 hours of ageing, the band becomes broader since a strong second fluorescence emission band appears at higher excitation wavelengths. The fluorescence spectra excited at 365 nm of both the dried samples and those aged for 15 hours show a band with a maximum at 450 nm; this band shifts to 470 nm for longer ageing periods, up to 320 hours. At 800 hours of ageing, the band shifts back and its maximum returns to 452 nm.

For the oil samples, the EE spectra of the dried samples show a maximum excitation/emission peak at 360/450 nm, which shifts to shorter excitation/emission wavelengths (330/435 nm) during the accelerated ageing. The band keeps approximately the same shape and position until 320 hours of ageing and it broadens and shifts to higher excitation/emission wavelengths after 800 hours.

With an excitation at 365 nm, the fluorescence spectra of dried dammar show a band, with a maximum at 446 nm. After ageing the samples during 15 and 30 hours, the band shifts to 452 nm, it increases of 2 nm more after 90 hours of ageing, then it moves back to 450 nm after 155 and 320 hours, and finally, after 800 hours of irradiation, the maximum returns to 444 nm, approximately to the initial value.

During the thermal ageing, the EE spectra of the spirit dammar show a long wavelength band, approximately at 370/450 nm, that remains almost in the same position after all the ageing periods. In the fluorescence spectra measured exciting at 365 nm, the fluorescence emission band at 444 nm becomes broader after 15 and 30 hours of ageing, then it shifts to long wavelengths for longer periods of ageing, i.e. to 452 nm after 90, 155 and 320 hours and 464 nm after 800 hours.

For the oil samples, the band shifts to higher excitation/emission wavelengths, from 360/450 nm to 370/475 nm. With an excitation at 365 nm, the maximum shifts towards higher wavelengths with the ageing time: 448 nm after 15 hours, 452 nm after 30 hours, approximately 458 nm after 90 and 155 hours, 460 nm after 320 hours and 470 nm after 800 hours.

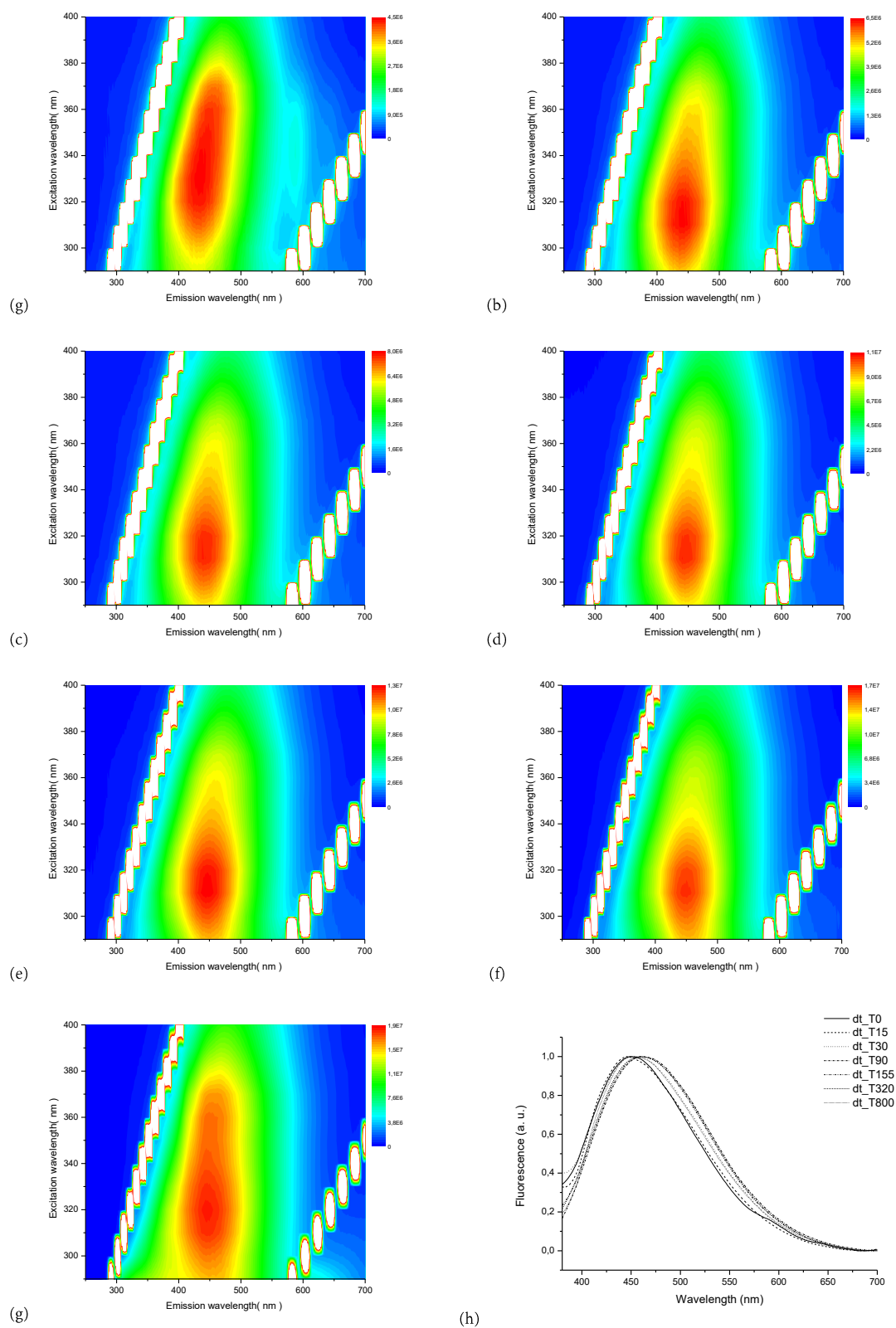


Fig. 168: Evolution of normalized excitation emission spectra of films of dammar in turpentine irradiated with artificial sunlight at 35°C: dried (a), irradiated during 15 hours (b), 30 hours (c), 90 hours (d), 155 hours (e), 320 hours (f) and 800 hours (g). Normalized emission fluorescence spectra for $\lambda_{\text{ex}} = 365 \text{ nm}$ (h).

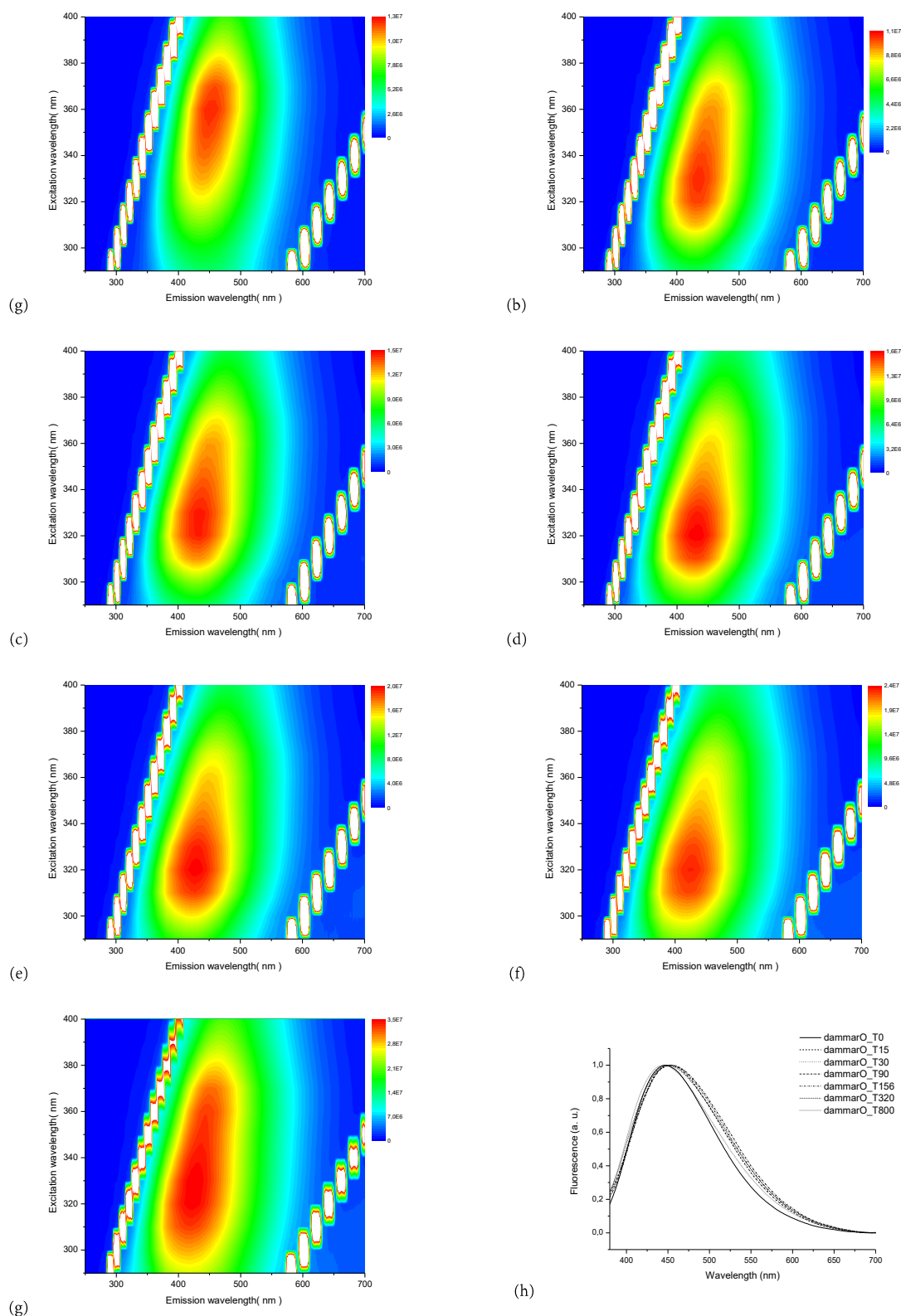


Fig. 169: Evolution of normalized excitation emission spectra of films of dammar in linseed oil irradiated with artificial sunlight at 35°C: dried (a), irradiated during 15 hours (b), 30 hours (c), 90 hours (d), 155 hours (e), 320 hours (f) and 800 hours (g). Normalized emission fluorescence spectra for $\lambda_{ex} = 365$ nm (h).

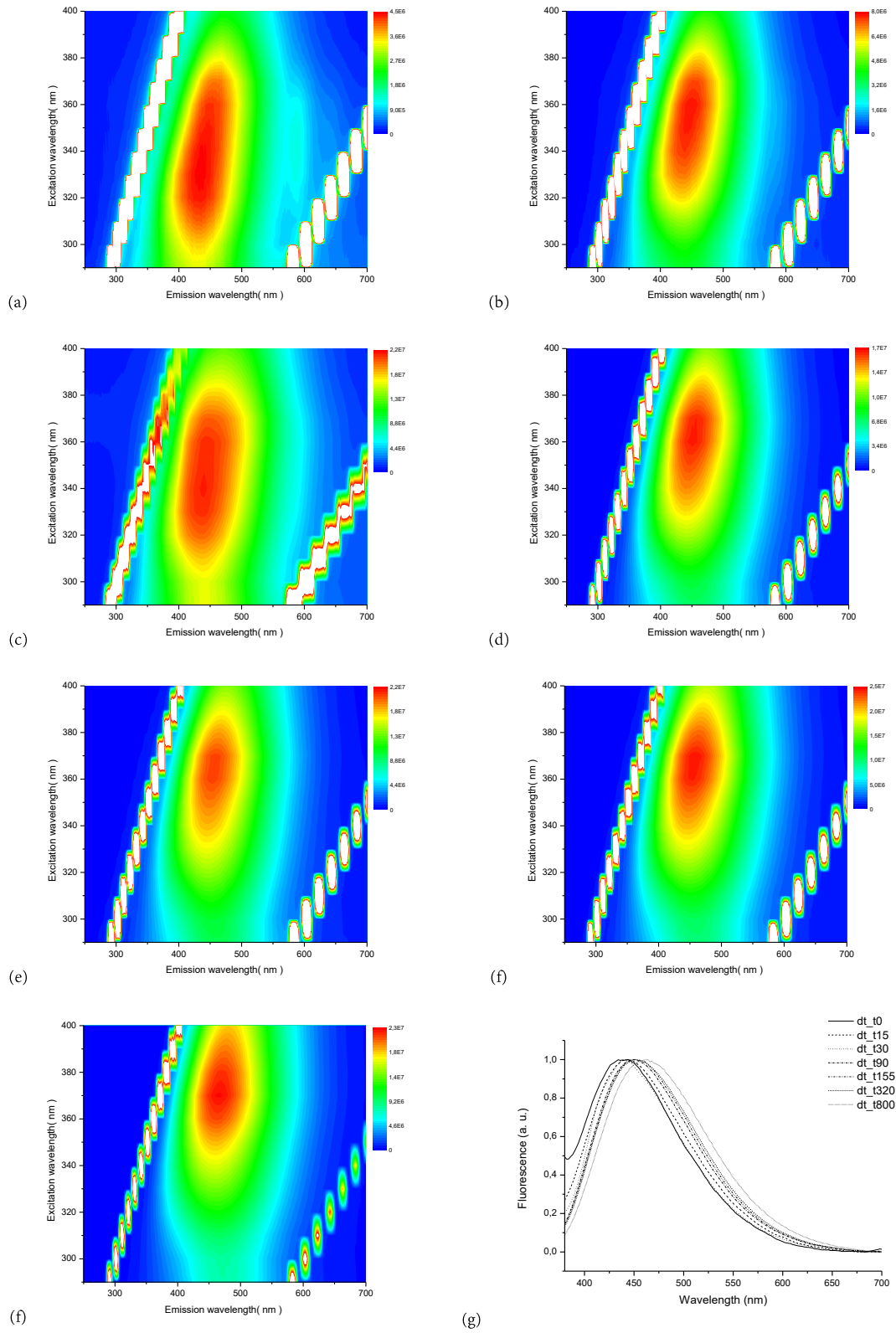


Fig. 170: Evolution of normalized excitation emission spectra of films of dammar in turpentine aged with the thermal method: dried (a), heated at 15 hours (b), 30 hours (c), 90 hours (d), 155 hours (e), 320 hours (f) and 800 hours (g). Normalized emission fluorescence spectra for $\lambda_{ex} = 365$ nm (h).

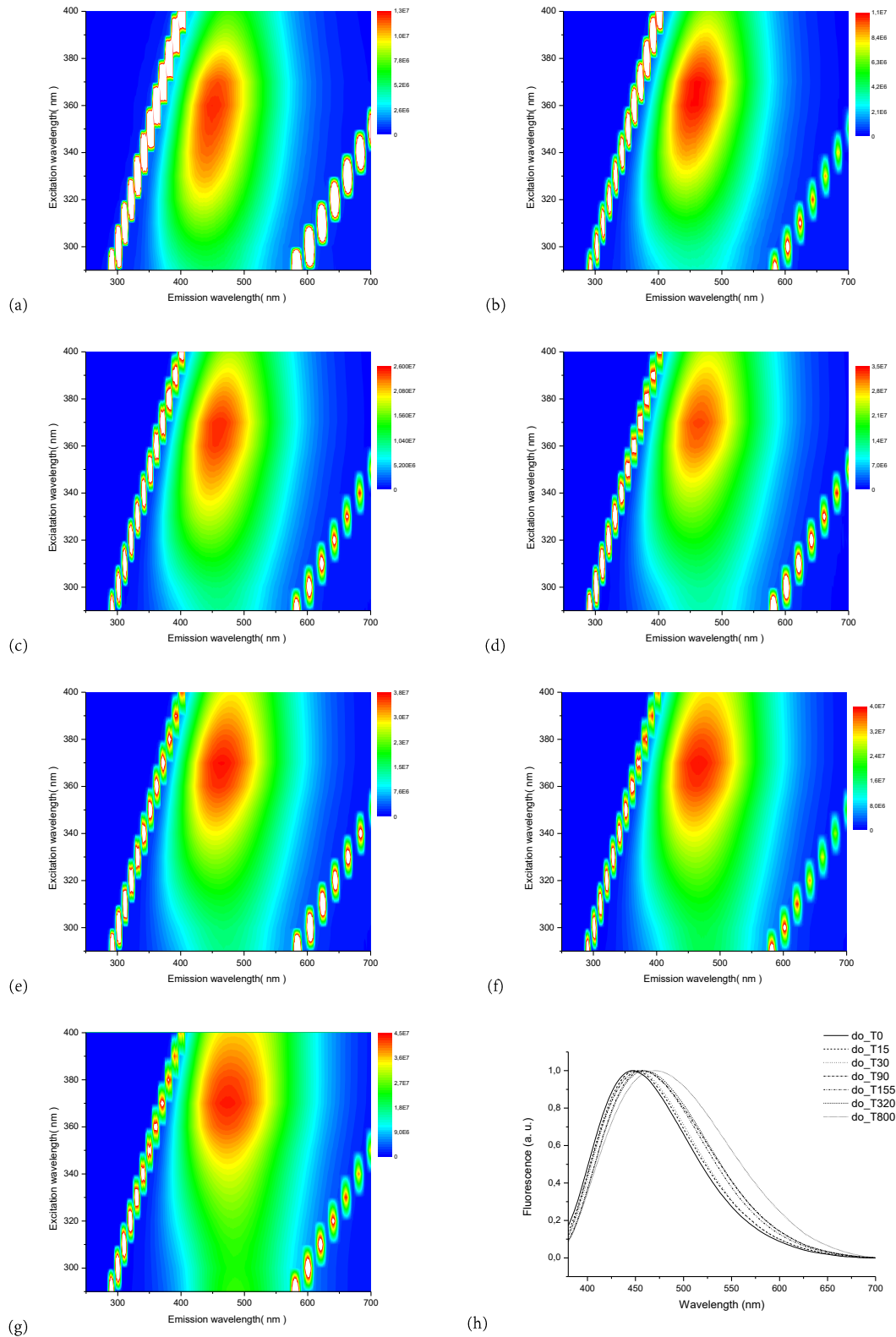


Fig. 171: Evolution of normalized excitation emission spectra of films of dammar in linseed oil aged with the thermal method: dried (a), heated at 15 hours (b), 30 hours (c), 90 hours (d), 155 hours (e), 320 hours (f) and 800 hours (g). Normalized emission fluorescence spectra for $\lambda_{ex} = 365$ nm (h).

3.5.2.3 Colophony

The EE spectra of the colophony samples are reported in Fig. 172, Fig. 173, Fig. 174 and Fig. 175.

The EE spectra of dried colophony show a broad emission band in the range 360-500 nm for the excitation wavelengths 310–380 nm. After a 15h of photodegradation, the broad band shifts to long emission wavelengths and it remains approximately in the same position until 90 hours of ageing. For 155, 320 and 800 hours of ageing the band shifts to shorter excitation wavelengths (310/475 nm). During accelerated ageing, the shapes of the EE spectra drastically change. Another fluorescence emission band appears around $\lambda_{ex}= 260$ nm. The fluorescence spectrum excited at 365 nm shows a band whose maximum is at 442 nm. After 15h of irradiation, this maximum becomes broader and shifts to 480 nm, it remains approximately at 490 nm for longer periods of ageing up to 320 hours and, finally, returns to 480 nm after 800 hours of photodegradation.

The EE spectra of the dried oil colophony is characterized by a broad band centred at 360/465 nm. After 30 hours of irradiation, the broad band shifts towards higher emission wavelengths, 400-550 nm, but shorter excitation wavelengths, 310-360 nm. In the EE spectra measured after 90 hours of ageing, the band remains approximately in the same position but its maximum shifts to 315/460 nm. After 155 and 320 hours the maximum keeps the position, but the tail of the fluorescence emission excited at the longest wavelengths decreases. After 800 hours of ageing both the shape and the position of the band change drastically: we can see two broad bands, one centred at 360/450 nm and the other one around 310-320/390-410 nm of excitation/emission. Probably a fluorescence emission excited at shorter wavelengths is also present.

In the fluorescence spectra excited at 365 nm, the emission spectrum of the dried oil colophony shows a band with a maximum at 454 nm, that goes through many changes after photoageing. After only 15 hours the maximum shifts to 496 nm and a shoulder appears at 442 nm; after additional 15 hours of ageing the maximum remains approximately in the same position but the emission of the shoulder increases; 90 hours of ageing cause the band to become much broader since probably it includes short wavelength fluorescence. After 155 hours of ageing the short

wavelength fluorescence increases, showing a maximum at 462 nm; finally, after 320 and 800 hours of ageing, this maximum shifts to 452 nm, while, during the last accelerated ageing steps, this band becomes broader at long wavelengths.

After a short period, the thermal ageing of the spirit colophony induces a shift of the fluorescence excitation/emission band maximum to 380/490 nm; it remains approximately in the same position during all the experiments. The fluorescence spectra excited at 365 nm, exhibit an emission band with a maximum at 442 nm for the dried samples that shifts at 468 nm from 15 to 320 hours of irradiation, then at 488 nm after 800 hours of ageing. For the oil samples, the band shift from 360/465 nm to 370/465 nm. In the fluorescence spectra excited at 365 nm, the fluorescence emission spectra of the dried samples show a band with a maximum at 456 nm. The maximum shifts to 450 nm after 15 hours and to 440 nm after 30 h irradiation. At 30h, two shoulders appear at approximately 414 nm and 460 nm. After 90 hours the band has moved to higher wavelengths, with a maximum at 462 nm and a shoulder at 474 nm. After 155 hours, a second band appears at 584 nm which disappears after 320h of irradiation. Finally, after 800 hours of ageing, the maximum shifts to 484 nm.

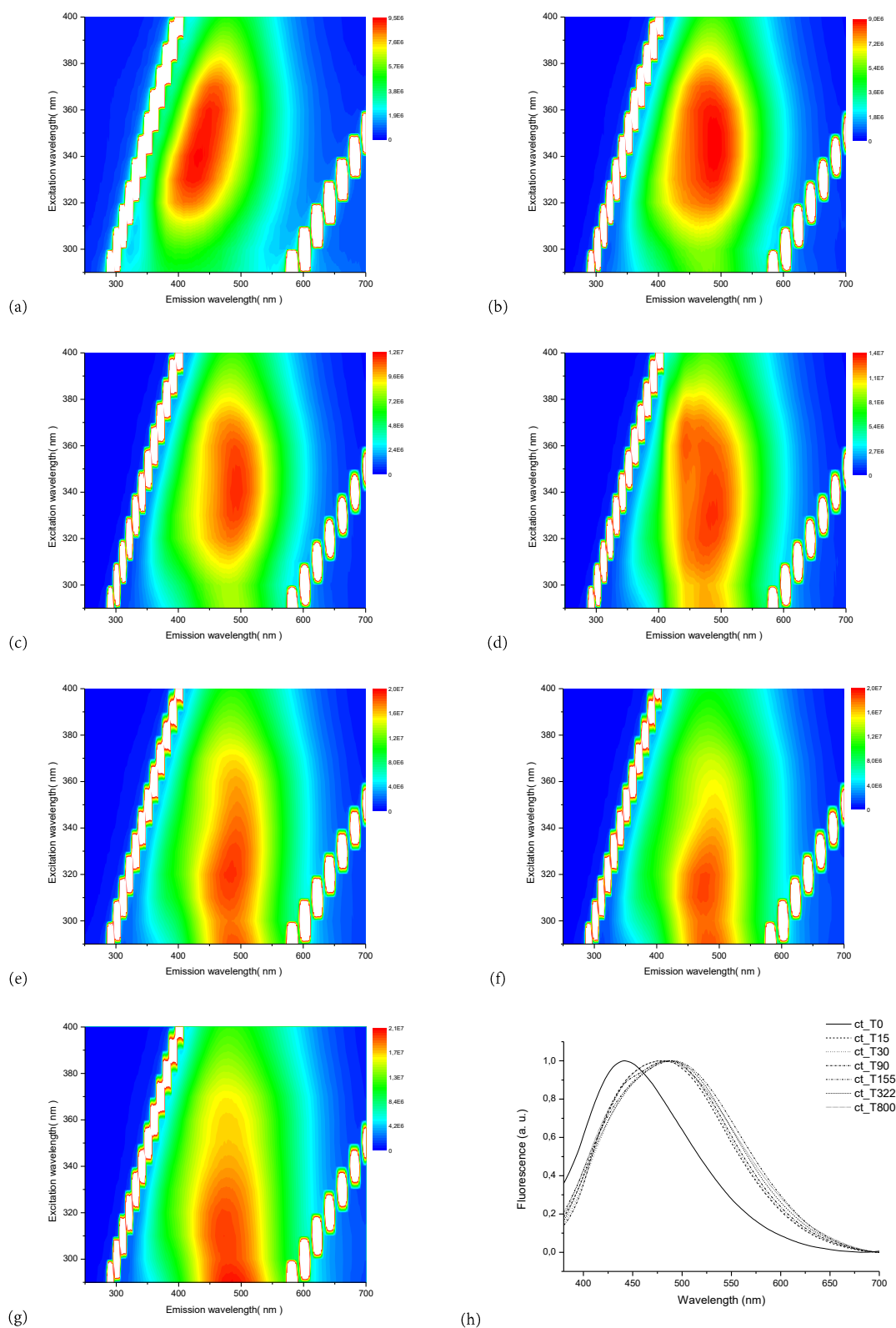


Fig. 172: Evolution of normalized excitation emission spectra of films of colophony in turpentine irradiated with artificial sunlight at 35°C: dried (a), irradiated during 15 hours (b), 30 hours (c), 90 hours (d), 155 hours (e), 320 hours (f) and 800 hours (g). Normalized emission fluorescence spectra for $\lambda_{ex} = 365$ nm (h).

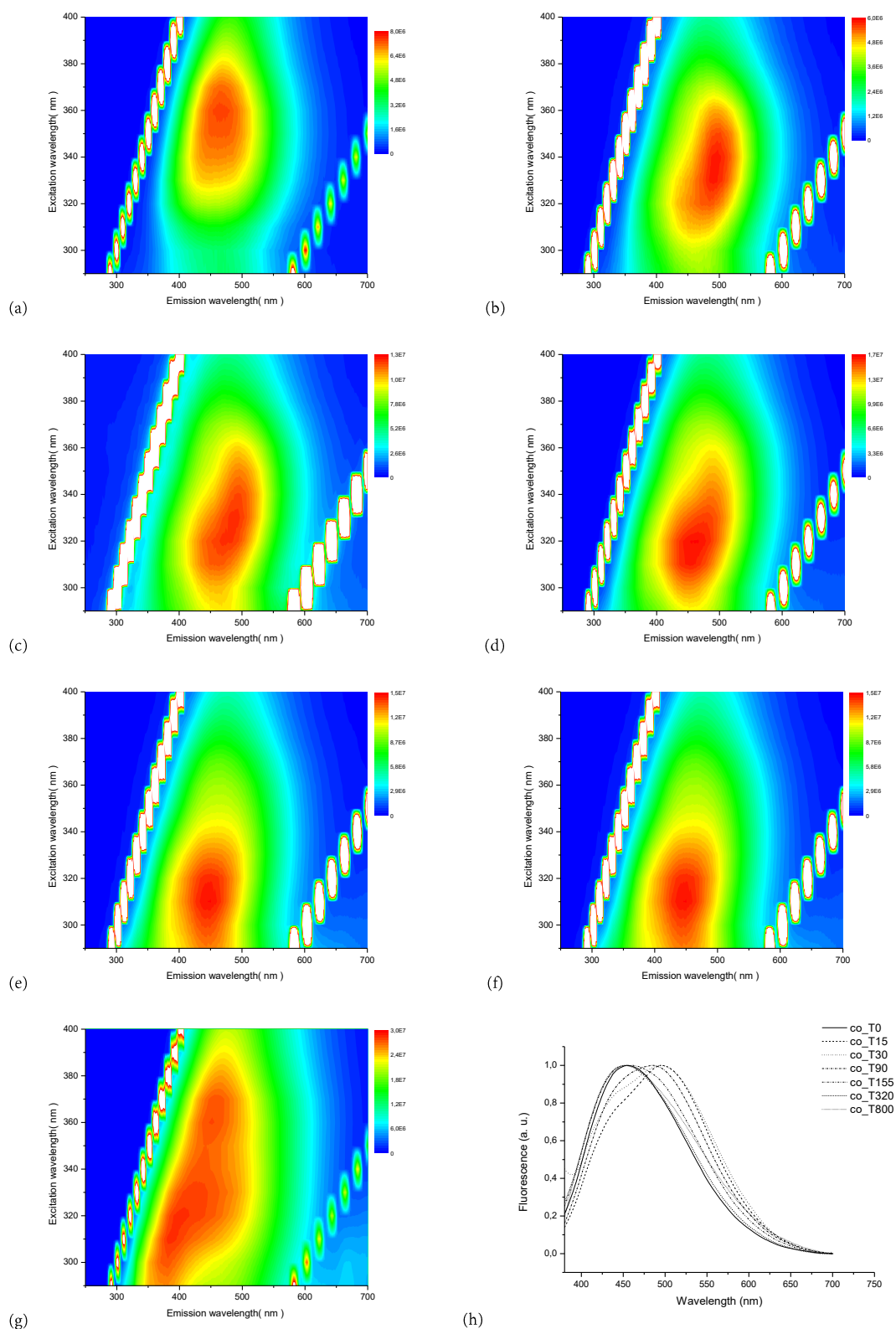


Fig. 173: Evolution of normalized excitation emission spectra of films of colophony in linseed oil irradiated with artificial sunlight at 35°C: dried (a), irradiated during 15 hours (b), 30 hours (c), 90 hours (d), 155 hours (e), 320 hours (f) and 800 hours (g). Normalized emission fluorescence spectra for $\lambda_{ex} = 365$ nm (h).

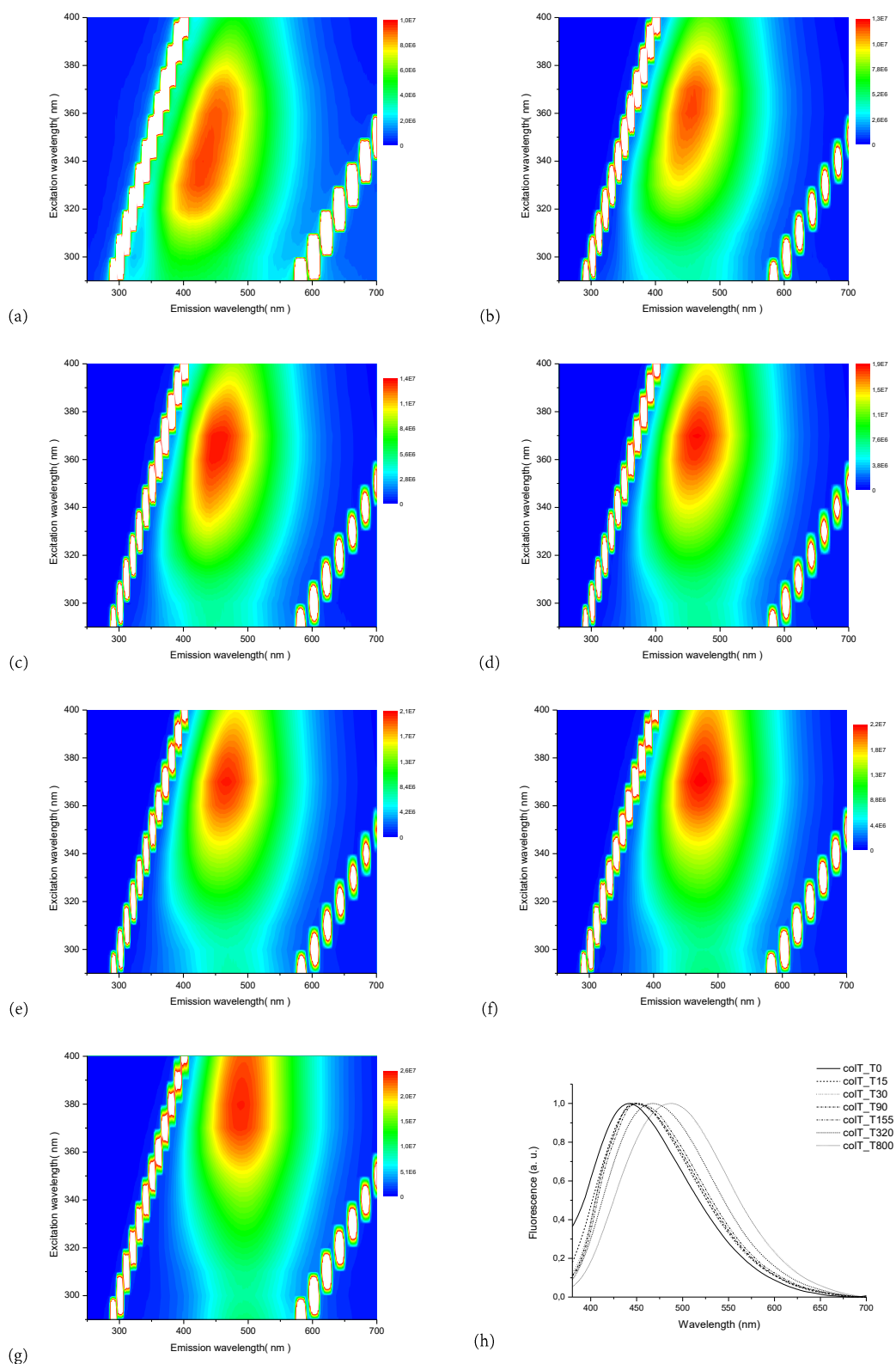


Fig. 174: Evolution of normalized excitation emission spectra of films of colophony in turpentine aged with the thermal method: dried (a), heated at 15 hours (b), 30 hours (c), 90 hours (d), 155 hours (e), 320 hours (f) and 800 hours (g). Normalized emission fluorescence spectra for $\lambda_{ex} = 365$ nm (h).

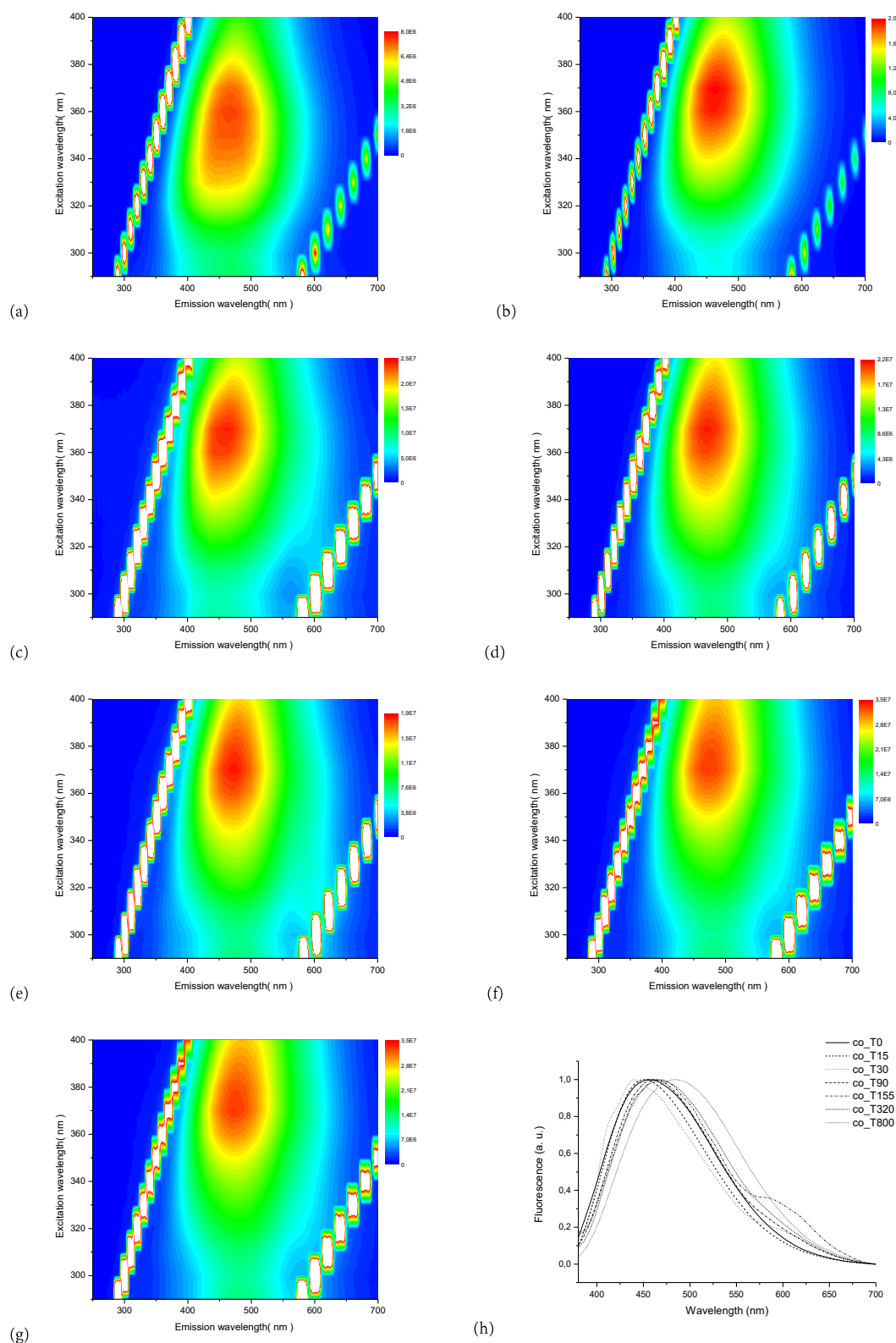


Fig. 175: Evolution of normalized excitation emission spectra of films of colophony in linseed oil aged with the thermal method: dried (a), heated at 15 hours (b), 30 hours (c), 90 hours (d), 155 hours (e), 320 hours (f) and 800 hours (g). Normalized emission fluorescence spectra for $\lambda_{ex} = 365$ nm (h).

To conclude, the fluorescence emission of varnishes changes with the excitation wavelength and the degradation state of the sample. This shows the importance to take in account the reaction of degradation when dealing with organic material.

In Tab. 5, we reported the wavelengths of the maxima of the varnishes fluorescence bands obtained after the two ageing processes. With an excitation at 365 nm, the shift induced by the ageing is lower for photochemical reactions than for thermal processes. Such effect may be linked to the formation of Polycyclic Aromatic compounds (for example, the retene in rosin) or related compounds during the thermal degradation of diterpens or triterpens presents in the resins. PAHs are highly fluorescent and, thus, can modify the global fluorescence even at very low level of concentration. The results from the PhD of Clara Azémard [Azemard C. (2014)] showed that photochemical reactions do not induce such type of products in the tested resins.

Tab. 5: Wavelengths of the maxima of the fluorescence bands of spirit and oil varnishes before ageing and after light and/or heat exposure for 800 hours. The resins diluted in turpentine are labelled "T"; the resins diluted in linseed oil are labelled "O".

Materials	Dried samples (λ_{\max})	Photochemical ageing (λ_{\max} at 800 hours)	Thermal ageing (λ_{\max} at 800 hours)
Mastic T	450 nm	460 nm	476 nm
Mastic O	450 nm	440 nm	478 nm
Dammar T	446 nm	452 nm	464 nm
Dammar O	446 nm	444 nm	470 nm
Colophony T	442 nm	488 nm	488 nm
Colophony O	456 nm	452 nm	484 nm

3.5.3. UV-VIS absorption spectra and yellowing

We measured the UV-VIS absorbance from 300 nm to 500 nm of the varnishes in order to have information on the penetration of UV radiation in aged varnishes; the corresponding spectra are reported in Fig. 176, Fig. 177, Fig. 178, Fig. 179, Fig. 180, Fig. 181, Fig. 182, Fig. 183, Fig. 184, Fig. 185, Fig. 186 and Fig. 187.

The photochemical reactions produce a peculiar trend in the absorbance spectra. However, from 400 nm to 500 nm the absorbance of almost all varnishes increases, shown in the inset of the figures; instead, at the shortest wavelengths, the absorbance decreases. Below 360 nm, the absorbance of the mastic in turpentine decreases up to 155 hours of ageing; the inversion point shifts towards short wavelengths, reaching the values of about 340 nm and 325 nm after 320 hours and 800 hours, respectively. Mastic in oil shows a decrease of absorbance up to 90 hours, but after 155 hours its absorbance increases above 310 nm. Dammar in turpentine shows an inversion point that shifts to shorter wavelengths up to 155 hours, but after 320 hours and 800 hours of ageing the entire absorbance spectrum increases. Dammar in oil shows a decrease of absorbance up to 320 hours, but after 800 hours its absorbance increases above 388 nm. The colophony in turpentine shows an inversion point at 365 nm after 15 hours and at 317 nm up to 155 hours; after 320 and 800 hours the inversion point shifts to shorter wavelengths (306 nm). Also colophony in oil presents several inversion points until 800 hours.

The thermal ageing causes an increase in absorbance for all varnishes on the whole UV-VIS range, Fig. 182, Fig. 183, Fig. 184, Fig. 185, Fig. 186 and Fig. 187. Such effect can be related to the formation of chromophores in the varnish such as aromatic cycle or conjugated systems. This may come from the cyclisation of the compounds and the formation of PAH during the thermal degradation as the degradation pathway of abietane proposed by Colombini [Colombini M. P. et al (2009)].

The increase of the absorbance of all varnishes from 400 nm to 500 nm is clearly responsible for their yellowing. In order to evaluate the changing of yellowing with ageing, for each sample we normalized the absorbance values measured at 450 nm with those measured after 15 hours of ageing; we assume that, after 15 hours of thermal ageing, the varnishes have dried completely. The results are shown in Fig. 188 and Fig. 189.

During the photoageing process, dammar and mastic are less sensitive to yellowing than colophony (lower absorbance ratio values). The thermal ageing induces a stronger yellowing than

with the light exposure. In this case colophony and mastic show more yellowing than dammar. In general, the absorbance ratio rises faster between 320 hours and 800 hours.

For the oil varnishes, we noticed a strong decrease of absorbance after 90 hours of irradiation, in particular in the spectral range between 400 nm and 500 nm, this can be associated with two factors: the decrease of the sample thickness due to the drying and/or the bleaching related to the light action [De la Rie R. (1988), Dietemann *et al.* (2009)]. On the contrary, the colophony in oil samples shows an increase of absorbance in these regions.

In general, we can conclude that the thermal ageing produces more yellowing than photodegradation both in spirit and oil varnishes.

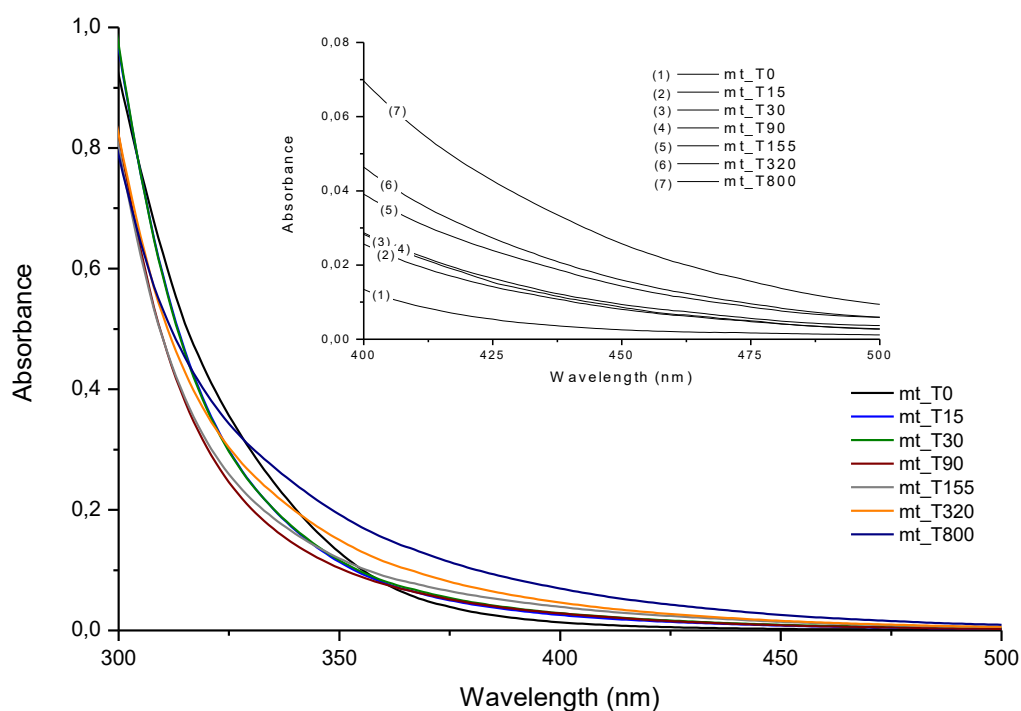


Fig. 176: UV-VIS spectra of mastic in turpentine before ageing (T0), after 15 hours (T15), 30 hours (T30), 90 hours (T90), 155 hours (T155), 322 hours (T322) and 800 hours of irradiation at 35°C.

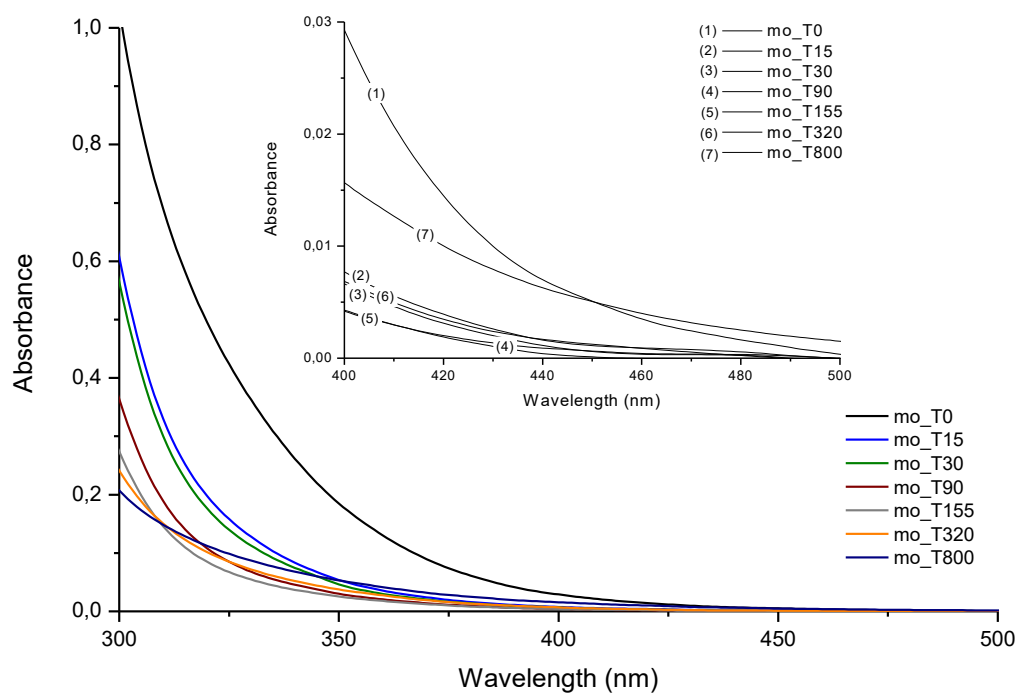


Fig. 177: UV-VIS spectra of mastic in linseed oil before ageing (T0), after 15 hours (T15), 30 hours (T30), 90 hours (T90), 155 hours (T155), 322 hours (T322) and 800 hours of irradiation at 35°C.

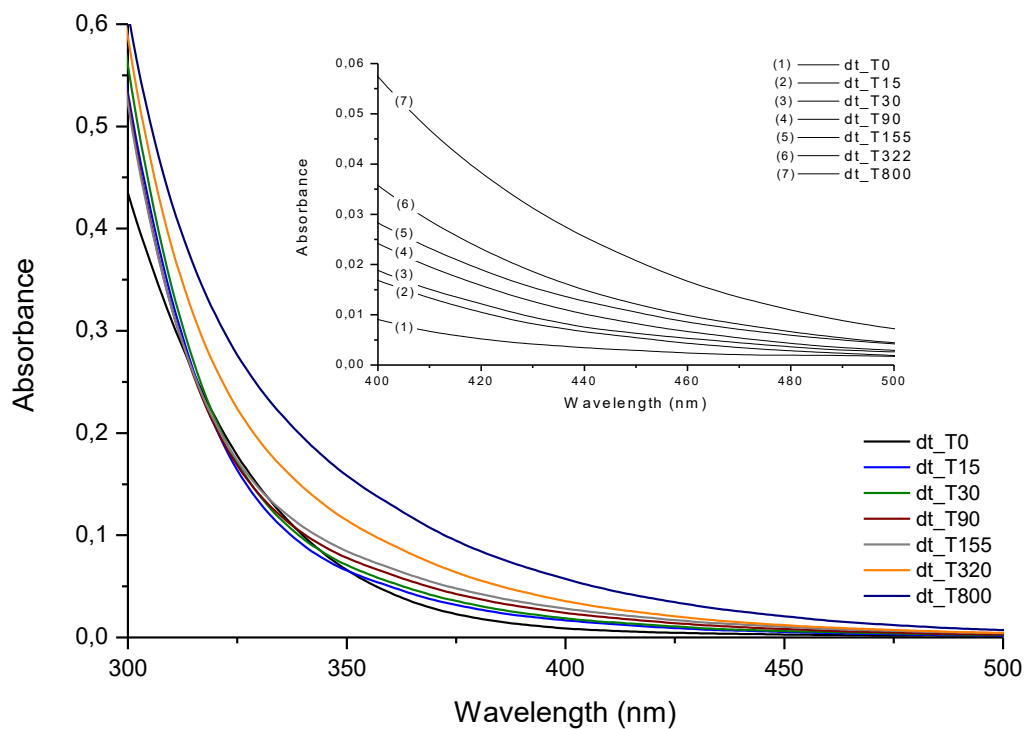


Fig. 178: UV-VIS spectra of dammar in turpentine before ageing (T0), after 15 hours (T15), 30 hours (T30), 90 hours (T90), 155 hours (T155), 322 hours (T322) and 800 hours of irradiation at 35°C.

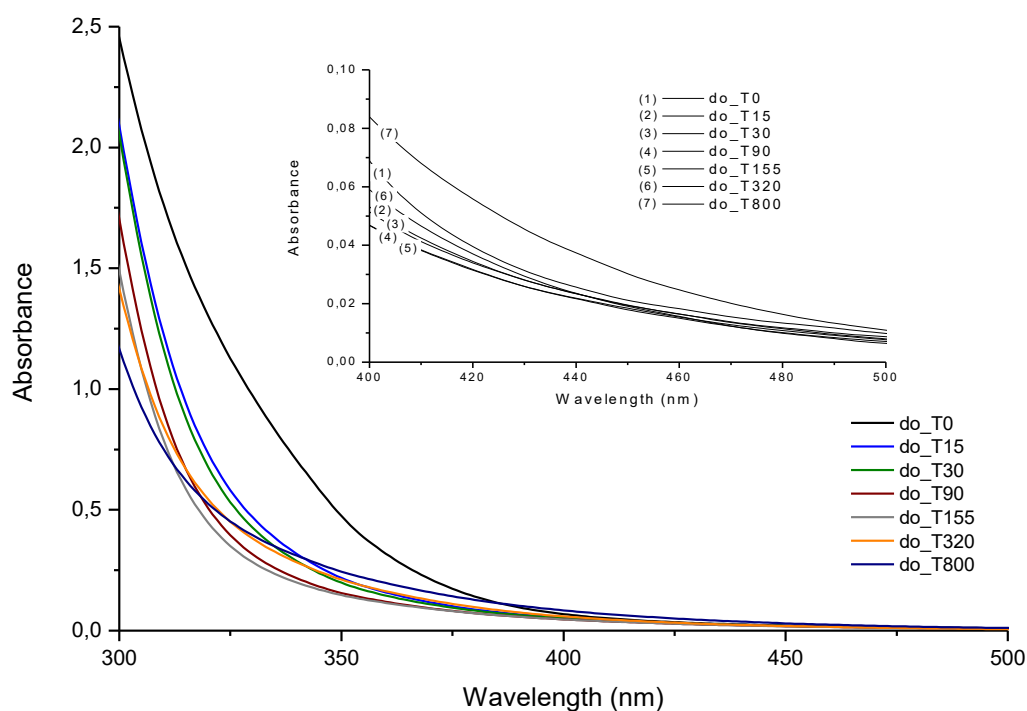


Fig. 179: UV-VIS spectra of dammar in linseed oil before ageing (T0), after 15 hours (T15), 30 hours (T30), 90 hours (T90), 155 hours (T155), 322 hours (T322) and 800 hours of irradiation at 35°C.

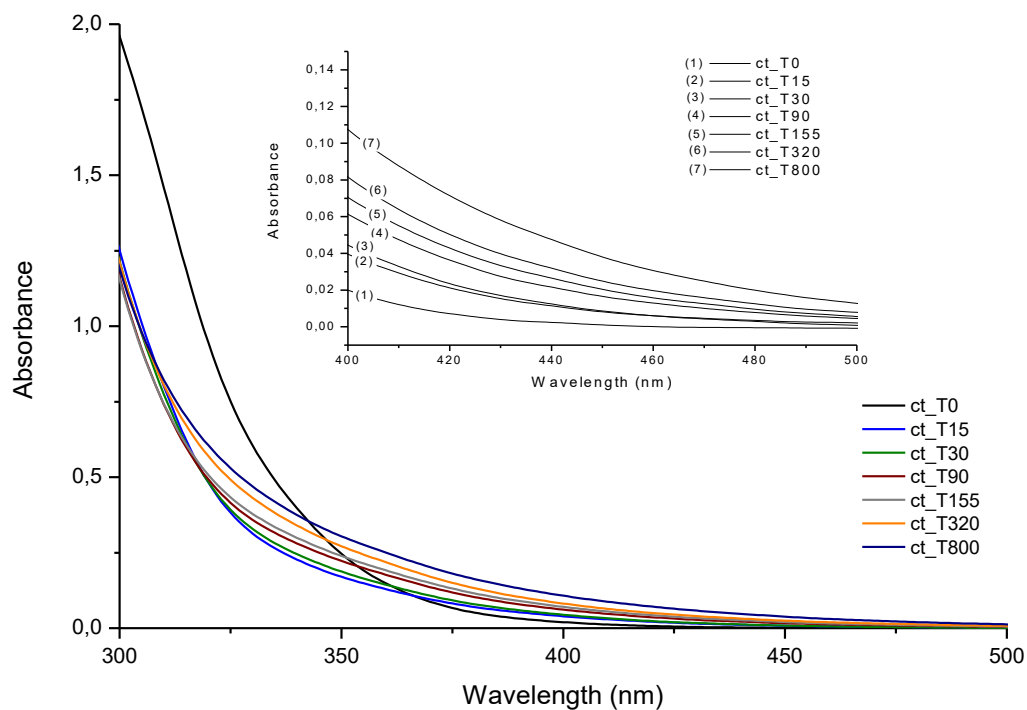


Fig. 180: UV-VIS spectra of colophony in turpentine before ageing (T0), after 15 hours (T15), 30 hours (T30), 90 hours (T90), 155 hours (T155), 322 hours (T322) and 800 hours of irradiation at 35°C.

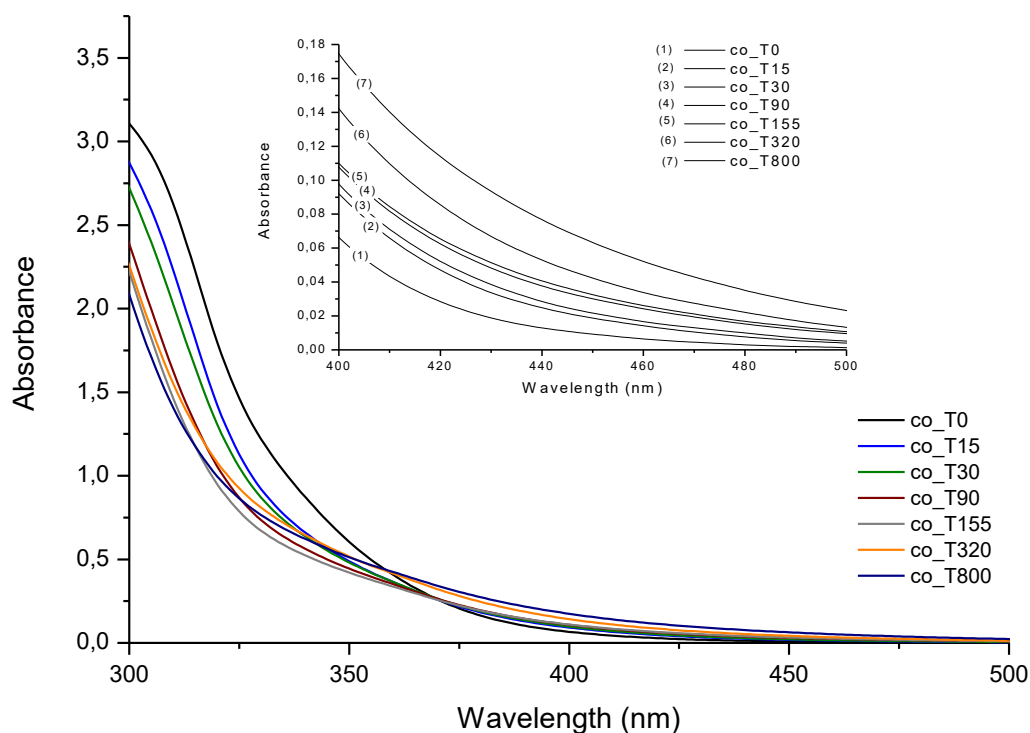


Fig. 181: UV-VIS spectra of colophony in linseed oil before ageing (T₀), after 15 hours (T₁₅), 30 hours (T₃₀), 90 hours (T₉₀), 155 hours (T₁₅₅), 322 hours (T₃₂₂) and 800 hours of irradiation at 35°C.

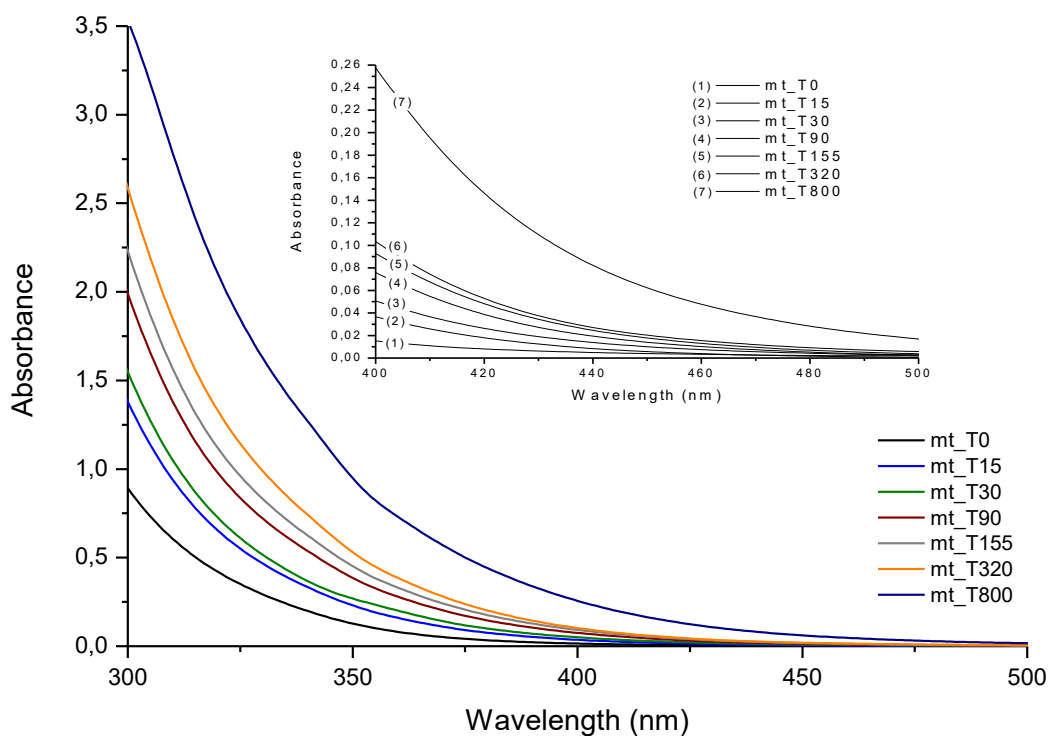


Fig. 182: UV-VIS spectra of mastic in turpentine before ageing (T₀), after 15 hours (T₁₅), 30 hours (T₃₀), 90 hours (T₉₀), 155 hours (T₁₅₅), 322 hours (T₃₂₂) and 800 hours of thermal ageing at 75°C.

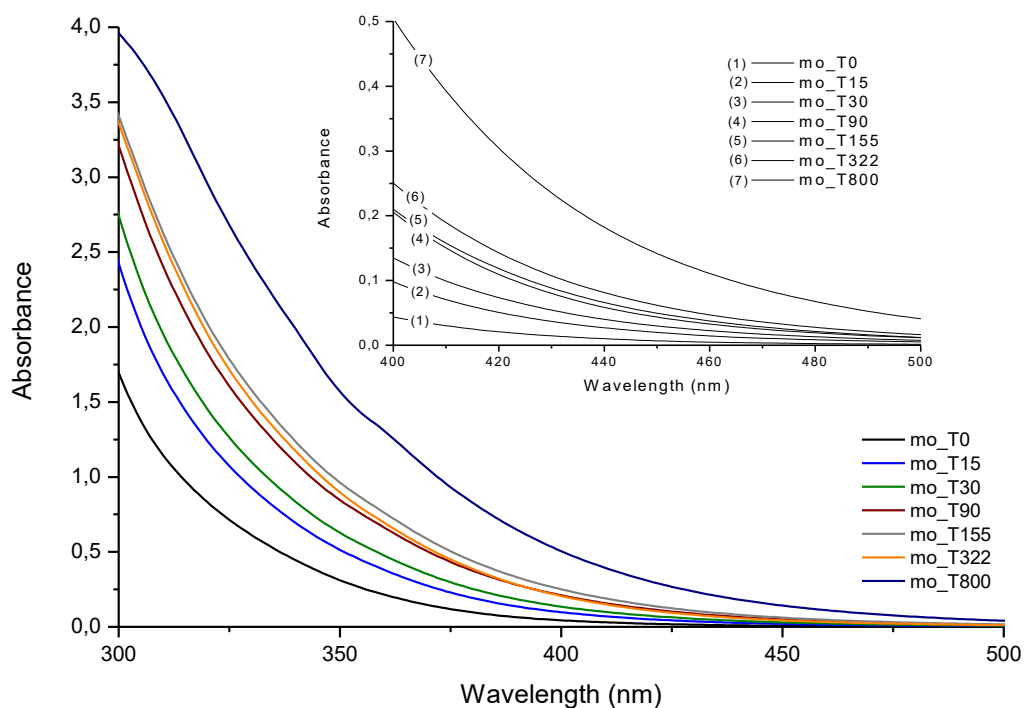


Fig. 183: UV-VIS spectra of mastic in linseed oil before ageing (T0), after 15 hours (T15), 30 hours (T30), 90 hours (T90), 155 hours (T155), 322 hours (T322) and 800 hours of thermal ageing at 75°C.

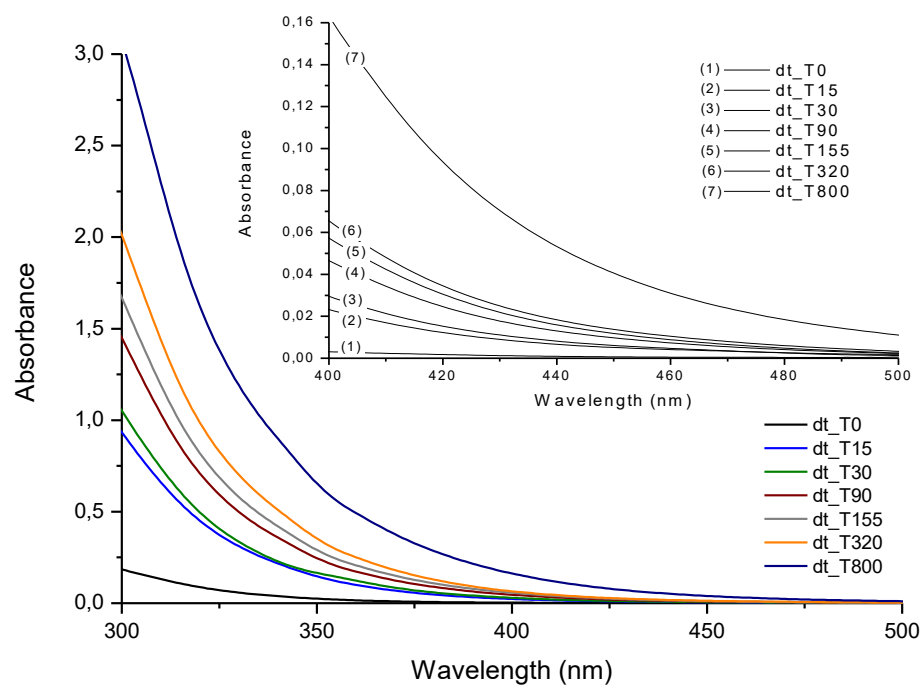


Fig. 184: UV-VIS spectra of dammar in turpentine before ageing (T0), after 15 hours (T15), 30 hours (T30), 90 hours (T90), 155 hours (T155), 322 hours (T322) and 800 hours of thermal ageing at 75°C.

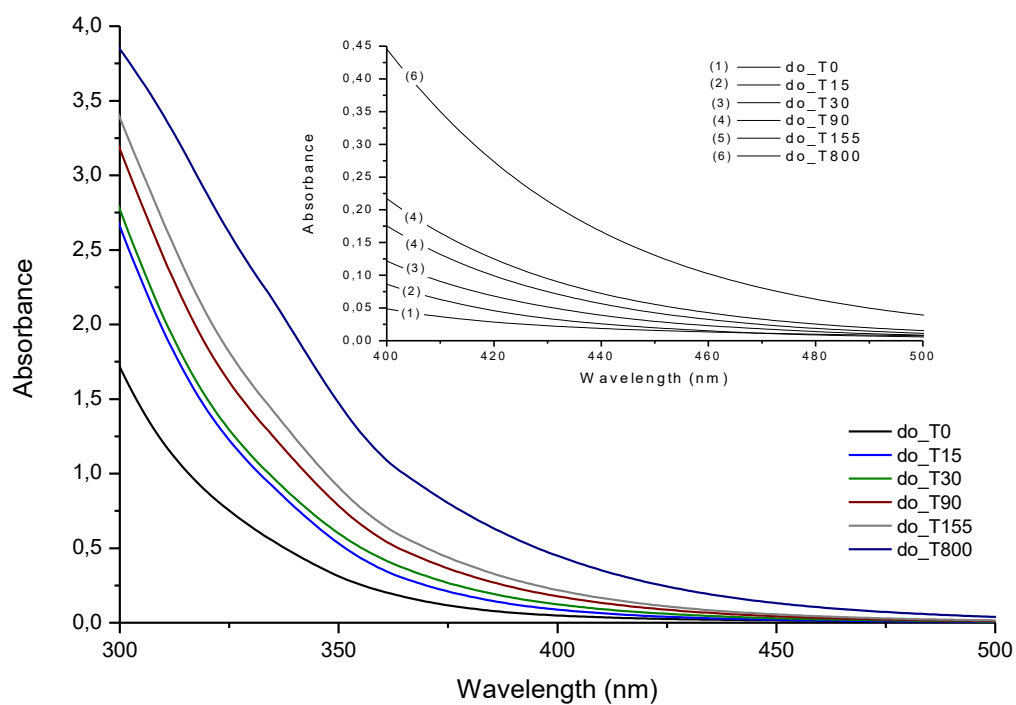


Fig. 185: UV-VIS spectra of dammar in linseed oil before ageing (T0), after 15 hours (T15), 30 hours (T30), 90 hours (T90), 155 hours (T155), 322 hours (T322) and 800 hours of thermal ageing at 75°C.

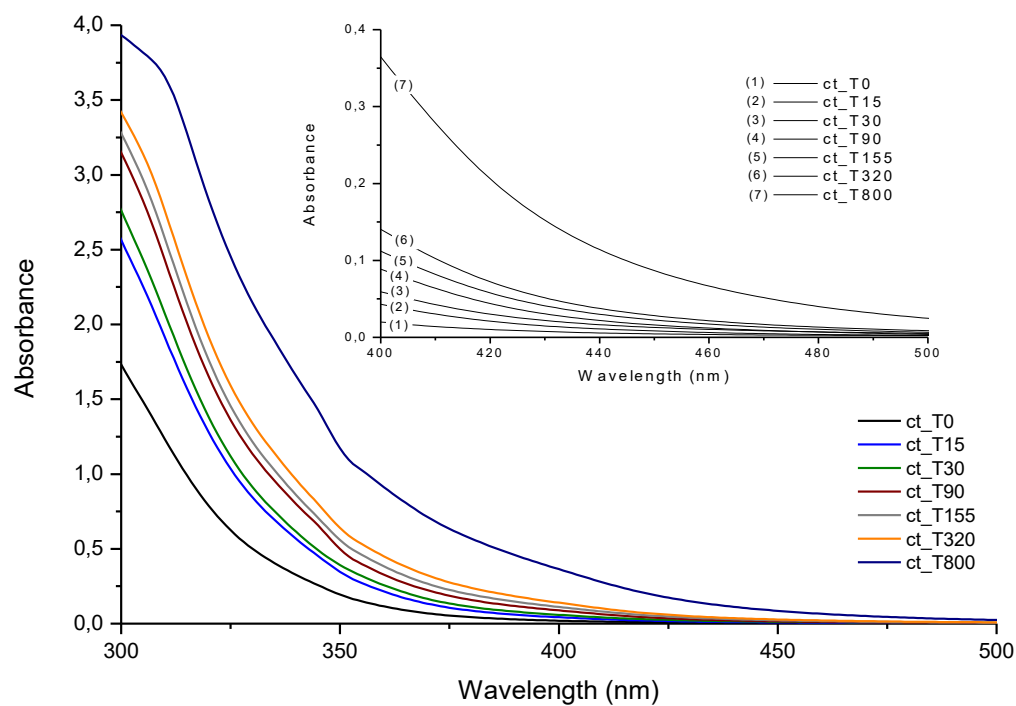


Fig. 186: UV-VIS spectra of colophony in turpentine before ageing (T0), after 15 hours (T15), 30 hours (T30), 90 hours (T90), 155 hours (T155), 322 hours (T322) and 800 hours of thermal ageing at 75°C.

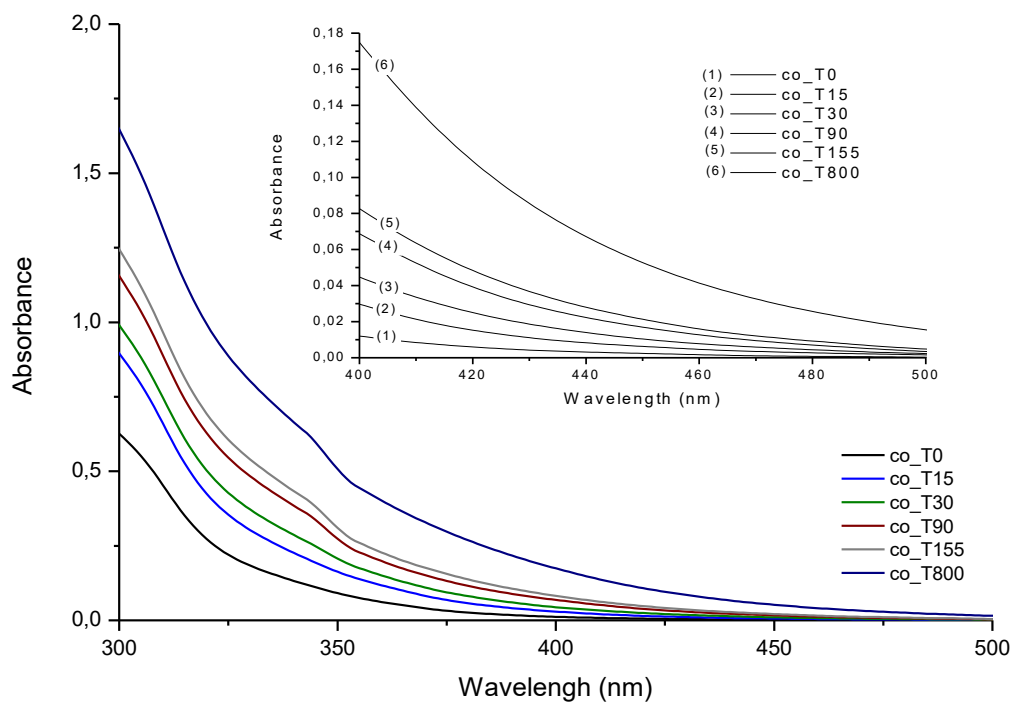


Fig. 187: UV-VIS spectra of colophony in linseed oil before ageing (T0), after 15 hours (T15), 30 hours (T30), 90 hours (T90), 155 hours (T155), 322 hours (T322) and 800 hours of thermal ageing at 75°C.

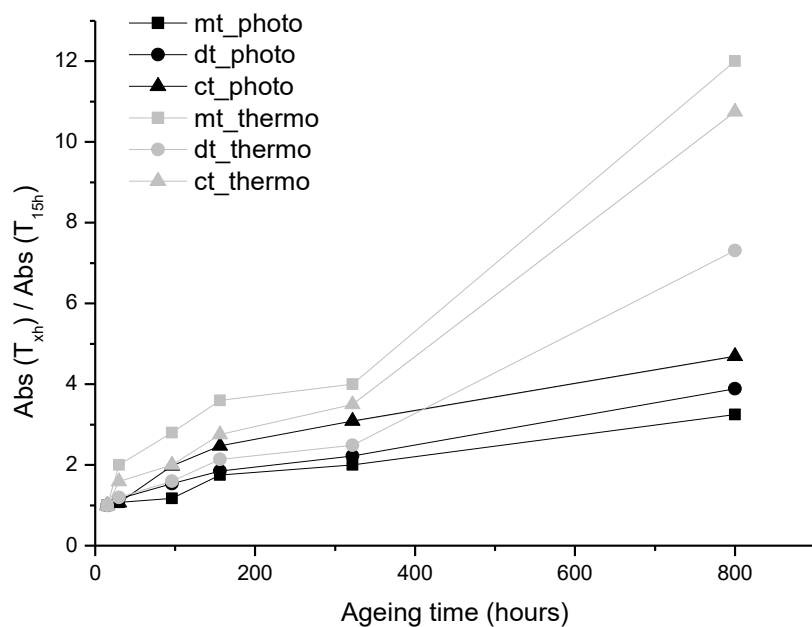


Fig. 188: Absorbance ratios between the absorbance values at a specific ageing time (T15h) and the values after 15 hours of accelerated ageing of spirit varnishes.

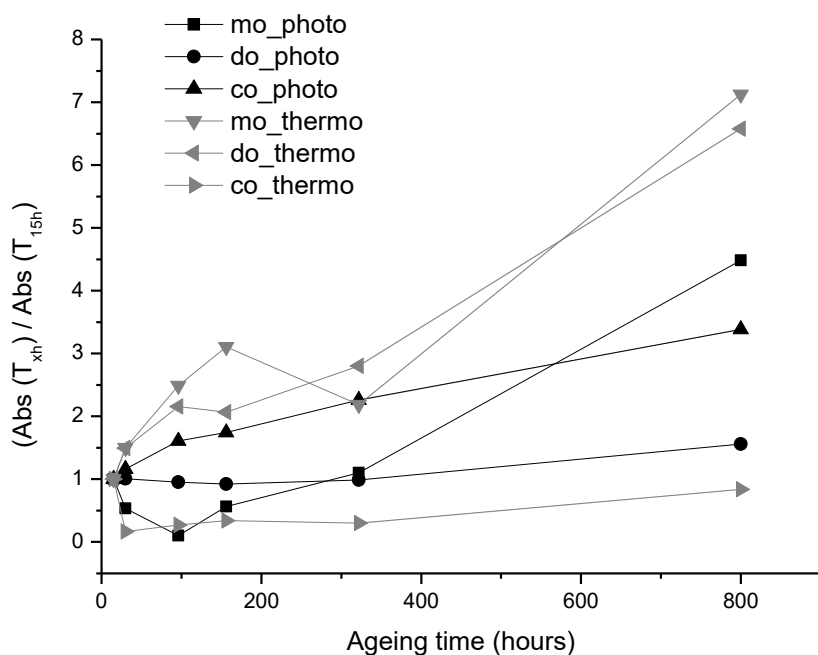


Fig. 189: Absorbance ratios between the absorbance values at a specific ageing time (T_{xh}) and the values after 15 hours (T_{15h}) of accelerated ageing of spirit varnishes.

3.5.4. Multispectral fluorescence imaging

We acquired UV multispectral fluorescence images of the varnish samples before the ageing process (T_0) and after 800h of photodegradation and thermal ageing. The UV multispectral fluorescence images were taken using the narrow band filters at 450 nm, 500 nm, 532 nm, 550 nm and 600 nm, Fig. 190, Fig. 191, Fig. 192. The fluorescence spectra reconstructed from the multispectral images are shown in Fig. 193, Fig. 194 and Fig. 195.

In the case of non-aged samples, the fluorescence intensity of the oil varnishes was higher than the spirit ones, probably for the additional contribution of the fluorescence of the linseed oil. After ageing, all the oil samples show higher fluorescence intensities than the spirit varnishes. Moreover, the oil samples show a maximum intensity at wavelengths between 450 and 470 nm, in

agreement with the fluorescence spectra acquired with the spectrofluorimeter. Instead, the maximum intensity of the spirit varnishes is probably below 450 nm.

After the photoageing, a general increase of the fluorescence intensity both for the spirit and oil varnishes has been noticed. In addition, the fluorescence emission band of the spirit colophony becomes broader, in agreement with the spectrofluorimetric measurements.

For the thermal ageing, we observed a general broadening of the peaks; thus the fluorescence contribution in the green and yellow regions is stronger than for the irradiated samples.

The spectra obtained with the multispectral imaging method shown spectral features similar to the spectra obtained with the spectroscopic measurements; some discrepancies can be ascribed to the spectral distribution of the UV sources used and to the lower resolution of the reconstructed spectra.

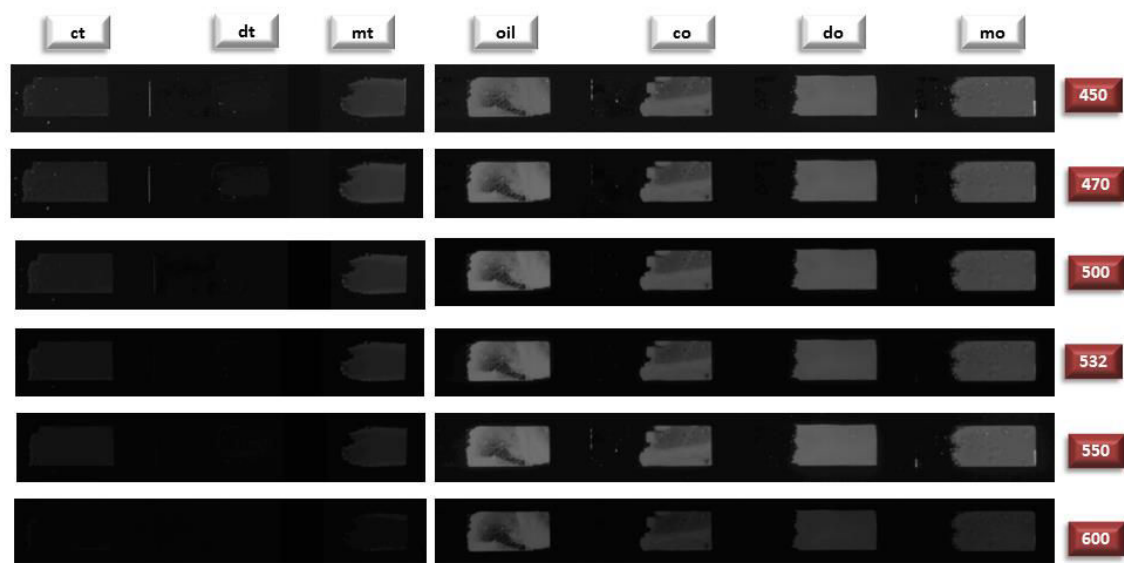


Fig. 190: UV multispectral images of the dried linseed oil and varnishes.

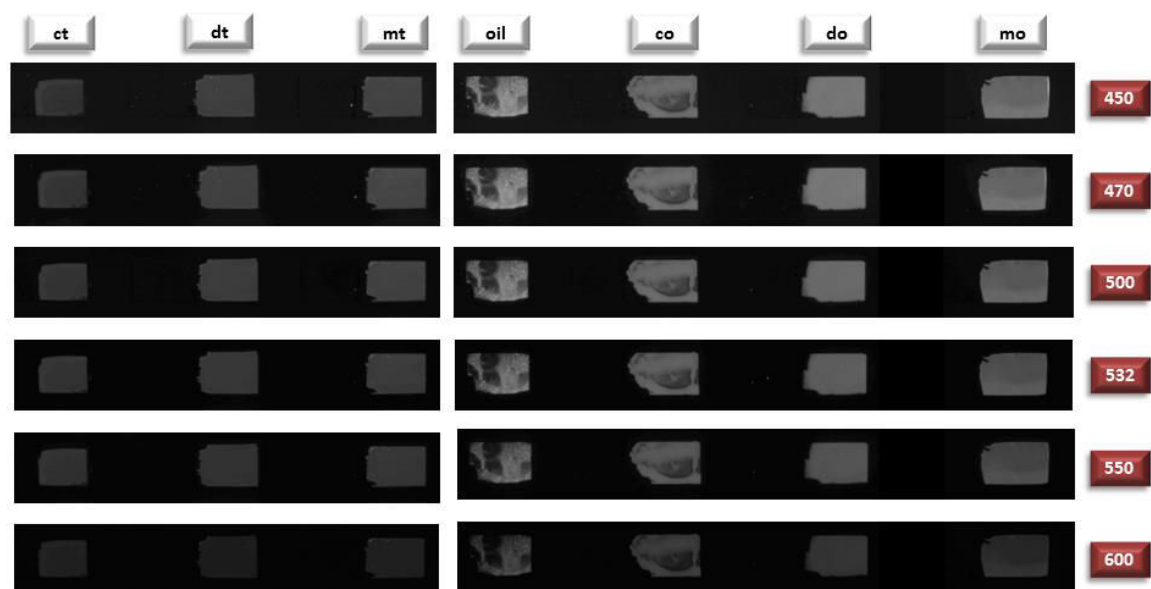


Fig. 191: UV multispectral images of the linseed oil and the varnishes irradiated with artificial sunlight during 800 hours at 35°C.

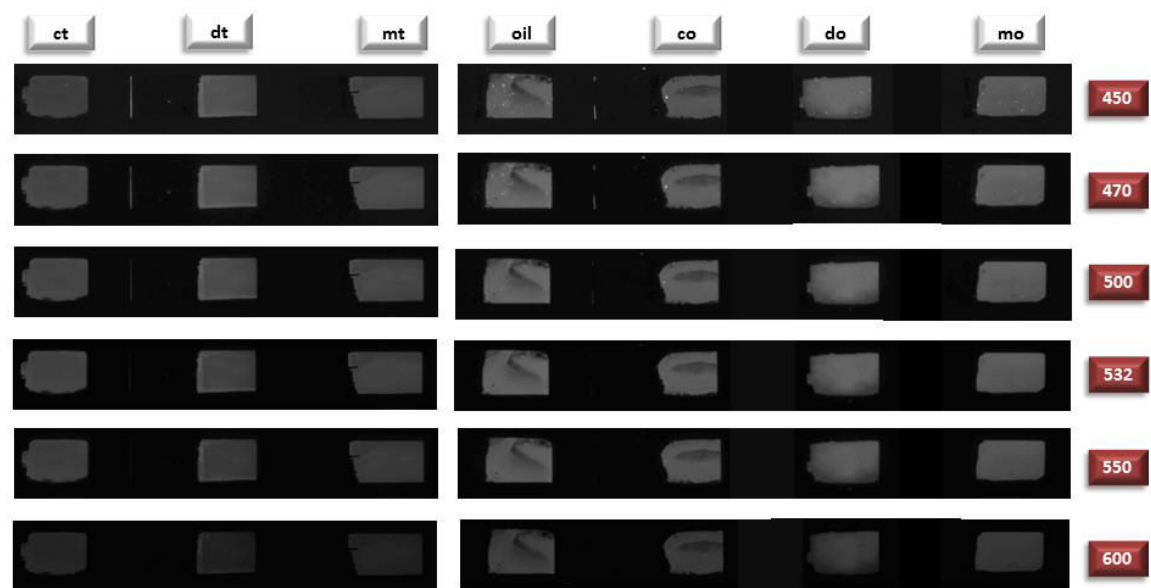


Fig. 192: UV multispectral images of the linseed oil and the varnishes thermal aged for 800 hours.

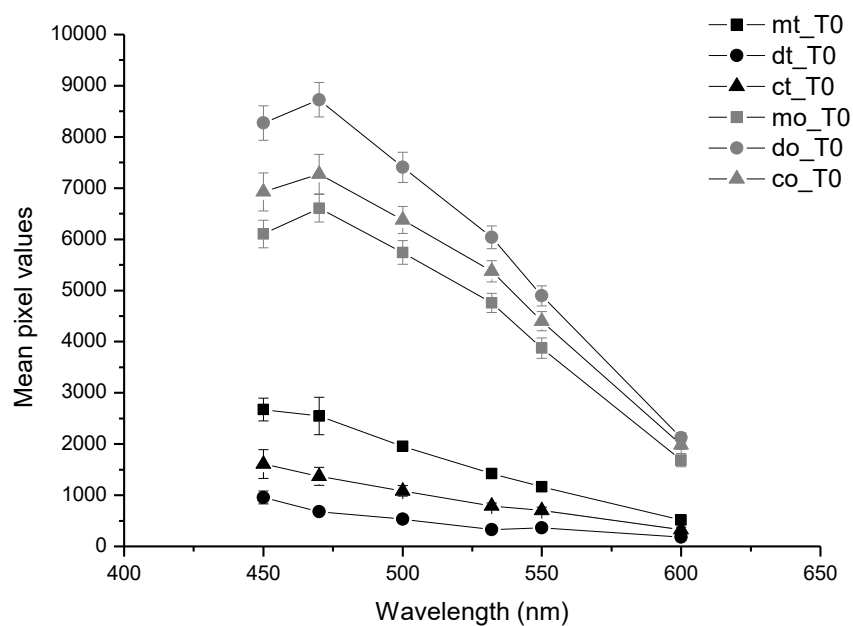


Fig. 193: Fluorescence spectral reconstruction from the UV-multispectral images of the dried varnishes

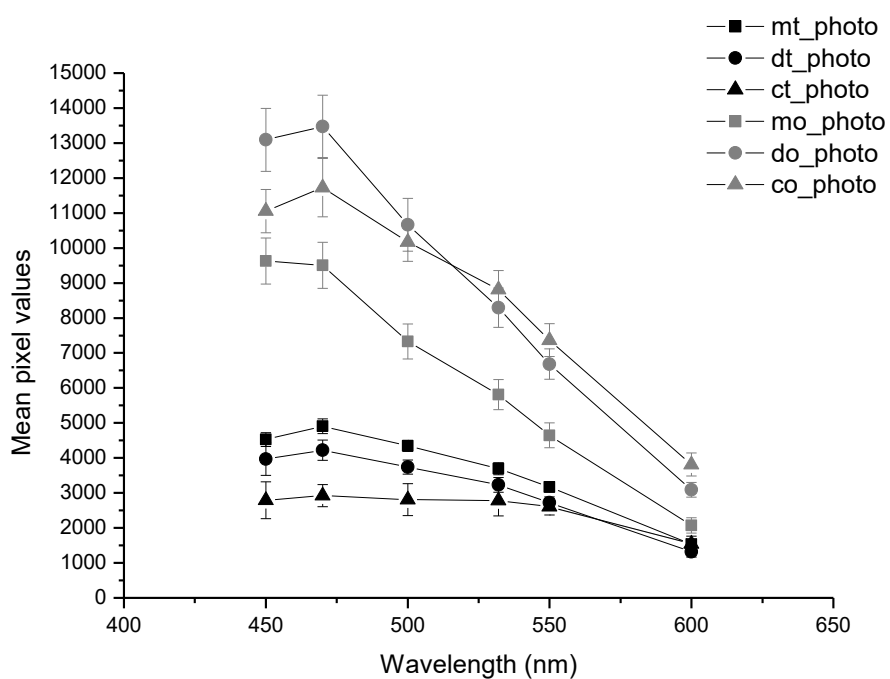


Fig. 194: Fluorescence spectral reconstruction of the UV-multispectral images of the varnishes irradiated with artificial sunlight during 800h at 35°C.

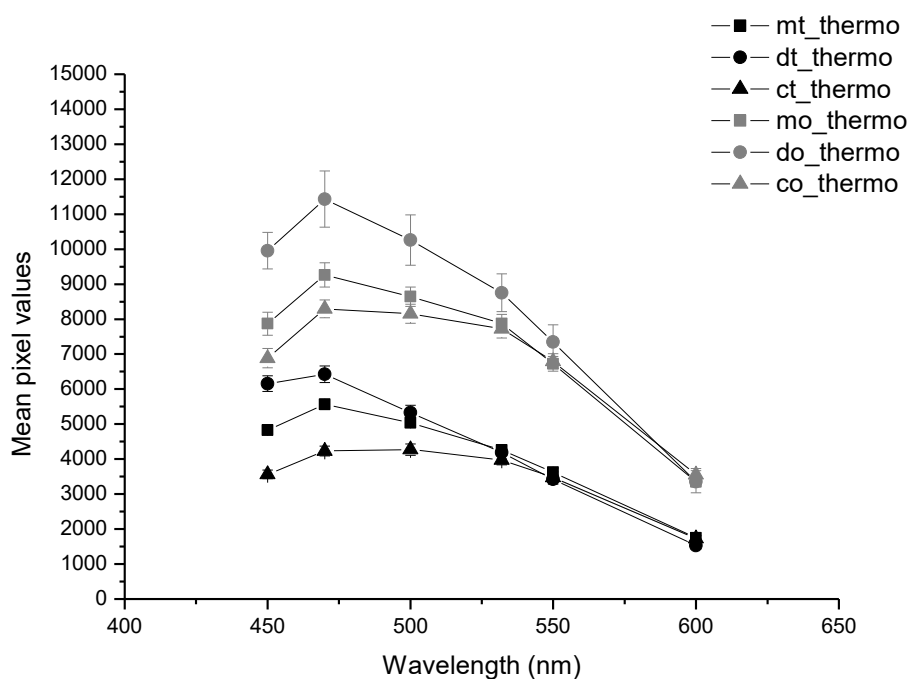


Fig. 195: Fluorescence spectral reconstruction from the UV-multispectral images of the thermal aged varnishes

In the "false" RGB image shown in Fig. 196, obtained combining the UV multispectral images taken at 532 nm, 500 nm and 470 nm, we observe that colophony, dammar and mastic in turpentine present a lower fluorescence intensity than the oil samples. After the photodegradation, colophony in turpentine can be distinguished from the other varnishes. The thermal aged samples appear very similar to each other, except for the dammar and mastic in turpentine.

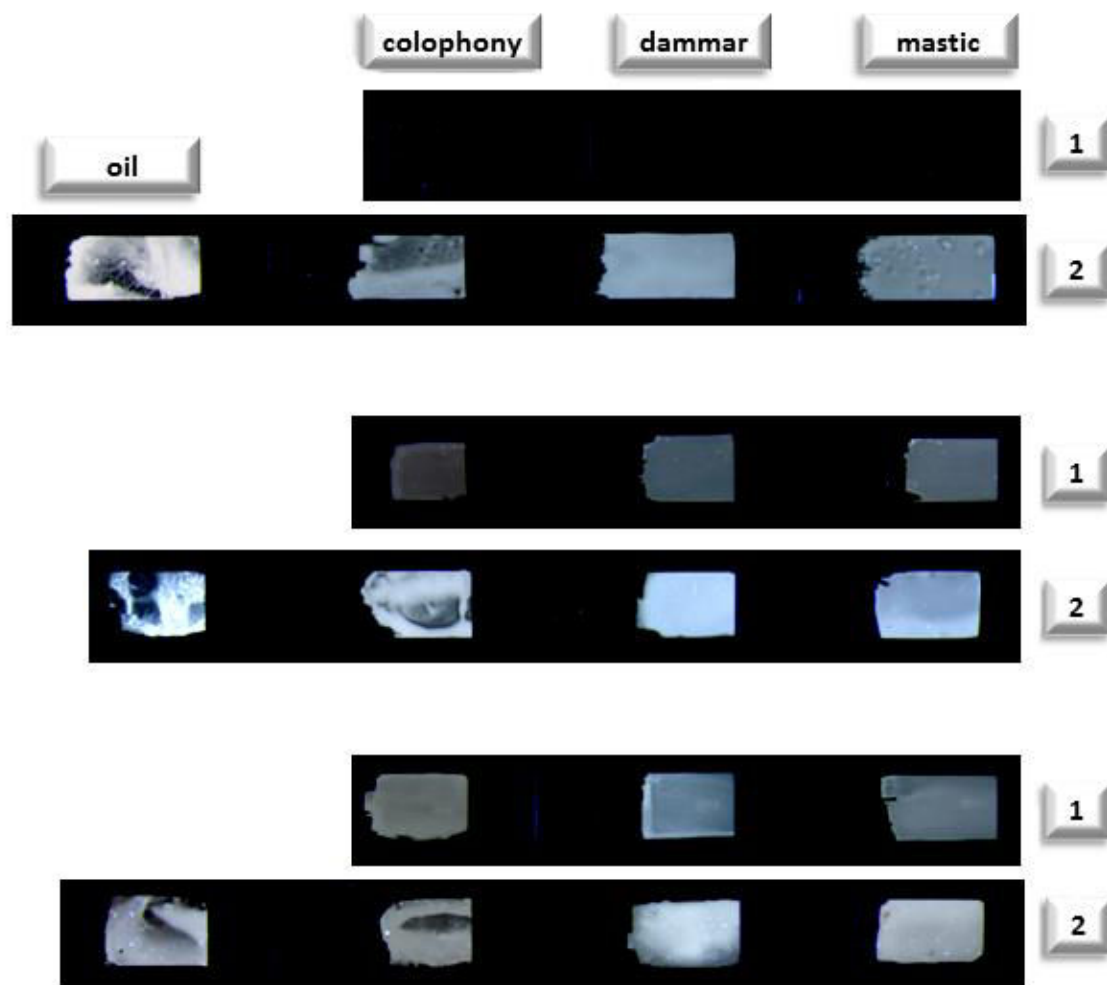


Fig. 196: “False” RGB combination of the varnish samples and linseed oil by using the images taken at 532 nm (R), 500 nm (G) and 470 nm (B). The dried varnishes are shown in the top panel (1: resins with turpentine, 2: resins with linseed oil), the samples irradiated with artificial sunlight (800h, 35°C) are in the centre panel and the thermal aged ones in the bottom panel.

3.6 Conclusions

The degradation of mastic, dammar and colophony dissolved in turpentine or in linseed oil upon irradiation was investigated by means of ATR-FTIR spectrometry, spectrofluorimetry, UV-VIS spectrometry and UV-multispectral imaging. Two accelerated ageing methods were tested in order to compare the different variations of the chemical and optical properties of the varnishes.

A strong degradation of the varnishes results of the photochemical ageing method that induces the diminution of the C-H and C=C bonds and the increase of the C=O and C-O bonds.

The formation of unsaturated and aromatised byproducts leads to the increase of the UV absorption and a high yellowing of the varnishes. Such effects are stronger after the thermal ageing than after the photodegradation. In most cases, during the photoageing tests, we observed a decrease of the absorbance values below 360 nm due to the bleaching phenomena induced by the light exposure [De la Rie R. (1982-2)]. These phenomena can also explain the shift of the fluorescence band, excited at 365 nm, towards short wavelengths, especially for oil samples. On the contrary, thermal ageing produces fluorescence emissions at longer wavelengths with the formation of several fluorophores that cause the broadening of the fluorescence band.

To conclude, the two methods are complementary. One bringing the information of thermal degradation and the other one on the photochemistry of varnishes. However, the differences in the results of the two types of degradation show the complexity of interpreting the fluorescence and UV-visible absorption of a painting varnish in real conditions of conservation. Thus, it shows the difficulties to confront experiments in laboratory and real cases from art objects.

Regarding the UV-multispectral fluorescence imaging, we can state that the fluorescence emissions of fresh varnishes are very weak, which limit the potentialities of using a commercial colour-camera to analyse them. However, the higher intensity of the fluorescence emission of the oil varnishes permits their discrimination from the spirit ones. Among the resins, the colophony is clearly identifiable due to its fluorescence emission compared with that of the two triterpenes, dammar and mastic.

PART III:

**MULTISPECTRAL IMAGING AS A DIAGNOSTIC
TOOL FOR PAINTINGS**

Chapter 1

Diagnostic study of two paintings of the Lazzaroni collection

Investigations of two paintings of the Lazzaroni collection, preserved in the Gallery of the Accademia di San Luca, were performed using a multi-analytical approach, based on ED-XRF analysis, reflectance measurements, radiography, fluorescence imaging and multispectral UV-VIS-NIR imaging in situ. UV fluorescence imaging was focused mainly on the individuation of retouching's or fluorescent compounds; multispectral reflectance imaging permitted to emphasize some inhomogeneity's of the pictorial film. The technical execution and the under-drawings were revealed by means of Multispectral Near Infrared imaging and radiography. ED-XRF and reflectance spectroscopies allowed the identification of the pigments used.

1.	Diagnostic study of two paintings of Lazzaroni's collection	209
1.1.	Introduction	209
1.2.	"Virgin and the Child and Saint Catherine of Alexandria" by Matteo di Giovanni's imitator	211
1.2.1.	Non-destructive stratigraphic investigation	211
1.2.2.	Pigments identification	222
1.3.	"Virgin and the Child" by Venetian school	230
1.3.1.	Non-destructive stratigraphic investigation	230
1.3.2.	Pigments identification	244
1.4.	Conclusions	252

1.1 Introduction

In this chapter we report a preliminary study of two paintings of the Lazzaroni collection belonging to the Gallery of the “Accademia di San Luca” (Rome):

- “Virgin and the Child and Saint Catherine of Alexandria” by Matteo di Giovanni’s imitator (XV century),
- “Virgin and the Child” by Venetian school (XV century).

The two paintings belonged to the Baron Michele Lazzaroni and they were donated to the “Accademia di San Luca” in 1935, after his death.

The entire Lazzaroni collection is the object of many studies; the Baron used to modify the paintings for reselling them, so that several doubts arise on their attributions and/or present iconographic uncertainties. In fact, the end of the XIX century and the beginning of the XX century were characterized by the phenomenon of “false of art”, which have involved all the world.

In order to avoid any damage on these paintings, we carried out a non-destructive approach, using analytical techniques that do not require to take samples from the painting.

We proceeded with the following diagnostic steps:

- Acquisition of UV-fluorescence images to evaluate the state of conservation of the superficial layers. At first, we took UV fluorescence photography's with a commercial digital camera (Coolpix P6000) illuminating with two Wood lamps (we could not eliminate the visible light contribution from the UV lamps). After selecting some interesting areas, we employed the multispectral system exciting the fluorescence with two UV LED sources. In both cases we avoided the ambient light using a portable dark room.
- Acquisition of NIR reflectography to visualize the under-drawings. We acquired the infrared images both with long-pass filters and band-pass filters in order to highlight the potentiality of the multispectral system.

- We took radiographic images for checking the state of conservation of the supports and to reveal some features of the under-drawings present in the most internal layers of the paintings. The radiographic images are complementary to NIR reflectography.
- Multispectral reflectance imaging was performed in order to emphasize some spectral features of the pictorial layer.
- Optical microscopy was used to monitor the pigment mixtures used in the different hues of the pictorial layers and to direct the point-to-point analysis.
- The identification of the pigments selected in the previous step was performed by means of ED-XRF and reflectance spectroscopies. The combined use of ED-XRF and FORS spectroscopy allowed us a preliminary stratigraphic individuation of the dyes and/or pigments employed due to the fact the FORS investigates superficial layers while ED-XRF also reaches the preparatory layer.

1.2 “Virgin and the Child and Saint Catherine of Alexandria”

1.2.1 Non-destructive stratigraphic investigations

The "Virgin and the Child and Saint Catherine of Alexandria" painting shows on the left side the Virgin, sit and turned towards right, with the Child on her knees, and Saint Catherine of Alexandria on the right side, Fig. 197. The picture, kindly provided by the “Accademia di San Luca”, has been shot after a recent restoration work.

The UV fluorescence image, in Fig. 198, taken with the Coolpix camera, shows a dominant green-blue color, due to the varnish layer in agreement with the fluorescence spectra of varnishes, that show a maximum at about 450-500 nm, as discussed in part II, Chap.3. The central area on the top seems to be yellower than the other parts of the painting, probably due to an old varnish layer. We can well distinguish modern extensive restoration works as black areas in the UV fluorescence

image: in the left side of the painting, along the knees of the Virgin, the Child's back, his hairs, his hand with the ring, and, finally, many smaller areas.

We acquired the multispectral UV-fluorescence images shown in Fig. 199, by using two UV LED lamps emitting at 350 nm and seven narrow-band filters transmitting at 450 nm, 470 nm, 500 nm, 532 nm, 550 nm and 600 nm.



Fig. 197: "Virgin and the Child and Saint Catherine of Alexandria" by Matteo di Giovanni's imitator (picture kindly provided by the Accademia di San Luca).

Multispectral fluorescence imaging emphasizes the inhomogeneous emissions also from small areas, alike in the Virgin's incarnate. All the retouching's on the Virgin's cheek are well distinguished with the 450 nm filter, but they are difficult to visualize in the other multispectral images as well as in Fig. 199, probably due to the fluorescence emission of the pictorial layer that is becoming dominant. In the images taken at and above 500 nm we can observe the retouching's also seen in the Fig. 199.

Moreover, we can detect a long retouching on the right side of the painting, appearing as a clear stripe with a thin fracture at the centre, in the images taken at 450 nm, 470 nm and partially at 532 nm.

The infrared reflectographic image¹, taken with the long-pass filter at 720 nm, Fig. 200, shows that the position of the Virgin's knee was changed, probably after the last restoration, since in the same position the UV fluorescence image is dark. Other "pentimenti" were identified in the length of the wheel, in the Saint's hand and in her right shoulder. In this latter area we can notice that the Saint's hair was painted above the landscape, since the two pictures are superimposed. The images of infrared reflectography also allow a preliminary assessment of the pigments and/or dyes used from their transparency in this spectral region: the pigments used for the Saint's mantle allow us to visualize the underlying drawing while we cannot distinguish any traits below the mantle of the Virgin, probably because it was painted with a pigment that absorbs in the near infrared. Regarding the robe of the Virgin, all the decoration traits are distinguishable, suggesting that they were designed in the preparatory drawing, except the red flowers, that were probably added during the color spreading. In general, the preparatory drawing seems to be very detailed, especially in the shaded areas, with a very compact hatch and a light, clear line that highlights the volumes.

By means of the NIR multispectral images at 800 nm, 900 nm and 1000 nm we were able to individuate other features of the underdrawing not detected with the high-pass filter. They are:

¹ The image is composed by twenty-two reflectographic images, that are united by means of "Photomerge" tool of "Adobe Photoshop CS6"

- the artist decided to cover or not to realize other mountains in the left part of the painting. This detail can be visualized with the filters at 900 nm and 1000 nm, Fig. 201.
- the castle at the center of the painting does not show the spires in the image taken at 1000 nm. This means that they were added during the spreading of the pictorial layer. Moreover, the basilica displays oblique lines, difficult to interpret, Fig. 202.
- The Virgin's dress does not show the traits of the drawing; probably the decoration was added during the pictorial execution, Fig. 203.
- The Saint Catherine's wheel seems more detailed with the infrared image at 1000 nm. Moreover, we can individuate a different behavior of Saint's dress that appears in the image taken at 1000 nm rather than the other NIR images, Fig. 204.

We performed the radiography of only selected areas of the painting: the face of the Virgin, Saint Catherine's face and hand, the top part with the aureole of the head of Saint Catherine, and the hands of the Virgin and the Child.

The radiographic image, as well as the infrared ones, shows a fracture that runs vertically along the right side of the face of the Virgin, probably a defect of the wood support; in fact the radiographic image reveals narrow black lines and different contrast areas, Fig. 205-a.

In some areas of the painting we can notice large mesh craquelures, such as that shown in Fig. 205-b, that are probably due to the shrinkage caused by overheating [Gilaroni A. (1977)].

As shown in the IR reflectography images, part of the Saint Catherine's hair was added during the spreading of the superficial layers due to its absence in the radiographic image, Fig. 205-c.

The Saint Catherine's crown is missing in the radiographic image, Fig. 205-d; this suggests that it was painted above the "aureole" with a radiographic transparent organic compound.

The radiography performed on the right side of the painting revealed that a part of Saint Catherine was painted on a second wood support; the execution technique employed on this part is different due to the transparency of the pictorial layer to X-rays, Fig. 205-e. The addition of a wood panel has caused the fracture, recently restored, showed in the fluorescence images of Fig. 198 and Fig. 199.

The use of chestnut for the painting support and of spruce for the “parchettatura” can be well identified from the wood texture observed with the radiographic image; for comparison, an example of the textures of chestnut and spruce is reported in Fig. 205-f and Fig. 205-g.

The repainted areas of the Child hand, observed with the fluorescence imaging, are probably linked to the deep fractures showed in the infrared and radiographic images, Fig. 206.



Fig. 198: UV fluorescence photography of the painting “Virgin and the Child and Saint Catherine of Alexandria”



Fig. 199: Multispectral UV-fluorescence imaging of a detail of the painting "Virgin and the Child and Saint Catherine of Alexandria". Multispectral fluorescence imaging at 450 nm (a), 470 nm (b), 500 nm (c), 532 nm (d), 550 nm (e) and 600 nm (f).

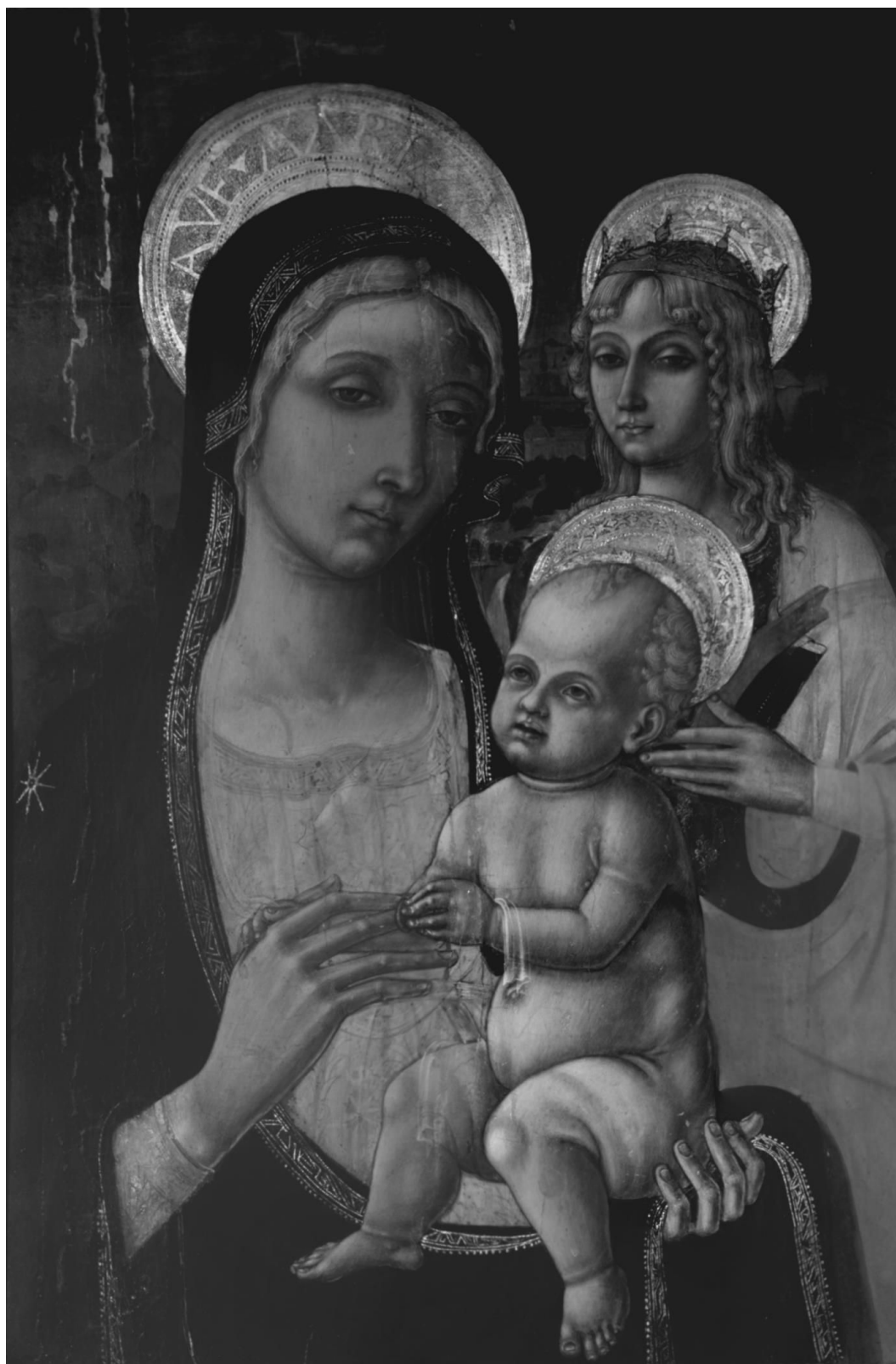


Fig. 200: NIR reflectography of the painting "Virgin and the Child and Saint Catherine of Alexandria" taken with the high-pass filter at 720 nm.

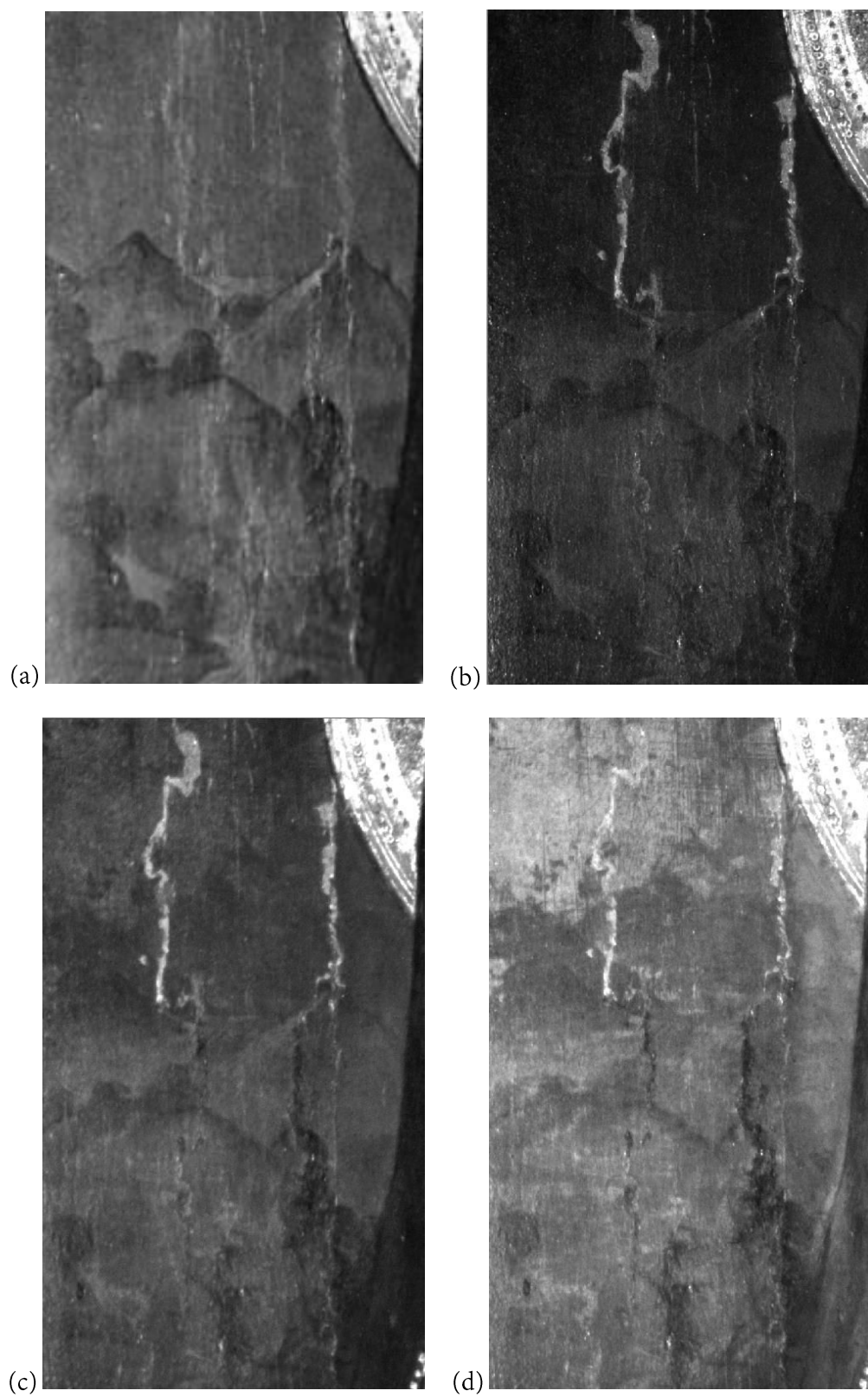


Fig. 201: Visible image (a) and multispectral NIR reflectography at 800 nm (b), 900 nm (c) and 1000 nm (d) of the left part of the painting.

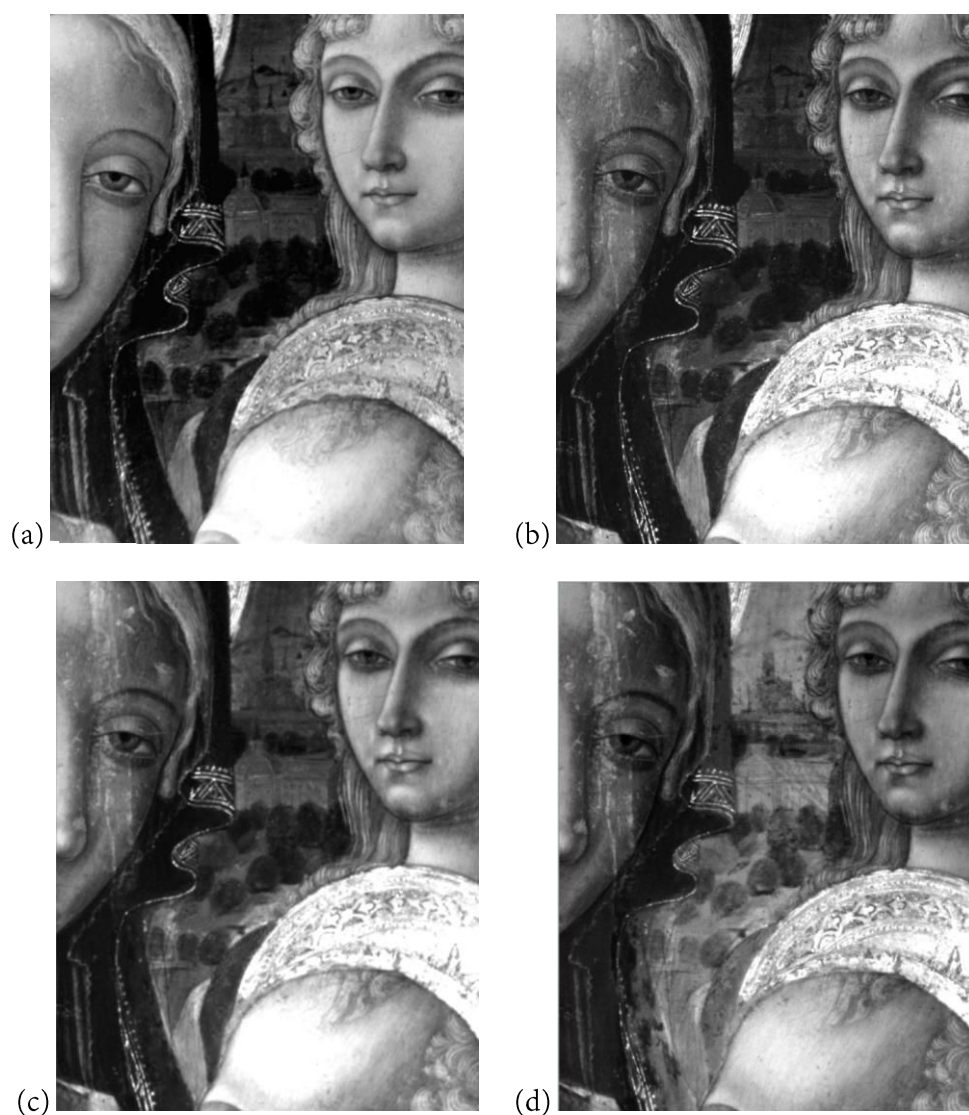


Fig. 202: Visible image (a) and multispectral NIR reflectography at 800 nm (b), 900 nm (c) and 1000 nm (d) of the central part of the painting.



Fig. 203: Visible image (left panel) and NIR reflectography with 720 filter (right panel)

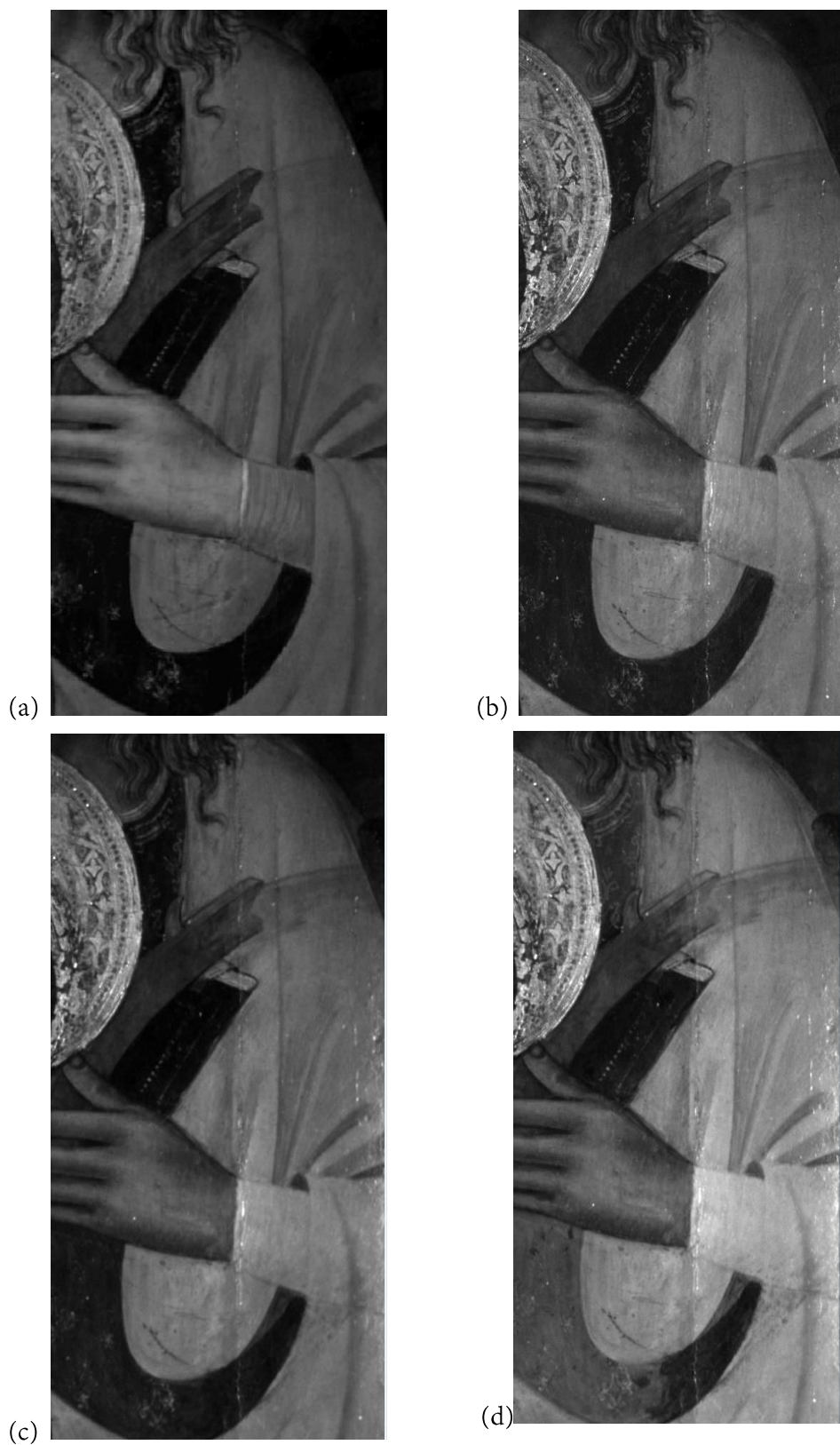


Fig. 204: Visible image (a) and multispectral NIR reflectography at 800 nm (b), 900 nm (c) and 1000 nm (d) of the left hand of Saint Catherine.

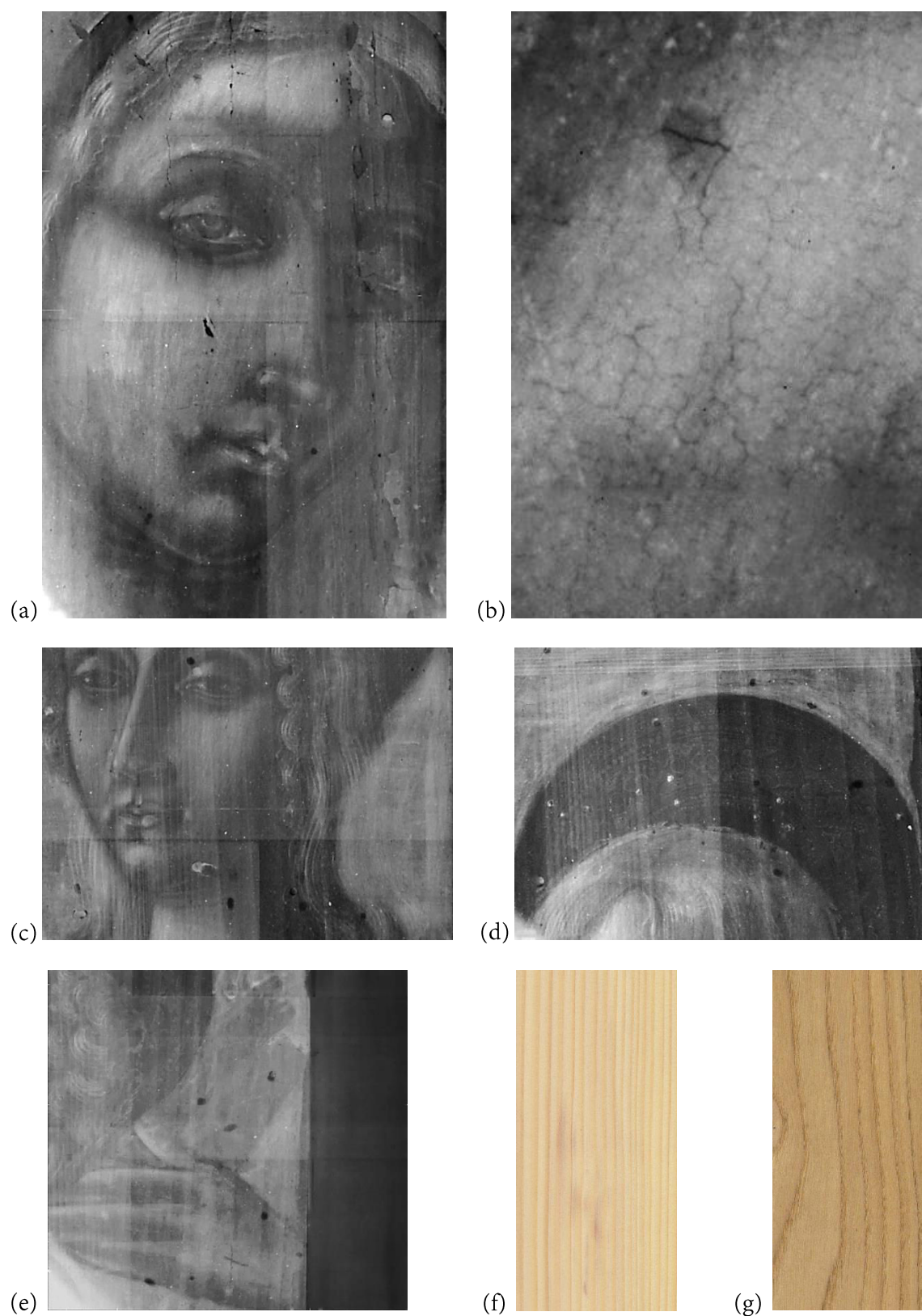


Fig. 205: Radiographic images. (a) Face of the Virgin, (b) detail of the craquelures, (c) face of the Saint Catherine, (d) head of Saint Catherine, (e) right side of the painting, (f) spruce texture and (g) chestnut texture.

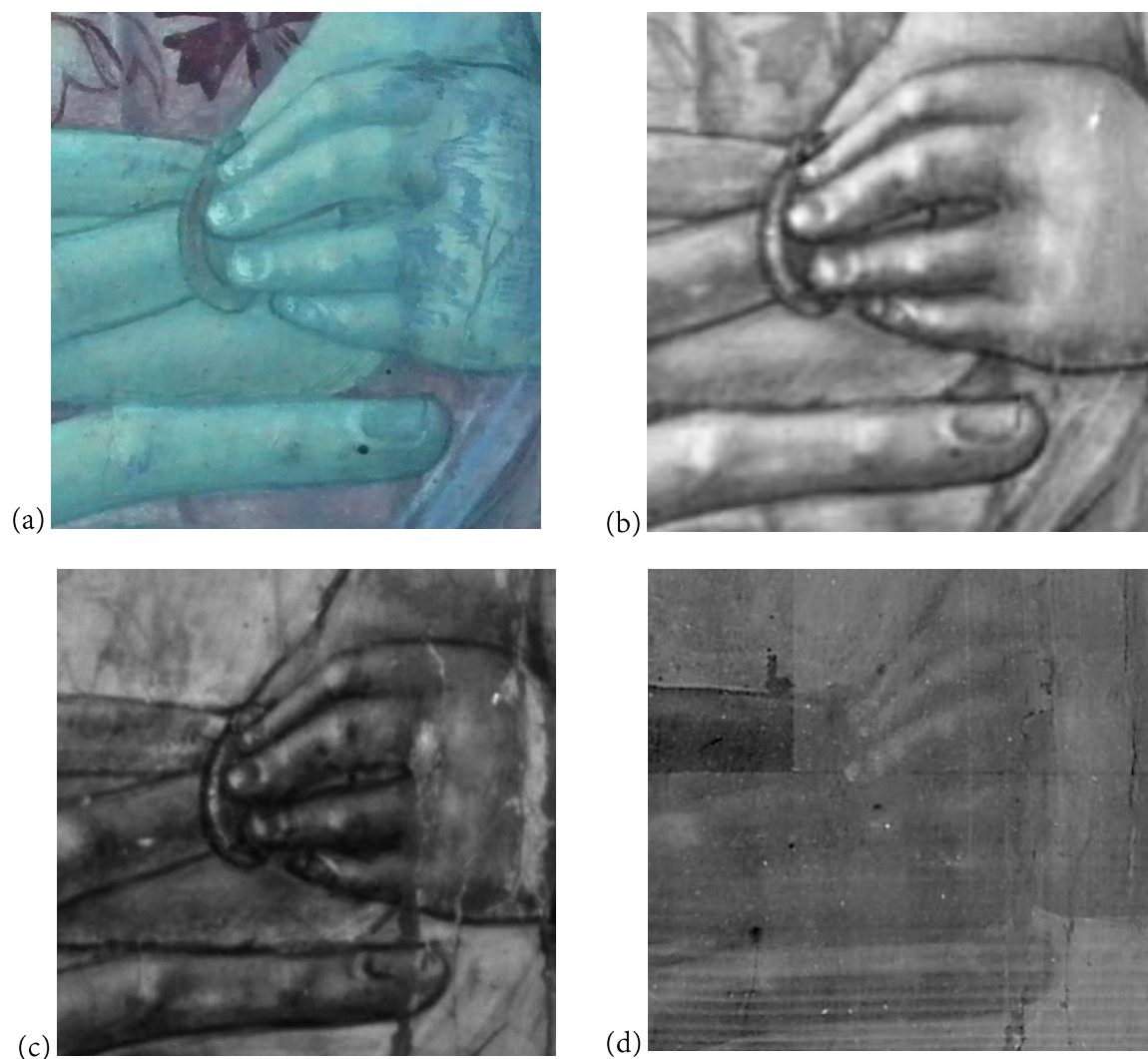


Fig. 206: Detail of the Child's hand. (a) Fluorescence image, (b) visible image, (c) infrared image at 1000 nm and (d) radiography.

1.2.2 Pigments identification

We present the results of FORS and ED-XRF analysis obtained for the sky, the clothes, the faces, the incarnates, the landscape and the gold elements. In appendix D we report on the ED-XRF analysis. The areas examined with the FORS are shown in Fig. 207.



Fig. 207: Image of the painting. White circles: areas investigated with the FORS.

The sky

The sky of the painting presents a blue-green hue, as shown in the microscope image of Fig. 208. The FORS spectra are characterized by a broad band with the maximum at 530 nm. Measuring from the dark areas to the light ones, a shift of the band towards long wavelengths and an increase of reflectance values occur. By means of ED-XRF analysis, we found that the elements characterizing this pictorial layer are copper and lead. Lead can be assigned to the preparatory layer and/or to a mixture of lead white with the green pigment. The latter is a copper-based

pigment, such as Malachite or Verdigris or copper acetate. We can also suppose a greenish chromatic degradation of azurite.

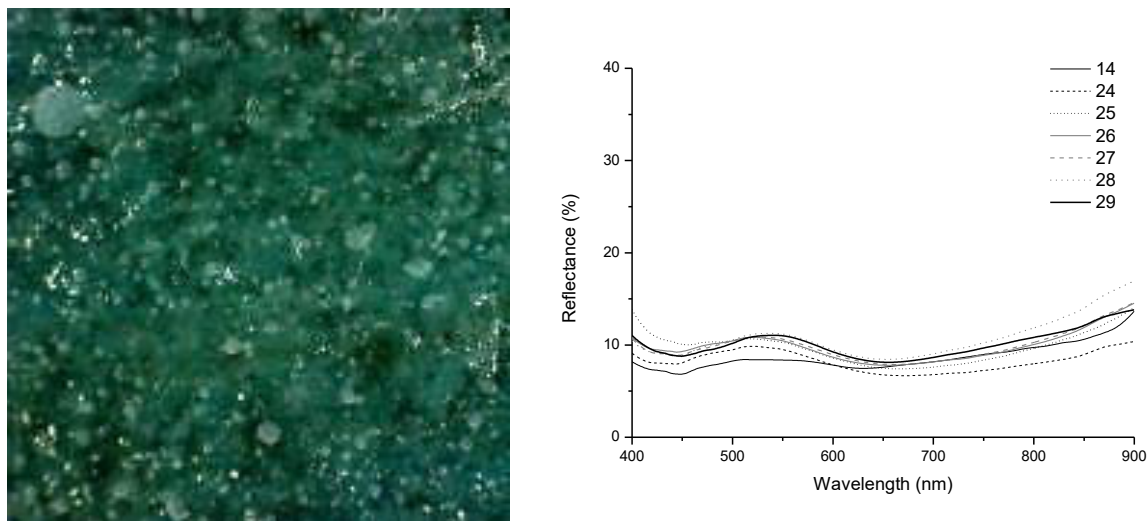


Fig. 208: Optical Microscope image (150X) of the sky (left panel) and FORS spectra of diverse areas of the sky (right panel). The numbers correspond to those reported in the Fig. 207

The presence of zinc can be associated with restoration works executed after the end of the XVIII century² or to the use of a Rosasite based pigment, $(\text{Cu,Zn})_2(\text{CO}_3)(\text{OH})_2$, revealed in other coeval paintings realized in the same geographic area [J.Dunkerton *et al.* 1996, N. Eastaugh *et al.* 2008].

Red clothes

The Saint Catherine's mantle is realized with cinnabar, identified both for the presence of mercury in the ED-XRF spectra, and for the inflection point at 600 nm of the FORS spectra, Fig. 209. The presence of chlorine could indicate the formation of calomel, Hg_2Cl_2 , a degradation product of Cinnabar [G. Poldi (2009)]. We detected chlorine also in other areas that could be associated with old restoration treatments [G. Poldi (2009)].

The presence of titanium, barium and zinc in the restored areas suggests that Cinnabar was mixed with an iron-based pigment and some modern white pigments.

² Zinc white has been introduced as a pigment only in the last decades of the XVIII century, see Part 2, Chap.1.3

The Virgin's dress is characterized by pigments made of lead and iron. We cannot exclude the presence of dyes containing only low atomic weight elements, that cannot be detected with our ED-XRF set up. The lead can be assigned either to the preparatory layer or to the addition of lead white for obtaining a pink hue. The presence of few counts of mercury indicates the presence of a small quantity of cinnabar, while the detection of copper can be associated with an under-layer with malachite or eventually rosasite. In the restored areas we found a similar elemental composition as that detected on Saint Catherine's mantle.

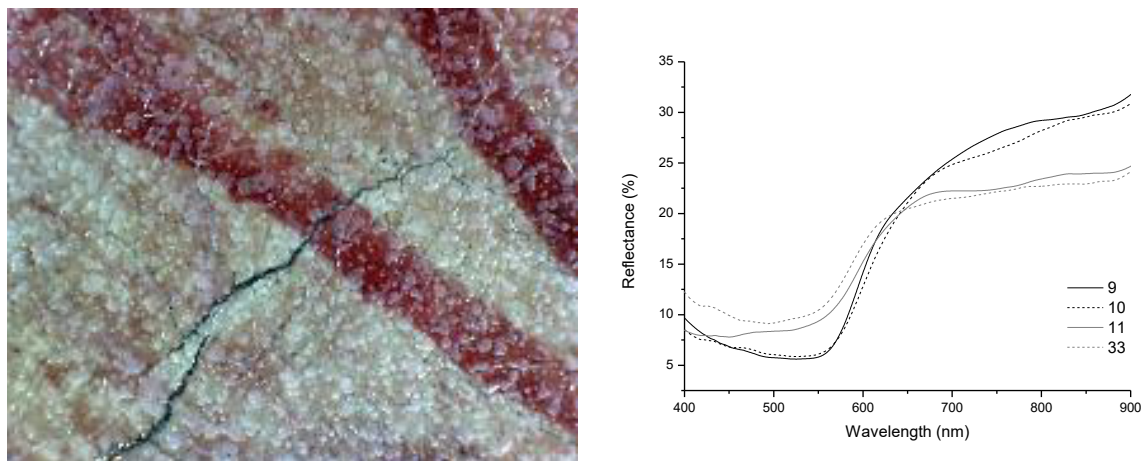


Fig. 209: Optical Microscope image (150X) of the Virgin's dress (left panel) and FORS spectra of several red areas (right panel). The numbers correspond to those reported in the Fig. 207.

Dark areas

The Saint Catherine's dress, the book and the Virgin's mantle present high counts of copper that can be associated with the use of azurite, although it seems black coloured, as shown in the two FORS spectra that we could measure, which appear very similar to a dark hue, Fig. 210.

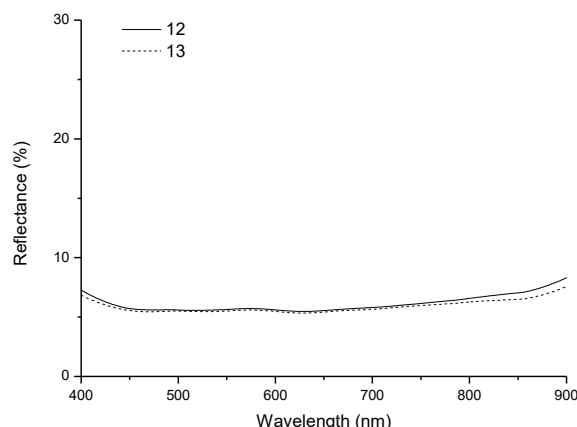


Fig. 210: FORS spectra of two dark-coloured areas of the Virgin's mantle. The numbers correspond to those reported in the Fig. 207.

We suppose that azurite suffered from a blackening in oil. This behaviour has been shown in other coeval paintings [J. Dunkerton et al. (1996)].

The presence of arsenic may be associated with a mixture with orpiment. We suppose the use of Prussian blue in the restored areas due to the presence of iron.

The mercury counts found on the book indicate that this pictorial layer was realized over the Saint Catherine's mantle. Mercury counts were also found on the Virgin's knee, where the presence of Cinnabar confirms the enlargement of the mantle, observed with the infrared images.

Incarnate

The observation of the surface with the optical microscope suggests the mixing of at least three pigments: a brown pigment, a light green one and a white one, Fig. 211.



Fig. 211: Optical microscope images (150X) of the incarnates

The ED-XRF analysis revealed high counts of iron in the dark areas and of the lead in the light areas. Since we detected small quantities of copper and manganese, we can exclude a copper-based pigment for the green hue and umber earths for the brown one. Traces of mercury indicate the presence of cinnabar..

In Fig. 212 we report the FORS spectra carried out on a dark area (n° 16) and on a light area (n° 8) of the Virgin's incarnate. The FORS spectrum of the dark area is characterized by an inflection point at about 550 nm and a band maximum at about 590 nm, followed by two broad bands with maxima at 680 nm and 840 nm, respectively. The light area spectrum is characterized by an inflection point at 570 nm, a knee at about 600 nm, a low wavelength, weak shoulder at 450 nm, and two broad bands with maxima at 680 nm and 840 nm (weak), respectively.

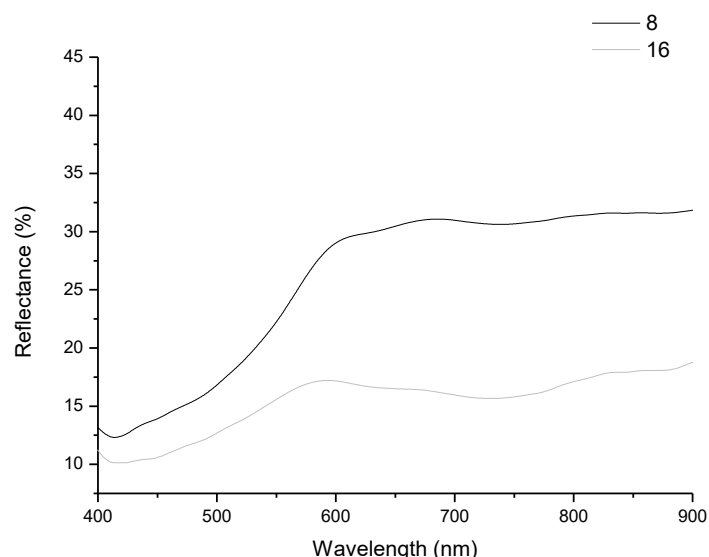


Fig. 212: FORS spectra of two incarnate areas. The numbers correspond to those reported in the Fig. 207.

From the FORS spectra obtained on mixtures of pigments (Part II, chap. 1) we can hypothesize a mixture of raw sienna earth and green earth, due to the positions of the inflection points and the band at 680 nm.

We performed FORS spectra from the dark areas to the light ones, shown in Fig. 213, obtaining a shift of the inflection point to short wavelengths and an increase of the reflectance values at long wavelengths, as expected when lead white is added to other pigments (Part II, chap. 2.2).

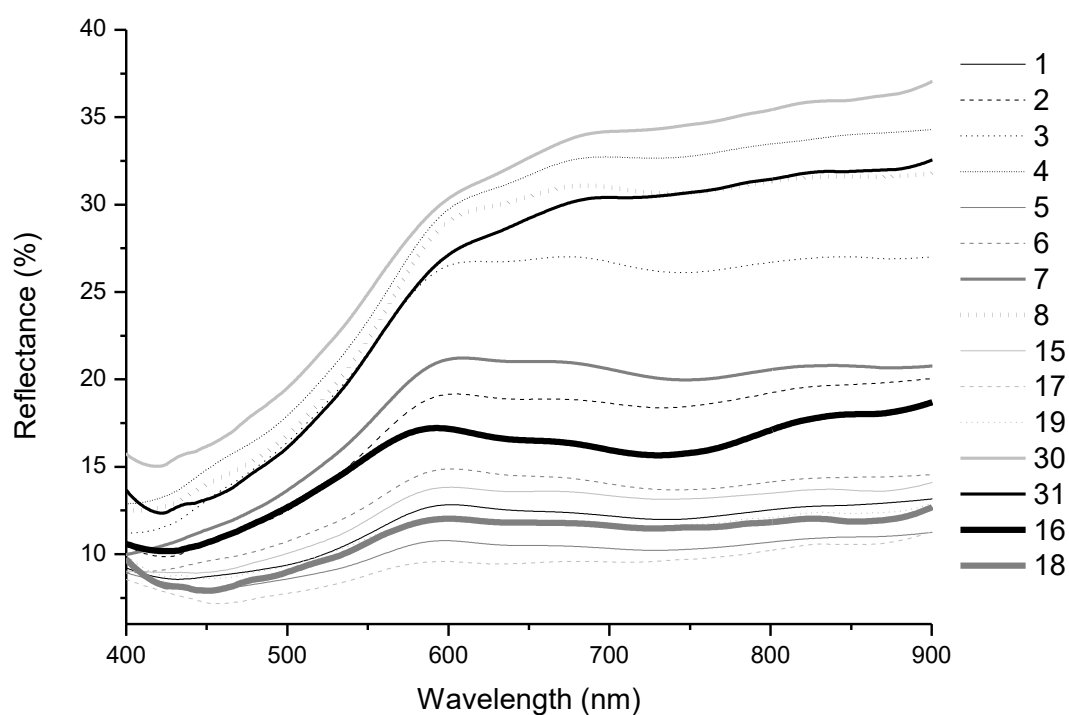


Fig. 213: FORS spectra of the incarnate areas. The numbers correspond to those reported in the Fig. 207.

Landscape

We performed FORS spectra only on two areas of the mountains in the left part of the painting, Fig. 214. The FORS spectrum of the point 22 can probably be attributed to green earth; the FORS spectrum of the point 23 seems to correspond to a mixture of green earth with brown earth.

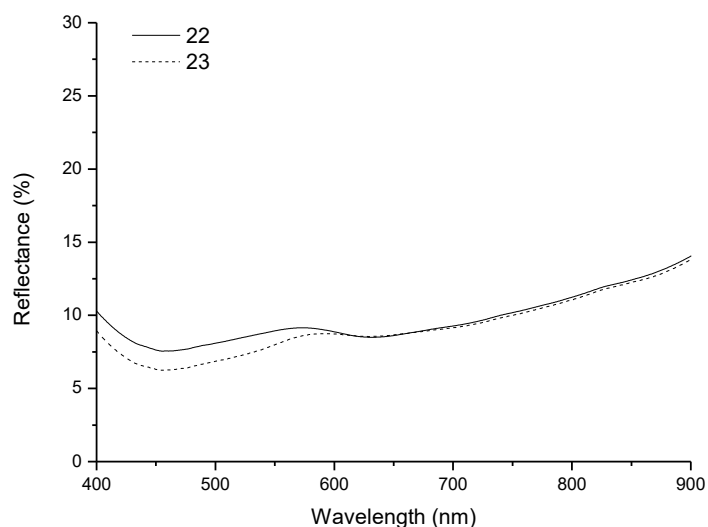


Fig. 214: FORS spectra of the dark-coloured areas. The numbers correspond to those reported in the Fig. 207

Gold elements

The aureole is characterized by the presence of gold and iron. They were realized by a gold leaf placed on a red-ochre pictorial layer (bolus), after that the decoration motives were impressed.

We were not able to detect the gold on the Child's ring, but it seems to be present by observing the areas with an optical microscope, Fig. 215.

The other golden decorations on the Virgin's mantle, on the book and on the Saint's dress are realized with orpiment, characterized by the relevant presence of arsenic in the ED-XRF spectra.



Fig. 215: Optical microscope image (150X) of the Child's ring

1.3 “Virgin and the Child”

1.3.1 Non-destructive stratigraphic investigation

The painting is composed by the Virgin sitting in the central part of the painting, with the Child standing on her left knee, Fig. 216. The picture, kindly provided by the “Accademia di San Luca”, has been shot after a recent restoration work.



Fig. 216: “Virgin and the Child” by Venetian school (picture kindly provided by the Accademia di San Luca).

The UV fluorescence image, shown in Fig. 217, shows a dominant light blue color, probably due to the fluorescence emission of the varnish layer, that show a maximum at about 450-500 nm, discussed in Part II, chap.3. We can identify some areas interested by the recent restoration, especially in the contours of the Child, in his hair, in the lower part of the Virgin's dress and in the left arm of the Virgin.

We performed multispectral UV-fluorescence imaging of the top half of the painting by using the interferential filters at 450 nm, 470 nm, 500 nm, 532 nm, 550nm and 600 nm; the corresponding images are shown in Fig. 218.

We observed a peculiar craquelures of the varnish above the Virgin's dress in the bottom left part of the painting, a detail of which is shown in Fig. 219. Probably it can be attributed to a strong heating of the fresh varnish layer. We obtained similar craquelures when we overheated in the oven freshly prepared swatches of varnish.

The multispectral UV fluorescence images highlighted different fluorescence regions in the incarnates of the Virgin and in the Child, indicating an inhomogeneous pictorial layer or varnish layer. The external part of the Child's hair seems darker than the part near the face in all the multispectral images; probably the dark part corresponds to a recently restored area. Moreover we can suppose a fluorescence emission of the sky due to the particularly light tone observed in the images.

The near-infrared reflectography's³ taken with the filters at 900 and 1000 nm are shown in Fig. 220 and Fig. 221, respectively.

Discontinuities in the top part and in the top right corner of the painting are displayed; they will be discussed below with the radiographic examinations, Fig. 223. Another anomaly is seen in the bottom part of the painting, which appears lighter than the upper parts.

³ The two images are composed by three reflectographic images each one, that was united by means of "Photomerge" tool of " Adobe Photoshop CS6"

We can distinguish two towers, topped by two domes, under the Lady's mantle in the bottom part of the painting, probably belonging to an underlying landscape, Fig. 222. However the two domes disappear using the filter at 1000 nm, indicating that this pictorial layer has a very little contrast at this wavelength.

Several small “pentimenti” were noticed concerning:

- the belt of the Virgin, initially more complex,
- the position of the pupil of the left eye of the Virgin,
- both hands of the Virgin,
- the right arm and the right hand of the Child,
- the drawings of both feet of the Child appear confused.



Fig. 217: UV fluorescence photograph of “Virgin and the Child”



Fig. 218: Multispectral UV-fluorescence images at 450 nm (a), 470 nm (b), 500 nm (c), 532 nm (d), 550 nm (e) and 600 nm (f)



Fig. 219: UV-fluorescence image of the Virgin's dress at 450 nm

The drawing was executed with different materials: charcoal at the top and with ink in the bottom part of the painting. The latter can be recognized from the small ink spots at the beginning of the lines and the trembling of some lines. Moreover some lines were traced to indicate the shaded areas, for example on the Child's front.

The radiographic image reveals that the discontinuities observed in the NIR images are related to the assemblage of several wooden planks; in fact the painting is composed by a central body of irregular shape and several wood pieces to complete the rectangular shape, as shown in the scheme in Fig. 224. The added wood planks are covered by pictorial materials transparent to X-

rays, unlike the central body of the painting. These additions are held together without nails, probably they are only pasted.

The left foot of the child appears to have been moved, opting for a more frontal view, Fig. 225.

The radiographic image also reveals the craquelures, that, in some parts of the painting, are probably due to the shrinkage caused by overheating [Gilaloni A. (1977)], Fig. 226.

Finally, the drawing of the Child displayed in the radiographic image is different from the final version, Fig. 227: the ear has a circular shape, the musculature and the facial features are more marked.



Fig. 220: Infrared image at 900 nm



Fig. 221: Infrared image at 1000 nm

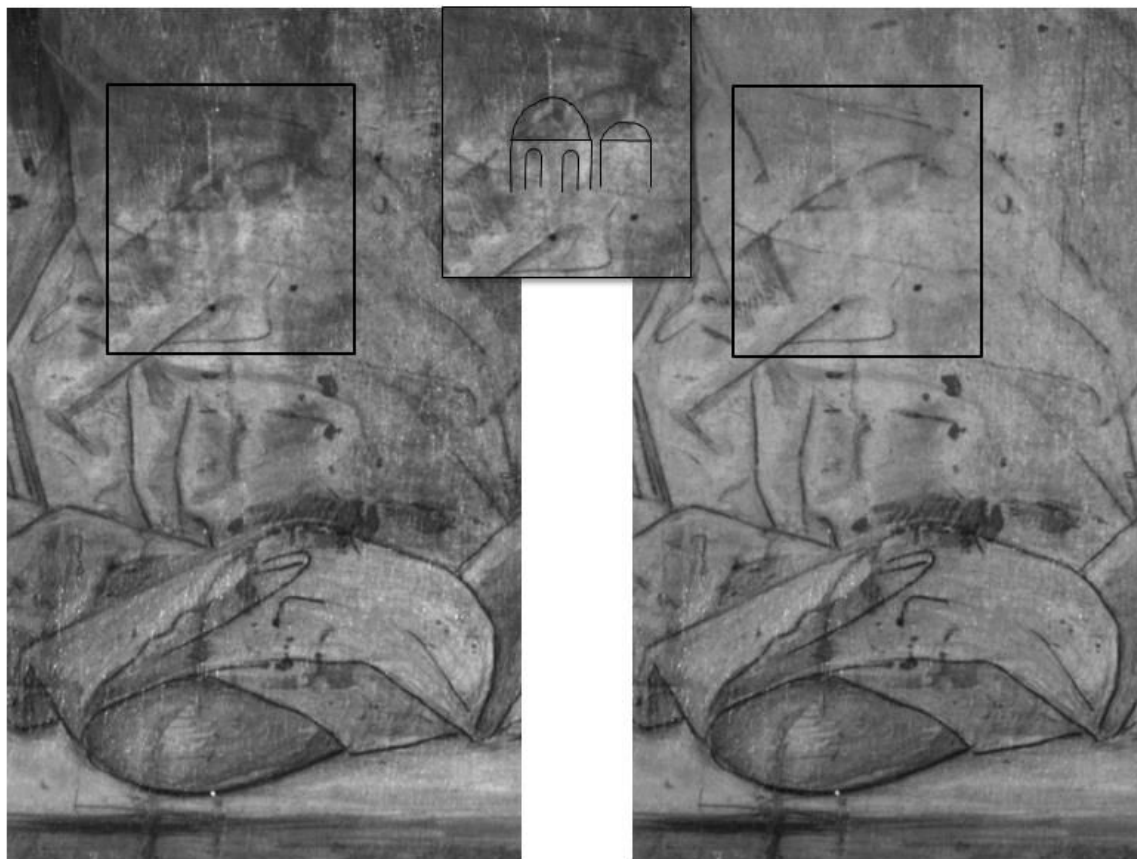


Fig. 222: Detail of the infrared images at 900 nm (left panel) and 1000 nm (right panel). In the central panel the domes have been marked on the infrared image at 900 nm.

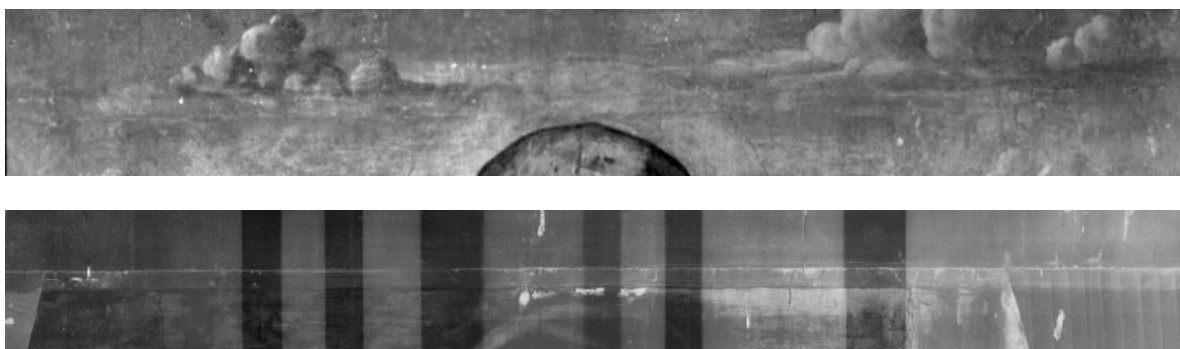


Fig. 223: Top part of the painting. Top panel: Visible image; Bottom panel: radiographic image.



Fig. 224: Scheme of the shapes and the arrangement of the wood panels based on the radiographic images

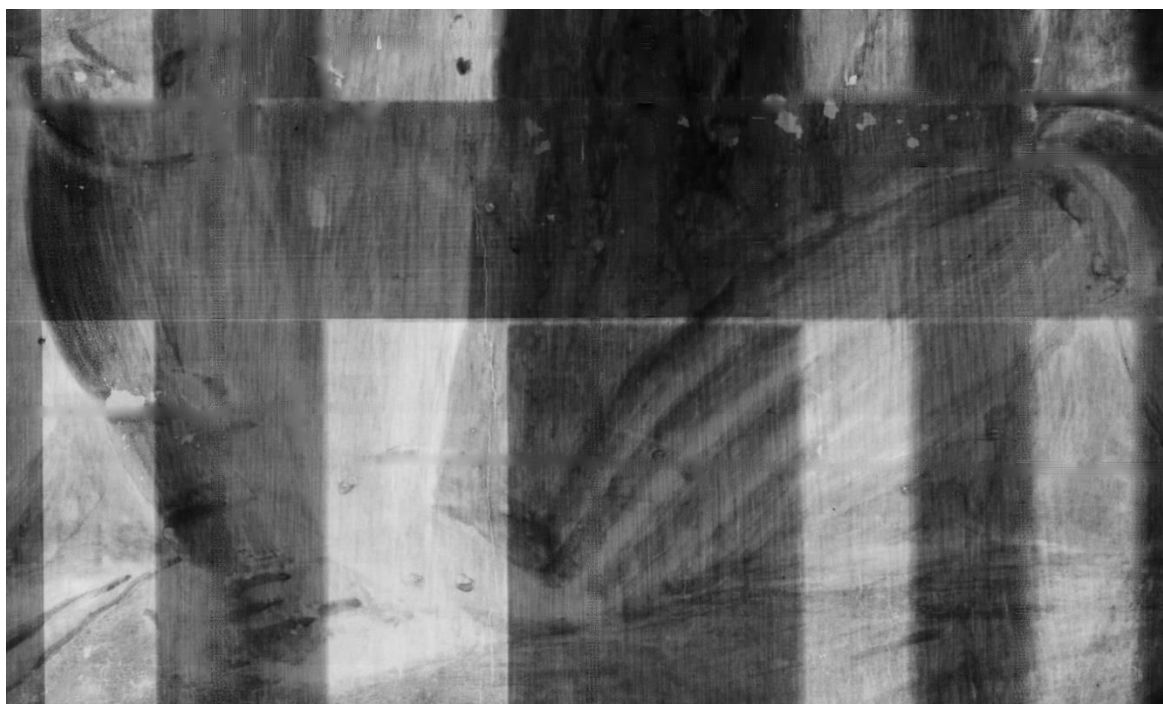


Fig. 225: Radiographic image of the Child's legs and the Virgin's left hand.

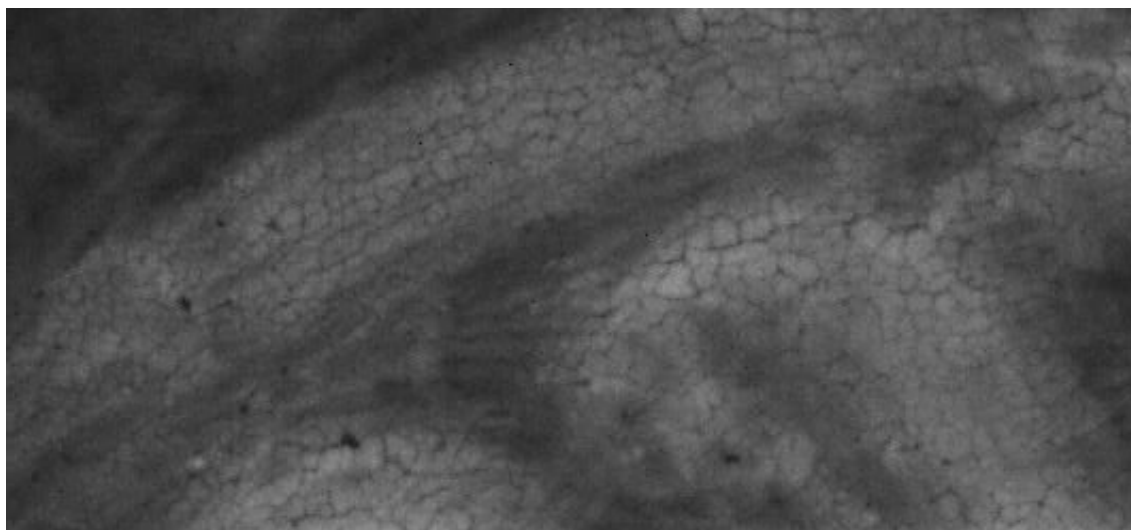


Fig. 226: Detail of the craquelures

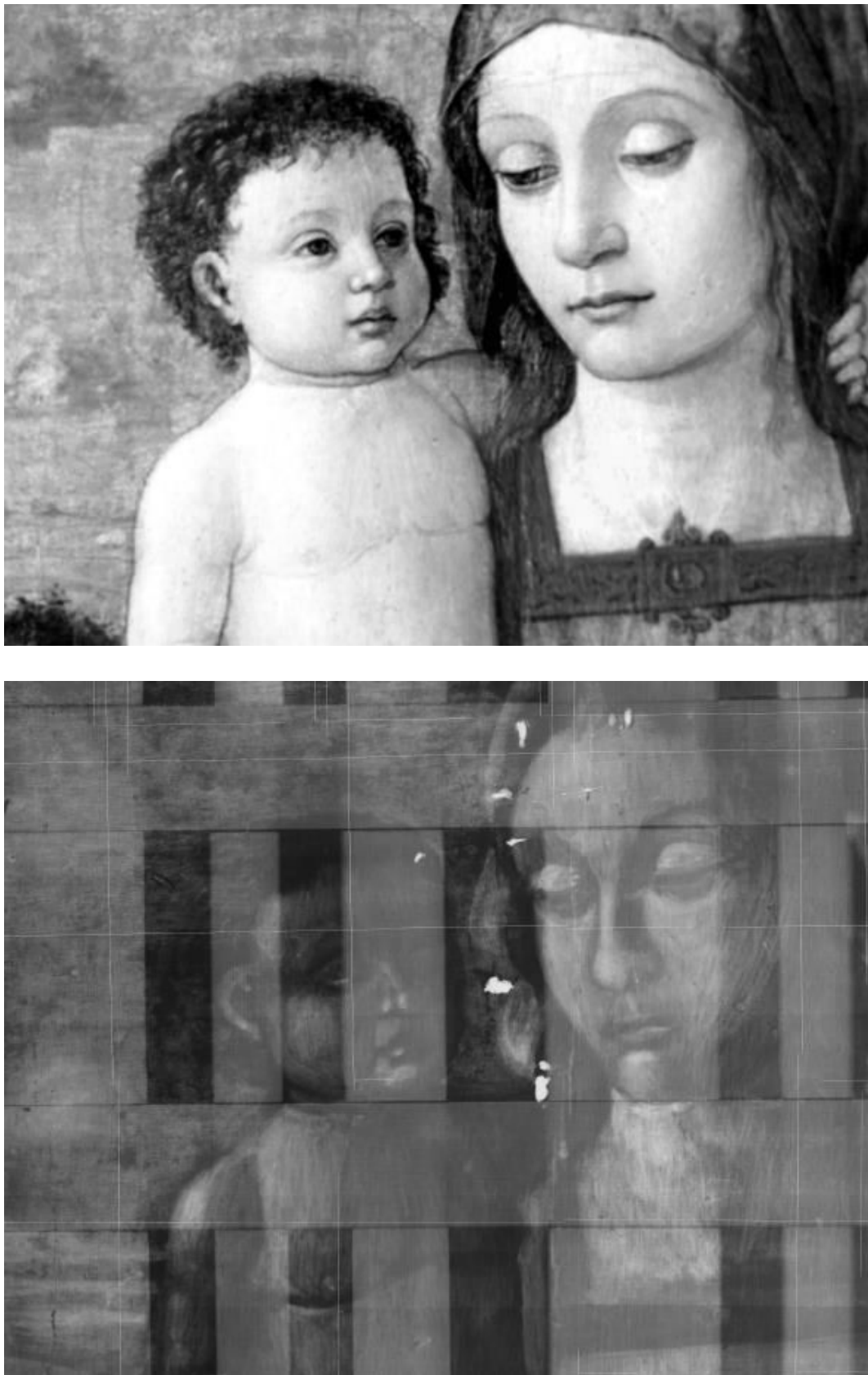


Fig. 227: Visible image (top panel) and radiographic image (bottom panel) of the Child and the Virgin.

We acquired multispectral reflectance images with seven filters at 400 nm, 450 nm, 500 nm, 550 nm, 600 nm, 650 nm, and 700 nm. By combining the reflectance images taken at 600 nm, 650 nm and 700 nm as a RGB image we can emphasize the inhomogeneous spectral features of the sky, as red and blue areas, Fig. 228.

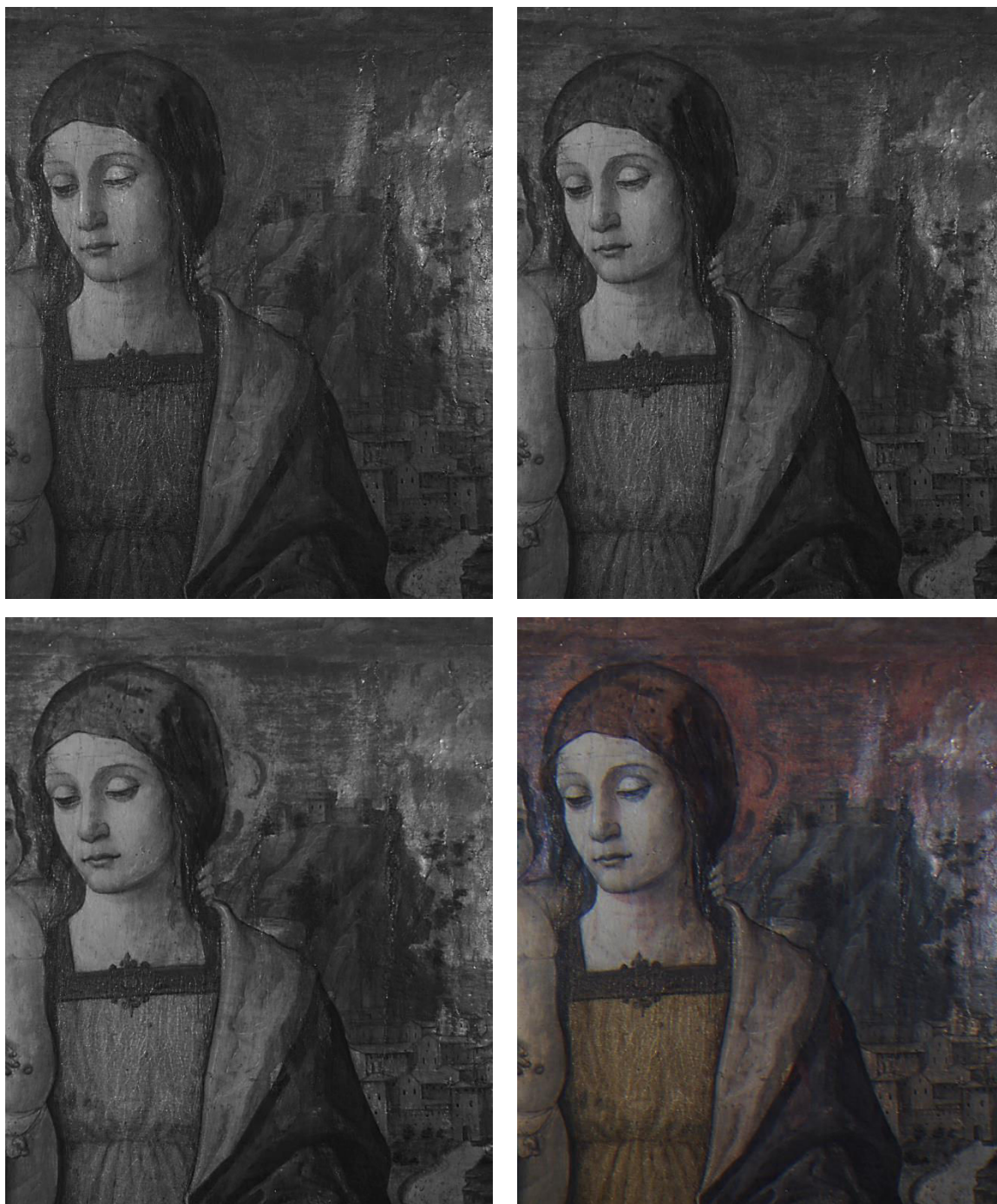


Fig. 228: Multispectral reflectance images at 600 nm (top left panel), 650 nm (top right panel) and 700 nm (bottom left panel) and "false" RGB reconstruction by using the above-mentioned images in the same order.

1.3.2 Pigments identification

As for the painting “Virgin and the Child and Saint Catherine of Alexandria”, we used ED-XRF and FORS spectroscopies to obtain a preliminary stratigraphic individuation of the dyes and/or pigments employed.

We present the results of FORS and ED-XRF analysis performed on the sky, the clothes, the Child’s hair, the incarnates and the landscape. In appendix D, we report on the ED-XRF analysis. The areas examined with the FORS are shown in Fig. 229.



Fig. 229: Image of the "Virgin and the Child" painting with the FORS areas investigated in black

Sky

Copper, iron, lead and zinc are the elements characterizing the sky pictorial layer, where small amounts of cobalt and tin were also detected. The FORS spectra present a broad peak at 550 nm and a shoulder at 710-720 nm, Fig. 230. The FORS spectra labelled "15" and "16" present a weak peak at 390 nm, that can be attributed to zinc white, see Part II, chap.1.2. The interpretation of these spectra is still under study, since it is possible to assume a complex mixture of a yellow pigment and blue dyes or pigments. In particular, the detection of tin can be associated with the use of lead-tin yellow, that could explain the reflectance band at 550 nm. The detection of cobalt in all the analyzed areas suggests the use of Smalt. This hypothesis could be supported by the discoloration of some parts of the sky due to the reaction of the glass with potassium oil carboxylic acids [G. Poldi1 (2009)], Fig. 231.

The spectrum measured on the clouds (labeled "2" in Fig 228) is characterized by an inflection point at about 550 nm, as the yellow hue (see Part II of Chap 2.1): probably lead-tin yellow has been used in this area.

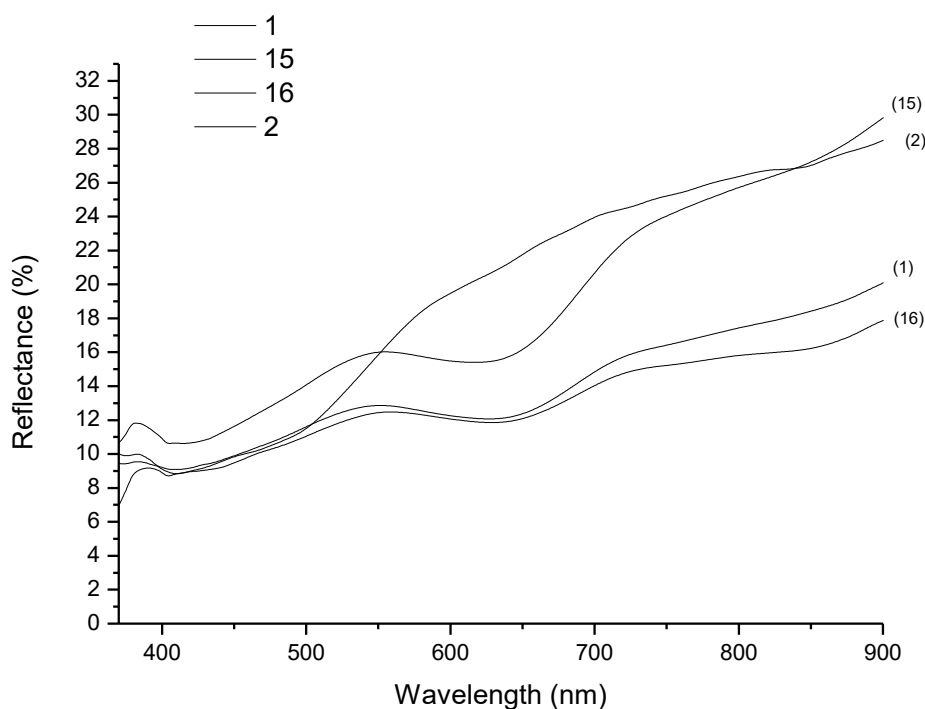


Fig. 230: FORS spectra of the sky. The numbers correspond to those reported in the Fig. 229

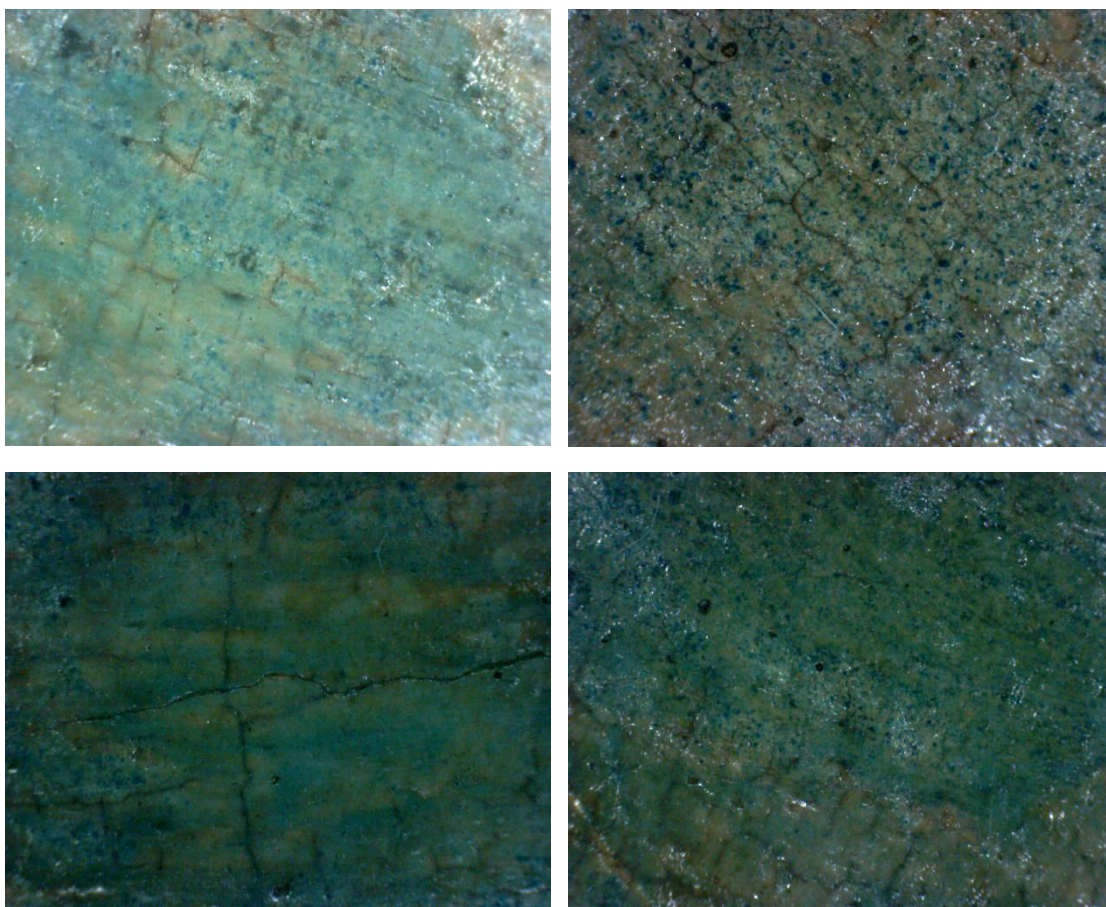


Fig. 231: Optical microscope images (150X) of the sky

The high counts of zinc and the band at 390 nm suggest the use of zinc white, introduced at the end of the 18th century as a pigment (Part II, chap. 2.2). Moreover, comparing our results with other scientific investigations carried out on venetian paintings dated from the 15th century, we found that the presence of high amounts of zinc can be also attributed to different causes:

- the colored glasses enter into the market due to the strong development of the glass industry during the Venetian Renaissance. Among the ingredients that compose the coloring pigments, "tuzia", a zinc oxide, has been recognized [B. H. Berrie et al. (2003)];
- lead, copper, zinc and manganese compounds are added in the preparation of bitumen. Some authors suggest the use of bitumen as a last slight haze by the Renaissance painters, especially

those from Veneto. In fact, the asphalt (bitumen) protects and gives to the painting a characteristic golden-yellow hue that blends the colors and gives depth to dark tones. In some paintings bitumen has been used in the oil technique for a first primer coating, sometimes in association with umber and white lead [S. Rinaldi (1986)].

Virgin's mantle

The ED-XRF analysis on the Virgin's mantle shows results similar to those found in the sky, with the exception that cobalt was not revealed. The FORS spectra do not show the shoulder at 710-720. Probably the pictorial layer is constituted by malachite or verdigris; in some cases (points 10 and 11 of Fig. 232), the presence of zinc white was found. The points 7 and 11 are dark-blue areas, probably characterized by the presence of Prussian blue revealed by the low values of reflectance, Fig. 232.

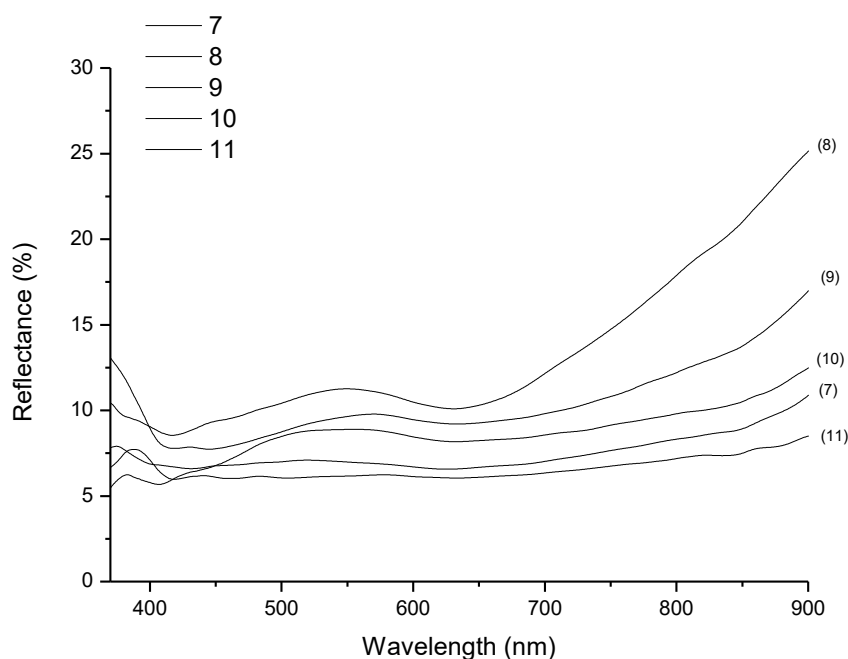


Fig. 232: FORS spectra of the Virgin's mantle. The numbers correspond to those reported in the Fig. 229.

Red clothes and yellow lapel

The ED-XRF analysis reveals the presence of iron, copper, zinc, mercury, and lead for the red dress. It is known that the pictorial stratigraphy of the Renaissance Venetian school paintings is very complex and often consists of a green layer onto which different types of lacquers are spread. In the Virgin's dress and the footwear, the amounts of mercury and iron suggest the use of cinnabar and red ochres. We can suppose that the typical "S" shape of the FORS spectrum of the red ochres is attenuated by the presence of cinnabar, Fig. 233. We cannot exclude the use of red dyes.

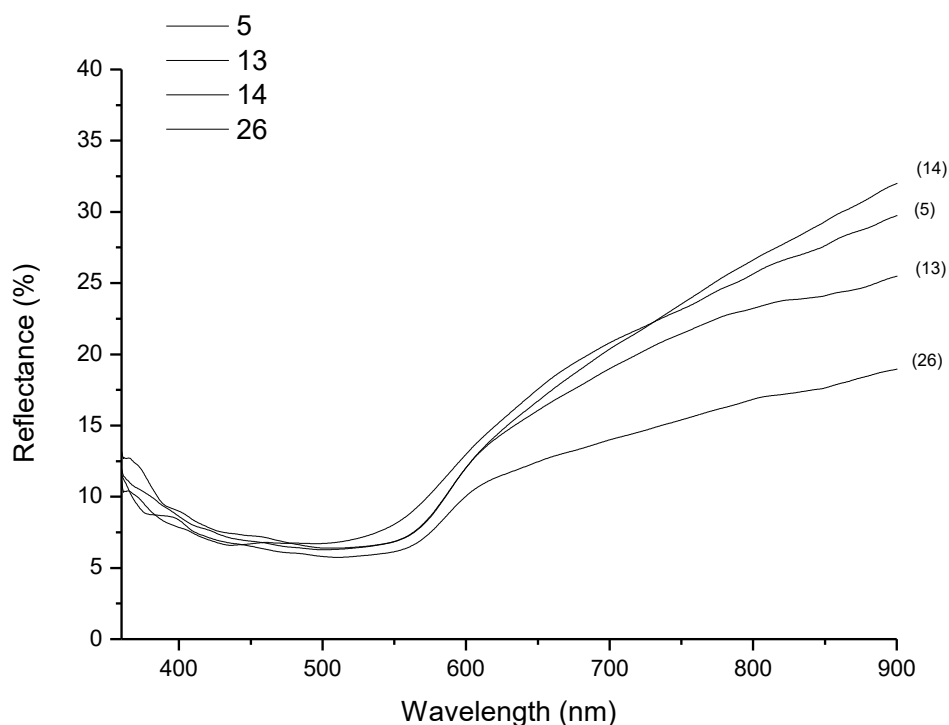


Fig. 233: FORS spectra of the red clothes. The numbers correspond to those reported in the Fig. 229.

The optical microscope images of the Virgin's dress reveal that the varnish was submitted to a strong heating, Fig. 234. Moreover it is clear that the craquelures of the varnish do not follow those of the pictorial layers; this means that the varnish layers are more recent than the painting ones.

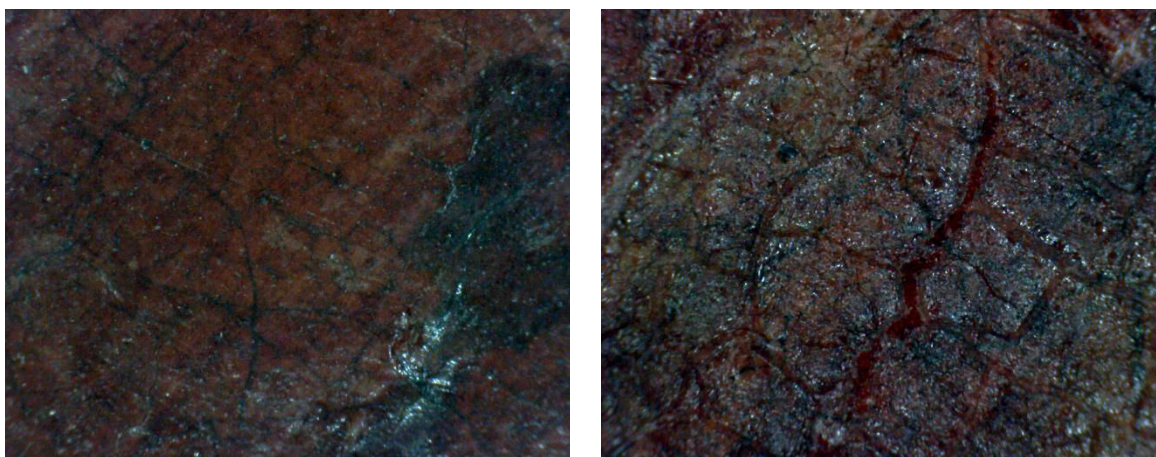


Fig. 234: Optical microscope image (150X) of the bottom part (left panel) and top part (right panel) of the Virgin's dress.

For the yellow lapel, the ED-XRF reveals the presence of iron, lead and zinc. We can recognize the spectral features of the yellow ochre in the FORS spectra of points 6 and 17, Fig. 235. The point 24 was acquired in a dark area of the lapel and we suppose the use of a mixture of yellow/brown pigments due to the absence of the peak at long wavelengths.

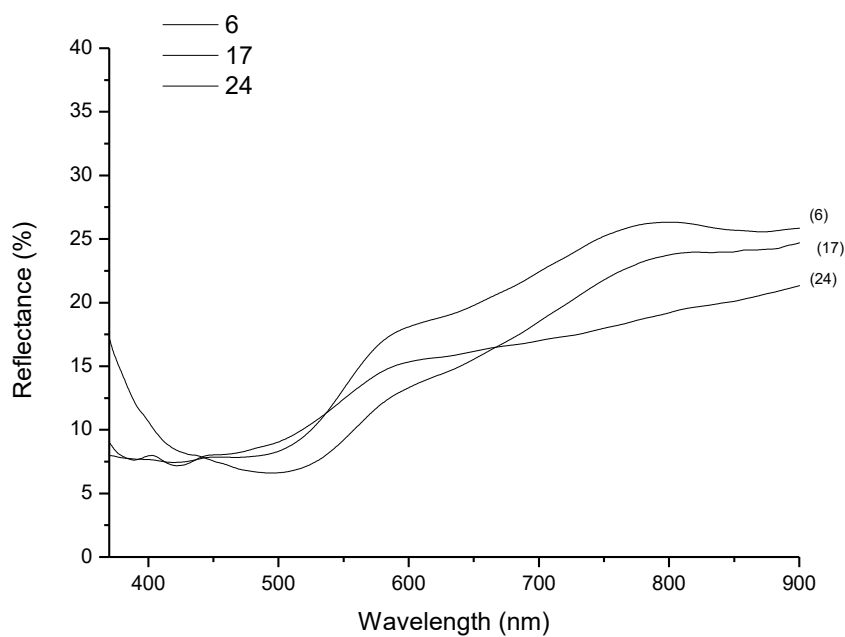


Fig. 235: FORS spectra of the yellow lapel. The numbers correspond to those reported in the Fig. 229.

Incarnate

The ED-XRF analysis reveals the presence of iron, zinc, mercury and lead. We can suppose the use of zinc white and lead white either as a white mixture or as superimposed layers. The red hue is probably due to an iron-based pigment such as hematite or red ochre mixed with cinnabar. From the microscope images we can assume that the shadows were mainly realized with brown pigments, Fig. 236. The FORS spectra support the use of earth pigments, due to the presence of a weak peak at short wavelengths (at about 450 nm), with the addition of white pigments. The presence of cinnabar can explain the shape of the reflectance curve, Fig. 237, as shown for the red hue. In some areas we can suppose the use of green earth due to the presence of a weak peak at 680 nm (point 4). The peak at 390 nm suggest the presence of zinc white.

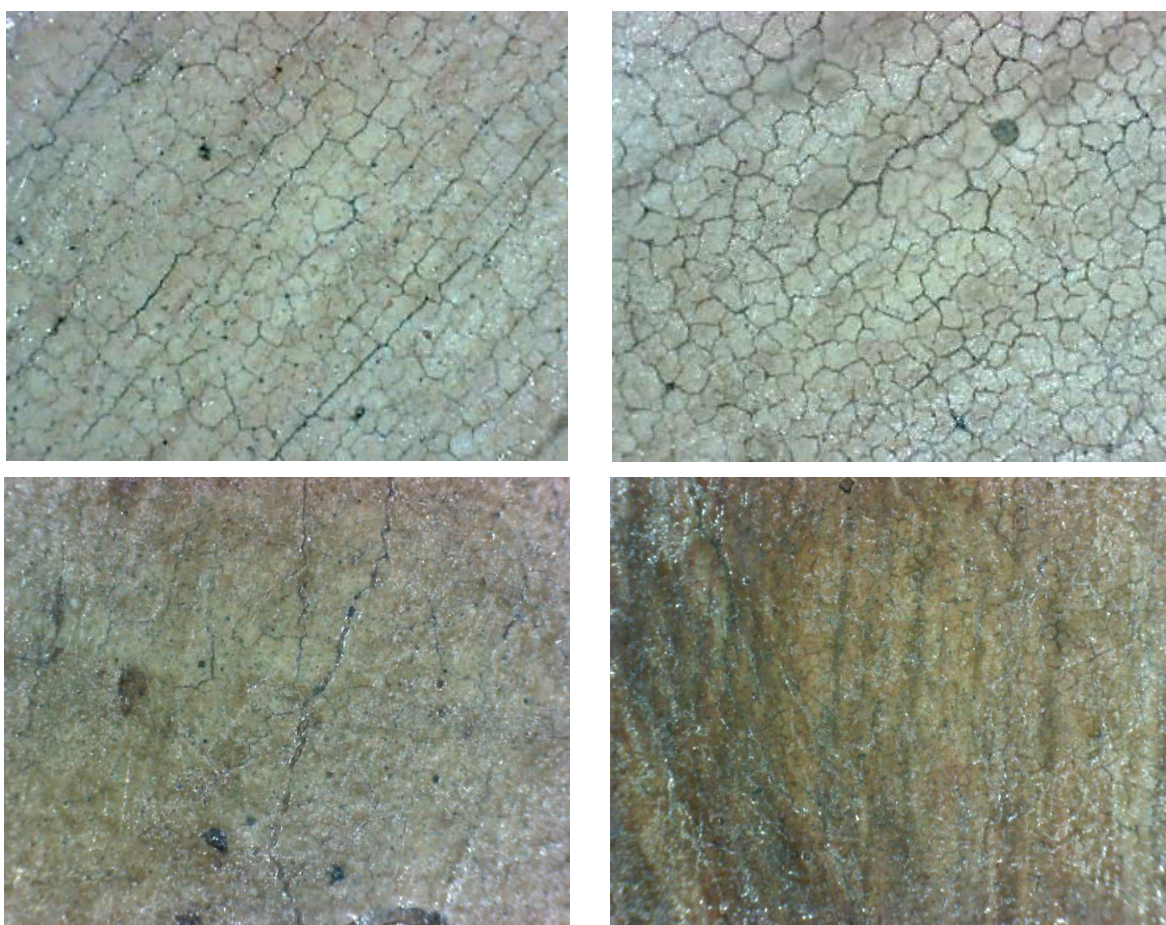


Fig. 236: Optical microscope images (150X) of the Child's incarnate (top panels) and the Virgin's incarnate (bottom panels).

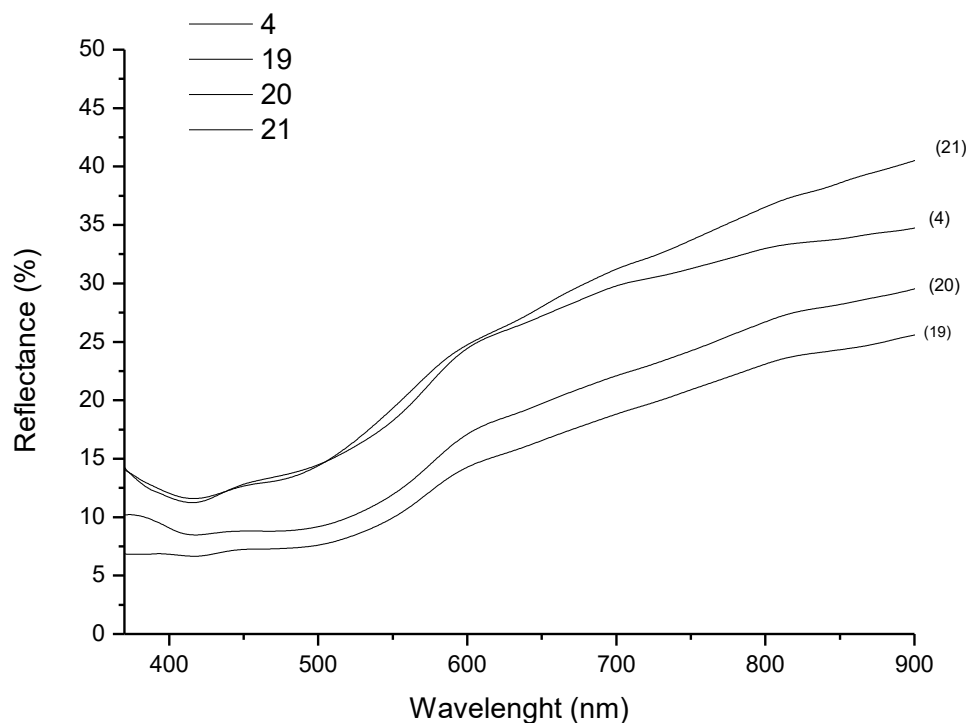


Fig. 237: FORS spectra of the incarnates. The numbers correspond to those reported in the Fig. 229.

Child's hair

We performed two ED-XRF measurements on the Child's hair: the first one near the face and the second one near the sky, since we assumed that the external part was added as shown in the UV fluorescence images and IR reflectographies. However the elements and their counts do not show significant differences, implying that the pigments employed in both areas are the same.

Landscape

The ED-XRF analysis reveals the presence of iron, copper, zinc and lead. In some points we also detected arsenic, mercury and tin, probably due to orpiment, cinnabar and lead-tin yellow traces,

respectively. In Fig. 238, the FORS curves related to the points 22 and 25 show a weak reflectance peak at 450 nm: this means the use of earth pigments.

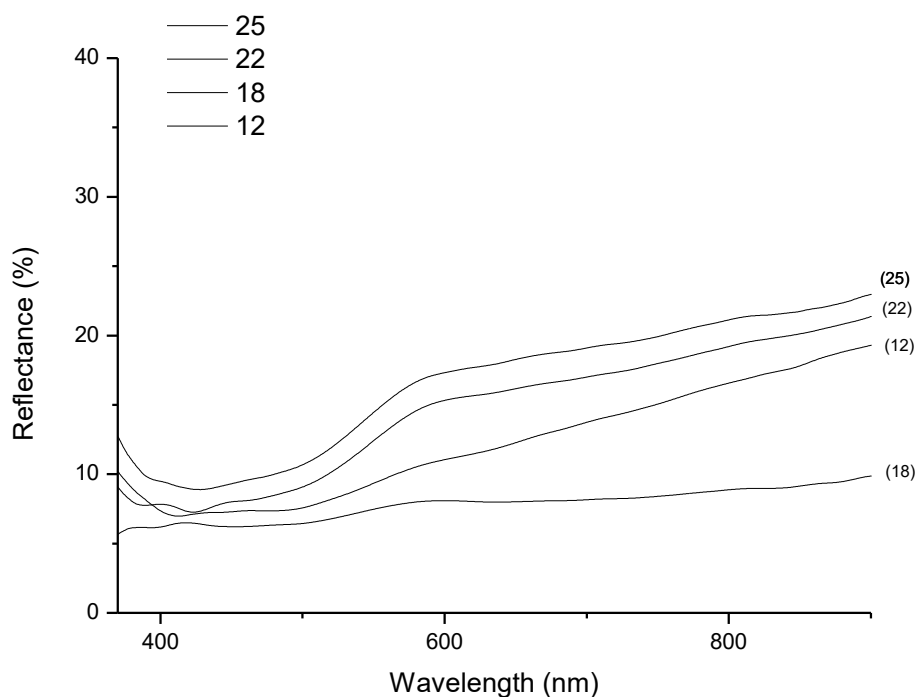


Fig. 238: FORS spectra of the landscape. The numbers correspond to those reported in the Fig. 229.

1.4 Conclusions

The painting of the “Virgin and the Child and Saint Catherine of Alexandria” shows technical and analytical features similar to coeval paintings. We affirm the use of cinnabar for the Saint’s mantle and red ochres and/or dyes for the Virgin’s dress, azurite for the dark-blue hues and Malachite or Verdigris or copper acetate for the sky. The shaded areas of the incarnates are characterized by the presence of green earth, probably mixed with other earth pigments (such as raw sienna earth) and lead white. The restored areas can be recognized by the presence of modern pigments such as Prussian blue, barium sulphate, titanium white and zinc white. Silver traces can be attributed to the use of silver in the preparatory drawing.

The multispectral UV fluorescence imaging has permitted the visualization of some inhomogeneity on the varnish layer thanks to the selection of specific spectral emission. Some “pentimenti” under the landscape and the underdrawing, only in part detected with the use of our long-pass filter, were revealed with Multispectral NIR reflectography.

The analysis carried out on the “Virgin and the Child” by Venetian school show a high amount of zinc in almost all the areas analysed, that could suggest a shift of the creation of the painting to more recent times; however we cannot exclude that the painting has undergone a heavy restoration work. The identification of the pigments employed is still under study due to the presence of complex mixtures. Nevertheless, we identified lead-tin yellow in the sky. All the green areas are characterized by the presence of copper, which can be attributed to malachite or Verdigris or copper acetate and the yellow areas are composed of yellow ochre.

The Multispectral reflectance imaging allows to locate inhomogeneity's of the pictorial layer, in particular in the sky. The multispectral NIR imaging demonstrates that an image taken with a narrow band filter can show pictorial features not distinguishable with other filters.

In both paintings, the radiographic images were useful to evaluate the state of conservation of the wooden supports, to detect the presence of wood panels assembled, and to identify the wood species. Moreover the radiographic image is complementary to IR images, since it can highlight “pentimenti” lying in the most internal layers.

General conclusions and perspectives

In this work we focused on the problem of identifying pigments, dyes and binders on paintings by using non-destructive, *in situ* techniques. In particular, we assessed the advantages and the limitations of multispectral imaging applied to paintings. This method required the support of other "local" techniques, such as microscopy, fluorescence spectroscopy, reflectance spectroscopy, ED-XRF spectroscopy, UV-VIS absorption spectroscopy and ATR-FTIR spectroscopy.

We validated the employment of the multispectral reflectance imaging for the identification of pictorial layers swatches, taking into account the type of binder (egg yolk or linseed oil) and the presence of a black or a white under-layer. We found that the presence of either underlayer does not influence significantly the pigment recognition. The application of PCA as a statistical tool to select the most significant multispectral images for pigment identification has proved that three images, taken with narrow-band filters, contain the maximum variance of the reflectance values and are sufficient to recognize the blue and the green pictorial layers. The spectral features of yellow, red, orange, and brown hues are rather similar to each other and this fact has prevented a clear identification. Probably they could be distinguished by selecting other spectral ranges and/or filters with a narrower band-pass than ours.

The multispectral reflectance images acquired on our swatches did not permit the recognition of the employed binder, except for the white and the ultramarine blue pictorial layers, that exhibit a diverse spectral behaviour according to the binder used.

We tested the possibility of recognizing the single pigments in a mixture. We discovered that Zinc White can also be identified in mixtures with other pigments, except when it is blended with Titanium White. In the visible range the spectral features of Titanium White are dominant also in the presence of other white pigments. In the case of the other mixtures that we have prepared, the reflectance curves have shown some spectral features of each pigment; nevertheless, we could not identify them with the multispectral images. Probably the limits were the selection of the spectral ranges and/or the band-pass of our filters.

Multispectral UV fluorescence imaging came out to be useful to recognize the fluorescence emission in the visible range of the pictorial layers obtained with the following blue and green hues: Cobalt Blue, Emerald Green, Egyptian Blue, Cobalt Violet, Ultramarine Blue, Ultramarine Ash, Still de Grain, Zinc White, and Lithopone. On the contrary, Smalt and Ultramarine blue were hardly distinguishable among them. Although the other pictorial layers exhibited fluorescence emissions in the visible range, detected with a spectrophotometer, they appeared dark in the multispectral images. This aspect was attributed to their low fluorescence intensities.

We investigated the possibility of distinguishing the white pigments (Zinc White, Lead White and Titanium White) in pictorial layers of their mixtures by means of the multispectral UV-fluorescence imaging. We found that Zinc White is the only pigment that we could identify in Lead White or in Titanium White mixtures. Moreover, the “false” RGB combination of the fluorescence images taken at 420 nm, 470 nm and 532 nm allowed us to discriminate egg yolk or linseed oil samples containing Zinc White and its mixtures with the other white pigments. On the contrary, Titanium White and its mixtures with Lead White appeared black even if they showed a weak fluorescence in linseed oil. Lead White could be identified if it is mixed only with linseed oil or yolk egg and not with the other white pigments.

We must underline that when the UV radiation reaches a pictorial surface, the light collected from it is due to several phenomena, described in Part I, chap. 1.3.2, among which the “true” fluorescence emission of the pictorial layer. For this reason, we applied the correction procedure suggested by Verri et al. (2008), taking into account the Kubelka-Munk theory, to eliminate the effects of the auto-absorption phenomena from the emission spectra in order to identify the fluorescent species. After obtaining the “true” fluorescence spectra, in most cases we could distinguish the swatches containing egg yolk as a binder from the linseed oil ones. The correction procedure applied for the UV-fluorescence spectra was also applied on the multispectral UV-fluorescence images, obtaining good results.

In the multispectral UV-fluorescence images we identified the Cadmium pigments and the Egyptian blue; all of them presented a strong NIR fluorescence emission.

All the analysis discussed above, done on pigment/binder swatches, were performed on fresh pictorial samples. The effects of an advanced natural ageing were not considered. We plan for the

future to measure the fluorescence emissions from advanced aged pictorial layers with the aim of improving the identification of egg yolk and linseed oil by means of multispectral UV imaging. Meanwhile we tested the possibility of identifying the binders and the varnishes with UV fluorescence spectroscopy and multispectral imaging by submitting dried swatches to photochemical and thermal accelerated ageing. The two ageing methods produced several degradation products, which exhibit different fluorescence emissions: the photoageing causes the bleaching of the samples, implying fluorescence emissions at shorter wavelengths; on the contrary, the thermal ageing generates a shift of the fluorescence emissions to long wavelengths and a strong yellowing of the samples. However, we found that colophony can be discriminated from dammar and mastic resins by means of Multispectral UV-fluorescence imaging due to its fluorescence emission at long wavelengths; instead, dammar and mastic showed similar fluorescence spectral features, which prevented their identification.

After the assessment of the advantages and the limitations of multispectral imaging on pictorial swatches, we turned to a study case, analysing two paintings of the Lazzaroni collection belonging to the Gallery "Accademia di San Luca" in Rome. We went through a multi-analytical method based on microscopy, ED-XRF analysis, reflectance measurements, radiography, UV fluorescence imaging and multispectral UV-VIS-NIR imaging.

The multispectral UV fluorescence imaging has permitted the visualization of some inhomogeneous areas of the varnish layer by selecting proper spectral emission bands. We could not distinguish which varnishes have been applied on the paintings, but we could well discriminate areas with different emission intensities although in the same spectral ranges. We must underline that the UV-multispectral images were radiometric calibrated, unlike the RGB images that simulate the human vision.

The Multispectral reflectance imaging allowed us to find other inhomogeneous areas of the pictorial layer, in particular in the sky of the "Virgin and the Child" painting. We could not recognize the spectral features of the pigments used, due to the presence of complex mixtures. We plan to prepare other swatches with mixtures simulating the ones of the painting, or we will use mathematical modelling, such as the Duncan theory (Part I, Chap. 1.2.1), to better exploit the potential of reflectance images.

Finally, the multispectral NIR imaging demonstrated that the images taken at specific wavelengths can show features in the under-drawing of the paintings, not distinguishable with the employment of other filters. This aspect was related to the transmittance properties of the upper pictorial layers that change with wavelengths.

In conclusion, we have confirmed that the use "in situ" of complementary "local" spectroscopic techniques make us identify the pigments and the binders in small areas of a painting. Multispectral UV-VIS-NIR imaging has been validated with the same aim as above on large areas. With our instrumental set-up we can identify only a limited number of pigments and/or binders; however, we can easily recognize areas with the same hue, but with different spectral features. In addition, in the NIR region we can see different pictorial underlayers, i.e. we can make a stratigraphic analysis.

We plan to improve the instrumental set up, to perform studies on the same swatches submitted to advanced ageing, and to study complex mixtures in order to overcome the difficulties encountered. It is worth highlighting that multispectral imaging is easily transportable for in situ analysis and it is also a rather inexpensive analytical system compared to hyperspectral imaging.

Bibliography

Aldrovandi A., Caruso O., Mariotti P. I., **2010**, “Caratterizzazione dei materiali pittorici nelle pitture murali mediante tecniche fotografiche”, *Rivista dell’Opificio delle Pietre Dure e Laboratori di Restauro di Firenze*, 22, 55-80.

Aldrovandi A., Picollo M., **2001**, "Indagini in fluorescenza UV", *Metodi di documentazione e indagini non invasive sui dipinti*, I Talenti, Il Prato, 67-84.

Anglos D., Solomidou M., Zergioti I., Zafiropulos V., Papazoglou T H. G. and Fotakis C., **1996**, “Laser-Induced Fluorescence in Artwork Diagnostics: An Application in Pigment Analysis”, *Applied Spectroscopy*, 50, 10, 1331-1334.

Attas M., Cloutis E., Collins C., Goltz D., Majzels C., Mansfield J. R., Mantsch H. H., **2003**, “Near-infrared spectroscopic imaging in art conservation: investigation of drawing constituents”, *Journal of Cultural Heritage*, 4, 2, 127-136.

Azémar C., Vieillescazes C., Ménager M., **2014**, “Effect of photodegradation on the identification of natural varnishes by FT-IR spectroscopy”, *Microchemical Journal*, 112, 137–149

Azémar C., **2014**, “Photodegradation of natural resins : application to artworks”, PhD thesis.

Bacci M., **2000**, “UV-VIS-NIR, FT-IR, FORS Spectroscopies”, *Modern Analytical Methods in Art and Archaeology*, Ed. Ciliberto E. and Spoto G., Chemical Analysis Series, 155, John Wiley and Sons, New York, 321 – 361.

Bacci M., Casini A., Cucci C., Muzzi A., Porcinai S., **2005**, “A study on a set of drawings by Parmigianino: integration of art-historical analysis with imaging spectroscopy”, *Journal of Cultural Heritage*, 6, 4, 329-336.

Bacci M., Casini A., Cucci C., Picollo M., Radicati B., Vervat M., **2003**, “Non-invasive

spectroscopic measurements on the Il ritratto della figliastra by Giovanni Fattori: identification of pigments and colourimetric analysis”, *Journal of Cultural Heritage*, 4, 4, 329-336.

Balas C., Papadakis V., Papadakis N., Papadakis A., Vazgiouraki E., Themelis G., **2003**, “A Novel hyper-spectral imaging apparatus for the non-destructive analysis of objects of artistic and historic value”, *Journal of Cultural Heritage*, 4, 1, 330–337.

Baronti S., Casini A., Lotti F., Porcinai S., **1998**, “Multispectral imaging system for the mapping of pigments in works of art by use of principal-component analysis”, *Applied Optics*, 37, 8, 1299–1309.

Berrie B. H. and Matthew L. C. , **2005**, "Material Innovation and Artistic Invention: New Materials and New Colors in Renaissance Venetian Paintings," *Scientific Examination of Art: Modern Techniques in Conservation and Analysis*, National Academy Press, Washington, 12-26.

Bisulca C., Picollo M., Bacci M., Kunzelman D., **2008**, “UV-Vis-NIR reflectance spectroscopy of red lakes in paintings”, 9th International Conference on NDT of Art, Jerusalem Israel, 25-30 May, 8.

Blazek J., Soukup J., Zitova B., Flusser J., Tichy T., Hradilova J., **2013**, ‘Low-cost mobile system for multispectral cultural heritage data acquisition’, *Digital Heritage International Congress IEEE*, Marseille, pp. 73- 79.

Bonaduce I., Ribechini E., Modugno F., Colombini M. P., **2016**, "Analytical Approaches Based on Gas Chromatography Mass Spectrometry (GC/MS) to Study Organic Materials in Artworks and Archaeological Objects", *Topics in Current Chemistry*, 374, 6, 1-37.

Bonifazzi C., Carcagnì, R. Fontana P., Greco M., Mastroianni M., Materazzi M., Pampaloni E., Pezzati L. and Bencini D., **2008**, "A scanning device for VIS-NIR multispectral imaging of paintings", *Journal of Optics A: Pure and Applied Optics*, 10, 6, 9.

Carcagnì P., Della Patria A., Fontana R., Greco M., Mastroianni M., Materazzi M., Pampaloni E.,

Pezzati L., **2007**, "Multispectral imaging of paintings by optical scanning", *Optics and Lasers in Engineering*, 45, 3, 360-367.

Cardinali M., De Ruggeri M. B., Falcucci C., **2002**, "Diagnostica artistica, Tracce materiali per la storia dell'arte e la conservazione", Roma, Palombi, 333.

Cennino C., 1971, "Libro dell'Arte", Italian edition by Franco Brunello, ed. Neri Pozza, Vicenza.

Clementi C., Rosi F., Romani A., Vivani R., Brunetti B. G., Miliani C., **2012**, "Photoluminescence Properties of Zinc Oxide in Paints: A Study of the Effect of Self-Absorption and Passivation", *Applied Spectroscopy*, 66, 10, 1233-1241.

Colombini M.P., Modugno F., Giannarelli S., Fuoco R., Matteini M., **2000**, "GC-MS characterization of paint varnishes", *Microchemical Journal* 67, 1-3, 385-396.

Colombini M.P., Modugno F., **2009**, "Organic Mass Spectrometry in Art and Archaeology", John Wiley & Sons, 508.

Comelli D., Nevin A., Valentini G., Osticioli I., Castellucci E. M., Toniolo L., Gulotta D., Cubeddu R., **2011**, "Insights into Masolino's wall paintings in Castiglione Olona: Advanced reflectance and fluorescence imaging analysis", *Journal of Cultural Heritage*, 12, 11-18.

Comelli D., Valentini G., Nevin A., Farina A., Toniolo L. and Cubeddu R., **2008**, "A portable UV-fluorescence multispectral imaging system for the analysis of painted surfaces", *Review of Scientific Instruments* 79, 3.

Cosentino A., **2014**, "FORS spectral database of historical pigments in different binders", *e-conservation Journal*, 2, 57-68.

Cosentino A., **2015**, "Multispectral imaging system using 12 interferential filters for mapping pigments", *Conservar Património*, 21, 25-38

Dietemann P., **2003**, "Towards More Stable Natural Resin Varnishes for Paintings", *The Aging of*

Triterpenoid Resins and Varnishes, PhD dissertation, 195.

Dietemann P., Edelmann M. J., Meisterhans C., Pfeiffer C., Zumbühl S., Knochenmuss R. and Zenobi R., **2000**, "Artificial photoageing of triterpenes studied by Graphote-Assisted Laser Desorption/Ionization Mass Spectrometry", *Helvetica Chimica Acta*, 83, 1766-1777.

Dietemann P., Kälin M, Zumbühl S, Knochenmuss R, Wülfert S, Zenobi R., **2001**, "A mass spectrometry and electron paramagnetic resonance study of photochemical and thermal aging of triterpenoid varnishes", *Analytical Chemistry*. 73, 2087-2096.

Daffara C., Pampaloni E., Pezzati L, Barucci M. and Fontana R., **2010**, "Scanning multispectral IR reflectography SMIRR: an advanced tool for art diagnostics, *Accounts of chemical research*, 23, 6, 847-856.

De la Rie E. R., **1982 a**, "Fluorescence of Paint and Varnish Layers (Part I)", *Studies in Conservation*, 27, 1, 1-7.

De la Rie E. R., **1982 b**, "Fluorescence of Paint and Varnish Layers (Part II)", *Studies in Conservation*, 27, 2, 65-69.

De la Rie E. R., **1982 c**, "Fluorescence of Paint and Varnish Layers (Part III)", *Studies in Conservation*, 27, 3, 102-108.

De la Rie E. R., **1988**, "Photochemical and Thermal Degradation of Films of Dammar Resin", *Studies in Conservation*, 33, 2, 53-70.

Delaney J. K., Zeibel J. G., Thoury M., Littleton R., Morales K. M., Palmer M., De la Rie E. R., **2009**, "Visible and Infrared Reflectance Imaging Spectroscopy of Paintings: Pigment Mapping and Improved Infrared Reflectography", *Proceedings of SPIE*, 7391, 8.

Delaney J. K., Zeibel J. G., Thoury M., Littleton R., Palmer M., Morales K. M., René de la Rie E., Hoenigswald A., **2010**, "Visible and infrared imaging spectroscopy of Picasso's, Harlequin Musician: mapping and identification of artist materials in situ", *Applied Spectroscopy*, 64, 6, 584-

Duncan D. R., 1962, “The identification and estimation of pigments in pigmented compositions by reflectance spectrophotometry”, *Journal of the Oil and Colour Chemist Association*, 45, 300-324.

Dunkerton J. and Roy A., 1996, “The Materials of a Group of Late Fifteenth-century Florentine Panel Paintings”, *National Gallery Technical Bulletin*, 27, 21-32.

Eastaugh N., Walsh V., Chaplin T. and Siddall R. 2008, “Pigment Compendium: A Dictionary and Optical Microscopy of Historical Pigments”, Elsevier, 958.

Edwards H.G.M., Farwell D.W., Daffner L., 1996, “Fourier-transform Raman spectroscopic study of natural waxes and resins I.”, *Spectrochimica Acta Part A: Molecular and Biomolecular Spectroscopy*, 52, 12, 1639–1648.

Felder-Casagrande S., and Odlyha M, 1997, “Development of standard paint films based on artists' materials”, *Journal of Thermal Analysis*, 49, 1585-1591.

Feller R.L., 1994, “Accelerated Aging: Photochemical and Thermal Aspects”, *Research in Conservation* 4, The Getty Conservation Institute, Los Angeles, 275.

Feller R. J., 2001, “Color Science in the Examination of Museum Objects: Nondestructive Procedures”, Getty Conservation Institute, Los Angeles, 385.

Feller R. L., 1985, “Artists' Pigments: A Handbook of Their History and Characteristics (Vol. 1)” National Gallery of Art, Washington, 300.

FitzHugh E. W., 1997, “Artists' Pigments: A Handbook of Their History and Characteristics (Vol. 3)”, National Gallery of Art, Washington, 368.

Gilardoni A., Ascani Orsini R., and Tacconi S, 1977, “X-Rays in Art: Physics, Technique, Applications”, Gilardoni S.p.A., Como, 231.

Green R. O., Eastwood M. L., Sarture C. M., Chrien T. G., Aronsson M., Chippendale B.J., Faust J. A., Pavri B. E., Chovit C. J., Solis M. S., Olah M. R., and Williams O., **1998**, "Imaging Spectroscopy and the Airborne Visible Infrared Imaging Spectrometer (AVIRIS)", *Remote Sensing of Environment*, 65, 227-248.

Juita, Dlugogorski B. Z., Kennedy E. M. and Mackie J. C., **2012**, "Low temperature oxidation of linseed oil: a review", *Fire Science Reviews*, 1:3, 36.

Karagiannis G., Salpistis C., Sergiadis G., Chrysosoulakis I., **2007**, "Non-destructive multispectral reflectoscopy between 800 and 1900 nm: An instrument for the investigation of the stratigraphy in paintings, *Review of Scientific Instruments*, 78, 6, 1-7.

Karoui R., Kemps B., Bamelis F., De Ketelaere B., Merten K., Schoonheydt R., Decuypere E., De Baerdemaeker J., **2006-1**, "Development of a rapid method based on front face fluorescence spectroscopy for the monitoring of egg freshness: 1—evolution of thick and thin egg albumens", *European Food Research and Technology*, 223, 303–312

Karoui R., Kemps B., Bamelis F., De Ketelaere B., Merten K., Schoonheydt R., Decuypere E., De Baerdemaeker J., **2006-2**, "Development of a rapid method based on front face fluorescence spectroscopy for the monitoring of egg freshness: : 2—evolution of egg yolk", *European Food Research and Technology*, 223, pp. 180–188

Kim M. S., Chen Y. R., and Mehl P. M., **2001**, "Hyperspectral reflectance and fluorescence imaging system for food quality and safety," *Transactions of the ASAE*, 44, 721-729.

Kubelka P. and Munk, F., **1931**, "Ein Beitrag zur Optik der Farbanstriche", *Zeitschrift für Technische Physik*, 12, 593-601.

Kubelka P., **1948**, "New Contribution of the Optics of Intensely Light-Scattering Materials. Part I", *Journal of the Optical Society of America (JOSA) A*, 38, 448-457.

Kurt N., Celik M. H., **2011**, "Front face fluorescence spectroscopy as a tool for comparison of

aromatic amino acids, nucleic acids, vitamin a and FMRP containing in different egg types”,
Annals. Food Science and Technology, 12, 2, 108-115

Lalli C., Lanterna G., **1990**, "Tecniche d'indagine chimico-stratigrafiche applicate alle pitture murali", Le pitture Murali: tecniche, problemi, conservazione, ed. Danti C., Matteini M., Moles A., Firenze, 161-166.

Landi M., Maino G., **2011**, “Multispectral Imaging and Digital Restoration for Paintings Documentation”, Image Analysis and Processing – ICIAP, Lecture Notes in Computer Science, 6979, 464-474.

Lazzari M., Chiantore O, **1999**, “Drying and oxidative degradation of linseed oil”, Polymer Degradation and Stability, 65, 303-313

Liang H., Keita K., Pannell C., Ward J., **2010**, “A SWIR Hyperspectral imaging system for art history and art conservation”, IX Congreso Nacional del Color, Publicaciones de la Universidad de Alicante, Alicante, 189-192.

Liang H., Saunders D., Cupitt J., **2005**, “A new multispectral imaging system for examining paintings”, Journal of Imaging Science Technology, 49, 6, 551–562.

Mallégol J., Gardette J.-L., Lemaire J., **1999**,“ Long-Term Behaviour of Oil-Based Varnishes and Paints I. Spectroscopic Analysis of Curing Drying Oils”, Journal of the American Oil Chemists' Society (JAOCS), 76, 8, 967-977.

Mallégol J., Gardette J.-L., Lemaire J., **2000**,“ Long-Term Behavior of Oil-Based Varnishes and Paints. Photo- and Thermooxidation of Cured Linseed Oil”, Journal of the American Oil Chemists' Society (JAOCS), 77, 3, 257-263.

Mallégol J., Gonon L., Lemaire J., Gardette J.-L., **2001**,“Long-term behaviour of oil-based varnishes and paints 4. Influence of film thickness and photo-oxidation”, Polymer Degradation and Stability, 72, 191-197.

Mannino M. R., Orecchio S., Gennaro G., **2013**, “Microanalytical method for studying paintings by use of fluorescence spectroscopy combined with principal component analysis”, *Microchemical Journal*, 110, 407–416.

Mansfield J. R., Attas M., Majzels C., Cloutis E., Collins C., Mantsch H. H., **2002**, “Near infrared spectroscopic reflectance imaging: a new tool in art conservation”, *Vibrational Spectroscopy*, 28, 59-66.

Martin M. E., Wabuyele M., Panjehpour M., Overholt B., DeNovo R., Kennel S., Cunningham G., and Vo-Dinh T., **2006**, "An AOTF-based dual-modality hyperspectral imaging system (DMHSI) capable of simultaneous fluorescence and reflectance imaging", *Medical Engineering and Physics*, 28, 149-155.

Mazzeo R., Prati S., Quaranta M., Joseph E., Kendix E., Galeotti M., **2008**, “Attenuated total reflection micro FTIR characterisation of pigment–binder interaction in reconstructed paint films”, *Analytical and Bioanalytical Chemistry*, 392, 1, 65–76.

Meilunas R. J., Bentsen J. G. and Arthur Steinberg, **1990**, “Analysis of Aged Paint Binders by FTIR Spectroscopy”, *Studies in Conservation*, 35, 1, 33-51.

Miliani C., Romani A., Favaro G., **1998**, “A spectrophotometric and fluorimetric study of some anthraquinoid and indigoid colorants used in artistic paintings”, *Spectrochimica Acta Part A: Molecular and Biomolecular Spectroscopy* 54, 4, 581–588.

Mills, J., White, R., **1980**, “Analyses of Paint Media”, *National Gallery Technical Bulletin* (Vol. 4), London, pp 65–67.

Nevin A., Cather S., Anglos D., Fotakis C., **2006-1**, “Analysis of protein-based binding media found in paintings using laser induced fluorescence spectroscopy”, *Analytica Chimica Acta* 573–574, 341–346

Nevin A. and Anglos D., **2006-1**, “Assisted Interpretation of Laser-Induced Fluorescence Spectra

of Egg-Based Binding Media Using Total Emission Fluorescence Spectroscopy”, *Laser Chemistry*, 6, 5.

Nevin A., Comelli D., Valentini G., Anglos D., Burnstock A., Cather S., Cubeddu R., **2007**, “Time-resolved fluorescence spectroscopy and imaging of proteinaceous binders used in paintings”, *Analytical and Bioanalytical Chemistry*, 388, 1897–1905.

Nevin A., Osticioli I., Anglos D., Burnstock A., Cather S. and Castellucci E., **2008-1**, “The analysis of naturally and artificially aged protein-based paint media using Raman spectroscopy combined with Principal Component Analysis”, *Journal of Raman Spectroscopy*, 39, 993–1000.

Nevin A., Anglos D., Cather S., Burnstock A., **2008-2**, “The influence of visible light and inorganic pigments on fluorescence excitation emission spectra of egg-, casein- and collagen-based painting media”, *Applied Physics A*, 92, 69–76.

Nevin A., Comelli D., Osticioli I., Toniolo L., Valentini G. and Cubeddu R., **2009**, “Assessment of the ageing of triterpenoid paint varnishes using fluorescence, Raman and FTIR spectroscopy”, *Analytical and Bioanalytical Chemistry*, 395, 2139–2149.

Oleari C., **1998**, “Misurare il colore”, Società Italiana di Ottica e Fotonica, Hoepli, Milano, 380.

Oleszko A., Olsztyńska-Janus S., Walski T., Grzeszczuk-Kuć K., Bujok J., Gałęcka K., Czerski A., Witkiewicz W., Komorowska M., **2015**, “Application of FTIR-ATR Spectroscopy to Determine the Extent of Lipid Peroxidation in Plasma during Haemodialysis” *BioMed Research International*, Int. 2015, 1–9.

Osticioli I., Nevin A., Anglos D., Burnstock A., Cather S., Becucci M., Fotakis C., and Castellucci E., **2008-1**, “Micro-Raman and fluorescence spectroscopy for the assessment of the effects of the exposure to light on films of egg white and egg yolk”, *Journal of Raman Spectroscopy*, 39, 307–313.

Pelagotti A., Pezzati L., Bevilacqua N., Vascotto V., Reillon V., Daffara C., **2005**, “A study of UV

fluorescence emission of painting materials”, Proceedings of Art’05, 8th International Conference on “Non Destructive Investigations and Micronalysis for the Diagnostics and Conservation of the Cultural and Environmental Heritage”, Ed. C. Parisi, G. Buzzanca, A. Paradisi, Rome, 14.

Pelagotti A., Pezzati L., Piva A. and Del Mastio A., **2006**, "Multispectral UV fluorescence analysis of painted surfaces", 14th European Signal Processing Conference (Eusipco 2006), Florence, Italy, 5.

Peris-Vicente J., Baumer U., Stege H., Lutzenberger K. and Gimeno Adelantado J. V., **2008**, “Characterization of Commercial Synthetic Resins by Pyrolysis-Gas Chromatography/Mass Spectrometry: Application to Modern Art and Conservation”, Analytical Chemistry, 81, 3180–3187.

Plytycz B., Homa J., Kozio B., Rózanowska M. and Morgan J., **2006**, “Riboflavin content in autofluorescent earthworm coelomocytes is species-specific”, Folia Histochemica Et Cytobiologica, 44, 4, 275-280.

Polder G., Van der Heijden G.W.A.M. and Young I.T., **2002**, "Spectral image analysis for measuring ripeness of tomatoes". Transactions of the ASAE, 45, 1155-1161.

Poldi G., **2009**, “Antonello da Messina between Sicily and Venice: The San Cassiano altarpiece. Technical examinations and comparisons, Technologische Studien: Konservierung, Restaurierung, Forschung, Technologie / Kunsthistorisches Museum, 6, 82-113.

Ramos M. E. and **Lagorio M. G.**, **2006**, “A model considering light reabsorption processes to correct *in vivo* chlorophyll fluorescence spectra in apples”, Photochemical and Photobiological Sciences, 5, 508-512.

Rencz A.N., Ryerson R.A., **1999**, “Manual of Remote Sensing (Vol. 3): Remote Sensing for the Earth Sciences”, Wiley & Sons, New York, 728.

Rinaldi S., **1986**, “La fabbrica dei colori”, Il Bagatto, Roma, 572.

Romani A., Clementi C., Miliani C., and Favaro G., **2010**, “Fluorescence Spectroscopy: A Powerful Technique for the Non invasive Characterization of Artwork”, *Accounts Of Chemical Research*, 43, 6, 837-846.

Roy A. ed., **1986**, “Artists' Pigments: A Handbook of Their History and Characteristics (Vol 2)”, National Gallery of Art, Washington, 323.

Sandu I. C. A., Roque A. C. A., Matteini P., Schäfer S., Agati G., Correia C. R., Pacheco J. F. F., **2011**, “Fluorescence Recognition of Proteinaceous Binders in Works of Art by a Novel Integrated System of Investigation”, *Microscopy Research And Technique*, 75, 3, 316–324.

Saunderson J. L., **1941**, “Calculation of the color pigmented plastics,” *Journal of the Optical Society of America*, 32, 727–736.

Smith G. J., Haskell T. J., **2000**, “The fluorescent oxidation products of dihydroxyphenylalanine and its esters”, *Journal of Photochemistry and Photobiology B: Biology*, 55, 103–108.

Stadelman W. J., and Cotteril O. J., **1995**, “Egg Science and Technology”, Fourth Edition, London, 579.

Theophilus P., **1979**, “On divers arts” Trans. Hawthorne J.G., Smith C.S., Dover Publications, Inc., New York.

Thoury M., Elias M., Frigerio J. M. and Barthou C., **2007**, "Nondestructive Varnish Identification by Ultraviolet Fluorescence Spectroscopy", *Applied Spectroscopy*, 61, 12, 1275-82.

Van den Berg K. J., Boon J. J., Pastorova I. I. and Spetter L. F. M., **2000**, “ Mass spectrometric methodology for the analysis of highly oxidized diterpenoid acids in Old Master paintings”, *Journal of Mass Spectrometry*, 35, 512–533.

Van der Doelen G. A., van den Berg K., J. and Boon J. J., **1998**, “Comparative Chromatographic and Mass-Spectrometric Studies of Triterpenoid Varnishes: Fresh Material and Aged Samples

from Paintings”, *Studies in Conservation*, 43, 4, 249-264.

Van der Doelen G. A. and Boon J. J., **2000**, “Artificial ageing of varnish triterpenoids in solution” *Journal of Photochemistry and Photobiology A: Chemistry*, 134, 45–57.

Vargas W. E. and Niklasson G. A., **1997**, “Applicability conditions of the Kubelka–Munk theory”, *Applied Optics*, 36, 5580–5586.

Verri G., Clementi C., Comelli D., Cather S., Piqué F., **2008**, “Correction of ultraviolet induced fluorescence spectra for the examination of polychromy”, *Applied Spectroscopy*, 62, 1295–1302.

Wendlandt W.W. and Hecht H.G., **1966**, “Reflectance Spectroscopy”, Interscience Publishers (John Wiley & Sons), New York, 298.

Zhao Y., Berns R. S., Taplin L. A., Coddington J., **2008**, “An investigation of multispectral imaging for the mapping of pigments in paintings”, *Computer Image Analysis in the Study of Art Proceeding SPIE*, 6810, 9.

<http://www.webexhibits.org/causesofcolor/10.html>

<http://fors.ifac.cnr.it>

APPENDIX A: EXPERIMENTAL CONDICTIONS AND SETUPS

REFLECTANCE AND FLUORESCENCE SPECTROSCOPY

The reflectance spectra were measured with the Minolta CM-2300d spectrophotometer, shown in Fig.1-a and the Avantes AvaSpec spectrophotometer equipped with optical fibers and a halogen lamp, shown in Fig. 1-b.

The Avantes device was used also for the acquisition of the fluorecence emission spectra.

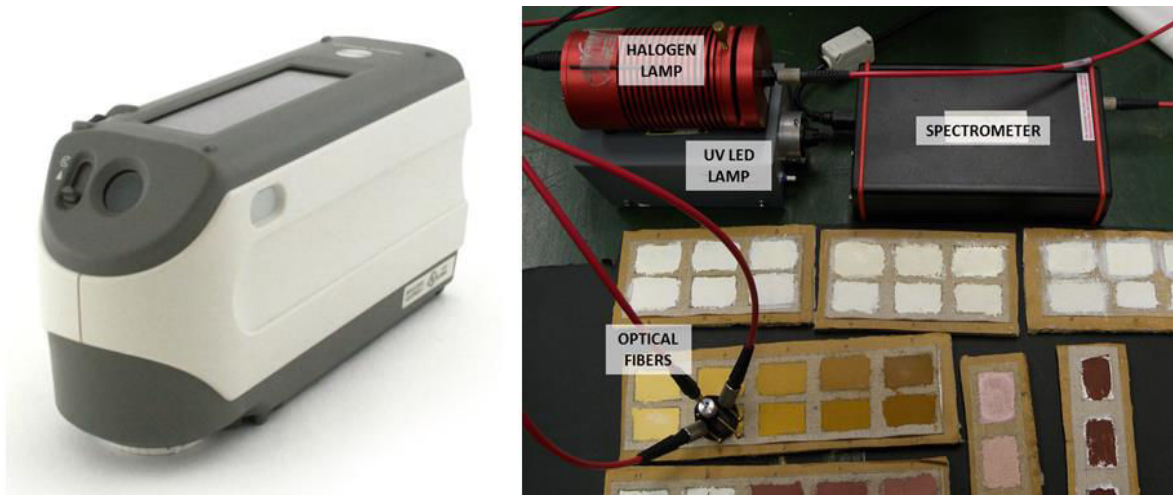


Fig. 1: a) Minolta CM-2300d instrument and b) Avantes AvaSpec instrument

The Minolta CM-2300d instrument is a portable integrating sphere spectrophotometer. It performs measurements at d/8 geometry (diffuse illumination, 8-degree viewing angle) and we performed the measurements in SCE (specular component excluded) mode. The light source is composed by two pulsed xenon lamps (X4) and the detector is a silicon photodiode array (dual 40 elements) with a diffraction grating for dispersing the light. This spectrometer covers the wavelength range from 360 nm to 740 nm at acquisition steps of 10 nm.

The Avantes AvaSpec spectrophotometer employs a halogen lamp with a tungsten filament (HL-2000 FHSA, Avantes) as light source. The spectrometer is composed by a diffraction grating of 300 lines/mm, blazed at 500 nm, that allows to cover the spectral range from 300 nm to 1100 nm,

and a CCD linear sensor (2048 pixels). The spectral resolution is 0.8 nm. We illuminated the samples at 45° with a bifurcated fiber (diameter of 600 μm), connected to the halogen lamp for the reflectance measurements and to a UV LED (emitting at 365 ± 10 nm) for the fluorescence measurements. The light from the samples was collected with a 200 μm diameter fiber at 90° respect to the surface.

SPECTROFLUORIMETRY

We acquired the fluorescence spectra by means of a Horiba FluoroMax-2 spectrometer, shown in Fig. 2, with a xenon lamp as the excitation source; it is equipped with a solid sample holder, that allows spectral acquisitions directly on sample laying on microscope slides. The samples were positioned with an angle of 75° with respect to the excitation source and 25° with respect to the detector.

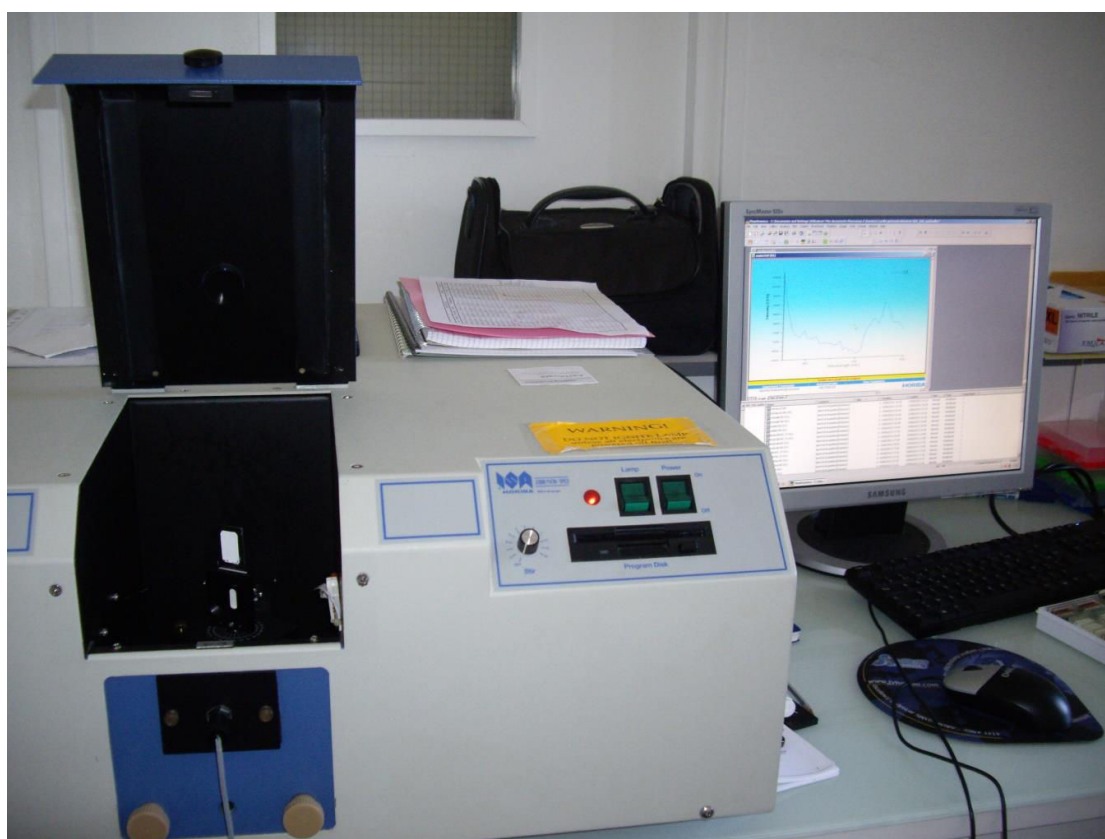


Fig. 2: Horiba FluoroMax-2 spectrometer

MULTISPECTRAL ACQUISITION SYSTEM

The multispectral acquisition system is described in the Part I, chap.2. In this section we show the instrumental set up in Fig. 3.



Fig. 3: a) multispectral acquisition set up, b) CCD camera, c) narrow-band filters, d) internal wheel, e) UV LEDs lamp.

UV-VIS SPECTROPHOTOMETER

The UV-VIS spectra were acquired with a Cary 100 (Agilent), shown in Fig. 4. The working conditions were: spectral range 200–600 nm, sampling interval 1 nm. In this work we report the absorbance spectra from 300 nm to 600 nm.



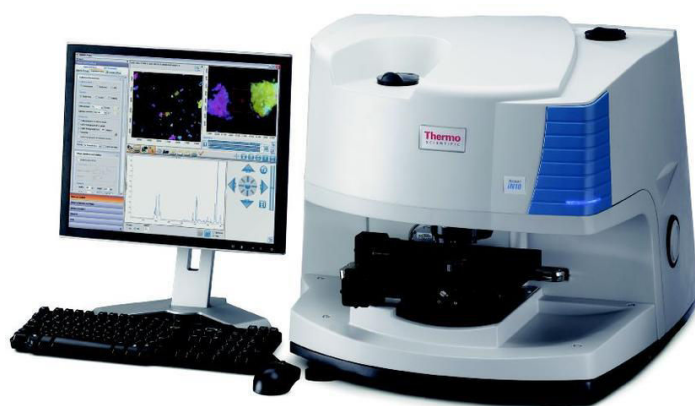
Fig. 4: Cary 100 UV-VIS spectrometer

INFRARED SPECTROSCOPY

We performed ATR-FTIR spectra by using two instruments: ATR- Infrared Imaging Microscope (Nicolet iN10 MX), Fig.5 a, and ATR-FTIR (Thermo-Nicolet), Fig.5 b. Both instruments are equipped with a germanium crystal.

In the ATR imaging configuration, the liquid nitrogen cooled MCT detector is coupled with an infrared microscope. The spectra were acquired from 4000 cm^{-1} to 650 cm^{-1} , with $1,93\text{ cm}^{-1}$ spectral resolution, averaging 64 scans. The spectra acquired with the Thermo-Nicolet instrument were collected between 4000 cm^{-1} to 800 cm^{-1} with $1,93\text{ cm}^{-1}$ spectral resolution averaging 32 scans.

a)



b)



Fig. 5: a) ATR- Infrared Imaging Microscope (Nicolet iN10 MX), b) ATR-FTIR (Thermo-Nicolet)

ED-XRF SPECTROSCOPY

The spectrometer consists of an X-ray tube with a palladium anode (EIS Ltd) and a Silicon Drift Detector (SDD), Peltier cooled with amplifier and integrated multi-channel analyser (Amptek X-123SDD). The surface of the sensor is 25 mm² and its thickness is 500 μm . The energy resolution is 140 eV FWHM at 5.9 keV. The spectra were acquired operating the X-ray tube at 40 kV and 0.4 mA. The device reveals chemical elements with atomic numbers (Z) > 15. The experimental set up is shown in Fig. 6.

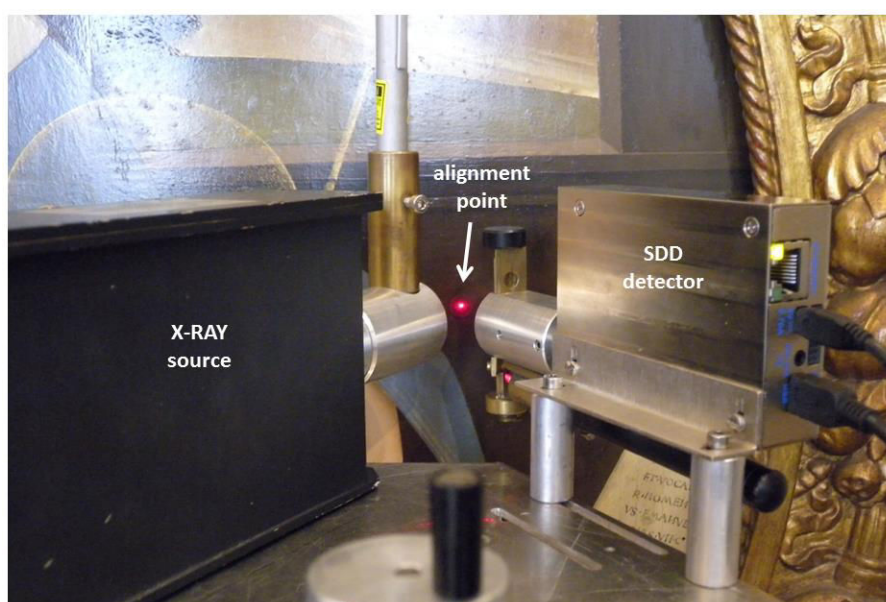


Fig. 6: ED-XRF configuration

OPTICAL MICROSCOPE

The microscope images were captured with an USB digital microscope (PCE-MM 200), shown in Fig. 7. This device has continuous magnification from 10X to 200X, (we used 150X). The sample is illuminated with six incorporated white LED's.



Fig. 7: USB digital microscope

RADIOGRAPHY

The acquisition set up for radiographic applications is constituted by a X-ray tube and an image detector for X-rays. The X-ray tube is the palladium anode (EIS Ltd) operating at 40 kV and 0.4 mA used for the ED-XRF measurements. We used a Hamamatsu C7942 flat panel sensor as detector. The sensor contains a CsI scintillator plate, a two-dimensional photodiode array with FET switches and a signal processing IC chip. The photodiode array has 2400×2400 pixels (pixel size $50 \mu\text{m}^2$). The control board converts the analogic signal into a 12-bit digital image (4096 grey levels).

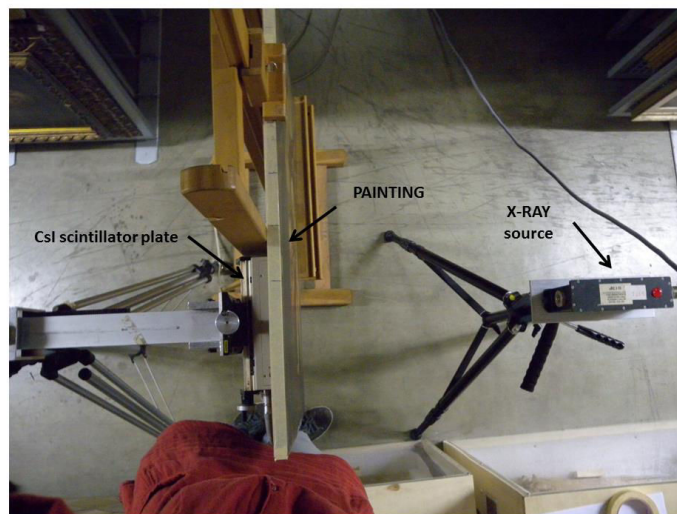


Fig. 8: Radiography configuration

SUN TEST

The accelerated ageing was performed by means of a Suntest CPS+photoreactor (Atlas), shown in Fig. 9, equipped with a xenon lamp and a filter that prevents the transmission of wavelengths shorter than 290 nm.

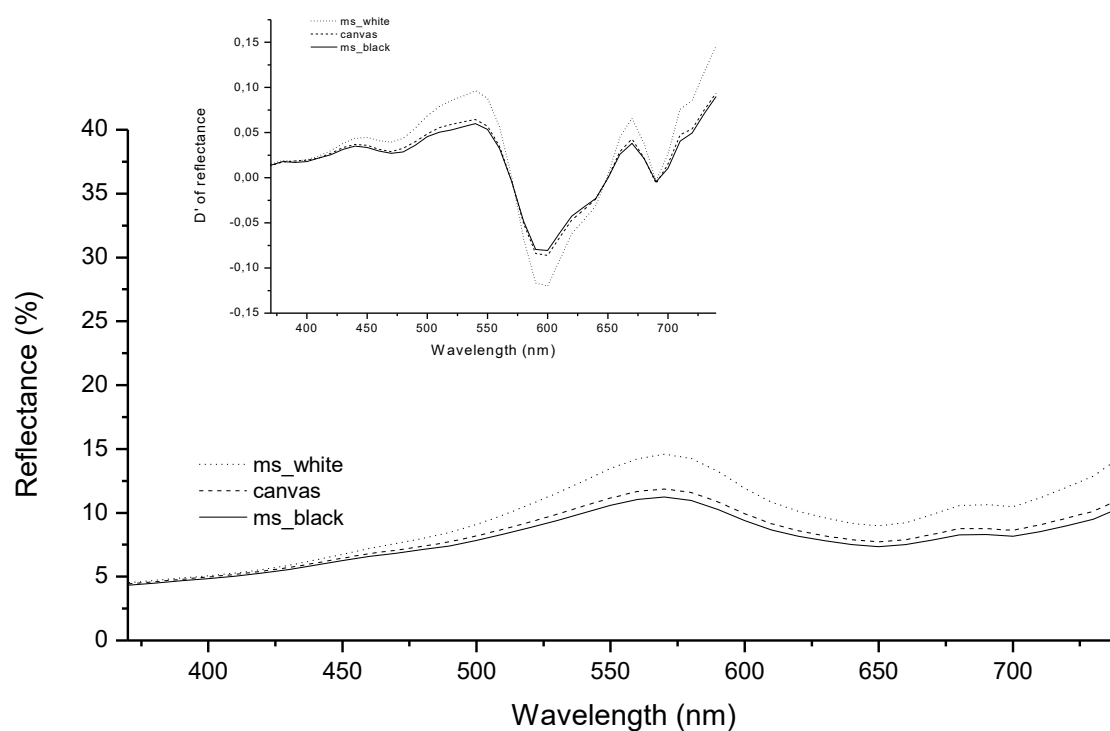


Fig.9: Suntest CPS+photoreactor

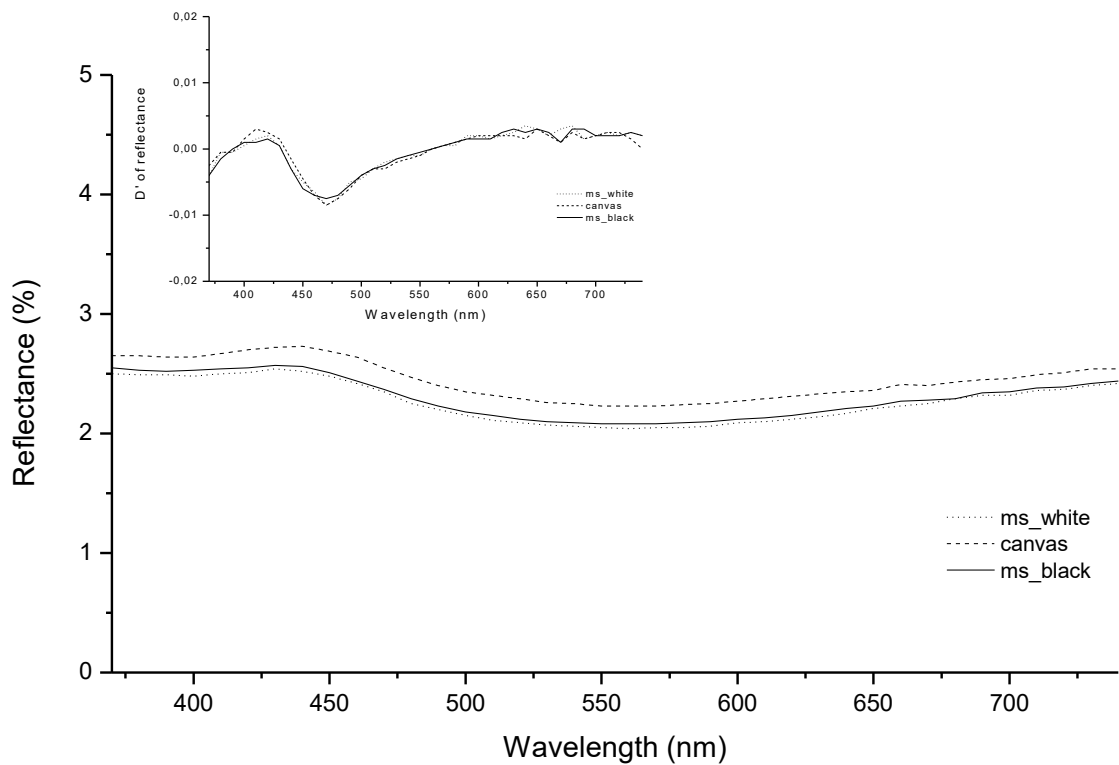
APPENDIX B: FORS SPECTRA with different backgrounds

We report the reflectance spectra of the fourty pictorial layers spread on different supports: black support (solid line), white support (dashed line) and on a lead white layer on canvas (dotted line). The first derivate of the reflectance spectra were shown in the insert of the figure. Reflectance measurements were carried out with the Minolta spectrometer.

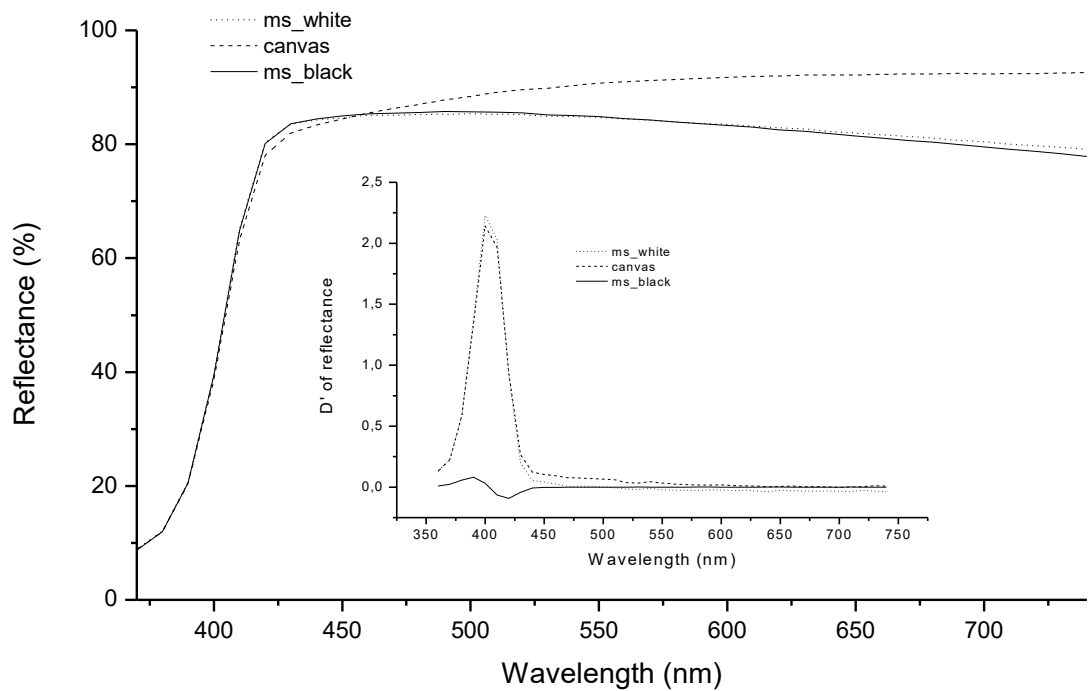
Green earth



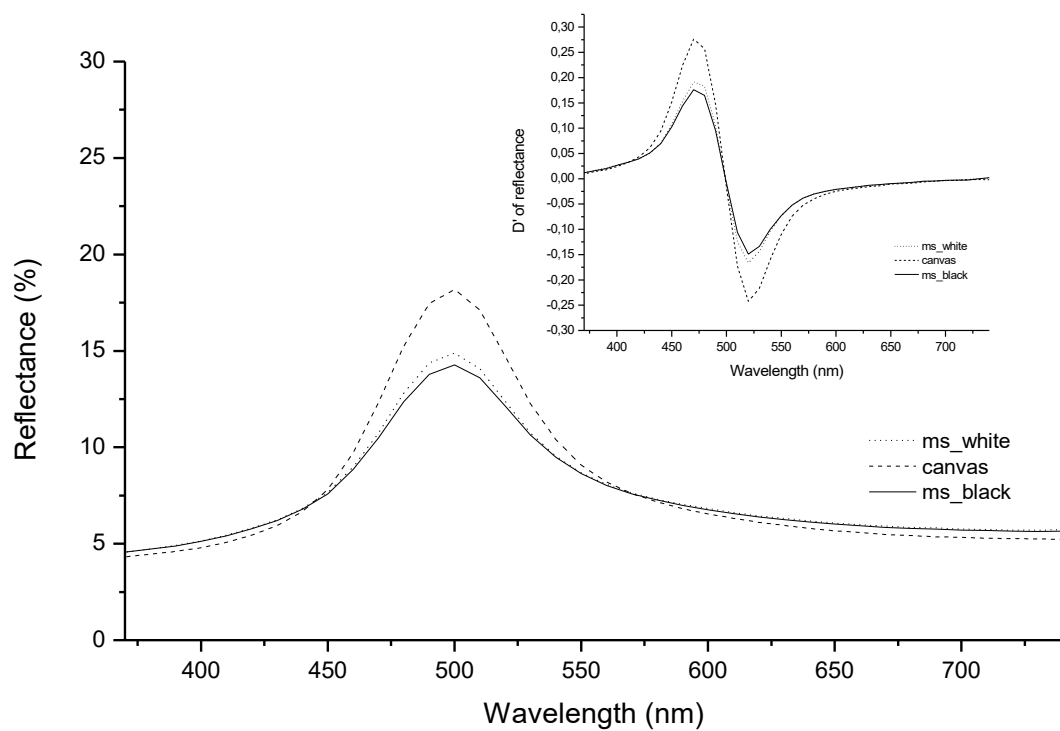
Prussian blue



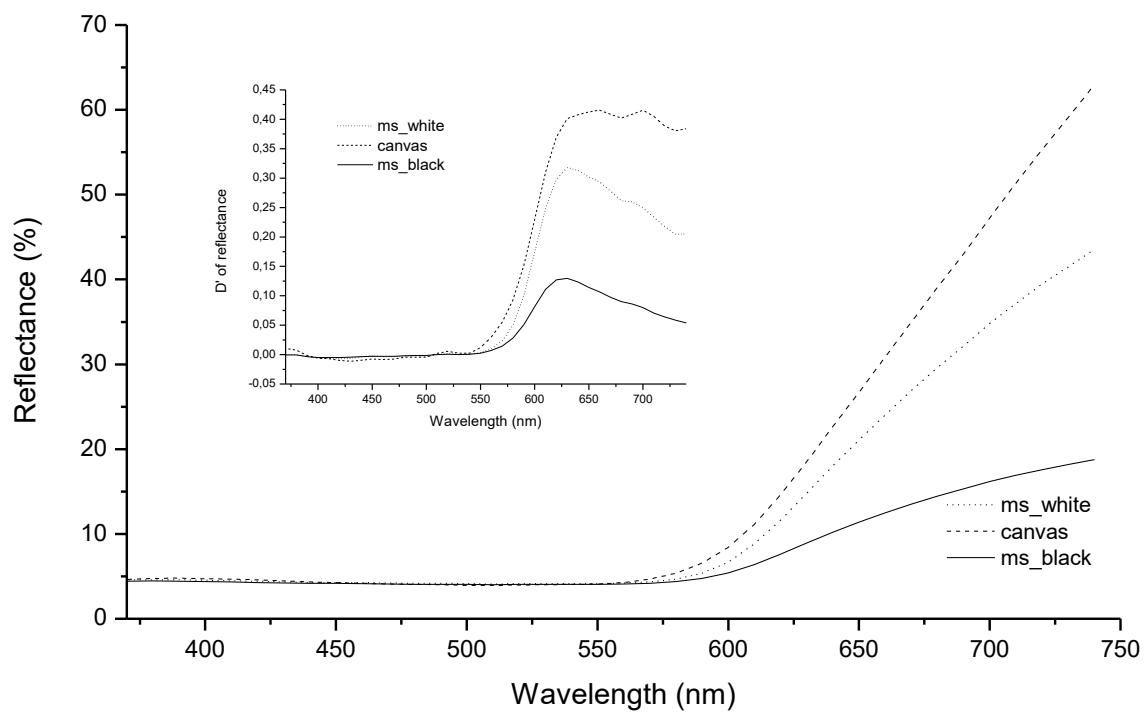
Titanium white



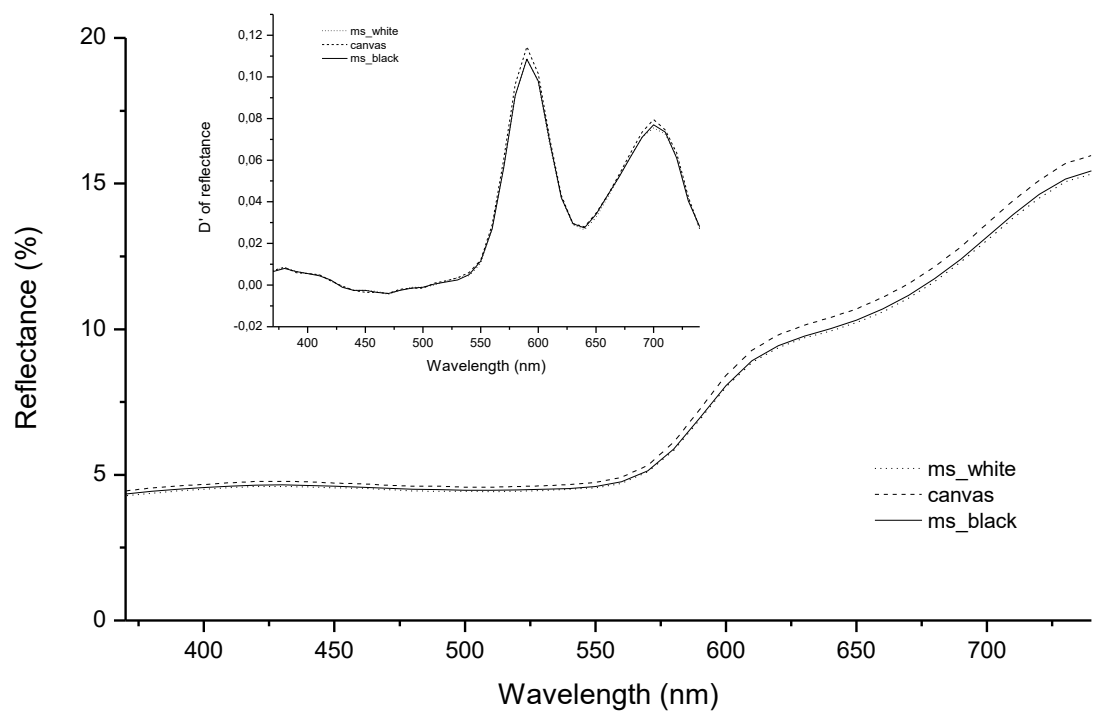
Verdigris



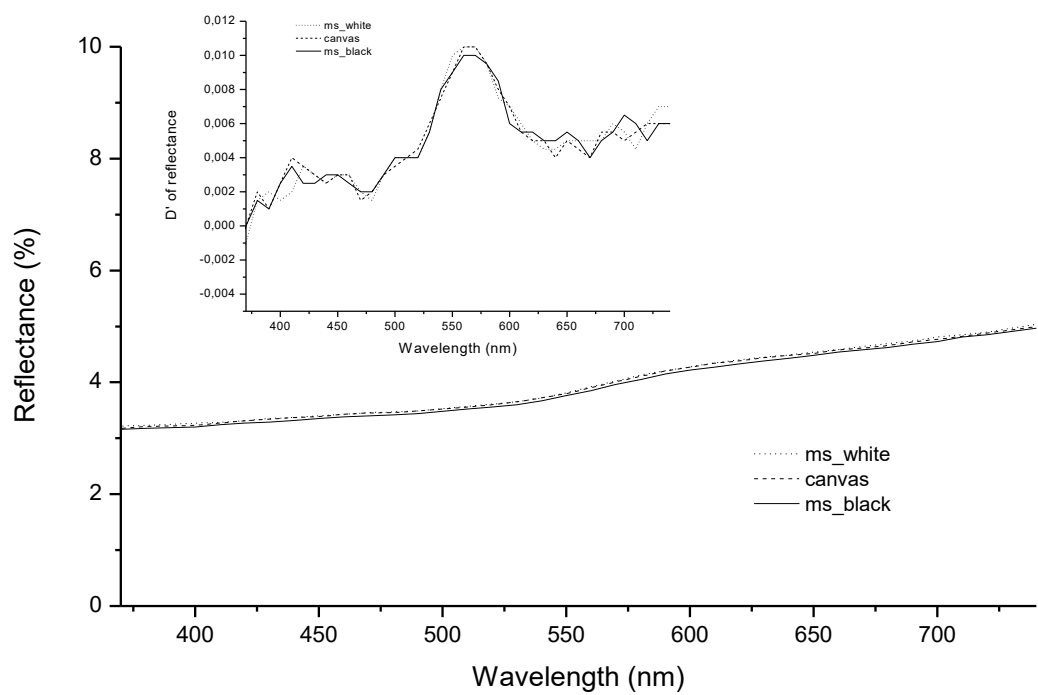
Madder lake



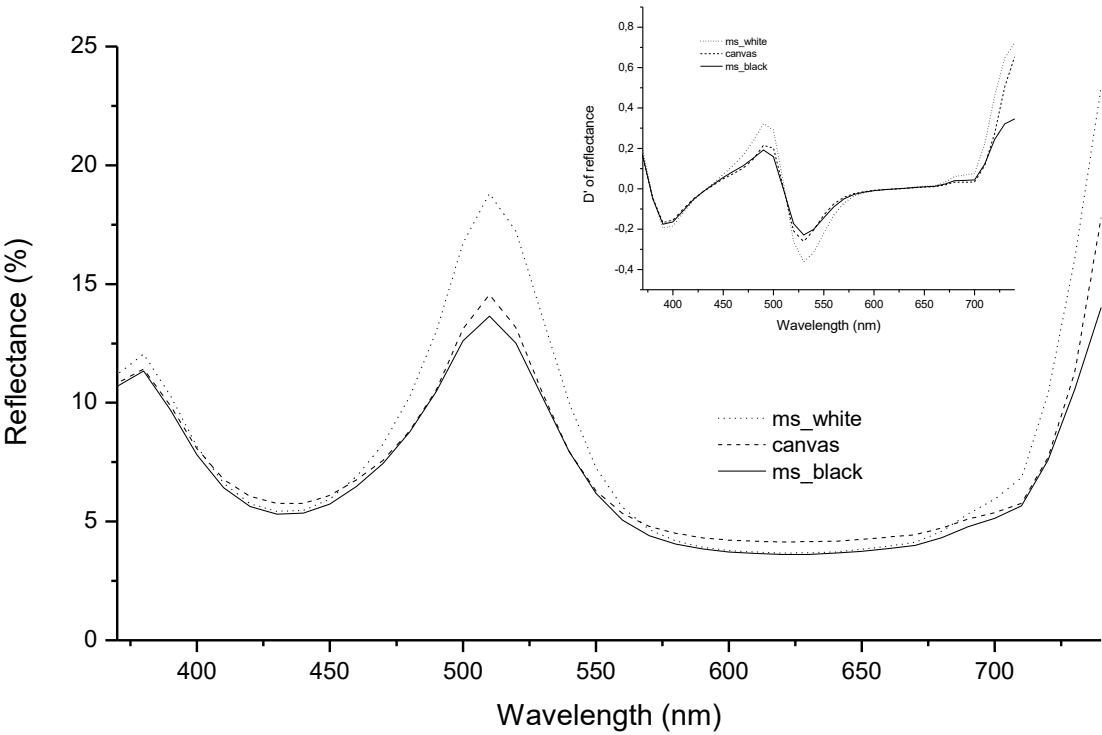
Caput mortum



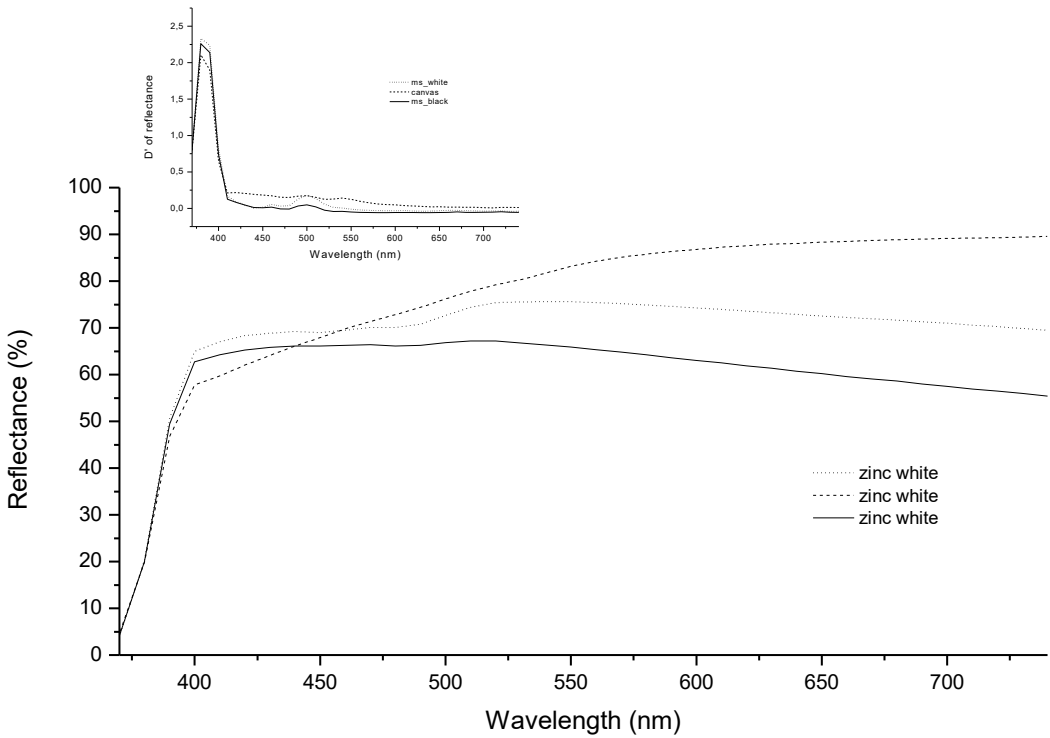
Burnt umber



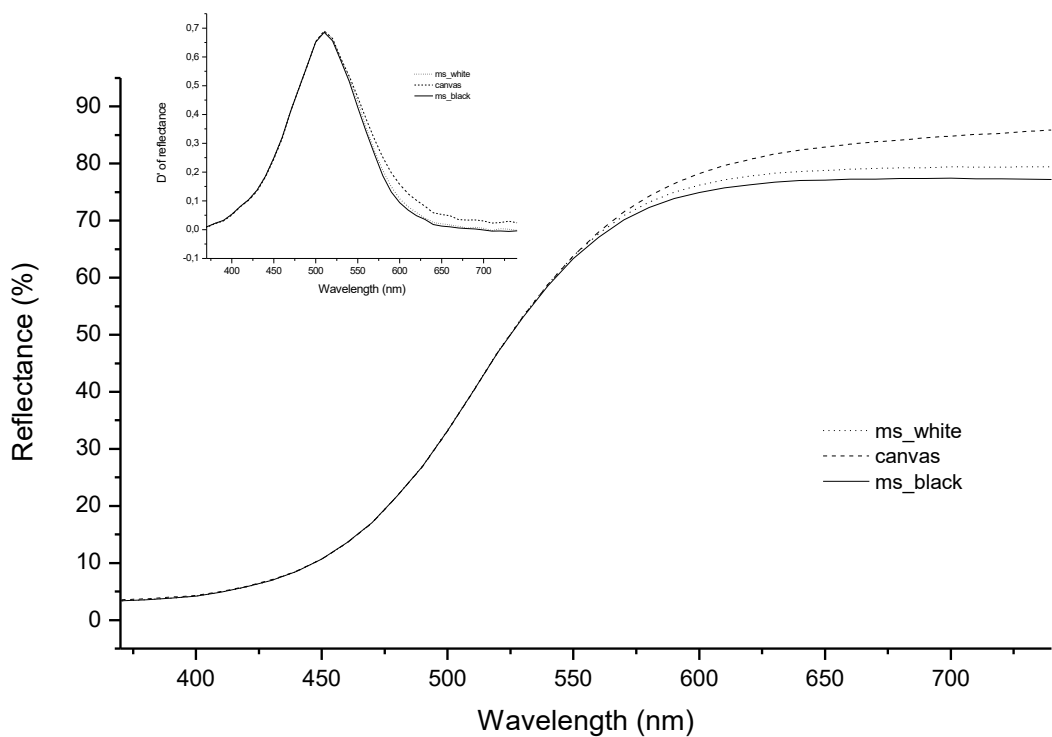
Emerald green



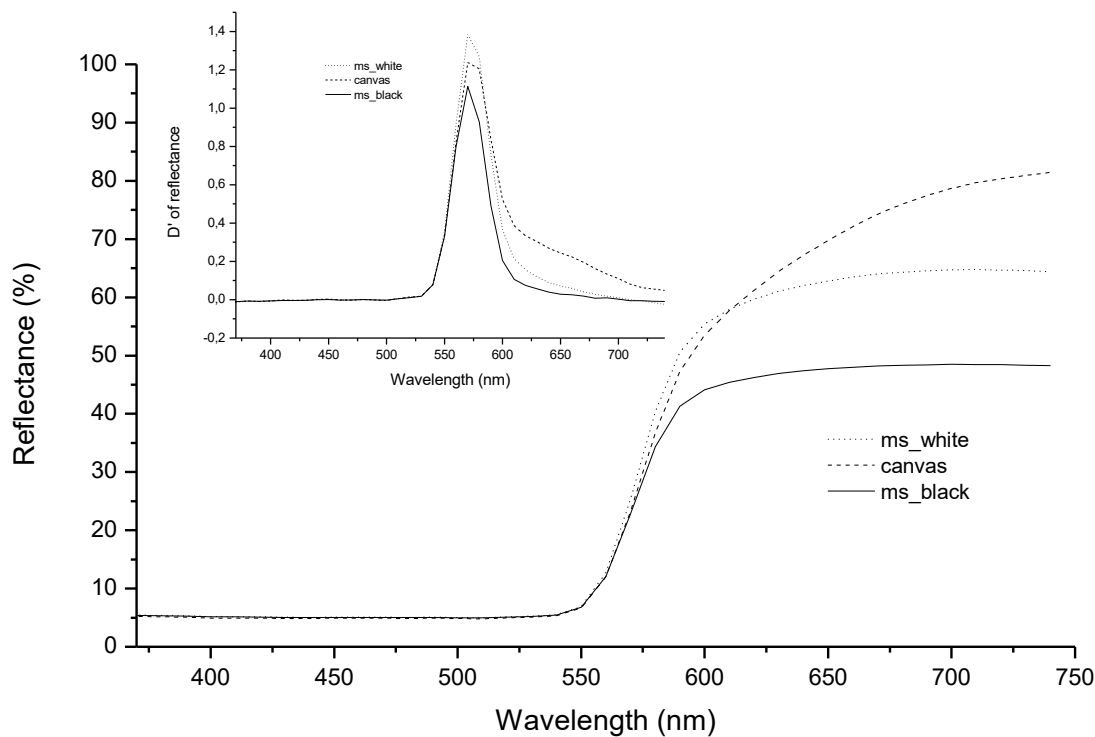
Zinc white



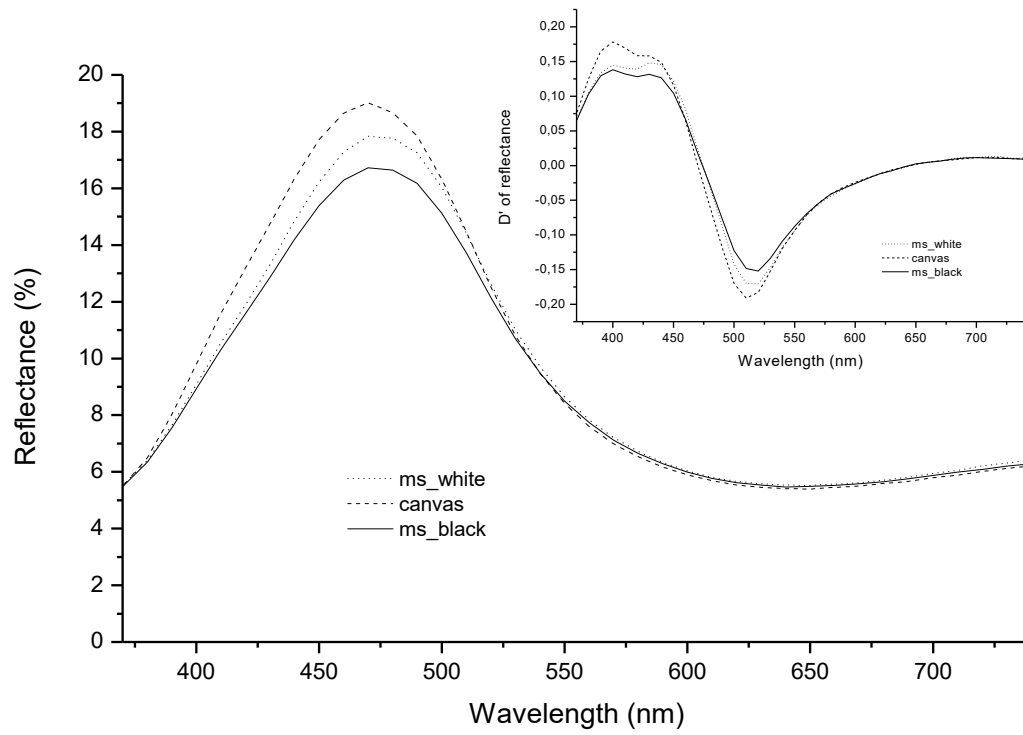
Naples yellow



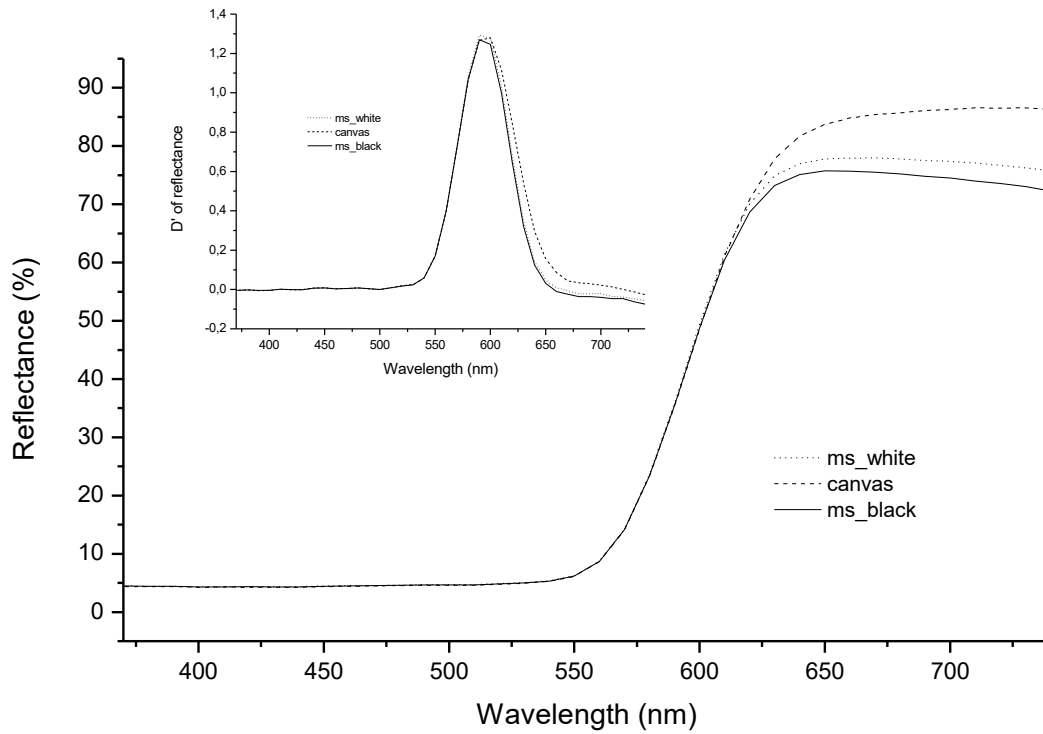
Minium



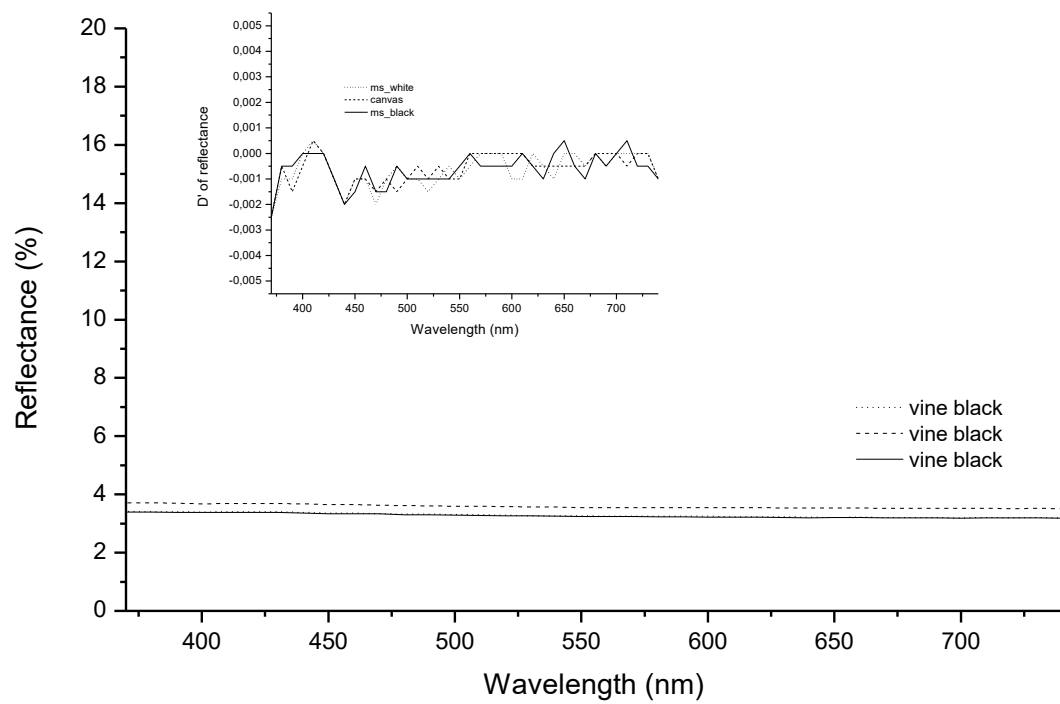
Azurite



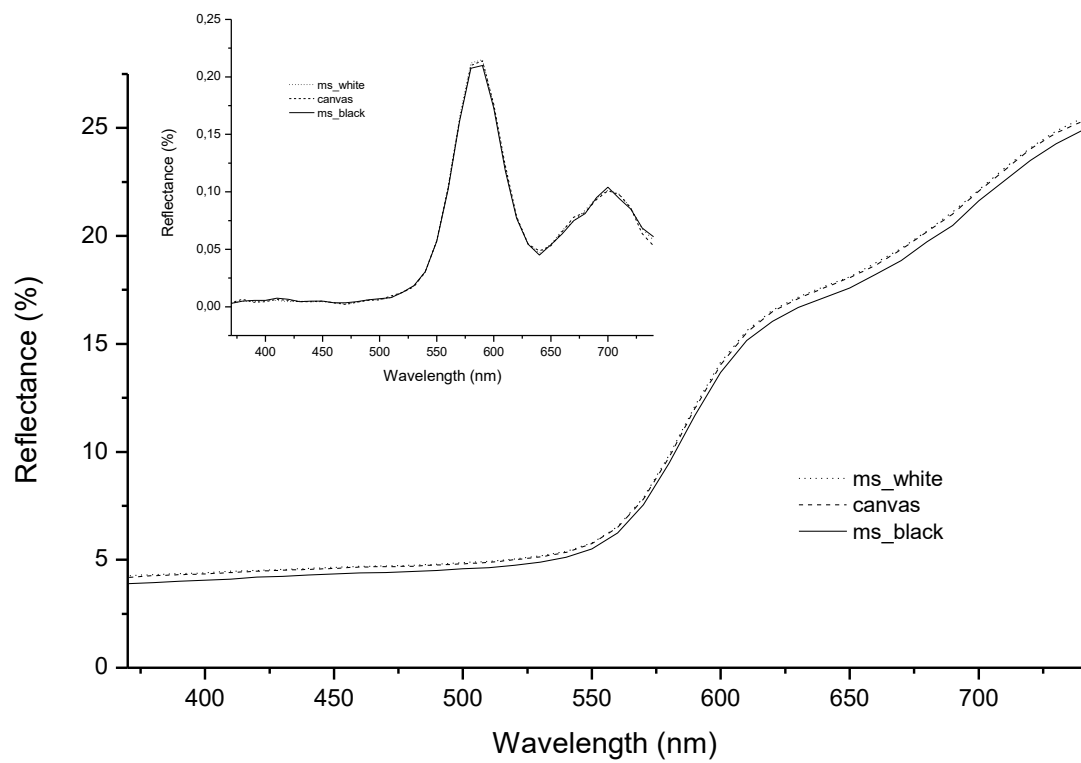
Chrome red



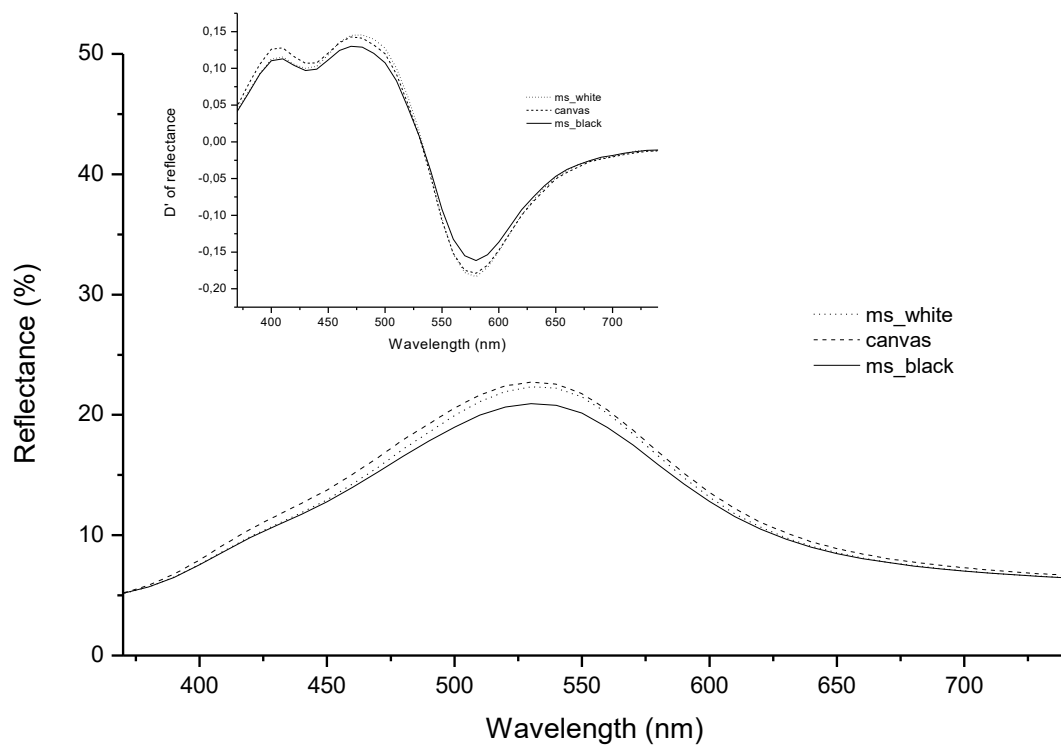
Vine black



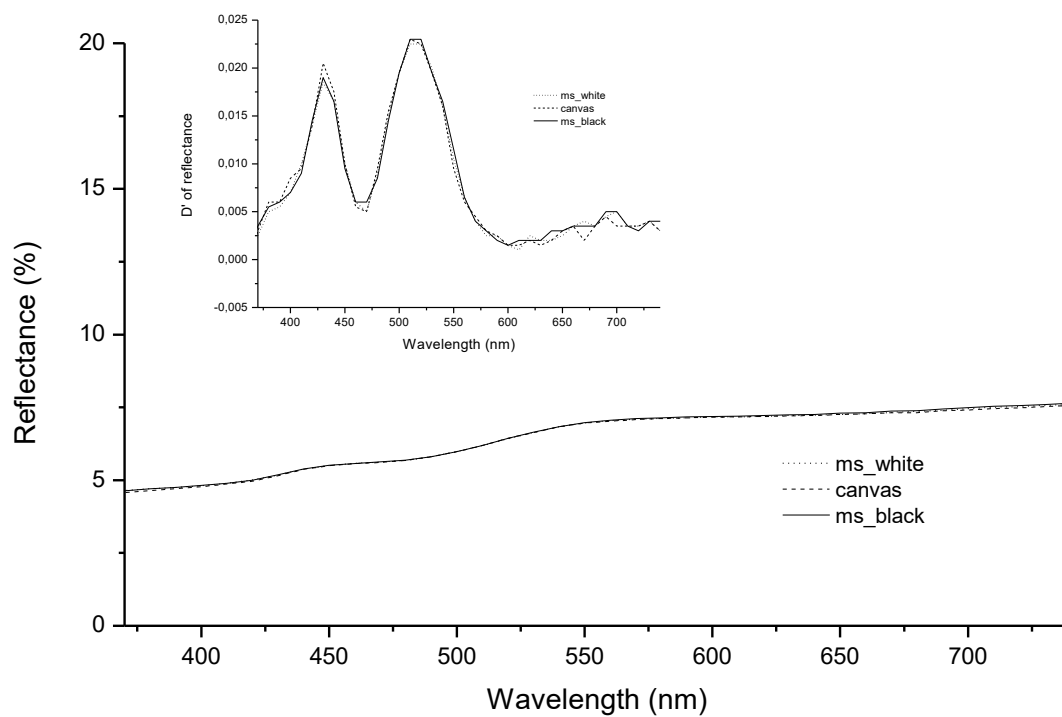
Hematite



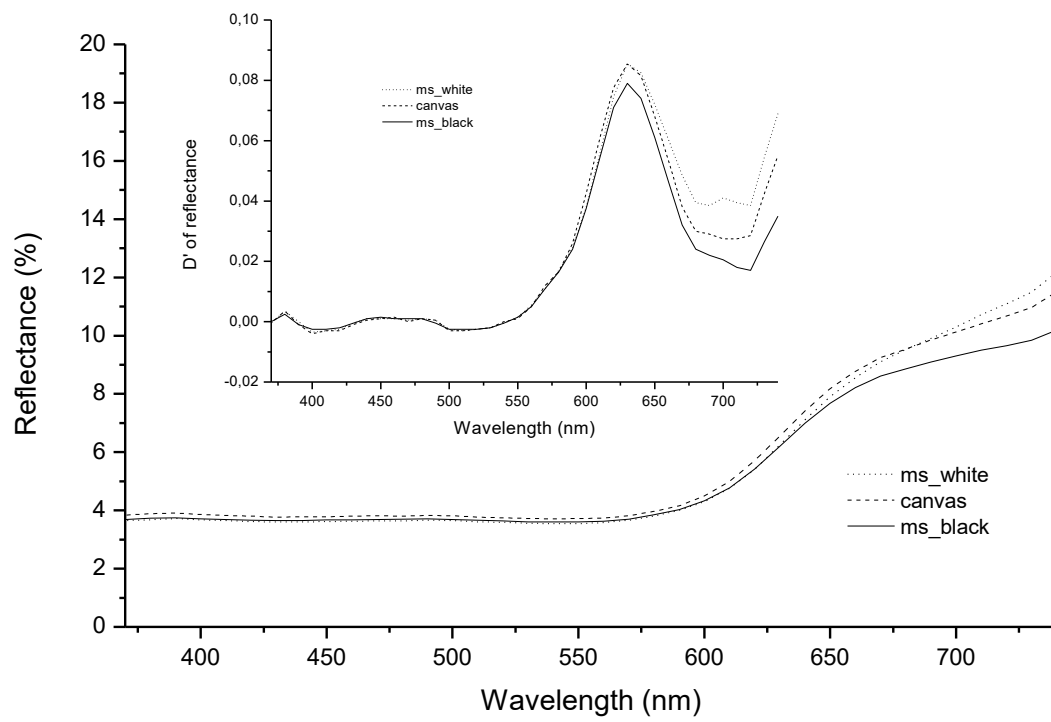
Malachite



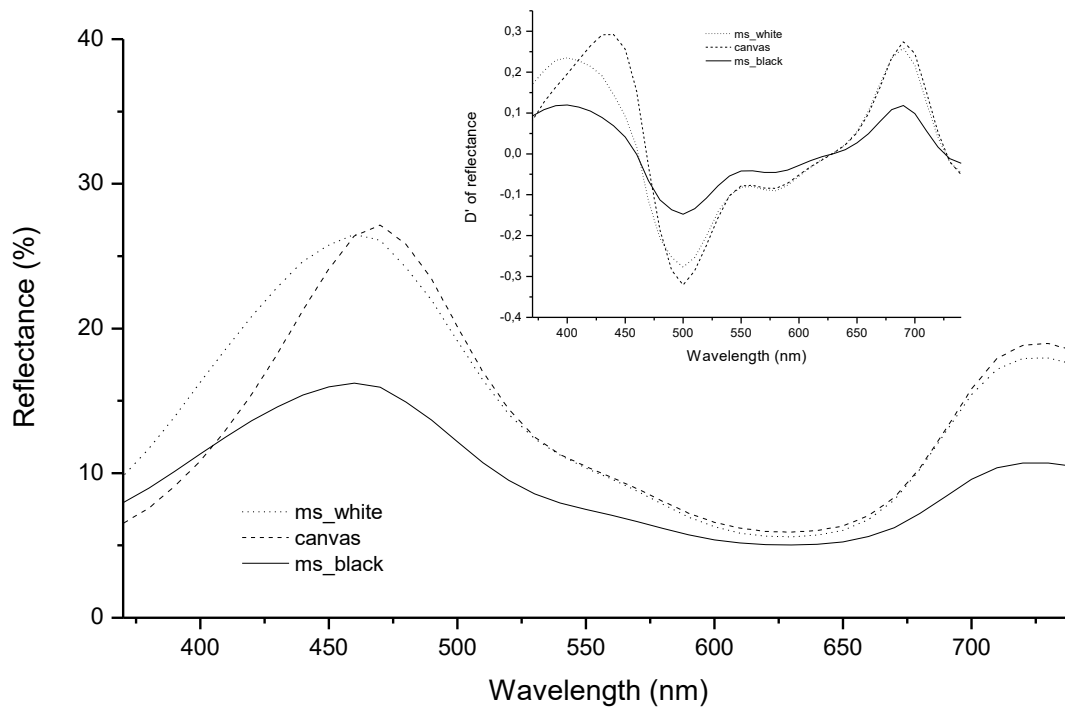
Verdaccio



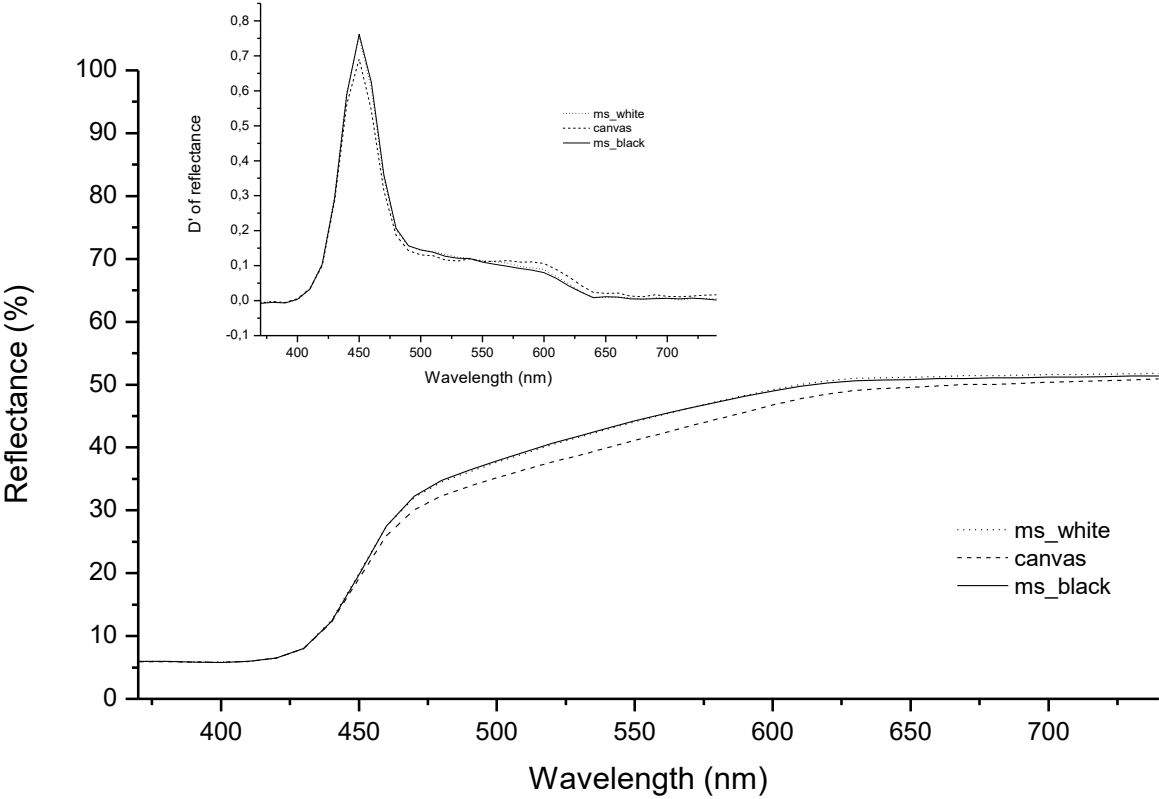
Alizarin crimson lake



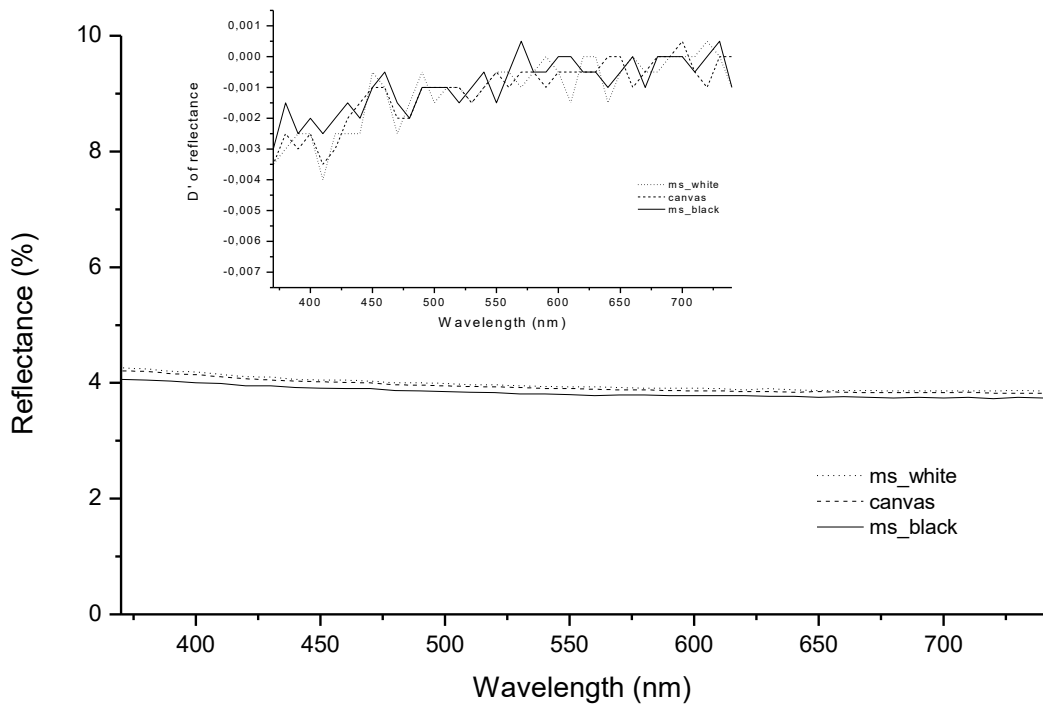
Egyptian blue



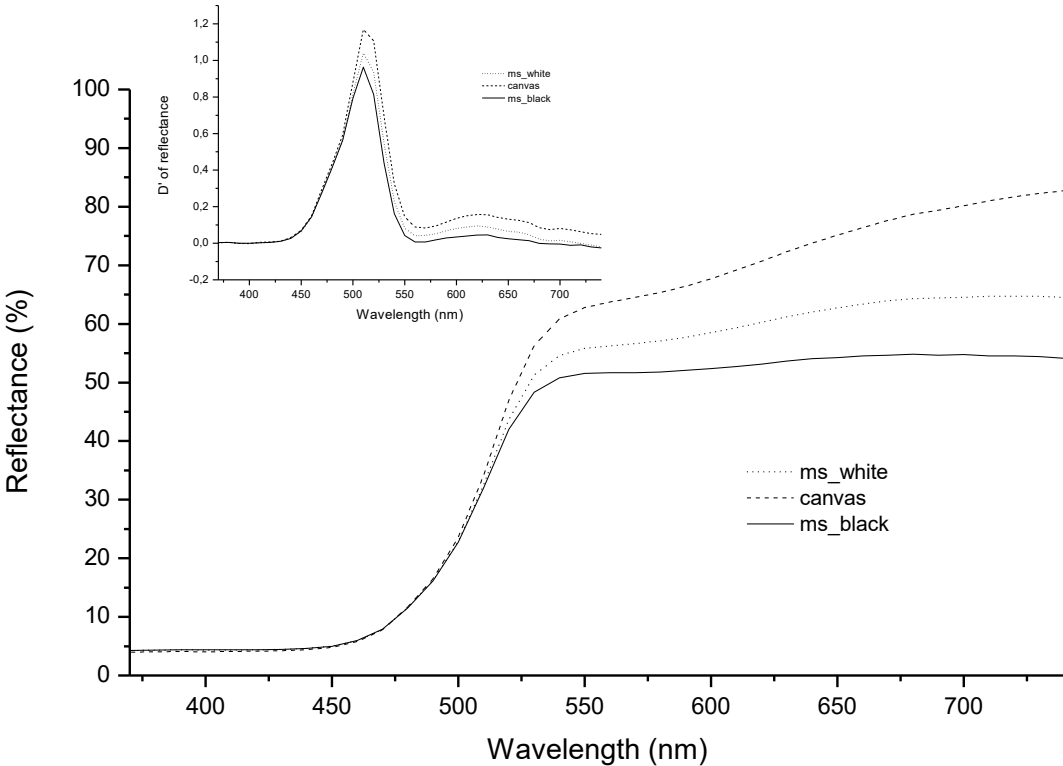
Litharge



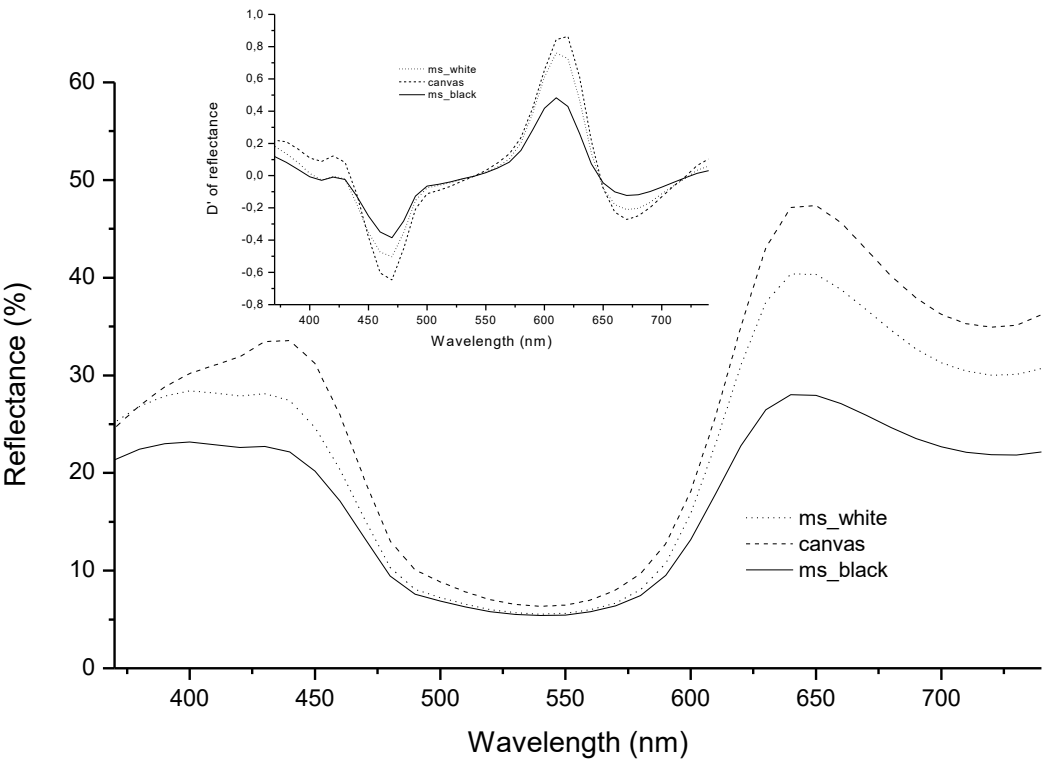
Ivory black



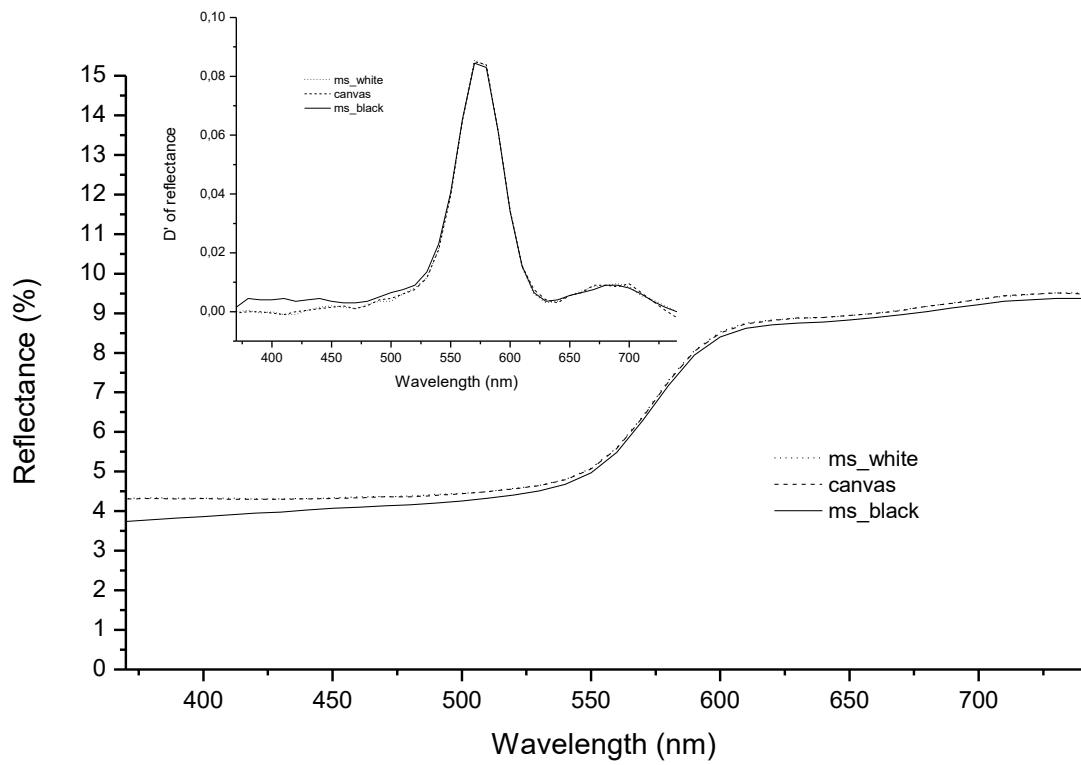
Zinc yellow



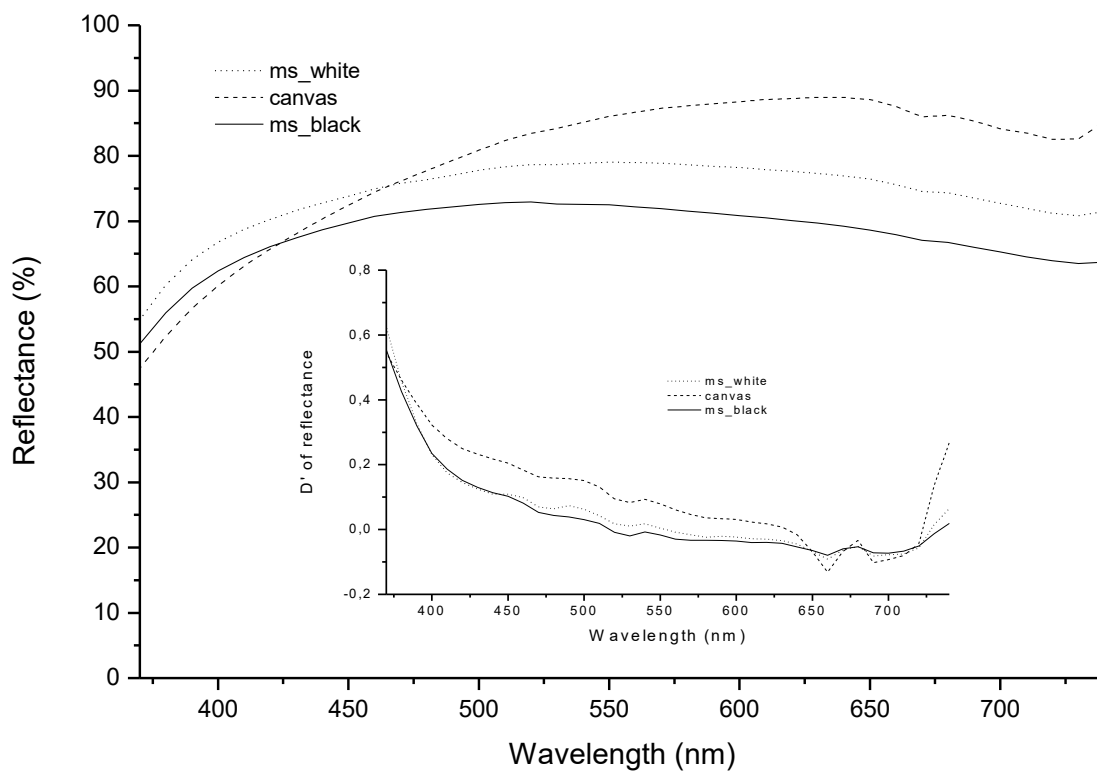
Cobalt violet



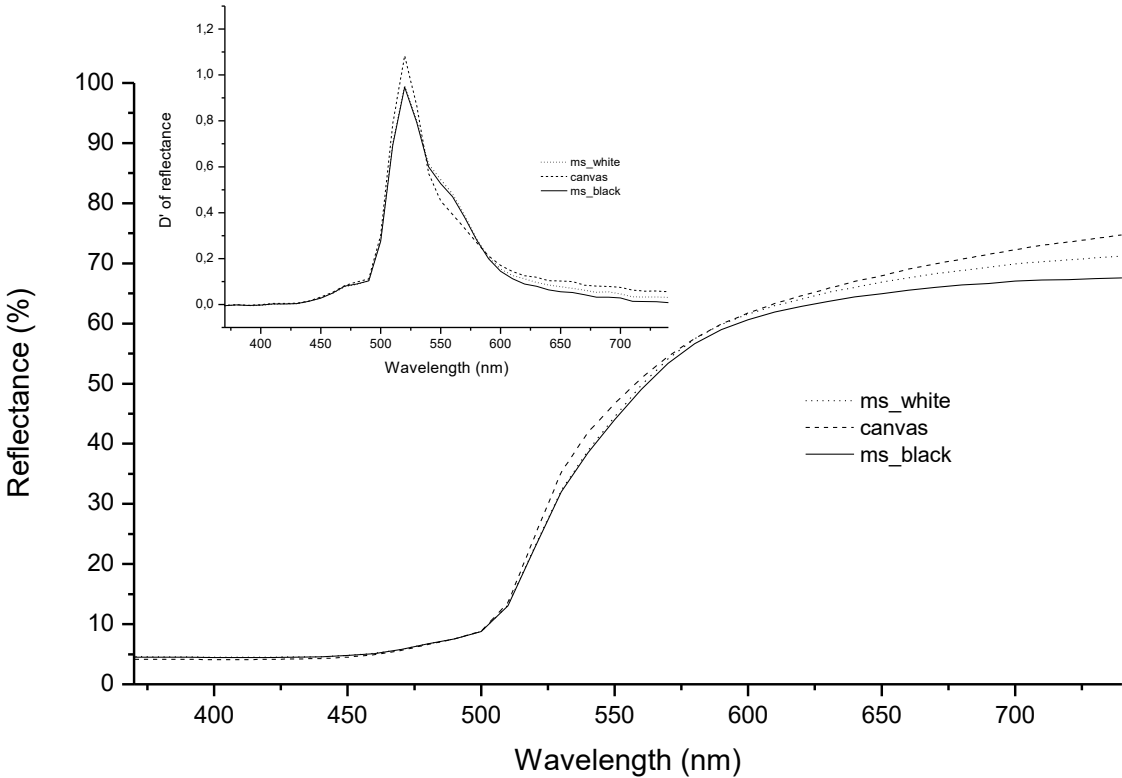
Mars brown



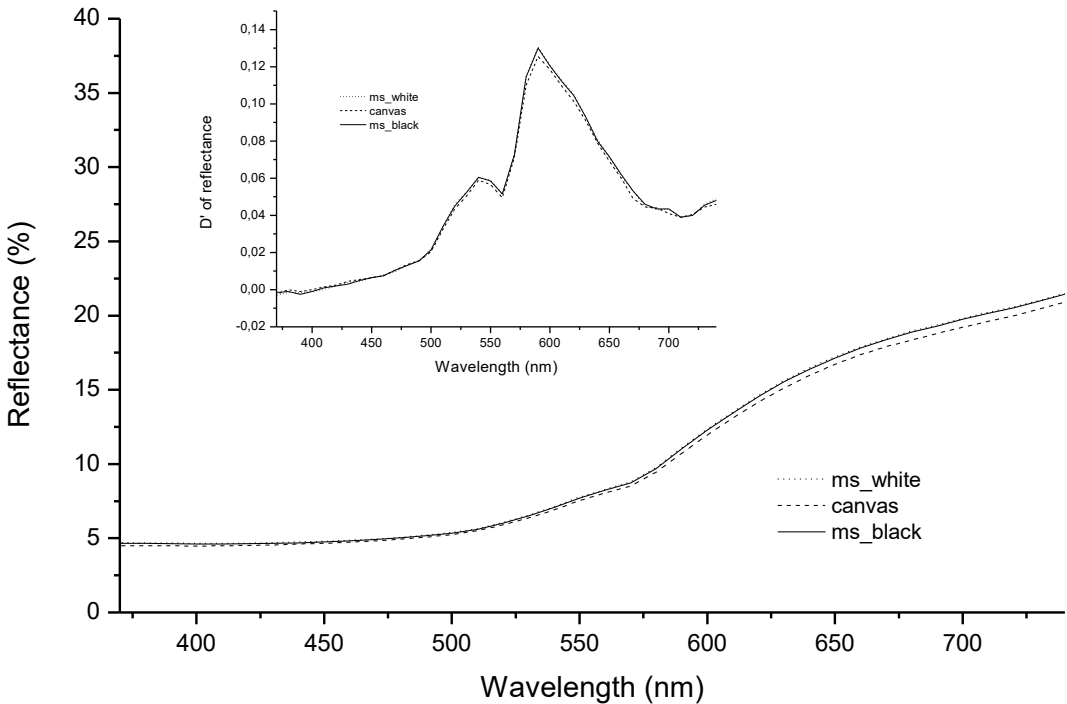
Lithopone



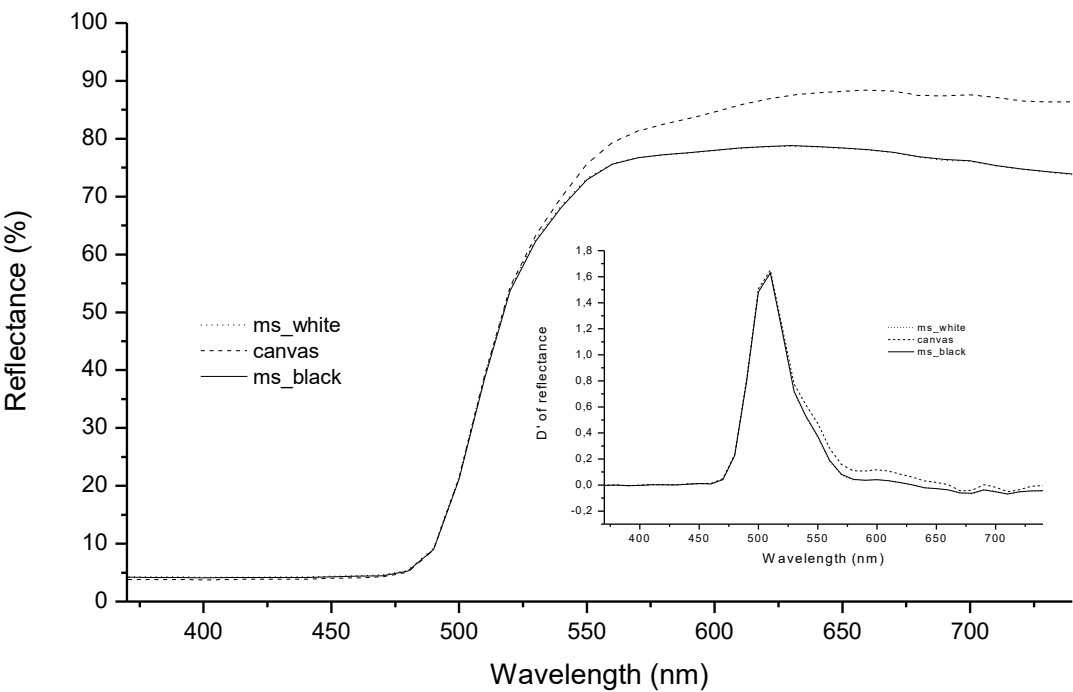
Orpiment



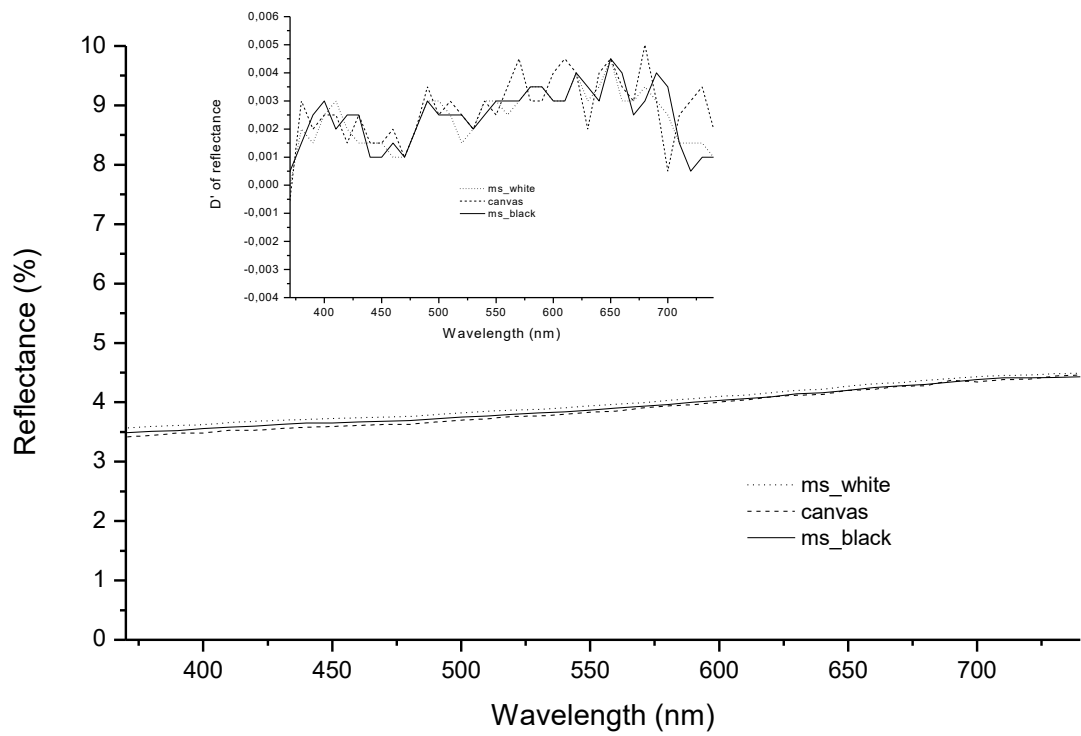
Manganese brown



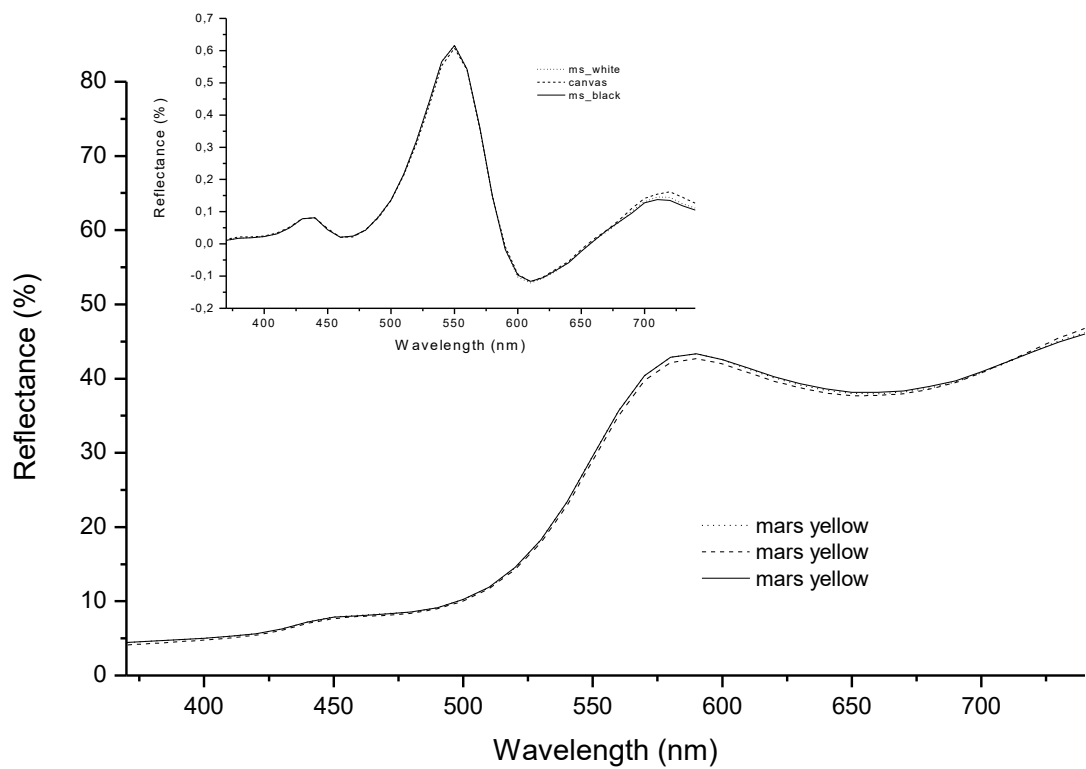
Cadmium yellow



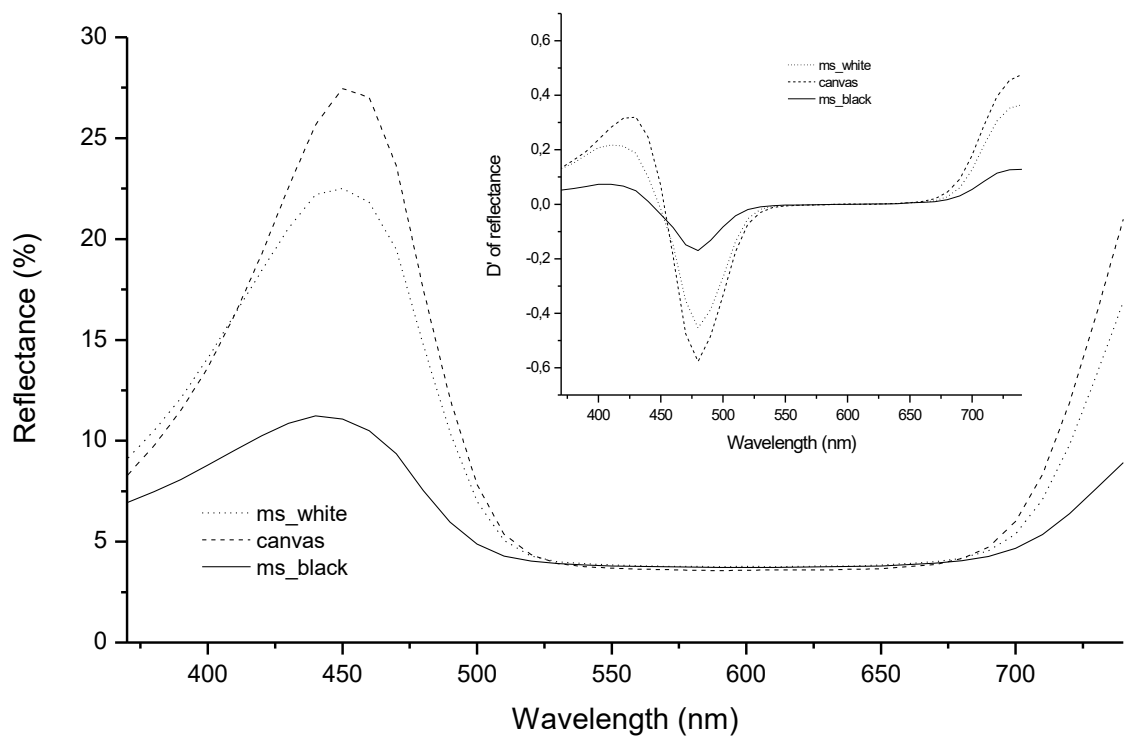
Mars black



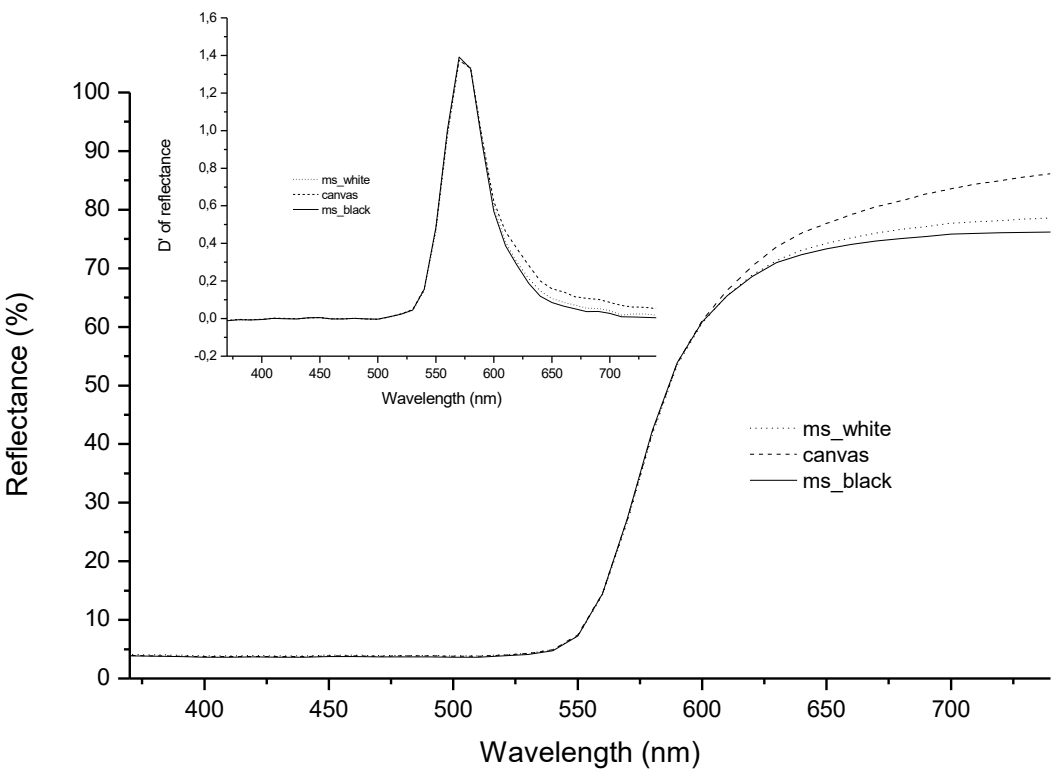
Mars yellow



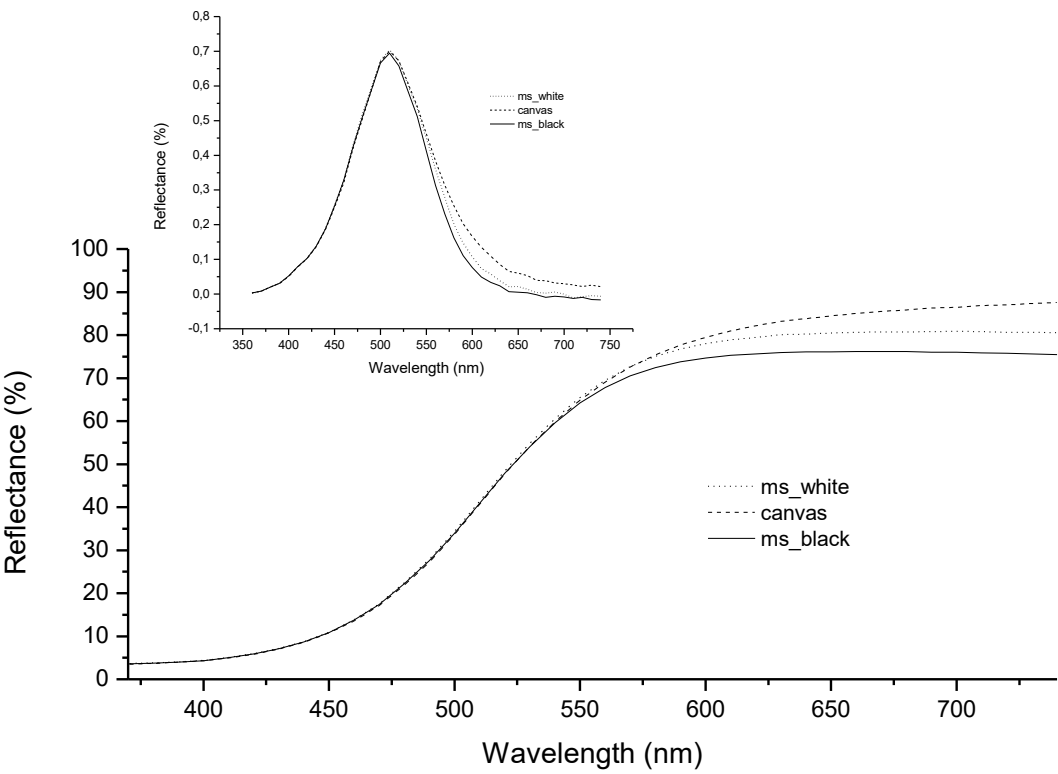
Light ultramarine blue



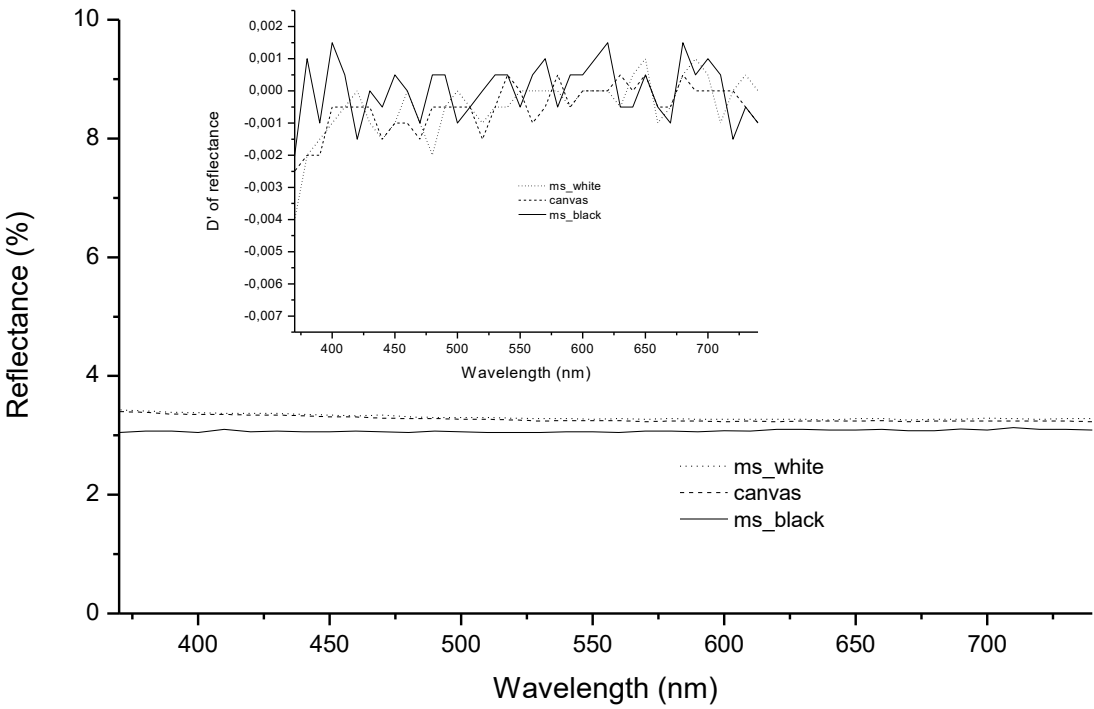
Saturn red



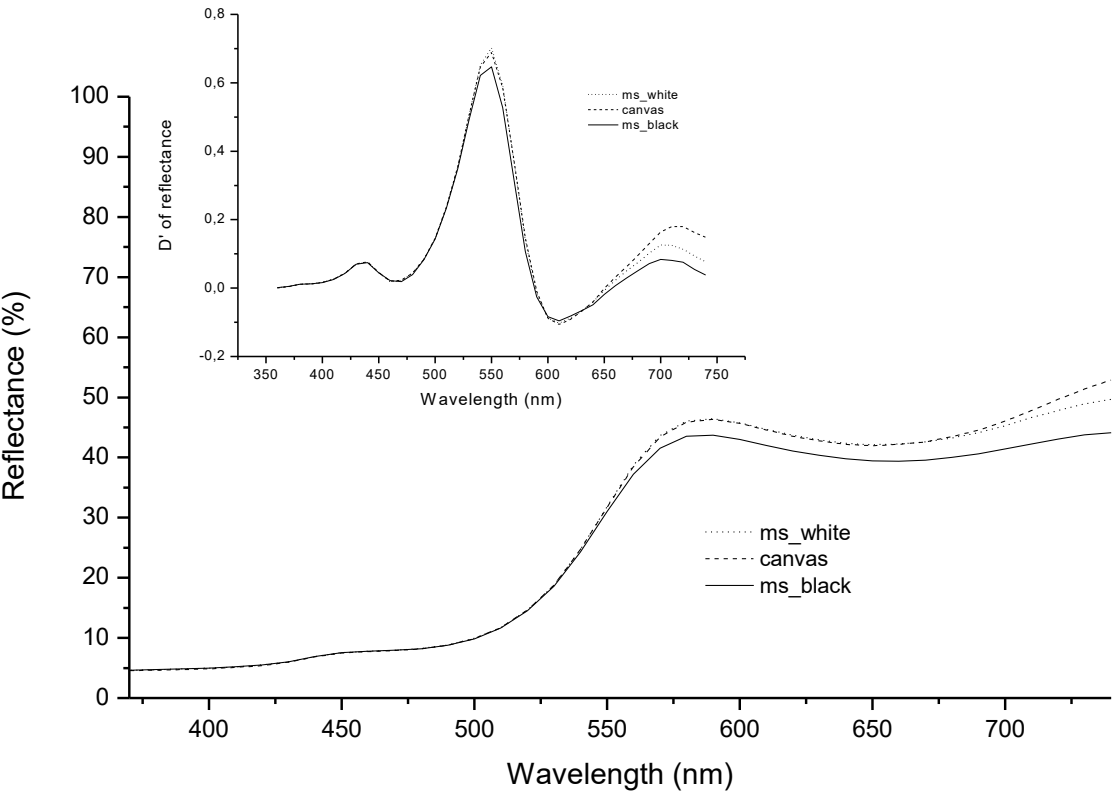
Lead-tin yellow



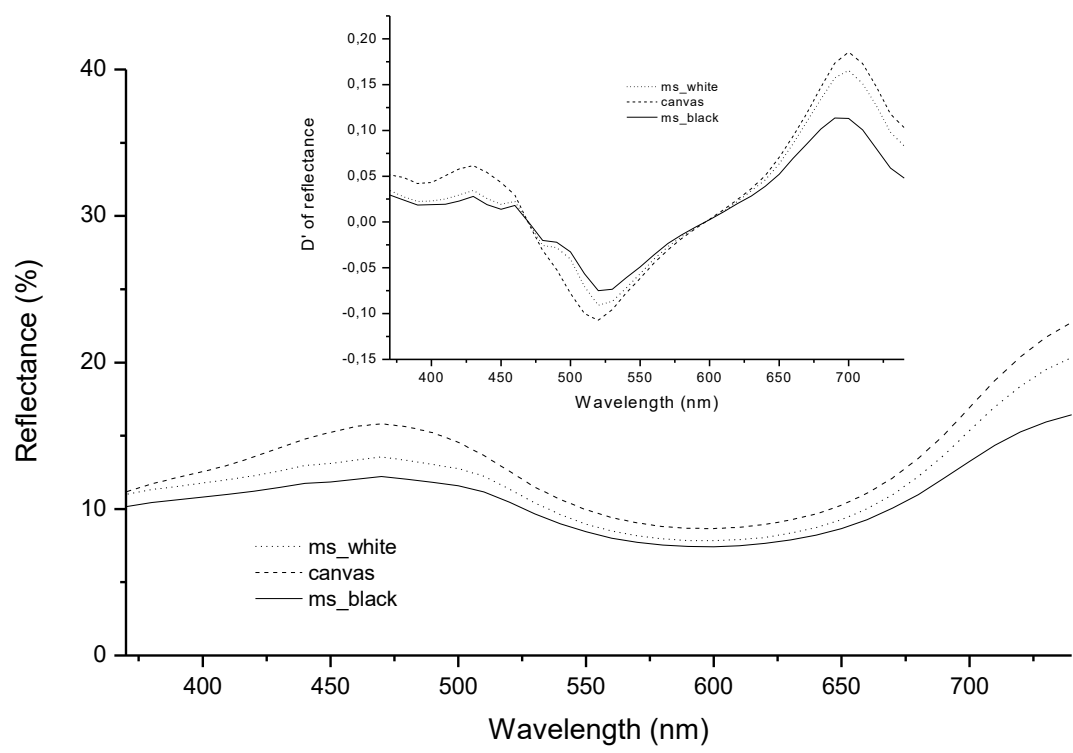
Carbon black



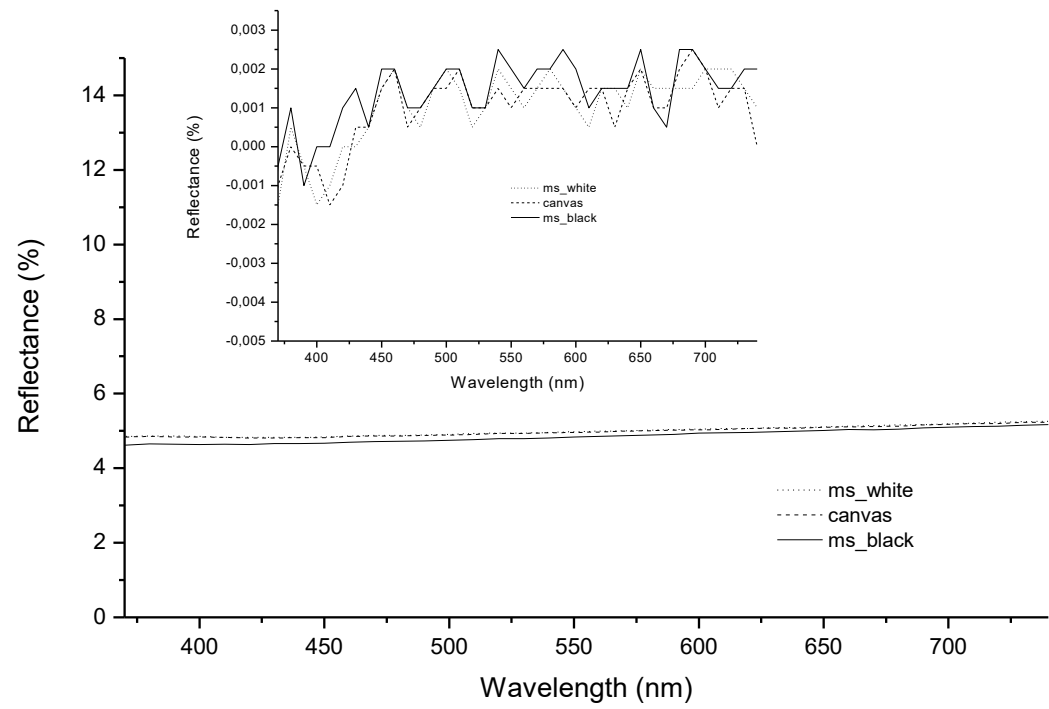
Yellow ochre



Ultramarine ash



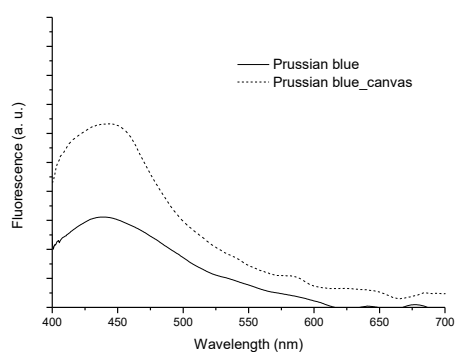
Manganese black



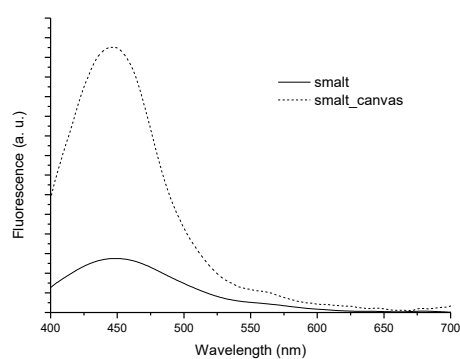
APPENDIX C: FLUORESCENCE SPECTRA with different backgrounds

We reports the fluorescence spectra of the forty-four pictorial layers spread on microscope slides laid on a black support (solid line) and those spread on the lead-white layer on canvas (dashed line).

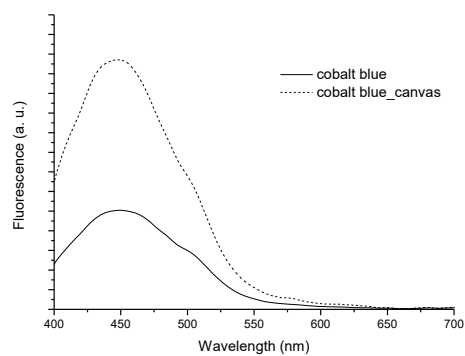
Prussian blue



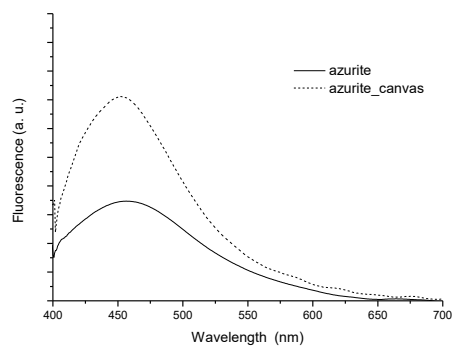
Smalt



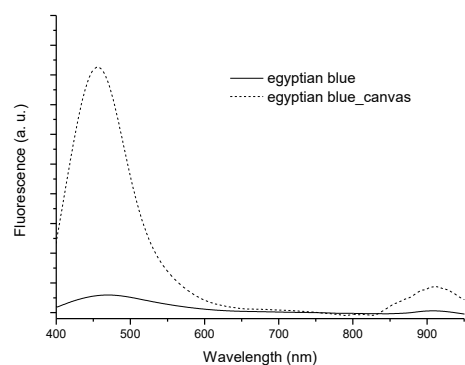
Cobalt blue



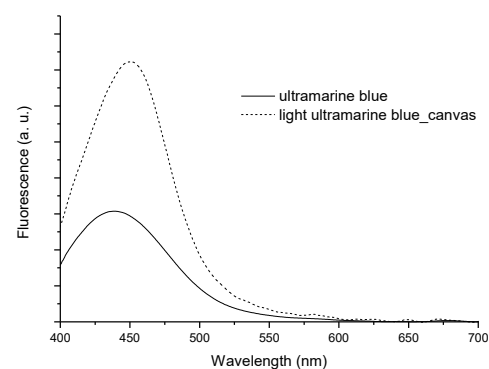
Azurite



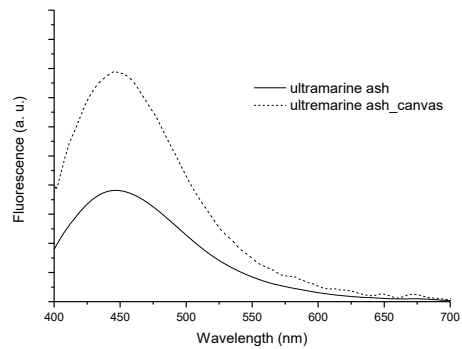
Egyptian blue



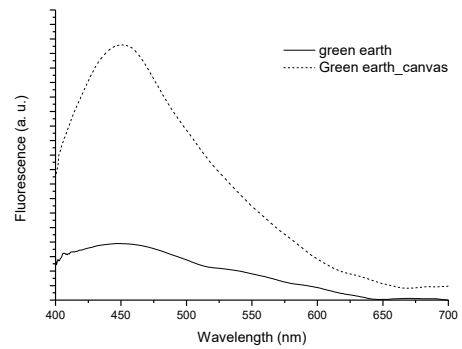
Ultramarine blue



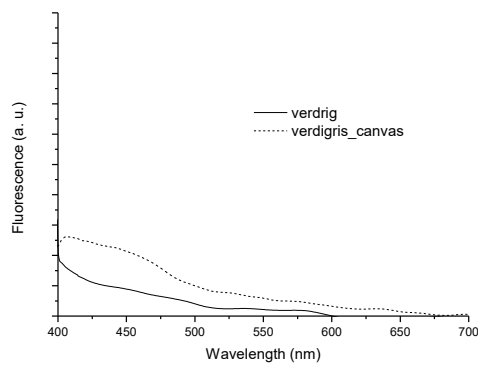
Ultramarine ash



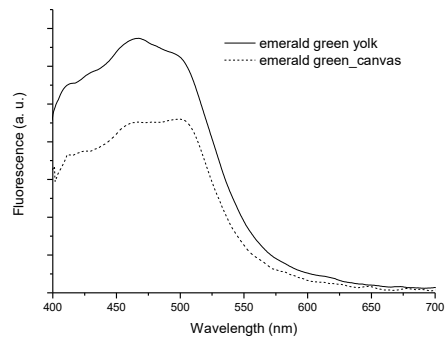
Green earth



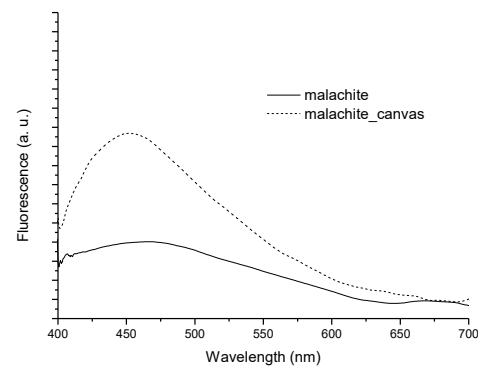
Verdigris



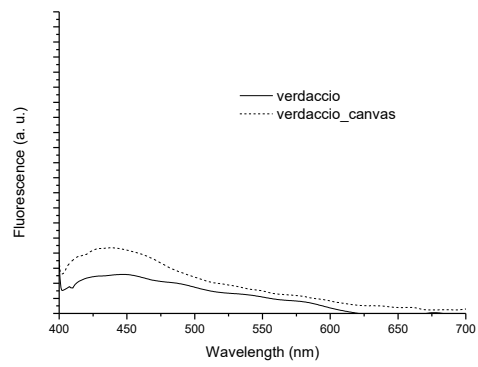
Emerald green



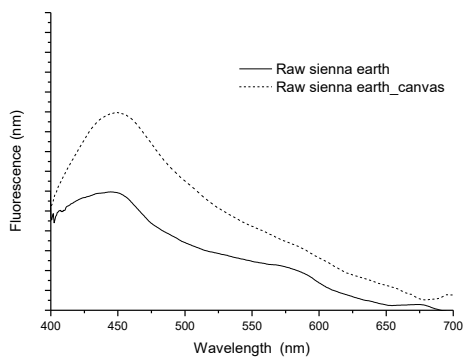
Malachite



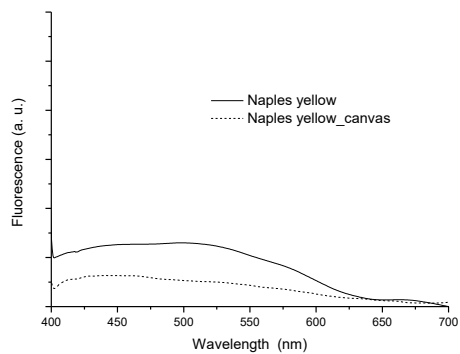
Verdaccio



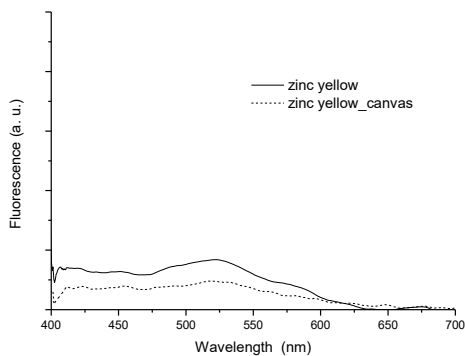
Raw sienna earth



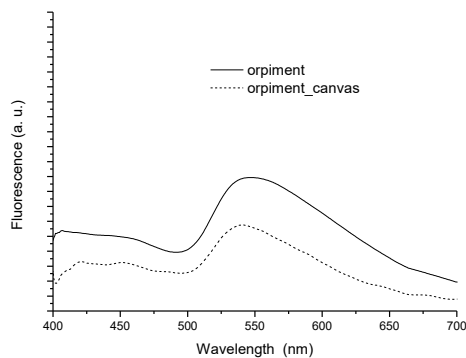
Naples yellow



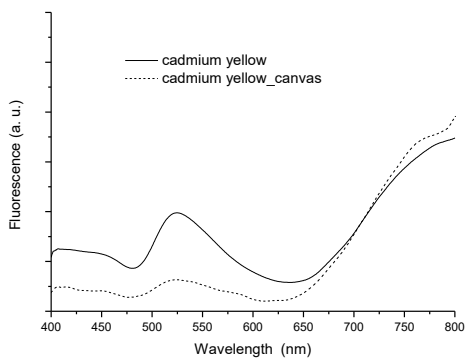
Zinc yellow



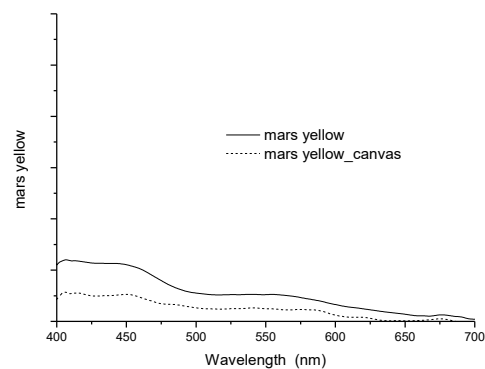
Orpiment



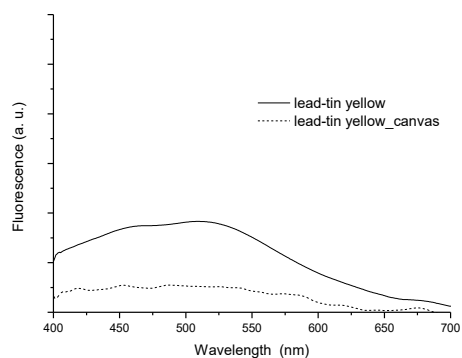
Cadmium yellow



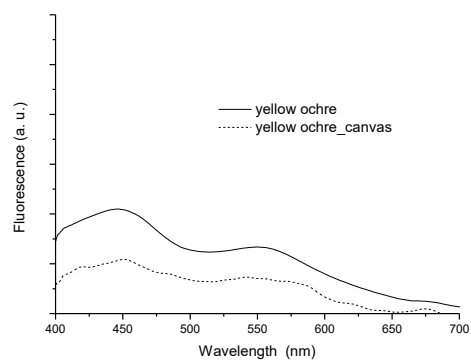
Mars yellow



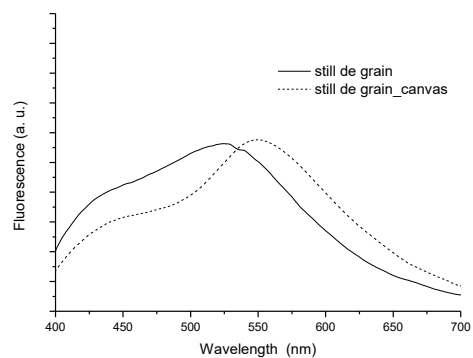
Lead-tin yellow



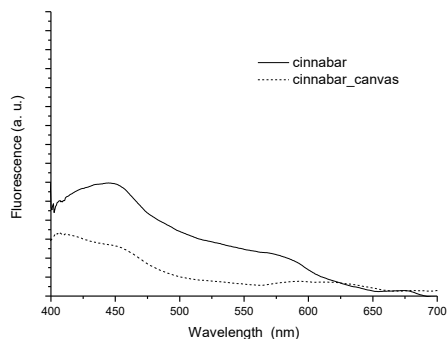
Yellow ochre



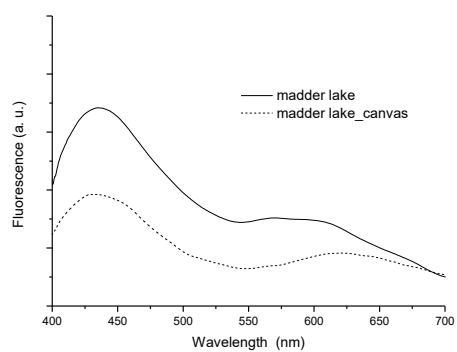
Still de grain



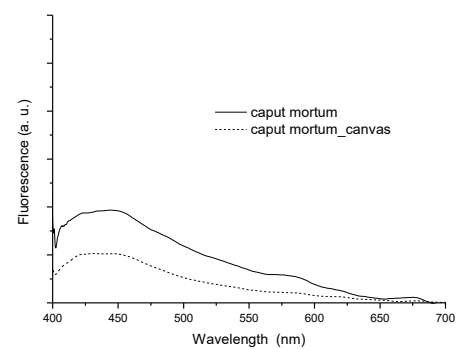
Cinnabar



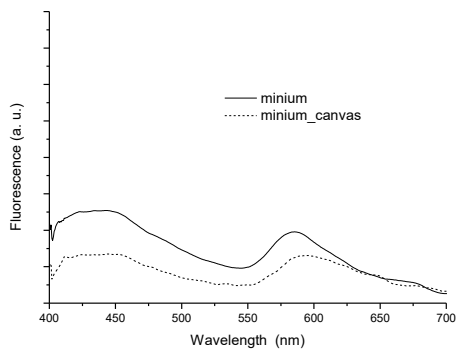
Madder lake



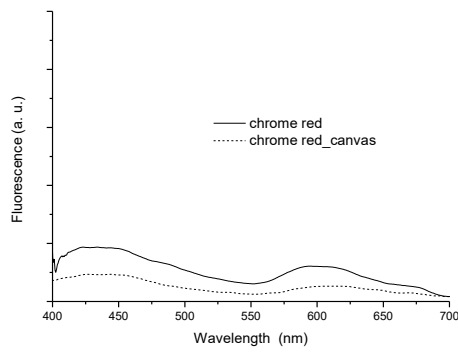
Caput mortum



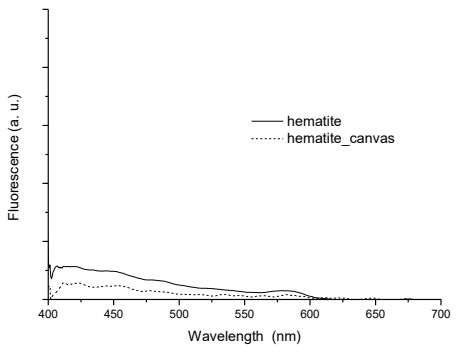
Minium



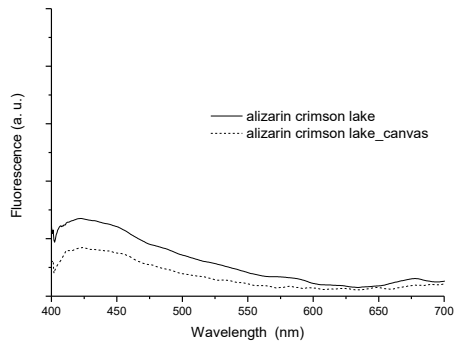
Chrome red



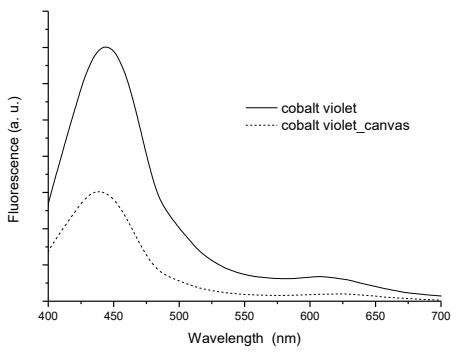
Hematite



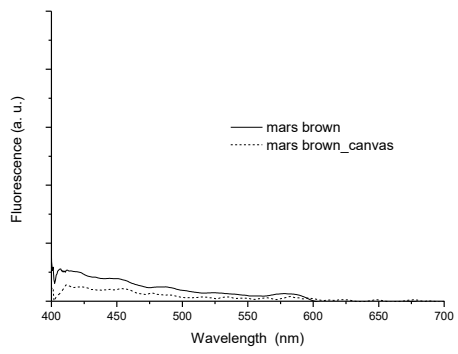
Alizarin crimson lake



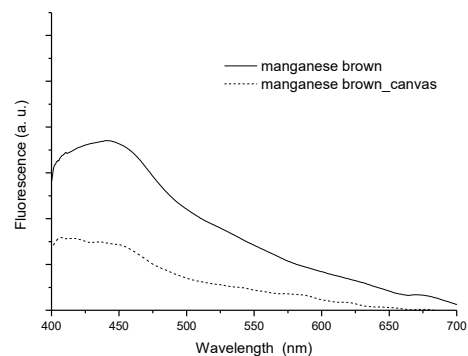
Cobalt violet



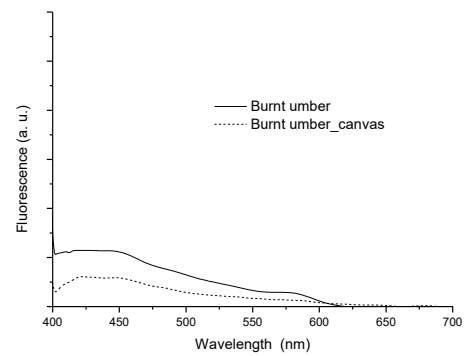
Mars brown



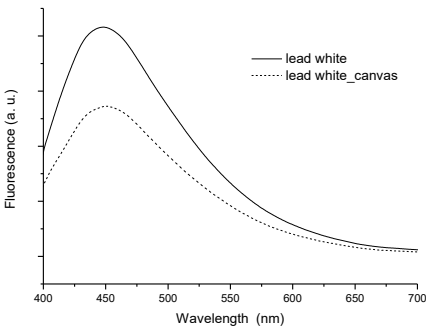
Manganese brown



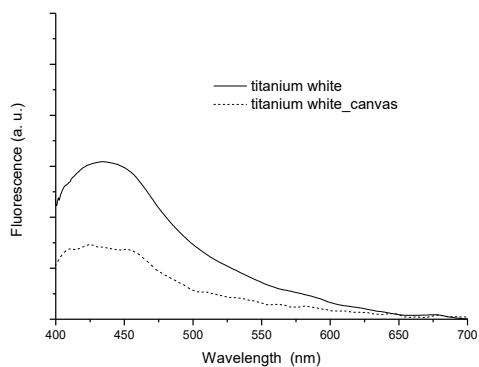
Burnt umber



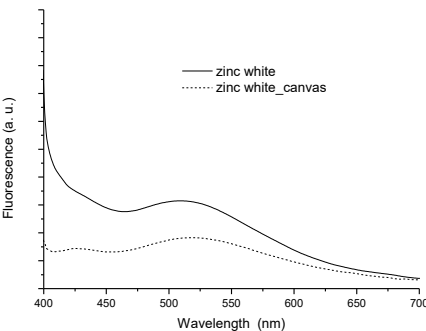
Lead white



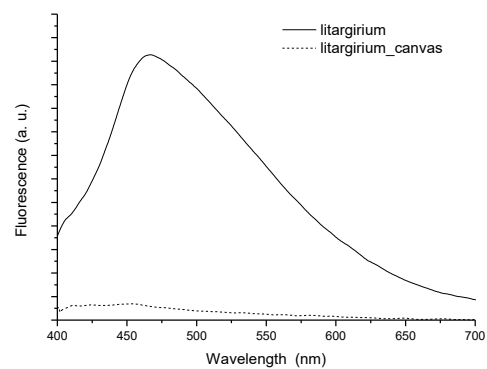
Titanium white



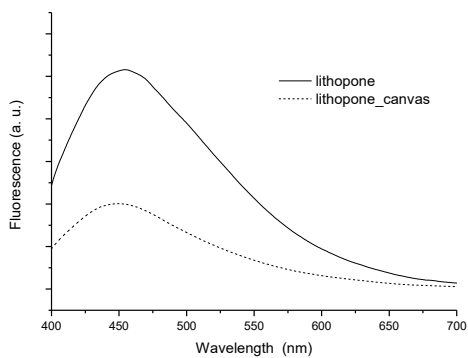
Zin white



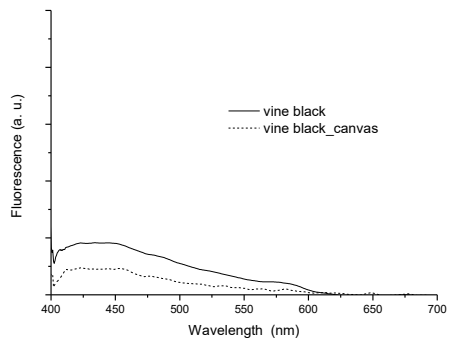
Litharge



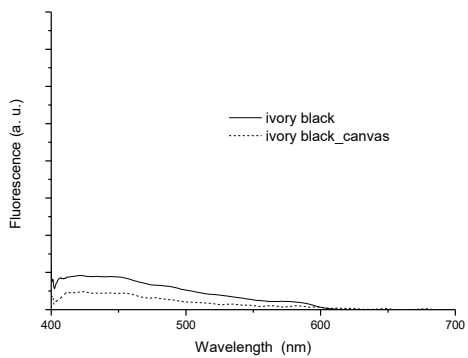
Lithopone



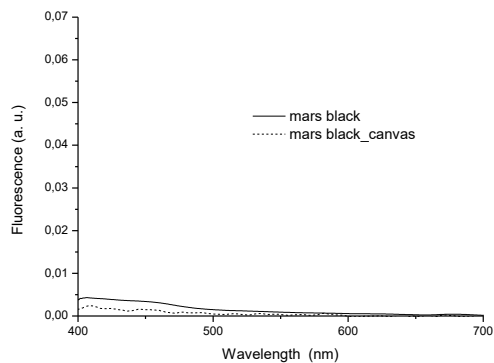
Vine black



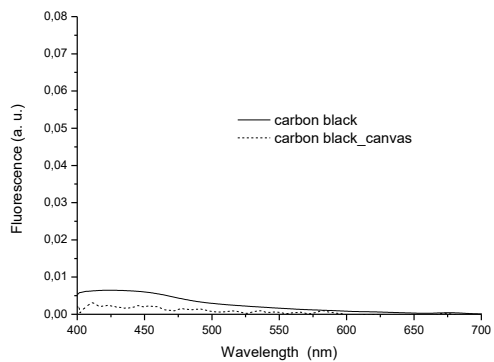
Ivory black



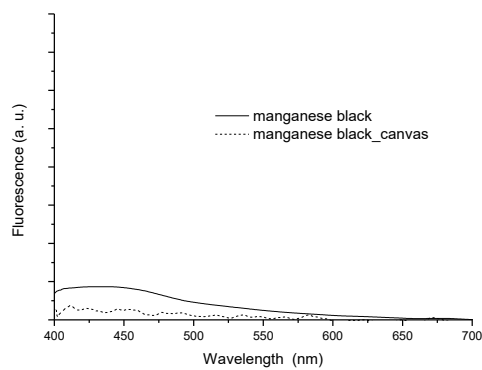
Mars black



Carbon black



Manganese black



APPENDICE D: XRF ANALYSIS

The analysed areas were reported as points in the paintings pictures. In the tables were reported the ED-XRF peaks areas for each point. Data refer to K- lines sum of each element, except for Sn, Hg, Pb, Ba, Au, Ag, (L lines). The “n. d.” indicates “not detected”.

1) “Virgin and the Child and Saint Catherine of Alessandria” by Matteo di Giovanni’s imitator

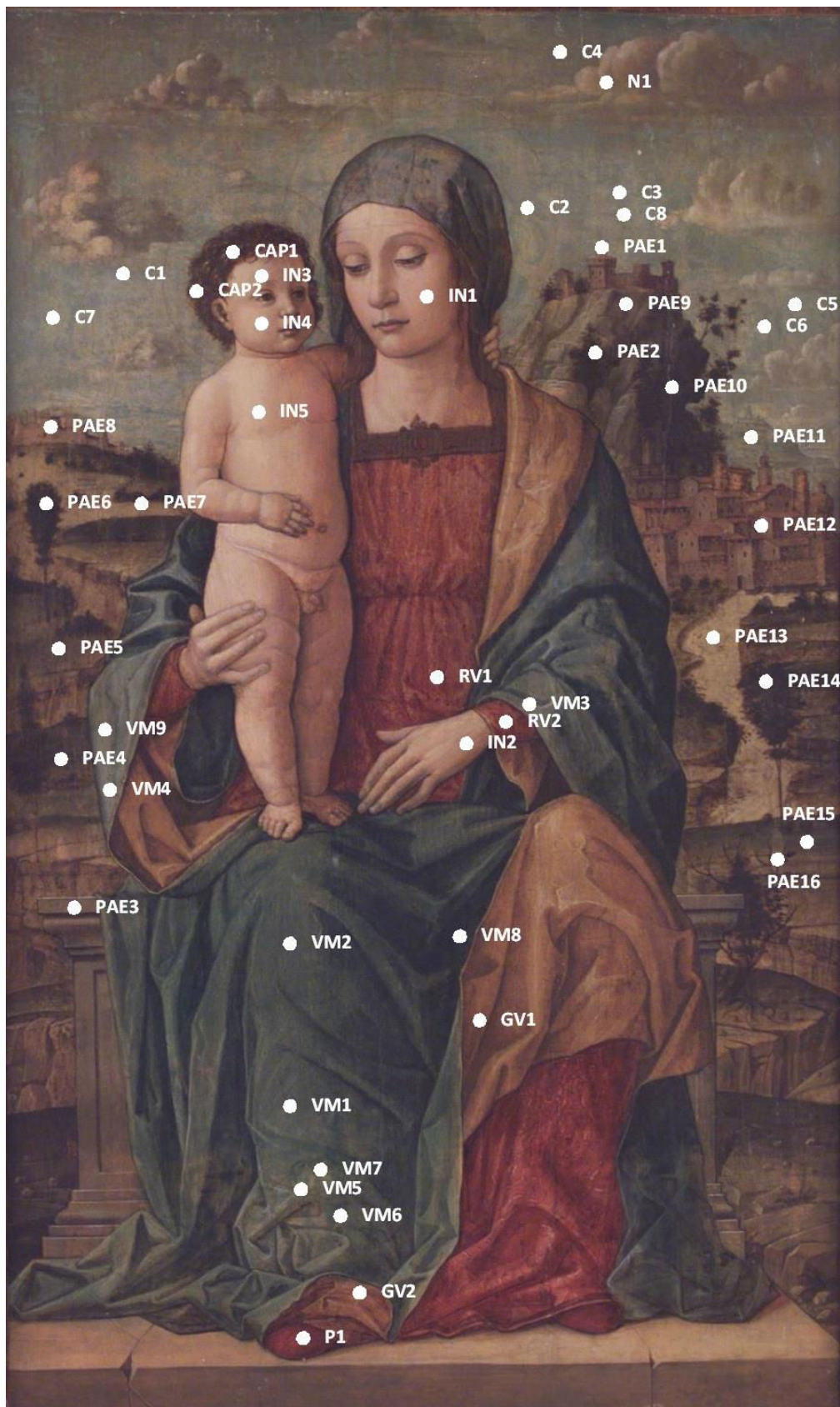


	S	Cl	K	Ca	Ti	Cr	Mn	Fe	Co	Ni	Cu	Zn	As	Sr	Sb	Ba	Au	Hg	Pb
SKY																			
6B	240	275	110	1977	2141	n.d.	n.d.	2102	n.d.	103	91783	4590	n.d.	976	n.d.	492	n.d.	n.d.	53763
7B	189	145	219	2886	595	162	n.d.	1242	n.d.	n.d.	142870	2915	n.d.	629	n.d.	n.d.	n.d.	n.d.	45783
RED AREAS																			
1A	645	n.d.	230	1974	n.d.	n.d.	33	116	n.d.	n.d.	1195	240	n.d.	249	n.d.	n.d.	n.d.	138	8207
2A	372	n.d.	271	1875	n.d.	n.d.	332	1417	d.n.	n.d.	597	627	n.d.	792	n.d.	34	n.d.	175	102271
3A	417	n.d.	327	2295	49	n.d.	149	1126	n.d.	n.d.	352	501	n.d.	259	n.d.	n.d.	n.d.	147	115636
4A*	46	n.d.	148	28808	3494	n.d.	1765	24272	n.d.	n.d.	282	5974	n.d.	1067	n.d.	439	n.d.	395	757
5A	756	110	0	1884	514	46	115	5967	n.d.	n.d.	600	1569	n.d.	727	n.d.	n.d.	n.d.	825	115765
6A*	270	184	59	6586	3727	n.d.	n.d.	9619	84	n.d.	n.d.	16426	n.d.	n.d.	n.d.	756	n.d.	17482	2976
7A	1064	58	0	1560	51	96	85	746	n.d.	n.d.	543	300	n.d.	n.d.	n.d.	n.d.	n.d.	56767	58387
8A	691	128	169	1295	1299	n.d.	107	6619	n.d.	n.d.	390	1829	n.d.	1266	n.d.	268	n.d.	784	91226
9A	504	288	181	3324	1446	n.d.	133	9430	n.d.	n.d.	784	2441	n.d.	2505	n.d.	n.d.	n.d.	229	67349
INCARNATE																			
1C	1516	170	0	786	n.d.	108	131	1308	n.d.	n.d.	335	395	n.d.	n.d.	n.d.	n.d.	n.d.	1150	123161
2C	385	n.d.	199	6332	4341	n.d.	n.d.	8779	n.d.	174	595	7232	n.d.	2661	n.d.	956	n.d.	640	38336
3C	867	n.d.	49	474	n.d.	n.d.	10	88	n.d.	1298	171	225	n.d.	n.d.	n.d.	n.d.	n.d.	21	3967
4C*	n.d.	60	n.d.	2762	2311	255	n.d.	3872	163	n.d.	257	n.d.	n.d.	718	n.d.	504	n.d.	n.d.	1559
5C	349	n.d.	n.d.	23054	3482	n.d.	184	10345	150	n.d.	320	6027	n.d.	3455	n.d.	76	n.d.	n.d.	208
6C	695	155	58	3080	2413	n.d.	n.d.	4623	n.d.	n.d.	286	4403	n.d.	1582	n.d.	516	n.d.	557	89475
7C	221	n.d.	100	12068	6089	n.d.	n.d.	8698	n.d.	101	287	14631	n.d.	2572	n.d.	1158	n.d.	867	14656
8C	1216	148	70	758	49	81	130	1974	n.d.	n.d.	601	490	n.d.	564	n.d.	n.d.	n.d.	1551	113014
9C	711	105	73	1383	2955	n.d.	n.d.	2662	86	n.d.	363	3809	n.d.	n.d.	n.d.	579	n.d.	874	125751
10C	1367	168	127	703	n.d.	n.d.	182	892	n.d.	n.d.	367	451	n.d.	n.d.	n.d.	n.d.	n.d.	804	133959
11C*	544	206	n.d.	4358	6062	n.d.	n.d.	3235	n.d.	n.d.	270	27310	n.d.	n.d.	n.d.	1174	n.d.	192	117089
12C	966	169	148	2117	54	81	114	4104	112	n.d.	528	585	n.d.	2472	n.d.	n.d.	n.d.	1683	64837

	S	Cl	K	Ca	Ti	Cr	Mn	Fe	Co	Ni	Cu	Zn	As	Sr	Sb	Ba	Au	Hg	Pb
13C	739	122	0	867	2642	n.d.	85	3938	3938	n.d.	272	3007	n.d.	1918	n.d.	495	n.d.	1023	98867
14C	1298	227	107	673	n.d.	n.d.	178	2077	n.d.	n.d.	430	497	n.d.	161	n.d.	n.d.	n.d.	880	128550
YELLOW AREAS																			
1D	902	152	n.d.	1562	719	n.d.	139	6248	n.d.	n.d.	412	1606	n.d.	n.d.	n.d.	134	n.d.	998	135386
2D	569	120	176	1638	651	n.d.	1188	17156	155	n.d.	617	1063	n.d.	1364	n.d.	79	n.d.	1186	86218
3D	721	129	n.d.	867	n.d.	n.d.	75	5279	138	n.d.	372	368	n.d.	392	n.d.	n.d.	n.d.	327	84102
4D	560	48	53	597	n.d.	40	53	3616	68	n.d.	394	271	n.d.	642	n.d.	22	n.d.	115	53317
5D	380	48	729	3181	n.d.	n.d.	113	5645	n.d.	n.d.	1096	551	n.d.	502	n.d.	n.d.	904	198	71261
GOLDEN INSERTS																			
1E	567	203	74	2924	2257	n.d.	n.d.	3632	120	n.d.	270	4406	n.d.	1462	n.d.	473	n.d.	1091	86498
2E	149	87	380	3421	643	n.d.	789	5422	n.d.	510	161215	9239	6993	1257	159	675	n.d.	363	17651
3E	n.d.	151	514	4590	74	n.d.	173	7753	n.d.	n.d.	857	520	n.d.	2953	n.d.	n.d.	n.d.	356	36654
4E	177	128	335	2451	88	n.d.	154	21771	320	n.d.	824	721	n.d.	1798	n.d.	n.d.	10350	n.d.	10839
5E	183	n.d.	558	7621	218	n.d.	135	34658	n.d.	679	316	4704	n.d.	3736	n.d.	n.d.	10338	126	1774
6E	251	116	294	5032	182	n.d.	123	3246	n.d.	147	226207	3704	n.d.	233	n.d.	n.d.	1227	312	53177
7E	292	71	391	3601	99	n.d.	187	28244	361	n.d.	658	529	n.d.	2870	n.d.	n.d.	7069	n.d.	6049
BLUE AREAS																			
1B	112	71	395	5892	56	n.d.	232	2536	n.d.	n.d.	287157	3822	2045	378	n.d.	n.d.	n.d.	n.d.	17128
2B	132	70	212	5373	829	n.d.	295	2196	n.d.	1593	295868	4920	2338	291	n.d.	1143	n.d.	n.d.	9611
3B*	116	68	n.d.	5127	3582	n.d.	368	24748	n.d.	575	165	13264	165	462	n.d.	1219	n.d.	16456	3674
4B*	131	n.d.	194	26552	8369	345	479	28694	n.d.	439	128	13201	1037	1256	n.d.	1499	n.d.	n.d.	641
5B	133	56	429	6620	138	n.d.	17	6331	110	n.d.	213368	12459	8152	1338	n.d.	n.d.	n.d.	n.d.	2193

*Retouched areas

2) “Virgin and the Child” by Venetian school



S	Cl	K	Ca	Ti	V	Cr	Mn	Fe	Co	Ni	Cu	Zn	As	Sr	Ag	Sn	Sb	Ba	Hg	Pb	Bi
---	----	---	----	----	---	----	----	----	----	----	----	----	----	----	----	----	----	----	----	----	----

RED CLOTHES

RV1	18	18	62	454	n.d.	n.d.	n.d.	48	1123	46	n.d.	480	1578	n.d.	n.d.	41	n.d.	n.d.	n.d.	n.d.	42199	n.d.
RV2	18	n.d.	60	459	n.d.	35	25	70	1111	n.d.	n.d.	468	756	684	188	129	n.d.	n.d.	n.d.	1005	24077	n.d.
P1	n.d.	n.d.	n.d.	1600	n.d.	n.d.	n.d.	46	4048	55	n.d.	50	7262	n.d.	120	100	n.d.	n.d.	167	1255	868	n.d.

INCARNATES

INC1	n.d.	38	16	373	n.d.	n.d.	n.d.	n.d.	1037	99	n.d.	204	6345	n.d.	135	65	31	n.d.	56	1781	40650	n.d.
INC2	n.d.	n.d.	37	277	n.d.	n.d.	n.d.	n.d.	2089	58	n.d.	239	985	n.d.	148	142	n.d.	n.d.	n.d.	326	22789	n.d.
INC3	62	22	n.d.	145	n.d.	n.d.	n.d.	n.d.	632	n.d.	n.d.	196	4073	n.d.	n.d.	n.d.	n.d.	n.d.	n.d.	248	43315	n.d.
INC4	38	n.d.	32	134	n.d.	n.d.	n.d.	n.d.	1047	n.d.	n.d.	200	12033	n.d.	93	n.d.	n.d.	n.d.	158	526	34603	146
INC5	n.d.	n.d.	n.d.	132	n.d.	n.d.	n.d.	47	626	51	n.d.	189	7994	n.d.	87	n.d.	n.d.	n.d.	n.d.	290	31393	n.d.

CHILD'S HAIR

CAP1	n.d.	n.d.	68	897	n.d.	n.d.	n.d.	n.d.	7790	73	n.d.	2861	1938	539	259	94	n.d.	n.d.	76	180	15517	n.d.
CAP2	n.d.	n.d.	80	1103	n.d.	n.d.	n.d.	n.d.	6971	n.d.	n.d.	4229	2723	n.d.	166	n.d.	n.d.	n.d.	56	n.d.	12285	n.d.

LANDSCAPE

PAE1	n.d.	n.d.	37	1009	n.d.	n.d.	n.d.	n.d.	2956	63	n.d.	986	1043	n.d.	218	164	n.d.	n.d.	n.d.	598	22174	n.d.
PAE2	n.d.	n.d.	86	752	n.d.	n.d.	n.d.	n.d.	3057	n.d.	n.d.	28832	1168	1159	n.d.	90	n.d.	n.d.	n.d.	n.d.	27356	n.d.
PAE3	n.d.	n.d.	n.d.	502	n.d.	n.d.	n.d.	n.d.	709	n.d.	n.d.	4247	682	706	n.d.	n.d.	n.d.	n.d.	n.d.	n.d.	45627	n.d.
PAE4	46	n.d.	236	6160	47	n.d.	n.d.	111	3695	n.d.	n.d.	50441	2115	3162	171	n.d.	n.d.	n.d.	n.d.	240	91318	n.d.
PAE5	50	n.d.	114	3060	n.d.	n.d.	n.d.	63	2649	118	n.d.	61732	2282	3800	151	n.d.	330	n.d.	n.d.	n.d.	91404	n.d.
PAE6	n.d.	64	186	1162	98	n.d.	n.d.	101	6345	131	n.d.	104982	4095	5163	144	n.d.	n.d.	n.d.	n.d.	171	78054	n.d.
PAE7	72	1330	n.d.	n.d.	128	128	5250	123	n.d.	14508	10090	1531	227	n.d.	n.d.	n.d.	n.d.	n.d.	102	n.d.	82634	n.d.
PAE8	n.d.	n.d.	56	1602	60	n.d.	n.d.	113	8046	138	n.d.	3754	1372	981	411	n.d.	n.d.	n.d.	n.d.	1237	72578	n.d.
PAE9	n.d.	67	171	2427	n.d.	n.d.	n.d.	103	5245	91	n.d.	35348	2938	1974	290	n.d.	n.d.	n.d.	98	159	88865	n.d.
PAE10*	n.d.	41	180	2341	n.d.	n.d.	60	113	14519	213	n.d.	60499	2903	3889	149	n.d.	n.d.	n.d.	91	351	72413	n.d.

	S	Cl	K	Ca	Ti	V	Cr	Mn	Fe	Co	Ni	Cu	Zn	As	Sr	Ag	Sn	Sb	Ba	Hg	Pb	Bi
PAE11	n.d.	n.d.	95	1682	n.d.	n.d.	n.d.	73	2399	n.d.	n.d.	68023	2853	n.d.	110	n.d.	n.d.	n.d.	n.d.	153	95271	n.d.
PAE12	122	n.d.	92	3166	48	n.d.	n.d.	60	8425	120	n.d.	2841	928	n.d.	535	n.d.	n.d.	n.d.	n.d.	3193	27795	n.d.
PAE13	n.d.	44	97	466	n.d.	n.d.	n.d.	110	3261	125	n.d.	11785	826	n.d.	204	n.d.	n.d.	n.d.	62	n.d.	88119	n.d.
PAE14	n.d.	47	190	2990	34	n.d.	n.d.	65	3205	123	n.d.	50754	1872	2883	154	n.d.	114	n.d.	n.d.	197	95391	227
PAE15	n.d.	n.d.	140	3458	82	n.d.	n.d.	56	7375	n.d.	n.d.	77096	4943	3962	149	131	n.d.	190	n.d.	146	52069	n.d.
PAE16	108	n.d.	397	12041	1853	n.d.	n.d.	91	10330	102	n.d.	4909	6987	n.d.	690	595	148	n.d.	3607	n.d.	16746	n.d.

*retouched areas